Experimental and Theoretical Characterization of a Hall Thruster Plume

by

Yassir Azziz

S.B., Aeronautics and Astronautics, Massachusetts Institute of Technology, 2001
S.M., Aeronautics and Astronautics, Massachusetts Institute of Technology, 2003

SUBMITTED TO THE DEPARTMENT OF AERONAUTICS AND ASTRONAUTICS
IN PARTIAL FULFILLMENT OF THE REQUIREMENTS FOR THE DEGREE OF

DOCTOR OF PHILOSOPHY
AT THE
MASSACHUSETTS INSTITUTE OF TECHNOLOGY

JUNE 2007

© 2007 Massachusetts Institute of Technology. All rights reserved.

Signature of Author . . . . . .
Department of Aeronautics and Astronautics
May 25, 2007

Certified by . . . . . .
Manuel Martinez-Sanchez
Professor of Aeronautics and Astronautics
Thesis Supervisor

Certified by . . . . . .
Daniel Hastings
Professor of Aeronautics and Astronautics and Engineering Systems

Certified by . . . . . .
Oleg Batishchev
Principal Research Scientist in Aeronautics and Astronautics

Certified by . . . . . .
Vladimir Hruby
President, Busek Company, Inc.

Accepted by . . . . . .
Jaime Peraire
Professor of Aeronautics and Astronautics
Chair, Committee on Graduate Students

Experimental and Theoretical Characterization of a Hall Thruster Plume

by

Yassir Azziz

Submitted to the Department of Aeronautics and Astronautics
on May 25, 2007 in partial fulfillment of the
requirements for the degree of
Doctor of Philosophy in Aeronautics and Astronautics
in the field of Space Propulsion

ABSTRACT

Despite the considerable flight heritage of the Hall thruster, the interaction of its plume with the spacecraft remains an important integration issue. Because in-flight data fully characterizing the plume in the space environment are currently unavailable, laboratory measurements are often used to understand plasma expansion and thereby minimize adverse plume-spacecraft interactions. However, experimental measurements obtained in ground facilities do not properly capture the wide angle plume effects most important for plume-spacecraft interactions because of the high background pressure of the laboratory environment. This research describes a method to determine the in-orbit plume divergence of a Hall thruster from laboratory measurements and characterizes the plasma properties of the in-orbit plume.

Plume measurements were taken with a Faraday probe and a Retarding Potential Analyzer at various background pressures to correlate changes in current density and ion energy distribution with changes in pressure. Results showed that current density increases linearly with background pressure at any given angle. This linear relationship was used to extrapolate laboratory measurements to zero background pressure, the in-orbit condition. Measurements from the Faraday probe and the Retarding Potential Analyzer were compared to ensure consistency. The effect of discharge voltage on plume divergence was also investigated. Measurements from both probes revealed that plume divergence decreases with an increase in discharge voltage.

Hall thruster plume expansion was also characterized using a numerical plume simulation. Comparison of plume simulation results for in-orbit conditions to extrapolated current density at zero pressure demonstrated good agreement. However, comparison of plume simulation and experimental results at a non-zero background pressure showed deficiencies in the collision model of the plume simulation.

An analytical expression for current density obtained using a self-similar plume model was compared to extrapolated current density at zero pressure and showed good agreement. In addition, an analytical model derived for current density of source ion collisions with neutrals was consistent with experimental measurements and confirms the deficiencies in the simulation's collision model.

In summary, experimental, numerical and analytical results indicate that the method of determining in-orbit plume divergence from laboratory measurements is valid and can be used to integrate Hall thrusters with the spacecraft.

Thesis Supervisor: Manuel Martinez-Sanchez
Title: Professor of Aeronautics and Astronautics

ACKNOWLEDGMENTS

This is the moment every graduate student awaits - writing the acknowledgments of a Ph.D. thesis. It means the end of a long and sometimes painful graduate career. It is really with mixed emotions that I depart this wonderful academic institution. I have just realized my lifetime academic goal of achieving a Doctorate degree at MIT. It would have been impossible for me to reach this point without the help of so many people.

I would like to thank my advisor, Professor Manuel Martinez-Sanchez, for his unwavering support, constant open door policy, and invaluable advice during all of my graduate years at MIT. I cannot thank him enough for his willingness to assist me in all of my endeavors. It was truly a pleasure working with him and I am going to miss my interactions with him. I would also like to heartily thank the members of my thesis committee Professor Daniel Hastings, Dr. Oleg Batishchev and Dr. Vlad Hruby for their guidance and support in my committee meetings. I would further like to thank Professor Paulo Lozano and Dr. James Szabo for reading my thesis and giving me valuable feedback.

Performing my thesis work would have been impossible without Busek Company. I would like to thank Dr. Vlad Hruby and Bruce Pote for their financial support and their guidance with my project. Not only did they allow me to work at their company, but they treated me as a friend and a colleague. I would also like to thank Dr. James Szabo for all of his exceptional help, whether it was with setting up my experiments or helping me with running the full PIC code.

I would not be at MIT without Dr. Malcolm Shuster who helped me with my MIT undergraduate application. Dr. Shuster was my freshmen advisor at the University of Florida. I really enjoyed our lengthy conversations. He always pushed me to transfer to MIT from the first conversation we had. I would not be at MIT without all the e-mails he sent to the MIT dean of admissions.

Graduate school would not be special without a great atmosphere. I would like to thank all members of SSL and SPL for organizing great outdoor activities and making MIT a fun place to be at. I would like to especially thank my best friends Noah Warner and Shannon Cheng. We have been through many tough times together at MIT from taking the Quals, the general exam, to thesis writing and the thesis defense. We have developed strong bonds over the years and this type of relationship is a lasting one. I am going to miss hanging out with them on a daily basis. I would also like to thank Shannon for her help with Aquila even when she was very swamped with her own work. A special thanks to Noah for all the nice conversations and fights we had.

I would like to dedicate this thesis to my parents. They have instilled in me the values of a good education and have driven me to succeed through all their love and support. I would also like to thank my brother Issam who was the first person to tell me about MIT when I was in Junior High. A special thanks to my sisters Samia, Amal and Ilhame for their love and teasing. When I get in trouble with my mom, they were always there to explain away my mishaps.

I would finally like to thank my wife Ania. She is my best friend. I would like to thank her for her understanding when I could not spend much time with her. She is smart, dedicated, principled and caring. Ania and I have grown together since we first met 9 years ago at MIT. She is such an amazing person. I am very proud of her. She is going to be a wonderful doctor. I am very lucky to be married to her.

Yassir Azziz
Cambridge, MA
May 25, 2007

TABLE OF CONTENTS

Abstract **3**

Acknowledgments **5**

Table of Contents **7**

List of Figures **11**

List of Tables **23**

Nomenclature **25**

Chapter 1. Introduction **29**

1.1 Hall Thrusters 30
1.1.1 Concept 30
1.1.2 Advantages 32
1.1.3 Issues 33
1.2 Review of Hall Thruster Plume Research 34
1.2.1 Computational Work 34
1.2.2 Experimental Work 35
1.3 Motivations 36
1.4 Objectives 37
1.5 Thesis Outline 38

Chapter 2. Experimental Apparatus **39**

2.1 BHT-1500 Hall Thruster 39
2.1.1 Thruster Description 39
2.1.2 Thruster Operation 42
2.1.3 Thruster Performance 44
2.2 Busek Vacuum Facility 46
2.3 Faraday Probe 49
2.3.1 Probe Description 49
2.3.2 Probe Design 50
2.3.3 Probe Construction 53
2.3.4 Design Verification 55

2.3.5 Probe Setup . . . 55
2.3.6 Sample Measurements . . . 57
2.4 Retarding Potential Analyzer . . . 59
2.4.1 Probe Description . . . 59
2.4.2 Probe Design . . . 59
2.4.3 Probe Construction . . . 64
2.4.4 Probe Setup . . . 66
2.4.5 Sample Measurements . . . 67

Chapter 3. Determination of In-Orbit Plume Divergence . . . 71

3.1 Causes of Plume Divergence . . . 72
3.1.1 Causes of Divergence Inside the Thruster Channel . . . 72
3.1.2 Causes of Divergence in the Plume . . . 74
3.2 Other Methods for Calculating Plume Divergence . . . 79
3.2.1 Analytical Methods . . . 80
3.2.2 Experimental Methods . . . 85
3.3 In-Orbit Extrapolation Method . . . 87
3.3.1 Current Density . . . 88
3.3.2 Ion Energy Distribution . . . 97
3.3.3 Experimental Consistency of the Extrapolation Method . . . 107
3.3.4 In-Orbit Plume Divergence . . . 115
3.3.5 Comparison to Previous Methods . . . 117
3.4 Effect of Discharge Voltage on Plume Divergence . . . 119
3.4.1 Current Density . . . 119
3.4.2 Ion Energy Distribution . . . 124
3.4.3 Plume Divergence . . . 127

Chapter 4. Numerical Plume Modeling . . . 131

4.1 Roadmap of Numerical Modeling . . . 131
4.2 Engine Code . . . 132
4.2.1 Code Description . . . 132
4.2.2 Code Performance . . . 134
4.3 Source Model . . . 136
4.3.1 Previous Source Model . . . 137
4.3.2 New Source Model . . . 146
4.4 Aquila . . . 150
4.4.1 Grid . . . 151

4.4.2 Potential Solver . . . 153
4.4.3 Collision Model . . . 154
4.5 Aquila Results . . . 154
4.5.1 Comparison of Source Models . . . 155
4.5.2 New Source Model Results . . . 156
4.5.3 Comparison of New Source Model to Experimental Data . . . 165
4.5.4 Discussion . . . 171

Chapter 5. Analytical Plume Models . . . 173

5.1 Analytical Estimate of Current Density from Source Ion Collisions with Tank Neutrals . . . 173
5.1.1 Charge Exchange Current Density . . . 176
5.1.2 Elastic Scattering Current Density . . . 177
5.1.3 Comparison to Experimental and Numerical Results . . . 178
5.2 Analytical Estimate of Current Density from Source Ion Collisions with Engine Neutrals . . . 181
5.3 Self-Similar Plume Model . . . 186

Chapter 6. Conclusions and Recommendations . . . 193

6.1 Summary of Results and Contributions . . . 193
6.1.1 Experimental Results . . . 193
6.1.2 Numerical Results . . . 196
6.1.3 Analytical Results . . . 197
6.2 Recommendations . . . 198
6.2.1 Experimental Work . . . 198
6.2.2 Numerical Work . . . 199

References . . . 201

Appendix A. Magnetic Field Effect on the BHT-1500 Plume . . . 207

A.1 Plume Structure . . . 207
A.1.1 Jet Mode . . . 207
A.1.2 Collimated Mode . . . 208
A.2 Plume Measurements . . . 211
A.2.1 Current Density . . . 211
A.2.2 Ion Energy Distribution . . . 215
A.2.3 Discussion . . . 221
A.3 Thermal Measurements . . . 223

A.4 Summary 229

LIST OF FIGURES

Figure 1.1 Cross-section of a Hall thruster. 31

Figure 1.2 Hall thruster concept diagram. 31

Figure 1.3 Plume-spacecraft interactions [15]. 33

Figure 2.1 The BHT-1500 Hall thruster. 40

Figure 2.2 Diagram of the BHT-1500 in cross-section. Not to scale. 41

Figure 2.3 Picture of the BHT-1500 operating in the minimum discharge current setting. The plume is blue in color. The thruster plume has a long narrow spike in the middle, which extends to approximately 20cm downstream from the exit plane. The bright spot in the top right corner is the cathode discharge plume. 43

Figure 2.4 Measured anode specific impulse versus discharge voltage for the BHT-1500 at a 2.44 mg/s xenon flow rate to the anode. 45

Figure 2.5 Measured anode efficiency versus discharge voltage for the BHT-1500 at a 2.44 mg/s xenon flow rate to the anode. 45

Figure 2.6 Busek T8 vacuum chamber. 46

Figure 2.7 Diagram of the propellant supply to the anode, cathode, and pressure variation feed lines. The pressure variation feed line is connected at the back of the tank. The flow rate of xenon is regulated by flow controllers with full scales of 20sccm, 50sccm, and 500sccm to the cathode, anode and pressure variation feed lines respectively. The background pressure of the tank is adjusted by xenon flow through the 500sccm flow controller. During thruster operation, the background pressure is 6×10^{-6} Torr when the xenon flow through the 500sccm flow controller is turned off. With 5mg/s xenon flow through the 500sccm controller, the background pressure increases to 1×10^{-5} Torr. 47

Figure 2.8 Top view diagram of the thruster setup inside the T8 vacuum tank. The tank is equipped with a thrust stand to characterize the performance of the BHT-1500. The tank is also setup to conduct plume diagnostics through an automated probe positioner system. 48

Figure 2.9 Schematic of a Faraday probe. The same voltage bias is applied to both the collector and the guard ring. The applied bias is negative with respect to the facility ground in order to repel electrons and collect only ion flux on the surface of the collector. 50

Figure 2.10 Drawing of the Faraday probe collector. The collector diameter is 4.45mm. The metallic rod attached to the back of the collector is used to apply a volt-

age bias and conduct current to the power supply. All dimensions are in millimeters. 51

Figure 2.11 Drawing of the Faraday probe guard ring. The outer diameter of the guard ring is 6.35mm. All dimensions are in millimeters. 51

Figure 2.12 Illustration of the Faraday probe assembly process. 54

Figure 2.13 Final Faraday probe design. 55

Figure 2.14 Picture of the experimental setup of the Faraday probe inside the T8. The probe is mounted on the automated positioner facing the BHT-1500. 56

Figure 2.15 Laser Alignment setup. The laser is used to calibrate the height and the angular position of the Faraday probe inside the T8. 56

Figure 2.16 Top-view schematic of the probe setup. 56

Figure 2.17 Electrical schematic of the Faraday probe. 57

Figure 2.18 Typical current density distribution for the BHT-1500 plume. The current density is plotted on a linear scale. V_d = 300V, I_d = 2A, P = 6.58×10^{-6} Torr, $\dot{m}_a$ = 2.44mg/s and sweep radius = 1m. 58

Figure 2.19 Typical current density distribution for the BHT-1500 plume. The current density is plotted on a logarithmic scale. V_d = 300V, I_d = 2A, P = 6.58×10^{-6} Torr, $\dot{m}_a$ = 2.44mg/s and sweep radius = 1m. 58

Figure 2.20 Schematic of a retarding potential analyzer and bias applied to grids. Diagram of RPA concept illustrates the effect of the grid bias on the plasma. 60

Figure 2.21 Picture of the retarding potential analyzer. 61

Figure 2.22 Cross-section schematic of the retarding potential analyzer [33]. . . . 61

Figure 2.23 Schematic showing the collimation angle of the retarding potential analyzer, θ_c. The RPA has a collimation angle of 22.8°. 62

Figure 2.24 Schematic showing that effectiveness of the grid bias depends on the grid opening. The grid opening must be smaller than the sheath thickness. If the grid opening is larger than the sheath thickness, the sheath will not extend across the opening within the grid. This creates a region within the grid opening where the plasma can pass through uninfluenced by the grid bias. The illustration on the left shows proper sizing of the grid opening. For a negatively biased grid, only ions pass through. The illustration on the right shows a grid with a large opening compared to the sheath thickness. For a negatively biased grid, both ions and electrons pass through. 63

Figure 2.25 Cross-section of the retarding potential analyzer. 65

Figure 2.26 Electrical schematic of the retarding potential analyzer. 66

Figure 2.27 Sample raw I-V curves at V_d = 300V, I_d = 2A, P = 7.5×10^{-6} Torr and $\dot{m}_a$ = 2.44mg/s. A smoothing spline fit is applied to the raw data. The plot on the left represents measurements 1m downstream from the exit plane of the thruster at -90°. The plot on the right represents measurements 1m downstream from the exit plane of the thruster at 0°. 67

Figure 2.28 Comparison of ion energy distributions obtained from raw data and spline-fit data. The thruster is operated at V_d=300V, I_d=2A, P=7.5×10^{-6} Torr and $\dot{m}_a$ = 2.44mg/s. The plot on the left represents measurements 1m downstream from the exit plane of the thruster at -90°. The plot on the right represents measurements 1m downstream from the exit plane of the thruster at 0°. 69

Figure 3.1 Schematic of neutral flow from the thruster. For simplicity, the calculation of the total neutral flow from the thruster assumes an internally mounted cathode and that the cathode and anode neutrals expand in the same direction. In reality, the cathode is mounted on top of the thruster as shown in Figure 2.1. 77

Figure 3.2 The uncorrected data curve represents current density measured with a Faraday probe at V_d = 300V, I_d = 2A, P = 6.58×10^{-6} Torr, $\dot{m}_a$ = 2.44mg/s and sweep radius = 1m. The corrected data curve represents the current density corrected for in-orbit conditions by extending the exponential portion of the current density in the 10-30° region to ±90°. 80

Figure 3.3 The uncorrected data curve represents current density measured with a Faraday probe at V_d = 300V, I_d = 2A, P = 6.58×10^{-6} Torr, $\dot{m}_a$ = 2.44mg/s and sweep radius = 1m. The corrected data are obtained by subtracting measured current density at 90° from the uncorrected data. 81

Figure 3.4 The forward data curve represents uncorrected current density measured with a Faraday probe facing the thruster exit plane; the backward data curve represents current density measured with a Faraday probe looking away from the thruster. The corrected data are the forward data minus the backward data. The measurements are obtained at V_d = 300V, I_d = 2A, $\dot{m}_a$ = 2.44mg/s and sweep radius = 1m. The plot on the top and the bottom show the correction method performed for P = 6.58×10^{-6} Torr and P = 2.02×10^{-5} Torr respectively. 83

Figure 3.5 Corrected current density at V_d=300V, $\dot{m}_a$ =2.44mg/s and sweep radius=1m. This figure shows that the correction made at 6.58×10^{-6} Torr does not match the correction made at 2.02×10^{-5} Torr, making this method unreliable for determining in-orbit current density and calculating plume divergence. 84

Figure 3.6 Pictures of different diagnostic instruments that are used to remove facility effects from plume measurements. 86

Figure 3.7 Effect of background pressure on current density. Vd = 300V, $\dot{m}_a$ = 2.44mg/s and sweep radius = 1m. 88

Figure 3.8 Effect of background pressure on current density at 90°, 75°, 60°, 45°, 10°, and 0°. V_d = 300V, $\dot{m}_a$ = 2.44mg/s and sweep radius = 1m. A linear relationship exits between current density and background pressure. Therefore, this linear relationship allows us to extrapolate the measurements to zero background pressure, the in-orbit condition. 92

Figure 3.9 Effect of background pressure on current density. V_d = 300V, $\dot{m}_a$ = 2.44mg/s and sweep radius = 1m. The in-orbit (P=0) current density is calculated using the extrapolation method. 93

Figure 3.10 Effect of background pressure on current density. V_d = 400V, $\dot{m}_a$ = 2.44mg/s and sweep radius = 1m. The in-orbit (P=0) current density is calculated using the extrapolation method. 93

Figure 3.11 Effect of background pressure on current density. V_d = 500V, $\dot{m}_a$ = 2.44mg/s and sweep radius = 1m. The in-orbit (P=0) current density is calculated using the extrapolation method. 94

Figure 3.12 Effect of background pressure on current density. V_d = 600V, $\dot{m}_a$ = 2.44mg/s and sweep radius = 1m. The in-orbit (P=0) current density is calculated using the extrapolation method. 94

Figure 3.13 Effect of background pressure on current density. V_d = 700V, $\dot{m}_a$ = 2.44mg/s and sweep radius = 1m. The in-orbit (P=0) current density is calculated using the extrapolation method. 95

Figure 3.14 Effect of background pressure on current density. V_d = 800V, $\dot{m}_a$ = 2.44mg/s and sweep radius = 1m. The in-orbit (P=0) current density is calculated using the extrapolation method. 95

Figure 3.15 Effect of background pressure on current density. V_d = 900V, $\dot{m}_a$ = 2.44mg/s and sweep radius = 1m. The in-orbit (P=0) current density is calculated using the extrapolation method. 96

Figure 3.16 Effect of background pressure on current density. V_d = 1000V, $\dot{m}_a$ = 2.44mg/s and sweep radius = 1m. The in-orbit (P=0) current density is calculated using the extrapolation method. 96

Figure 3.17 Effect of background pressure on ion energy distribution at angular positions of –90° to 0° in 10° increments. V_d = 300V, $\dot{m}_a$ = 2.44mg/s and sweep radius = 1m. Data are plotted on the same scale for angles between –90° and –50°. The retarding potential is referenced with respect to the facility ground whereas the discharge voltage is referenced with respect to the cathode potential, which is approximately –20V. To reference measurements with respect to the cathode potential, the ion energy distribution must be shifted to the right by 20V. 99

Figure 3.18 Effect of background pressure on ion energy distribution at angular positions of –90° to 0° in 10° increments. V_d = 400V, $\dot{m}_a$ = 2.44mg/s and sweep radius = 1m. Data are plotted on the same scale for angles between –90° and –50°.

The retarding potential is referenced with respect to the facility ground whereas the discharge voltage is referenced with respect to the cathode potential, which is approximately –20V. To reference measurements with respect to the cathode potential, the ion energy distribution must be shifted to the right by 20V. 100

Figure 3.19 Effect of background pressure on ion energy distribution at angular positions of –90° to 0° in 10° increments. V_d = 500V, $\dot{m}_a$ = 2.44mg/s and sweep radius = 1m. Data are plotted on the same scale for angles between –90° and –50°. The retarding potential is referenced with respect to the facility ground whereas the discharge voltage is referenced with respect to the cathode potential, which is approximately –21V. To reference measurements with respect to the cathode potential, the ion energy distribution must be shifted to the right by 21V. 101

Figure 3.20 Effect of background pressure on ion energy distribution at angular positions of –90° to 0° in 10° increments. V_d = 600V, $\dot{m}_a$ = 2.44mg/s and sweep radius = 1m. Data are plotted on the same scale for angles between –90° and –40°. The retarding potential is referenced with respect to the facility ground whereas the discharge voltage is referenced with respect to the cathode potential, which is approximately –22V. To reference measurements with respect to the cathode potential, the ion energy distribution must be shifted to the right by 22V. 102

Figure 3.21 Effect of background pressure on ion energy distribution at angular positions of –90° to 0° in 10° increments. V_d = 700V, $\dot{m}_a$ = 2.44mg/s and sweep radius = 1m. Data are plotted on the same scale for angles between –90° and –40°. The retarding potential is referenced with respect to the facility ground whereas the discharge voltage is referenced with respect to the cathode potential, which is approximately –20V. To reference measurements with respect to the cathode potential, the ion energy distribution must be shifted to the right by 20V. 103

Figure 3.22 Ion energy distribution at angular positions of –90° to 0° in 10° increments. V_d = 800V, $\dot{m}_a$ = 2.44mg/s, sweep radius = 1m and P = 7.5×10^{-6} Torr. Data are plotted on the same scale for angles between –90° and –40°. The retarding potential is referenced with respect to the facility ground whereas the discharge voltage is referenced with respect to the cathode potential, which is approximately –22V. To reference measurements with respect to the cathode potential, the ion energy distribution must be shifted to the right by 22V. 104

Figure 3.23 Effect of background pressure on ion energy distribution at angular positions of –90° to 0° in 10° increments. V_d = 900V, $\dot{m}_a$ = 2.44mg/s and sweep radius = 1m. Data are plotted on the same scale for angles between –90° and –40°. The retarding potential is referenced with respect to the facility ground whereas the discharge voltage is referenced with respect to the cathode potential, which is approximately –22V. To reference measurements with

respect to the cathode potential, the ion energy distribution must be shifted to the right by 22V. 105

Figure 3.24 Ion energy distribution at angular positions of –90° to 0° in 10° increments. V_d = 1000V, $\dot{m}_a$ = 2.44mg/s, sweep radius = 1m and P = 7.5×10^{-6} Torr. Data are plotted on the same scale for angles between –90° and –40°. The retarding potential is referenced with respect to the facility ground whereas the discharge voltage is referenced with respect to the cathode potential, which is approximately –21V. To reference measurements with respect to the cathode potential, the ion energy distribution must be shifted to the right by 21V. 106

Figure 3.25 Comparison of current density measured with the Faraday probe and current density calculated from RPA data. V_d = 300V, $\dot{m}_a$ = 2.44mg/s, sweep radius = 1m and P = 7.5×10^{-6} Torr. 108

Figure 3.26 Comparison of current density measured with the Faraday probe and current density calculated from RPA data. V_d = 300V, $\dot{m}_a$ = 2.44mg/s, sweep radius = 1m and P = 2.0×10^{-5} Torr. 108

Figure 3.27 The Faraday probe and RPA measurements are corrected for in-orbit conditions and compared to each other. The Faraday probe and RPA data at zero pressure are in good agreement. V_d = 300V, $\dot{m}_a$ = 2.44mg/s, sweep radius = 1m and P = 0 Torr. 109

Figure 3.28 Comparison of scaled and measured current density at a background pressure of 6.26×10^{-6} Torr. V_d = 300V and $\dot{m}_a$ = 2.44mg/s. 112

Figure 3.29 Comparison of scaled and measured current density at a background pressure of 1.07×10^{-5} Torr. V_d = 300V and $\dot{m}_a$ = 2.44mg/s. 112

Figure 3.30 Comparison of scaled and measured current density at a background pressure of 1.55×10^{-5} Torr. V_d = 300V and $\dot{m}_a$ = 2.44mg/s. 113

Figure 3.31 Comparison of scaled and measured current density at a background pressure of 2.15×10^{-5} Torr. V_d = 300V and $\dot{m}_a$ = 2.44mg/s. 113

Figure 3.32 Comparison of the scaled in-orbit current density from 0.5m and 0.75m sweep radii measurements and the in-orbit measurements at 1m. V_d = 300V and $\dot{m}_a$ = 2.44mg/s 114

Figure 3.33 Schematic of an ion energy distribution. The blue portion of the ion energy distribution is integrated to calculate the current collected due to source ions. 115

Figure 3.34 Plot of the in-orbit current density and the source ion current density. RPA measurements are used to determine the contribution of source ions to the total current density. V_d=300V, $\dot{m}_a$ =2.44mg/s and sweep radius=1m. . 116

Figure 3.35 Comparison of in-orbit current densities obtained using method A, method B and the extrapolation method. V_d = 300V, $\dot{m}_a$ = 2.44mg/s and sweep radius = 1m. 117

Figure 3.36 Comparison of in-orbit current densities obtained using method A, method B and the extrapolation method. V_d = 500V, $\dot{m}_a$ = 2.44mg/s and sweep radius = 1m. 118

Figure 3.37 Effect of discharge voltage on current density. V_d = 300-1000V, $\dot{m}_a$ = 2.44mg/s, sweep radius = 1m and P = 6.5×10^{-6} Torr. 119

Figure 3.38 Effect of discharge voltage on current density. V_d = 300-600V, $\dot{m}_a$ = 2.44mg/s, sweep radius = 1m and P = 6.5×10^{-6} Torr. 120

Figure 3.39 Effect of discharge voltage on current density. V_d = 700-1000V, $\dot{m}_a$ = 2.44mg/s, sweep radius = 1m and P = 6.5×10^{-6} Torr. 120

Figure 3.40 Effect of discharge voltage on utilization efficiency for the BHT-1500 operating at an anode flow rate of 2.44mg/s. 122

Figure 3.41 Effect of discharge voltage on in-orbit current density. V_d = 300-1000V, $\dot{m}_a$ = 2.44mg/s and sweep radius = 1m. 123

Figure 3.42 Effect of discharge voltage on source ion current density. V_d = 300-1000V, $\dot{m}_a$ = 2.44mg/s and sweep radius = 1m. 123

Figure 3.43 Effect of discharge voltage on the ion energy distribution at –90°. V_d = 300-1000V, $\dot{m}_a$ = 2.44mg/s, sweep radius = 1m and P = 7.5×10^{-6} Torr. . . . 125

Figure 3.44 Effect of discharge voltage on the ion energy distribution at –80°. V_d = 300-1000V, $\dot{m}_a$ = 2.44mg/s, sweep radius = 1m and P = 7.5×10^{-6} Torr. . . . 125

Figure 3.45 Effect of discharge voltage on the ion energy distribution at –70°. V_d = 300-1000V, $\dot{m}_a$ = 2.44mg/s, sweep radius = 1m and P = 7.5×10^{-6} Torr. . . . 126

Figure 3.46 Effect of discharge voltage on the ion energy distribution at –60°. V_d = 300-1000V, $\dot{m}_a$ = 2.44mg/s, sweep radius = 1m and P = 7.5×10^{-6} Torr. . . . 126

Figure 3.47 Effect of discharge voltage on the ion energy distribution at –50°. V_d = 300-1000V, $\dot{m}_a$ = 2.44mg/s, sweep radius = 1m and P = 7.5×10^{-6} Torr. . . . 127

Figure 3.48 Effect of discharge voltage on the 95% half-angle divergence for source ions. V_d = 300-1000V and $\dot{m}_a$ = 2.44mg/s, ... 128

Figure 3.49 Plot of the predicted peak electron temperature versus discharge voltage for the BHT-1500 using an area ratio of 0.3. 129

Figure 4.1 Flow diagram of the process that was followed to obtain numerical plume results and compare them to experimental measurements. 132

Figure 4.2 Computational grid for the BHT-1500. 133

Figure 4.3 Profiles of the anomalous Hall parameters that are imposed on the simulation. 135

Figure 4.4 Computational grid of the BHT-1500. Dimensions of the R and Z axes are in centimeters. The sampling plane is placed at z = 4cm because the potential due to the engine falls off by the time ions reach this axial location. . . 137

Figure 4.5 Single ion input parameters. v_z, v_r and $v\phi$ are axial, radial and azimuthal velocities respectively. V_d = 300V and $\dot{m}_a$ = 2.44mg/s. 141

Figure 4.6 Double ion input parameters. v_z, v_r and $v\phi$ are axial, radial and azimuthal velocities respectively. V_d = 300V and $\dot{m}_a$ = 2.44mg/s. 142

Figure 4.7 Neutral input parameters. v_z, v_r and $v\phi$ are axial, radial and azimuthal velocities respectively. Source neutrals represent neutral propellant that did not ionize. CEX neutrals represent ions that transformed into neutrals through charge exchange collisions. V_d = 300V and $\dot{m}_a$ = 2.44mg/s. 143

Figure 4.8 Comparison between an axial velocity distribution and a Maxwellian fit to the distribution. The raw distribution is a normalized axial velocity distribution for the near-side single ions generated by the full PIC code at r = 3.1cm. The Maxwellian fit is the distribution by which the near-side single ions are injected into the plume simulation at r = 3.1cm. 145

Figure 4.9 Ion flux lines. Ion flux at high angles is not captured by the sampling plane in the previous source model. 147

Figure 4.10 Radial sampling plane and a cylindrical sampling section are used to generate the new source model. 148

Figure 4.11 Geometrical parameters used to explain the method of projecting distribution functions generated from particles crossing the cylindrical section onto the radial plane. 149

Figure 4.12 3D view of the simulated vacuum tank. 151

Figure 4.13 Cross-section of simulation grid. 152

Figure 4.14 Grid resolution of thruster face. All particles are injected into the simulation domain of Aquila from the thruster face. 152

Figure 4.15 Current density from the previous and new source model compared to experimental results. The simulation results are obtained from source models generated for the anomalous Hall parameter profile depicted in case A. V_d = 300V, $\dot{m}_a$ = 2.44mg/s, P = 2.35×10^{-5} Torr and sweep radius = 1m. . . . 156

Figure 4.16 Contour plot of electron temperature obtained with Aquila using source model A. T_e is in eV. V_d=300V, $\dot{m}_a$ =2.44mg/s and P=2.35×10^{-5} Torr. . 158

Figure 4.17 Contour plot of electron temperature obtained with Aquila using source model B. T_e is in eV. V_d=300V, $\dot{m}_a$ =2.44mg/s and P=2.35×10^{-5} Torr. . 158

Figure 4.18 Contour plot of plasma potential obtained with Aquila using source model A. V_d = 300V, $\dot{m}_a$ = 2.44mg/s and P = 2.35×10^{-5} Torr. 159

Figure 4.19 Contour plot of plasma potential obtained with Aquila using source model B. V_d = 300V, $\dot{m}_a$ = 2.44mg/s and P = 2.35×10^{-5} Torr. 159

Figure 4.20 Logarithmic contour plot of the density of source ions obtained with Aquila using source model A. The source ions include both source single and double ions. V_d = 300V, $\dot{m}_a$ = 2.44mg/s and P = 2.35×10^{-5} Torr. 160

Figure 4.21 Logarithmic contour plot of the density of source ions obtained with Aquila using source model B. The Source ions include both source single and double ions. V_d = 300V, $\dot{m}_a$ = 2.44mg/s and P = 2.35×10^{-5} Torr. 160

Figure 4.22 Logarithmic contour plot of the density of charge exchange ions obtained with Aquila using source model A. The plotted charge exchange ions include ions produced through collisions with tank and engine neutrals. V_d = 300V, $\dot{m}_a$ = 2.44mg/s and P = 2.35×10^{-5} Torr. 161

Figure 4.23 Logarithmic contour plot of the density of charge exchange ions obtained with Aquila using source model B. The plotted charge exchange ions include ions produced through collisions with tank and engine neutrals. V_d = 300V, $\dot{m}_a$ = 2.44mg/s and P = 2.35×10^{-5} Torr. 161

Figure 4.24 Logarithmic contour plot of the density of elastically scattered ions obtained with Aquila using source model A. The plotted elastically scattered ions include ions produced through collisions with tank and engine neutrals. V_d = 300V, $\dot{m}_a$ = 2.44mg/s and P = 2.35×10^{-5} Torr. 162

Figure 4.25 Logarithmic contour plot of the density of elastically scattered ions obtained with Aquila using source model B. The plotted elastically scattered ions include ions produced through collisions with tank and engine neutrals. V_d = 300V, $\dot{m}_a$ = 2.44mg/s and P = 2.35×10^{-5} Torr. 162

Figure 4.26 Current density distribution of different ion populations obtained with Aquila using source model A. V_d = 300V, $\dot{m}_a$ = 2.44mg/s, P = 2.35×10^{-5} Torr and sweep radius = 1m. 164

Figure 4.27 Current density distribution of different ion populations obtained with Aquila using source model B. V_d = 300V, $\dot{m}_a$ = 2.44mg/s, P = 2.35×10^{-5} Torr and sweep radius = 1m. 164

Figure 4.28 Simulated current density obtained with Aquila using source model A compared to experimental data. V_d = 300V, $\dot{m}_a$ = 2.44mg/s, P = 2.35×10^{-5} Torr and sweep radius = 1m. 166

Figure 4.29 Simulated current density obtained with Aquila using source model A compared to experimental data. V_d = 300V, $\dot{m}_a$ = 2.44mg/s, P = 0 Torr and sweep radius = 1m. 166

Figure 4.30 Simulated current density obtained with Aquila using source model B compared to experimental data. V_d = 300V, $\dot{m}_a$ = 2.44mg/s, P = 2.35×10^{-5} Torr and sweep radius = 1m. 167

Figure 4.31 Simulated current density obtained with Aquila using source model B compared to experimental data. V_d = 300V, $\dot{m}_a$ = 2.44mg/s, P = 0 Torr and sweep radius = 1m. 167

Figure 4.32 Simulated current density obtained with Aquila using source model B compared to experimental data. V_d = 300V, $\dot{m}_a$ = 2.44mg/s, P = 2.35×10^{-5} Torr and sweep radius = 1m. The cross-section of charge exchange and elastic scattering ion-neutral collisions is doubled compared to the case in Figure 4.30. 169

Figure 4.33 Simulated current density obtained with Aquila using source model B compared to experimental data. V_d = 300V, $\dot{m}_a$ = 2.44mg/s, P = 0 Torr and sweep radius = 1m. The cross-section of charge exchange and elastic scattering ion-neutral collisions is doubled compared to the case in Figure 4.31. . 170

Figure 5.1 Schematic of a Hall thruster plume showing geometrical parameters used in the analytical model of current density from source ion collisions with tank neutrals. 174

Figure 5.2 Comparison of current density from source ion collisions with tank neutrals obtained from both analytical model and experimental data. In the plot, the experimental data are represented by squares and the analytical model is represented by solid lines. The comparison between experimental data and the analytical model is performed at different background pressures. A set of squares and a line plotted using the same color represent a comparison performed at the same background pressure. 179

Figure 5.3 Comparison of current density from source ion collisions with tank neutrals obtained from analytical and numerical models. The results of the numerical model are produced with Aquila using source models A and B. The comparison is performed at a background pressure of 2.35×10^{-5} Torr. 180

Figure 5.4 Schematic of a Hall thruster cross-section defining geometrical parameters that are used in the analytical estimation of current density from source ion collision with engine neutrals. 182

Figure 5.5 Extrapolated current density for zero pressure is plotted in the form expressed in Equation 5.40 using a γ value of 1.3. The small circles represent the data and the line represents the linear fit to the data. V_d = 300V, $\dot{m}_a$ = 2.44mg/s and sweep radius = 1m. 188

Figure 5.6 Extrapolated current density for zero pressure is plotted in the form expressed in Equation 5.40 using a γ value of 1.67. The small circles represent the data and the line represents the linear fit to the data. V_d = 300V, $\dot{m}_a$ = 2.44mg/s and sweep radius = 1m. 188

Figure 5.7 Comparison of current density obtained using the self-similar model to extrapolated current density for zero pressure. V_d = 300V, $\dot{m}_a$ = 2.44mg/s, sweep radius = 1m, γ = 1.3 and $\theta_{1/2}$ = 20.46°. 190

Figure 5.8 Comparison of current density obtained using the self-similar model to extrapolated current density for zero pressure. V_d = 300V, $\dot{m}_a$ = 2.44mg/s, sweep radius = 1m, γ = 1.67 and $\theta_{1/2}$ = 23.78°. 190

Figure A.1 Picture of the BHT-1500 operating in jet mode. 209

Figure A.2 Discharge oscillations of the thruster operating in jet mode. V_d = 500V and $\dot{m}_a$ = 2.44mg/s. 209

Figure A.3 Picture of the BHT-1500 operating in collimated mode. 210

Figure A.4 Discharge oscillations of the thruster operating in collimated mode. V_d = 500V and $\dot{m}_a$ = 2.44mg/s. 210

Figure A.5 Comparison of current densities obtained with the thruster operating in jet and collimated modes. V_d = 400V, $\dot{m}_a$ = 2.44mg/s, P = 7×10^{-6} Torr and sweep radius = 1m. 212

Figure A.6 Comparison of current densities obtained with the thruster operating in jet and collimated modes. V_d = 500V, $\dot{m}_a$ = 2.44mg/s, P = 7×10^{-6} Torr and sweep radius = 1m. 212

Figure A.7 Comparison of current densities obtained with the thruster operating in jet and collimated modes. V_d = 600V, $\dot{m}_a$ = 2.44mg/s, P = 7×10^{-6} Torr and sweep radius = 1m. 213

Figure A.8 Comparison of current densities obtained with the thruster operating in jet and collimated modes. V_d = 700V, $\dot{m}_a$ = 2.44mg/s, P = 7×10^{-6} Torr and sweep radius = 1m. 213

Figure A.9 Comparison of current densities obtained with the thruster operating in jet and collimated modes. V_d = 800V, $\dot{m}_a$ = 2.44mg/s, P = 7×10^{-6} Torr and sweep radius = 1m. 214

Figure A.10 Comparison of current densities obtained with the thruster operating in jet and collimated modes. V_d = 900V, $\dot{m}_a$ = 2.44mg/s, P = 7×10^{-6} Torr and sweep radius = 1m. 214

Figure A.11 Comparison of current densities obtained with the thruster operating in jet and collimated modes. V_d = 1000V, $\dot{m}_a$ = 2.44mg/s, P = 7×10^{-6} Torr and sweep radius = 1m. 215

Figure A.12 Comparison of ion energy distributions obtained with the thruster operating in jet and collimated modes. V_d = 400V, $\dot{m}_a$ = 2.44mg/s, P = 7×10^{-6} Torr and sweep radius = 1m. The retarding potential is referenced with respect to the facility ground whereas the discharge voltage is referenced with respect to the cathode potential, which is approximately –20V. 217

Figure A.13 Comparison of ion energy distributions obtained with the thruster operating in jet and collimated modes. V_d = 500V, $\dot{m}_a$ = 2.44mg/s, P = 7×10^{-6} Torr and sweep radius = 1m. The retarding potential is referenced with respect to the facility ground whereas the discharge voltage is referenced with respect to the cathode potential, which is approximately –21V. 218

Figure A.14 Comparison of ion energy distributions obtained with the thruster operating in jet and collimated modes. V_d = 600V, $\dot{m}_a$ = 2.44mg/s, P = 7×10^{-6} Torr and

sweep radius = 1m. The retarding potential is referenced with respect to the facility ground whereas the discharge voltage is referenced with respect to the cathode potential, which is approximately –22V. 219

Figure A.15 Comparison of ion energy distributions obtained with the thruster operating in jet and collimated modes. V_d = 700V, $\dot{m}_a$ = 2.44mg/s, P = 7×10^{-6} Torr and sweep radius = 1m. The retarding potential is referenced with respect to the facility ground whereas the discharge voltage is referenced with respect to the cathode potential, which is approximately –20V. 220

Figure A.16 Schematic of the ionization region in collimated and jet modes. The ionization region is thought to be closer to the anode for the collimated mode, which results in greater ion loss to the thruster walls. 222

Figure A.17 Schematic of the thermocouple setup used to measure the outer exit ring temperature. 223

Figure A.18 Outer exit ring temperature measurements. The thruster's discharge voltage is increased from 300-800V in 100V increments. The thruster is operated in collimated and jet modes starting from a discharge voltage of 400V. During these measurements, the anode flow rate is kept constant at 2.44mg/s. The data plotted in this figure are divided into several plots representing temperature measurements at each discharge voltage and show when the thruster is operating in jet and collimated modes. 225

Figure A.19 Outer exit ring temperature of the thruster operating at a discharge voltage of 300V and an anode flow rate of 2.44mg/s. The thruster is run in jet mode. 226

Figure A.20 Outer exit ring temperature of the thruster operating at a discharge voltage of 400V and an anode flow rate of 2.44mg/s. The thruster is run in both jet and collimated modes. 226

Figure A.21 Outer exit ring temperature of the thruster operating at a discharge voltage of 500V and an anode flow rate of 2.44mg/s. The thruster is run in both jet and collimated modes. 227

Figure A.22 Outer exit ring temperature of the thruster operating at a discharge voltage of 600V and an anode flow rate of 2.44mg/s. The thruster is run in both jet and collimated modes. 227

Figure A.23 Outer exit ring temperature of the thruster operating at a discharge voltage of 700V and an anode flow rate of 2.44mg/s. The thruster is run in both jet and collimated modes. 228

Figure A.24 Outer exit ring temperature of the thruster operating at a discharge voltage of 800V and an anode flow rate of 2.44mg/s. The thruster is run in both jet and collimated modes. 228

LIST OF TABLES

TABLE 2.1 Estimates of the BHT-1500 plasma parameters used to calculate the Debye length at various distances from the thruster exit plane. 52

TABLE 2.2 Calculation of the maximum spacing between the electron repelling and the ion retarding grids to avoid space charge limitation. A potential difference, V, of 30V was used in this calculation because it is the potential at which the space charge effects are greatest. 64

TABLE 2.3 Dimensions of the ceramic insulating washers. 65

TABLE 3.1 Mean free path of Coulombic collisions. 75

TABLE 3.2 Ion-neutral mean free path for elastic scattering and CEX collisions. . 78

TABLE 4.1 Results of the full PIC for different anomalous Hall parameter profiles at V_d = 300V and $\dot{m}_a$ = 2.44mg/s. 136

TABLE 4.2 Source model temperatures in eV for single ions. 144

TABLE 4.3 Source model temperatures in eV for double ions. 144

TABLE 4.4 Source model temperatures in eV for neutrals. 144

NOMENCLATURE

A	thruster exit area [m^2]
A_c	probe collection area [m^2]
$A_{cathode}$	cathode orifice area [m^2]
A_{det}	detector collection area [m^2]
A_{eff}	effective collection area of the RPA [m^2]
$\underline{c}$	beam exhaust speed [m/s]
c_e	mean electron thermal speed [m/s]
c_n	neutral thermal speed [m/s]
c_r	relative velocity [m/s]
e	electron charge [C]
$f()$	distribution function
H	height of discharge channel [m]
I	probe current [A]
I_b	beam current [A]
$I_{background}$	current from ionization of background neutrals [A]
I_d	discharge current [A]
I_{in}	current from source ion collisions with neutrals [A]
I_{rpa}	current collected by the RPA [A]
j	current density [A/m^2]
j_{cex}	charge exchange current density [A/m^2]
j_{in}	current density from ion-neutral collisions [A/m^2]
j_{sc}	elastic scattering current density [A/m^2]
k	Boltzmann constant [J/K]
L	length of vacuum chamber [m]
$\dot{m}$	mass flow rate [mg/s]
$\dot{m}_a$	anode flow rate [mg/s]
$\dot{m}_c$	cathode flow rate [mg/s]
$\dot{m}_i$	ion flow rate [mg/s]
$\dot{m}_n$	neutral flow rate [mg/s]
m_e	electron mass [kg]
m_i	ion mass [kg]
m_n	neutral mass [kg]
n	density [m^{-3}]
n_e	electron density [m^{-3}]
n_{eo}	reference electron density [m^{-3}]
n_i	ion density [m^{-3}]
n_n	neutral density [m^{-3}]
$ln\Lambda_e$	Coulomb logarithm
$ln\Lambda_i$	Coulomb logarithm
P	tank pressure [Torr]

P_b	base pressure [Torr]
P_c	corrected pressure [Torr]
P_i	indicated pressure [Torr]
q	particle charge [C]
r	sweep radius [m]
$\overline{R}$	mid-channel radius [m]
R_{cex}	production rate of charge exchange ions [$m^{-3}s^{-1}$]
R_{in}	rate of ion-neutral collisions [$m^{-3}s^{-1}$]
T	thrust [N]
T_e	electron temperature [K]
T_{eo}	reference electron temperature [K]
T_i	ion temperature [K]
T_n	neutral temperature [K]
t_s	sheath thickness [m]
T_w	wall temperature [K]
u_i	ion velocity [m/s]
v	particle velocity [m/s]
V_d	discharge voltage [V]
v_i	net ion velocity [m/s]
$\underline{v}_{ir}$	ion radial velocity [m/s]
$\underline{v}_r$	average radial velocity [m/s]
$\underline{v}_z$	average axial velocity [m/s]
v_ϕ	average azimuthal velocity [m/s]
Z	ion charge state
β_a	anomalous Hall parameter
γ	specific heat ratio
ε_o	permittivity of free space [F/m]
η_u	thruster utilization efficiency
η_u'	cathode utilization efficiency
θ	angular position [deg]
θ_c	RPA collimation angle [deg]
θ_{div}	half-angle plume divergence [deg]
$\theta_{1/2}$	angle where plasma density falls to half centerline value [deg]
λ_d	Debye length [m]
λ_{in}	ion-neutral mean free path [m]
λ_{ie}	ion-electron mean free path [m]
λ_{ii}	ion-ion mean free path [m]
ν_t	electron collision frequency [s^{-1}]
ν_a	anomalous electron collision frequency [s^{-1}]
ν_c	classical electron collision frequency [s^{-1}]
ν_{ie}	ion-electron collision frequency [s^{-1}]
ν_{ii}	ion-ion collision frequency [s^{-1}]
σ_{cex}	charge exchange cross section [m^2]
σ_{in}	ion-neutral collision cross section [m^2]
σ_{sc}	elastic scattering cross section [m^2]

ϕ	potential [V]
ϕ_o	reference potential [V]
Ω	solid angle [rad]
ω_{ce}	electron cyclotron frequency [s^{-1}]

Chapter 1

INTRODUCTION

With geostationary satellites increasing in power, size and lifetime, satellite manufacturers are turning to electric propulsion systems for in-orbit propulsion. The large quantities of propellant that are required by chemical thrusters for an in-orbit lifetime of 15 years render geostationary satellites prohibitively expensive. To reduce the cost of the spacecraft and to stay competitive in the space industry, major satellite manufacturers are currently either using electric propulsion systems or are planning on using them. For example, Boeing Integrated Defense Systems uses the 25cm Xenon Ion Propulsion System (XIPS), Space Systems/Loral uses the SPT-100 Hall thruster and Lockheed Martin Space Systems is in the process of flight qualifying the BPT-4000 Hall thruster [1, 2, 3]. Electric propulsion is also used for scientific missions. For example, NASA used an ion engine for the Deep Space One and Dawn missions [4, 5]. Also, the European Space Agency (ESA) used a PPS-1350 Hall thruster in the SMART-1 spacecraft as the primary propulsion system to travel to the moon [6].

Despite the fact that electric propulsion systems have an extensive flight heritage, they still remain the subject of considerable research studies. These studies are aimed at understanding the physics of electric propulsion systems through experimental and numerical work. One important area of research is the spacecraft's interaction with the plume of the electric propulsion thruster. The plume-spacecraft interaction is of great concern particu-

larly for Hall thrusters as their beam divergence is wider than that of other electric propulsion systems.

1.1 Hall Thrusters

The Hall thruster concept was first envisioned in the United States but was abandoned due to inability to control thruster discharge oscillations [7, 8]. The former Soviet Union was the first to successfully implement the Hall thruster as a propulsion device. Morozov was the lead scientist in this endeavor, and through his efforts, Hall thrusters transitioned from a laboratory experimental device to a propulsion system used on Soviet satellites [9]. Russia has currently several flight proven Hall thrusters, which include the SPT-50, SPT-60, SPT-70, SPT-100 and the D-55 [10]. Starting in the 1990s, with US-Russian scientific cooperation, Hall thruster research has gained momentum in the US. However, the US is still lagging in the number of flight proven US built Hall thrusters. Currently, the Busek-built BHT-200 is the only US built Hall thruster operational in space [11, 12, 13].

1.1.1 Concept

A Hall thruster is an axisymmetric device in which plasma is created in an annular channel, as shown in Figure 1.1. The typical propellants used in Hall thrusters are noble gases such as xenon, argon, and krypton. Xenon is usually utilized due to its high molecular weight and low ionization potential. Inner and outer magnetic poles surrounding the annular channel establish a radial magnetic field. The potential applied between the anode and the external cathode creates an axial electric field.

Figure 1.2 describes the process by which thrust is generated by a Hall thruster. The external cathode emits electrons, which are accelerated by the electric field toward the anode. The strong magnetic field inside the channel reduces the Larmor radius of electrons to values smaller than the thruster dimensions. Therefore, the electrons are trapped in an azimuthal $\vec{E} \times \vec{B}$ drift around the annular channel. The azimuthal drift current of electrons is referred to as the Hall current. Xenon, which is injected at the anode, is ionized through

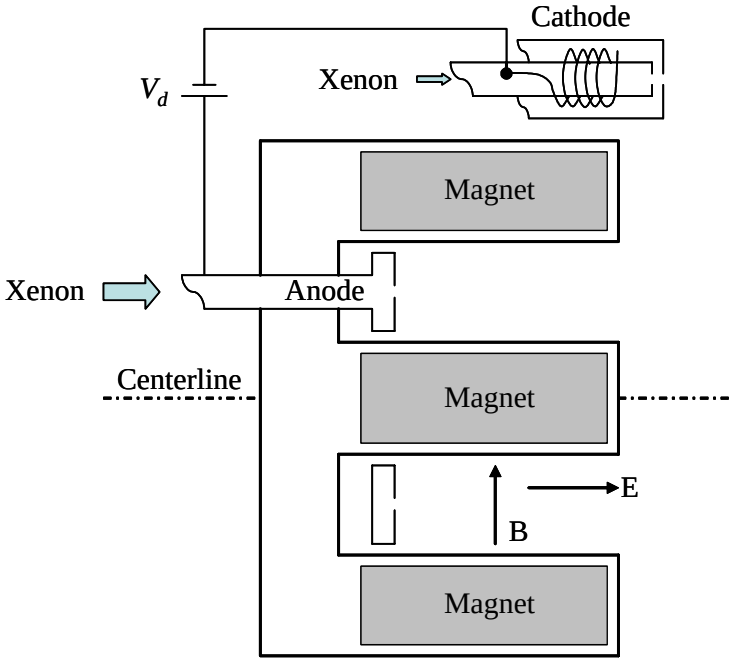

Figure 1.1 Cross-section of a Hall thruster.

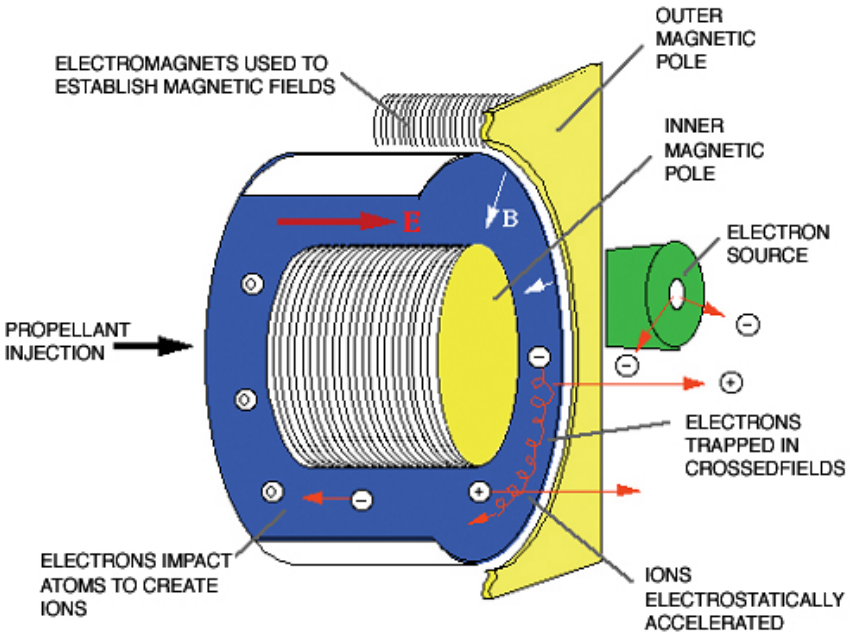

Figure 1.2 Hall thruster concept diagram.

collisions with trapped electrons. The electron-neutral collisions cause the electrons to diffuse towards the anode. The xenon ions, unaffected by the magnetic field due to their large Larmor radius, are axially accelerated out of the thruster by the electric field. As electrons accelerate towards the anode, the magnetic field acts to slow their axial motion so as to increase diffusion time. This causes the electrons to transfer their axial momentum into the magnets resulting in a magnetic force. Therefore, in a Hall thruster, thrust is transmitted to the thruster body magnetically. Summing the forces on all particles, the electrostatic pull of the anode on electrons is balanced by the electrostatic acceleration of ions, which leaves the magnetic force of electrons on the thruster as the only source of thrust. In addition to supplying electrons for ionization, the external cathode also serves as a neutralizer. Electrons ejected by the cathode neutralize the ion beam in the plume to avoid charging of the host spacecraft.

1.1.2 Advantages

Hall thrusters offer several advantages over other propulsion systems. Compared to chemical propulsion, Hall thrusters operate at a much higher specific impulse. The energy stored within the propellant of a chemical thruster limits the specific impulse to a maximum of approximately 450s. Hall thrusters, in contrast, rely on input from the power supply and can achieve a specific impulse of 1600s at 300V. Experimental results also show that the specific impulse can reach 3500s by increasing the discharge voltage [14]. The specific impulse of a Hall thruster is only limited by the power supply and materials of the thruster. Compared to ion engines, Hall thrusters have a simplistic design, which does not include grids. This enables them to operate at reasonable voltages. For example, Hall thrusters can operate at a discharge voltage of 100V, whereas ion engines require an acceleration voltage of 1000V to avoid space charge saturation between the grids. Hall thrusters also offer a wide range of thrust capabilities. Because the plasma of the thruster is quasi-neutral everywhere, the thrust density can be increased by simply increasing the mass flow rate of the propellant. In addition, Hall thrusters require fewer power supplies than ion engines. In Hall thrusters, power supplies are needed for the anode and cathode. In flight,

the electromagnets for a Hall thruster are powered with the anode power supply. On the other hand, for ion engines, power supplies are needed for the grids, discharge cathode and neutralizer, rendering the processing unit of the power supply more complex.

1.1.3 Issues

Although Hall thrusters offer many advantages, several issues need to be addressed in order to successfully integrate them in the spacecraft. One of those issues concerns Hall thruster plume interactions with the spacecraft since Hall thruster plumes have a wider divergence compared to other electric propulsion plumes. Figure 1.3 summarizes the different type of plume-spacecraft interactions.

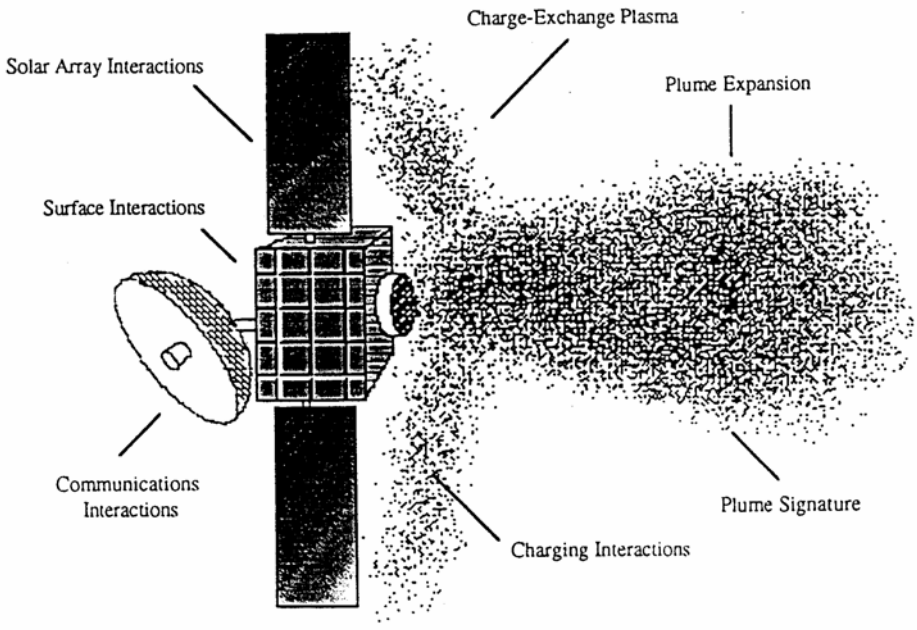

Figure 1.3 Plume-spacecraft interactions [15].

Hall thruster plumes primarily consist of electrons, high energy source ions, and low energy charge exchange ions. These particles can interact with and subsequently damage the spacecraft. For example, high energy ions can impact the surface of the spacecraft

resulting in material erosion. In turn, the eroded material can contaminate solar arrays and other sensitive surfaces. The low energy charge exchange ions, which are created through collisions of ions with neutrals, do not have sufficient energy to overcome the potential setup by the ambi-polar field of the plume. This causes the charge exchange ions to backstream to the spacecraft and alter its potential. The charge exchange ions can also acquire enough energy from the sheath of the solar array surface to cause erosion. Plume impingement on solar arrays can also result in thrust loss and torque perturbation, causing a change in spacecraft attitude. In addition, plume optical emission can interfere with sensitive optical instruments and the plume electromagnetic field can lead to distortion of communication signals.

1.2 Review of Hall Thruster Plume Research

Significant research has been performed in the area of Hall thruster plumes. This section provides a brief overview of both the computational and experimental research that has been conducted, with a specific emphasis on the important work that is relevant to the topic of this research.

1.2.1 Computational Work

Quasi3 is the first computational model used to study Hall thruster plumes [16]. It is a hybrid Particle-In-Cell (PIC) simulation developed at MIT by Oh. The computational model investigates plasma expansion in three dimensions and its interaction with surfaces. Quasi3 calculates the electric field based on the assumption of quasi-neutrality. The plume collision model uses Direct Simulation Monte Carlo (DSMC) methodology and includes charge exchange collisions. The simulation allows for a user-specified geometry and background pressure. Quasi3 uses a cartesian grid, which limits the geometry to rectangular shapes. The original source model represents the plasma flow from an SPT-100 Hall thruster. Particles are injected into the plume simulation domain with a distribution that is constructed from near-field experimental measurements by Gavryushin and Kim [17]. One of the limitations of the simulation is the assumption of a constant electron tempera-

ture throughout the simulation domain, which experimental measurements have shown not to be the case. The electron temperature can vary from 10eV at the thruster exit to 1eV at 1m away from the thruster exit. The limitation of the simulation is evident in the lack of similarity between simulated and experimentally measured current density. Despite its short comings, Quasi3 was the state of the art model at the time of its conception and was an important tool that led to the development of improved plume models.

To address the limitations of Quasi3, a new plume code, termed Aquila, was developed [18, 19, 20]. One of Aquila's major improvements over Quasi3 includes the use of a 3D unstructured tetrahedral mesh, which allows for modeling realistic geometries. Aquila also includes a non-neutral potential solver to calculate the electric field in regions where quasi-neutrality breaks down. The plume simulation further allows for a variable electron temperature model throughout the simulation domain. The source model of Aquila relies on velocity distributions generated by an engine code that models the discharge region of the thruster. Aquila's current density results show a significant improvement in matching experimental current density as compared to Quasi3.

1.2.2 Experimental Work

There is a wealth of experimental work on Hall thruster plumes. The effort is led by both industry and academia. Extensive plume measurements on the SPT-100 are published in the US literature as it is the first Hall thruster to fly on a US commercial satellite [21, 22, 23]. Plume characterization includes measurements of current density, electron density, electron temperature, plasma potential, ion energy distribution and ion species fractions. The aim of these measurements is to increase the physical understanding of plume expansion to allow for better integration of Hall thrusters with the spacecraft.

All experimental characterization of Hall thruster plumes is performed in vacuum tanks, which do not have the pumping speed to produce space vacuum conditions. Plume expansion in ground facilities include tank artifacts that do not exist in space conditions. Several studies were performed to characterize facility effects on the Hall thruster plume. Man-

zella used a nude Faraday probe to measure the current density at different tank pressures [24]. He showed that as the background pressure increases, charge exchange collisions increase and change the profile of the current density distribution. Walker also studied facility effects on thruster performance and plume expansion [25, 26, 27]. To correct for tank artifacts on thruster performance, Walker recommends using numerical models. He suggests that experimental data should be used to cross-calibrate numerical models at a certain background pressure and then the numerical model should be run at in-orbit conditions to determine the in-orbit thruster performance. Walker also recommends using a magnetically filtered Faraday probe to obtain the in-orbit current density distribution. However, there are a few concerns with using this probe. For example, the magnetically filtered Faraday probe removes all low energy charge exchange ions from the measurements. At in-orbit conditions, some charge exchange ions exist from ion collisions with engine neutrals and should not be filtered out from the current density distribution. Therefore, more work needs to be done to develop a more accurate method of correcting measurements solely for facility effects.

1.3 Motivations

Hall thrusters are often used for North-South stationkeeping of geostationary satellites where the solar arrays are extended from the north and south faces of the spacecraft. This creates a conflict with the solar arrays as the north-south line is also the desired direction of plume expansion. To avoid damage of the spacecraft by the plume, Hall thrusters are canted at a certain angle, which reduces the effective specific impulse. An important metric that is used to determine the appropriate cant angle is the “in-orbit” plume divergence. The plume divergence obtained from laboratory measurements is different than the in-orbit plume divergence because of facility effects. The electric propulsion community currently does not have a standard method for calculating the in-orbit plume divergence. Several different techniques exist, however they all employ subjective methods for correcting plume measurements for facility effects. This makes it difficult to compare the plume divergences of different thrusters taken at different facilities. The establishment of a sim-

ple and accurate method to determine the in-orbit plume divergence in a laboratory environment will aid spacecraft designers in determining the proper positioning of the thruster within the spacecraft and will provide the electric propulsion community with an objective view of the thruster's performance.

1.4 Objectives

This thesis is both experimental and computational in nature. The first objective of the experimental work is to develop a method to determine the Hall thruster in-orbit plume divergence from laboratory measurements. In the process of achieving this objective, facility effects on the behavior of a Hall thruster plume are investigated. The thruster used in this research, the Busek built BHT-1500, is a high specific impulse Hall thruster that operates up to 3500s [14]. The high specific impulse is achieved by operating the thruster at high discharge voltages. Therefore, a second objective of this thesis is to increase physical understanding of high specific impulse Hall thruster plumes through characterizing the effect of the discharge voltage on the plume. To achieve these experimental objectives, suitable plume diagnostic instruments are designed, built and tested. Furthermore, the experimental results of this thesis serve as a database to support ongoing computational models.

The objective of the computational work is to cross-calibrate Aquila against experimental measurements. The source model of the plume simulation relies on inputs from a full PIC engine code [28]. The comparison of plume simulation results to the experimental measurements determines the accuracy of both the engine and plume models. If computational results do not agree well with experimental data, then recommendations for possible areas of improvement in the engine and plume models should be identified.

1.5 Thesis Outline

Chapter 2 describes the experimental hardware and setup used to characterize the plume of a Hall thruster. It includes a detailed description of the BHT-1500 Hall thruster, the Busek vacuum facility where the experimental work was conducted, and the plume diagnostic instruments that were designed, built and tested for use in this research. Chapter 3 presents all the experimental measurements obtained to develop a method for calculating the in-orbit plume divergence. A comparison of measurements obtained with the different diagnostic probes is also presented. Chapter 3 also covers the effect of discharge voltage on the plume divergence. Chapter 4 details the numerical portion of the research. It includes a description of both the engine and plume models. A previous and a new method of generating a source model are also presented. Chapter 4 also discusses the numerical results and includes a comparison to experimental measurements. In Chapter 5, experimental and numerical results are compared to analytical models of estimating current density from source ion collisions with neutrals. Additionally, a model of current density based on self-similar solutions is compared to the experimental current density to determine the model's validity. Chapter 6 summarizes the contributions of this thesis and provides recommendations for future work. This thesis also includes Appendix A, which shows experimental measurements obtained to study the effect of the magnetic field on the plume of a Hall thruster.

Chapter 2

EXPERIMENTAL APPARATUS

This chapter describes the experimental hardware and setup used to characterize a Hall thruster plume. The experimental setup includes the Hall thruster, vacuum facility, and diagnostic probes. All the experiments were conducted at Busek Company using the BHT-1500 Hall thruster. The plume experiments include measurements of current density and ion energy distribution. The diagnostic instruments used to generate these measurements consist of a nude Faraday probe and a retarding potential analyzer. All the diagnostic probes were designed and built in-house. This chapter covers the design decisions and the construction process that was followed to build the probes and contains the physics governing their operations. Sample measurements from each diagnostic probe are also included in this chapter.

2.1 BHT-1500 Hall Thruster

2.1.1 Thruster Description

The BHT-1500 Hall thruster, shown in Figure 2.1, was used for this research. It is a single stage Hall thruster designed to operate at power levels ranging from 0.6 to 2.3kW [14]. It was developed by Busek Company for high specific impulse operation under a Phase II Small Business Innovation Research (SBIR) program sponsored by NASA with a goal of achieving 100mN of thrust at 3200s of specific impulse [29].

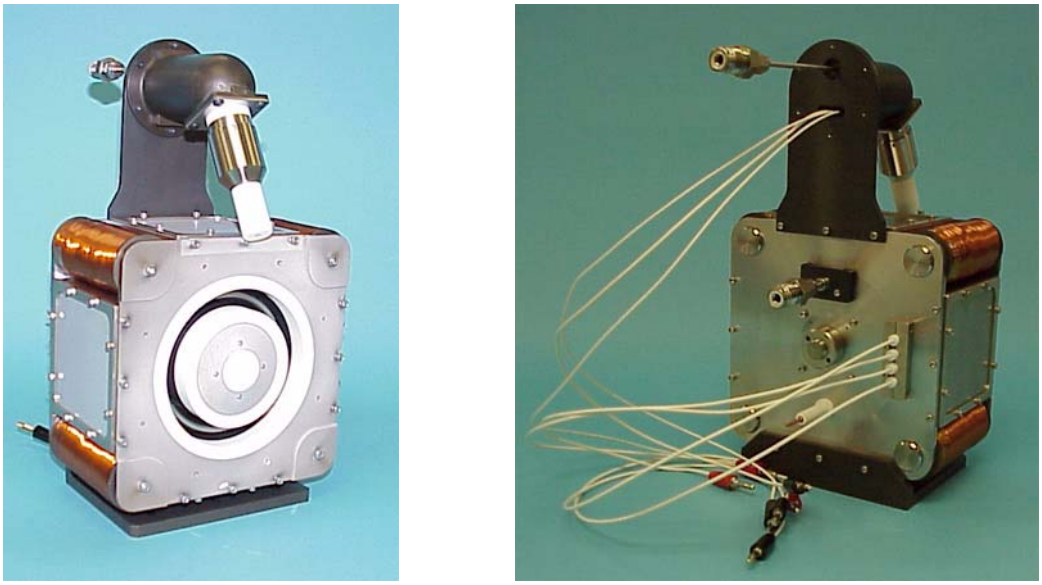

Figure 2.1 The BHT-1500 Hall thruster.

The BHT-1500 measures 152x152x93mm with a mid-channel diameter of 82mm. The thruster features Busek's patented anode assembly. A diagram of the internal discharge of the BHT-1500 is shown in Figure 2.2. The anode of the BHT-1500 consists of a wedge shaped annular piece enclosed in an annular channel shaped piece. The outer anode piece, the anode housing, has a relatively large volume that acts as a propellant reservoir. The inner anode piece distributes the propellant inside the discharge channel. As the propellant flows from the main line to the anode, it is chocked at the inlet of the wedged shaped piece and is azimuthally distributed through a set of radial holes. The propellant travels inside the thruster discharge channel with approximately a zero mean velocity and a thermal velocity that is determined by the anode wall temperature. This provides the neutrals with a long residence time and increases electron impact ionization.

The BHT-1500 is equipped with dielectric exit rings. Erosion of the exit rings is the main life limiting factor in Hall thrusters. The exit rings are made of Boron Nitride (BN) because of its excellent thermal stability, high dielectric strength at high temperatures and low sputter yield.

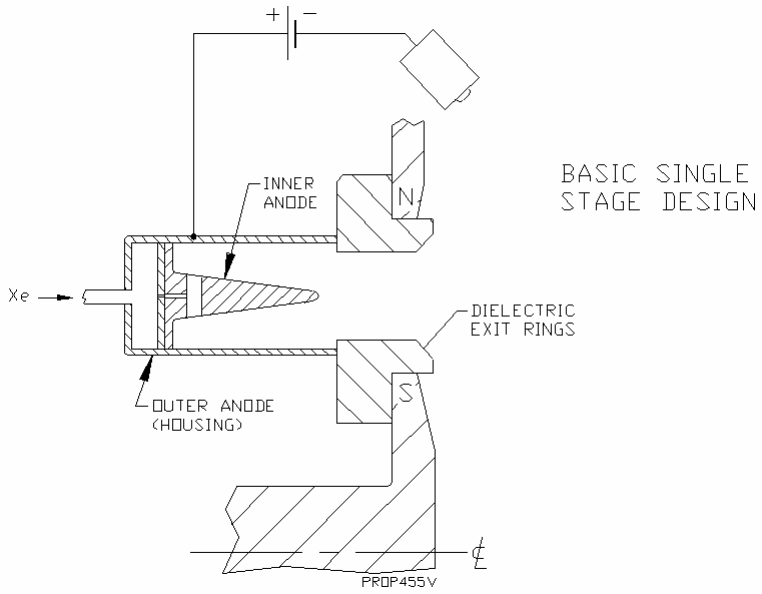

Figure 2.2 Diagram of the BHT-1500 in cross-section. Not to scale.

The magnetic circuit is driven by five solenoids, four around the outside of the thruster and one placed inside the center stem. The magnetic material is made of Hiperco, which consists mostly of iron, cobalt and vanadium. The anode housing shunts a portion of the magnetic field creating a magnetic lens with a sharp drop in field magnitude close to the anode.

The BHT-1500 uses a Busek Hollow Cathode to provide a source of electrons to ionize the propellant and neutralize the beam. The hollow cathode is a thermionic cathode capable of emitting up to 10A of current. The cathode emitter is made of a barium oxide impregnated tungsten insert that is housed inside a 0.25in cathode discharge tube. The cathode is heated to start electron emission by passing current through a coil that is wound around the cathode tube. In addition, a small amount of propellant flows through the cathode, which is approximately 10% of the anode flow rate. The cathode is a poor ionizer; only 10% of the cathode flow is ionized. The cathode ions are born at a low potential and do not contribute to thrust. The purpose of the propellant flow through the cathode is to create ions to prevent space charge saturation, which can limit electron emission. Despite the fact that the

propellant flow through the cathode decreases the total specific impulse by 10%, it is necessary for the operation of the thruster.

2.1.2 Thruster Operation

This section outlines the general operating procedures for the BHT-1500. Before the engine can be started, the cathode must first be ignited. The cathode emitter is very sensitive to moisture and oxygen. Therefore, it is important to condition the cathode if it was exposed to air. The cathode ignition process starts by flowing 0.25mg/s (10% of the anode flow rate) through the cathode for half an hour to fill the lines connecting the xenon tank to the cathode in order to drive out water and air that have been absorbed by the lines. Then, the cathode heater is supplied with 2A of current for an hour. The heater current is increased by 0.5A every half an hour until the heater current reaches 6.5A. Next, the cathode keeper power supply is turned on. A keeper voltage of 600V is usually required to start the cathode ignition. When cathode ignition starts, the keeper power supply switches from voltage mode to current mode. The keeper current is then set to 0.5A. Finally, the cathode heater is turned off, and the cathode is in standby mode. At this time a small purple plume can be seen outside the cathode discharge tube.

After the cathode discharge is ignited, the flow rate to the anode is started. In this research, the flow rate to the anode is kept constant at 2.44mg/s. The discharge voltage is increased and the plasma is ignited around 60-70V. At this time, a glow discharge is observed. The magnetic field power supply is then turned on. The current of the magnetic field power supply and the discharge voltage are both increased. The discharge voltage is set to the operating voltage, usually 300V. The magnetic field is adjusted to minimize the discharge current. If the magnetic field is increased past the minimum discharge current setting, the thruster can become unstable, which is demonstrated by high discharge current oscillations and plasma flickering. The oscillations can get large enough to turn the thruster off. Figure 2.3 shows a picture of the thruster operating at the minimum discharge current setting. The plume is in a “jet mode” where a long narrow “spike” is observed in the middle

of the plume stretching from the thruster exit plane to about 20cm downstream from the exit plane.

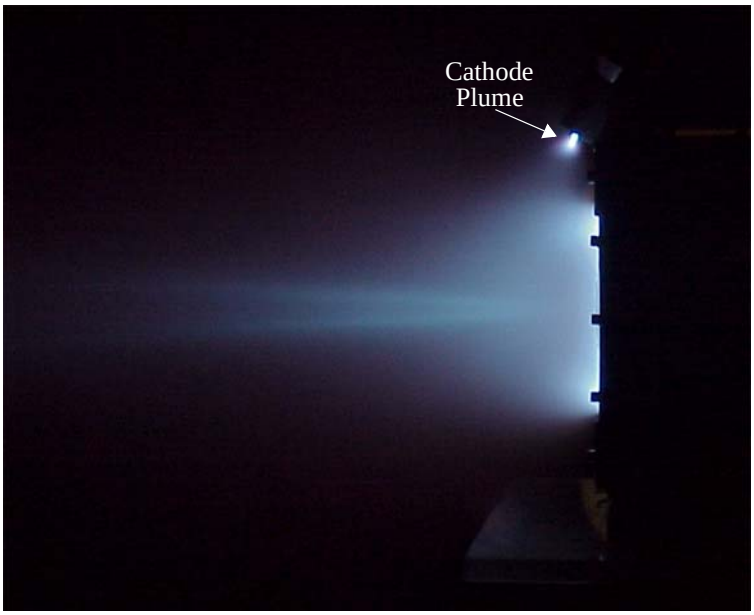

Figure 2.3 Picture of the BHT-1500 operating in the minimum discharge current setting. The plume is blue in color. The thruster plume has a long narrow spike in the middle, which extends to approximately 20cm downstream from the exit plane. The bright spot in the top right corner is the cathode discharge plume.

For this research, the BHT-1500 is operated at discharge voltages ranging from 300V to 1000V in 100V increments. The propellant used to operate the thruster is Research Grade xenon, which is 99.9995% pure. The flow rate of xenon is kept at 2.44mg/s to the anode and 0.25mg/s to the cathode. After a discharge is established at a particular operating voltage, the magnetic field is adjusted to minimize the discharge current. The magnetic field for a minimum discharge current increases roughly linearly with discharge voltage. The discharge is powered with a Universal Voltronics BRC 10,000 power supply that is connected between the anode and cathode. A 40 μF capacitor is placed in parallel with the discharge power supply to minimize the discharge oscillations. The discharge current oscillations are monitored using a LeCroy Waverunner LT354 oscilloscope by placing a

current probe around the anode lead. The cathode is allowed to float, and usually hovers between 15-20V below the facility ground. The thruster is run for 1-2 hours before plume measurements are taken to allow the discharge chamber walls to outgas and reach a thermal steady state.

2.1.3 Thruster Performance

The performance of the BHT-1500 has been extensively characterized at Busek Company [14, 29]. The thruster has been tested at discharge voltages up to 1200V and anode flow rates up to 4.88mg/s. At 2.44mg/s of xenon flow to the anode and a discharge voltage of 1000V, the BHT-1500 produces a thrust of 77mN, a specific impulse of 3200s, and an efficiency of 51.6%. The thruster achieves a maximum efficiency of 60% at a discharge voltage of 800V and an anode flow rate of 3.91mg/s. The highest measured specific impulse is 3430s at a discharge voltage of 1200V and an anode flow rate of 2.44mg/s.

Figures 2.4 and 2.5 represent the anode specific impulse and anode efficiency respectively at various discharge voltages and an anode flow rate of 2.44mg/s. The results shown in both figures were not measured during characterization of the thruster plume. However, the thruster operating conditions shown in these figures are similar to the operating conditions during plume testing. As seen in Figure 2.4, for 2.44mg/s of xenon flow rate to the anode, the specific impulse increases with discharge voltage from 1500s at 300V to 3200s at 1000V. The specific impulse increases faster than the square root of discharge voltage because the utilization efficiency improves with discharge voltage. The effect of discharge voltage on utilization efficiency is discussed in Section 3.4.1. Figure 2.5 shows that the BHT-1500 anode efficiency increases with discharge voltage and levels off at 900V. For 2.44mg/s of xenon flow rate to the anode, the efficiency increases from 46.8% at 300V and reaches a maximum of 52.9% at 900V. A complete performance map of the BHT-1500 at different flow rates was published by Szabo [14, 29].

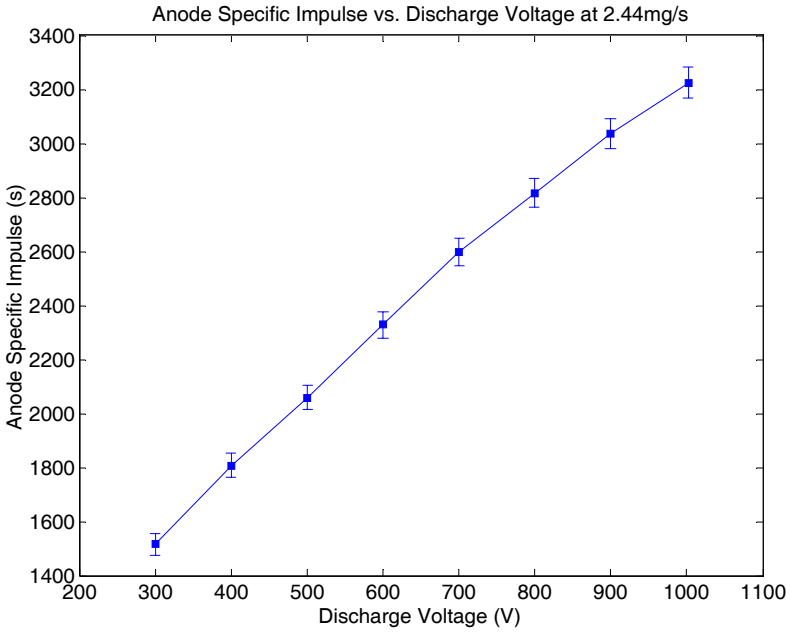

Figure 2.4 Measured anode specific impulse versus discharge voltage for the BHT-1500 at a 2.44 mg/s xenon flow rate to the anode.

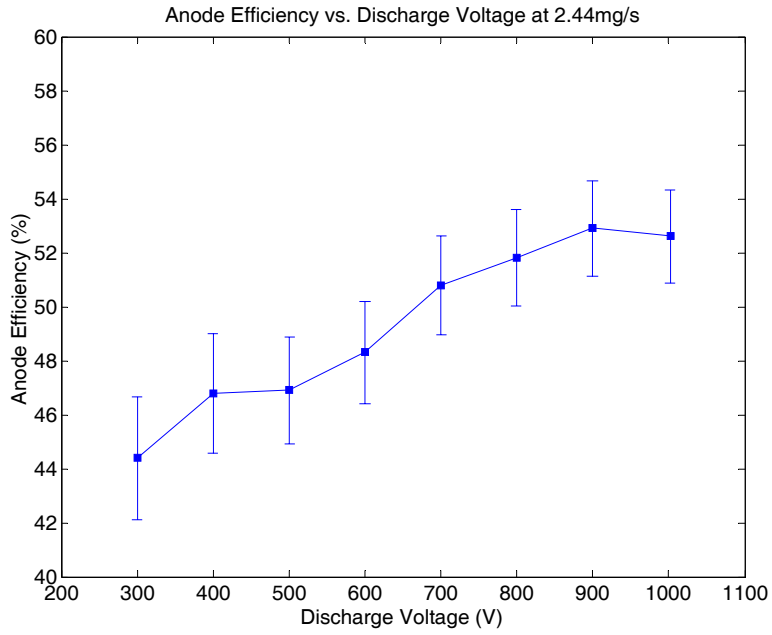

Figure 2.5 Measured anode efficiency versus discharge voltage for the BHT-1500 at a 2.44 mg/s xenon flow rate to the anode.

2.2 Busek Vacuum Facility

All plume measurements were conducted in Busek's T8 vacuum test facility. The tank, shown in Figure 2.6, is made of stainless steel and measures 5m in length by 2.4m in diameter. The T8 uses a mechanical roughing pump, a blower, and three two-stage and five single-stage cryogenic pumps capable of evacuating approximately 200,000L/s of xenon. The tank is also equipped with a liquid nitrogen cooled target. The tank pressure, which is monitored by a hot-cathode ionization gauge, is approximately 1×10^{-6} Torr before turning on the thruster propellant flow. Pressure readings from the ionization gauge, which are calibrated for nitrogen, are corrected for xenon using

$$P_c = \frac{P_i - P_b}{2.87} + P_b \tag{2.1}$$

where P_c is the corrected pressure for xenon, P_b is the base pressure, and P_i is the indicated vacuum pressure.

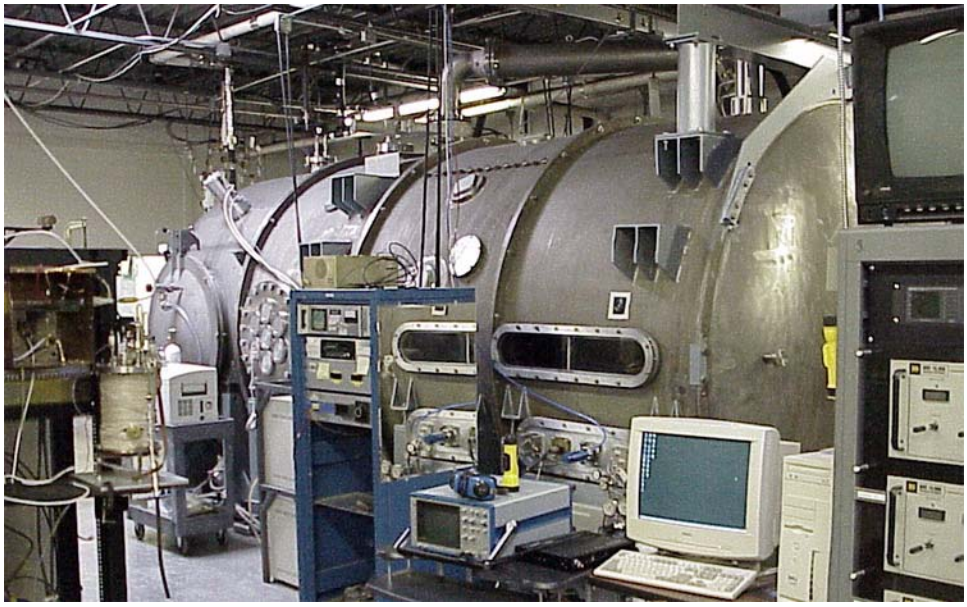

Figure 2.6 Busek T8 vacuum chamber.

Plume measurements were taken at various background pressures. The background pressure is increased by flowing xenon in the tank using a propellant line that is connected to the back end of the tank. For example, flowing 5mg/s of xenon increases the tank pressure from 6×10^{-6} Torr to 1×10^{-5} Torr. Figure 2.7 shows the propellant supply to the anode, cathode, and the pressure variation feed lines. Xenon is supplied from a compressed bottle to the thruster and the pressure variation line through separate stainless steel feed lines. Unit Instruments model UFC 7300 flow controllers with full scales of 20sccm, 50sccm, and 500sccm regulate the xenon flow to the cathode, anode and the pressure variation feedlines respectively. The UFC 7300 flow controllers have an accuracy of ±1% full scale.

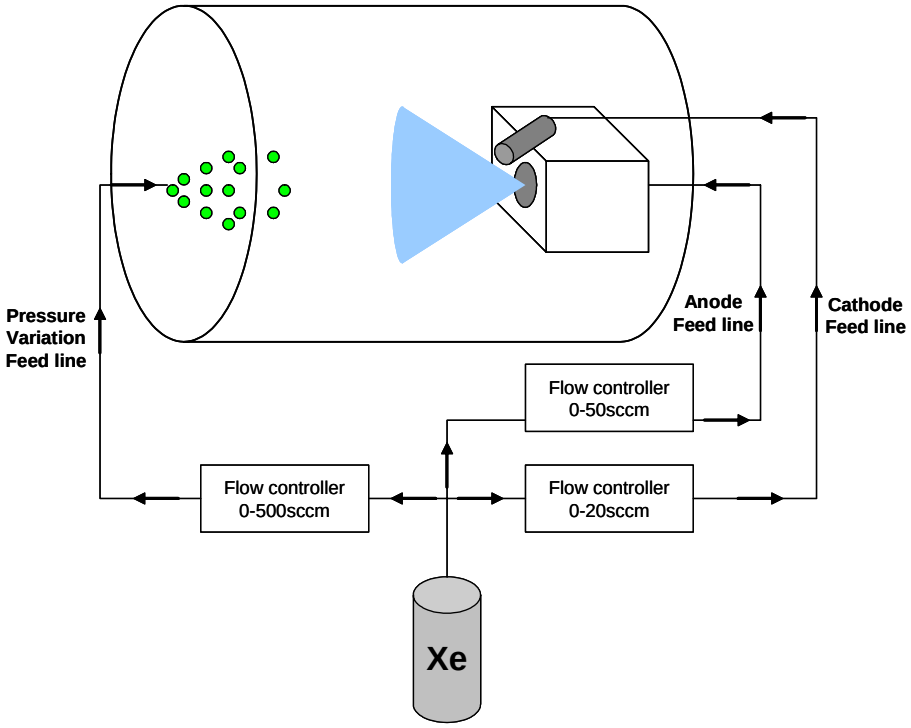

Figure 2.7 Diagram of the propellant supply to the anode, cathode, and pressure variation feed lines. The pressure variation feed line is connected at the back of the tank. The flow rate of xenon is regulated by flow controllers with full scales of 20sccm, 50sccm, and 500sccm to the cathode, anode and pressure variation feed lines respectively. The background pressure of the tank is adjusted by xenon flow through the 500sccm flow controller. During thruster operation, the background pressure is 6×10^{-6} Torr when the xenon flow through the 500sccm flow controller is turned off. With 5mg/s xenon flow through the 500sccm controller, the background pressure increases to 1×10^{-5} Torr.

The BHT-1500 is mounted on a thrust stand with the exhaust beam aligned with the vacuum chamber's longitudinal axis, as shown in Figure 2.8. The thruster plume is allowed to freely expand approximately 4.0m along the longitudinal axis. The T8 vacuum chamber is equipped with an inverted pendulum type thrust stand, originally developed at the NASA Glenn Research Center [30, 31]. The thrust stand uses a Schaevitz 050 HR Linear Variable Differential Transformer (LVDT) that measures displacement and produces an output voltage proportional to thrust. The signal is read into a computer data acquisition card so that the thrust signal can be filtered and monitored using a National Instruments LabView program. Thermal expansion of the thrust stand leads to drift of the thrust signal. The error due to the signal drift is minimized by periodically shutting the thruster down to recalibrate the thrust signal.

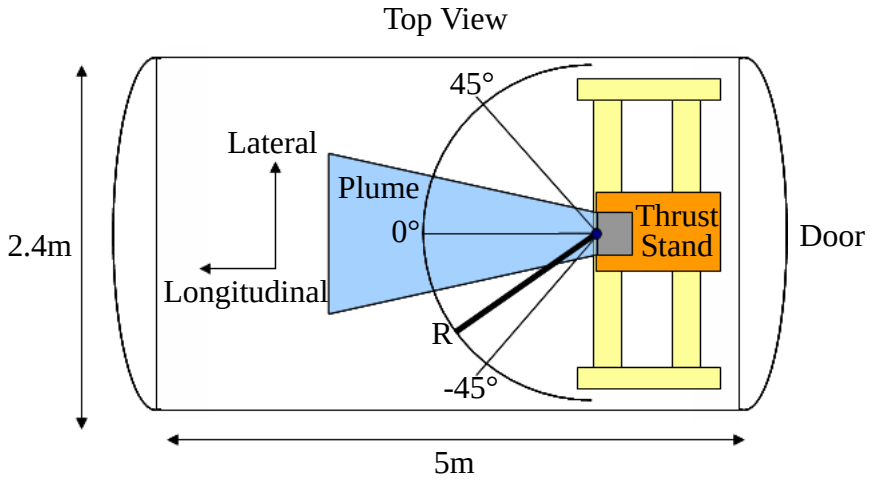

Figure 2.8 Top view diagram of the thruster setup inside the T8 vacuum tank. The tank is equipped with a thrust stand to characterize the performance of the BHT-1500. The tank is also setup to conduct plume diagnostics through an automated probe positioner system.

The T8 vacuum chamber is also equipped with the capabilities to perform plume diagnostics. The chamber contains an automated probe positioner that features a rotating extendable arm. A 180° rotation is accomplished through a Danaher Precision Systems RTR-6 rotary stage. The positioner is capable of varying the radius of rotation with a Danaher

custom linear stage. Vacuum rated Empire Magnetics model U22-VC stepper motors drive both the rotation and the linear stages. The pivot axis is positioned below the exit plane of the thruster. A LabView program controls the positioner. The program commands a Galil DMC-2123 2-axis Ethernet based motion controller with an ICM-20105 opto-isolated I/O module. The Galil controller, in turn, commands Applied Motion model 3540M stepper motor drivers. The user can specify in the LabView program the sweep radius, the boundaries of the angular rotation, the increment of the angular rotation, and the dwell time which is the time the arm is allowed to pause after it is moved.

2.3 Faraday Probe

2.3.1 Probe Description

The Faraday probe is a diagnostic instrument that measures current density. Figure 2.9 shows a schematic of a Faraday probe. It consists of a flat collector enclosed in a guard ring that is biased at potentials between −12V and −30V to repel electrons. Both the collector and guard ring are biased at the same potential to minimize edge effects by creating a flat uniform sheath in front of the collector. However, current is only measured from the collector itself [27]. The collector is generally made of stainless steel and is sprayed with tungsten to reduce secondary electron emission from ion bombardment. The guard ring is used to shield the collector from low energy ions arriving from outside the collector's line of site.

Current density is measured in the following way. As ions hit the face of the collector, electrons contained within the metal of the Faraday probe stream to the probe's face to neutralize the collected ions. These moving electrons make up the probe current, which is equal to the ion current. Current density is determined by measuring the ion current and dividing by the area of the collector. The current density is measured for different angular positions with respect to the thruster centerline to obtain a current density distribution. The current density distribution is integrated to yield the beam current from which the half-angle plume divergence is obtained.

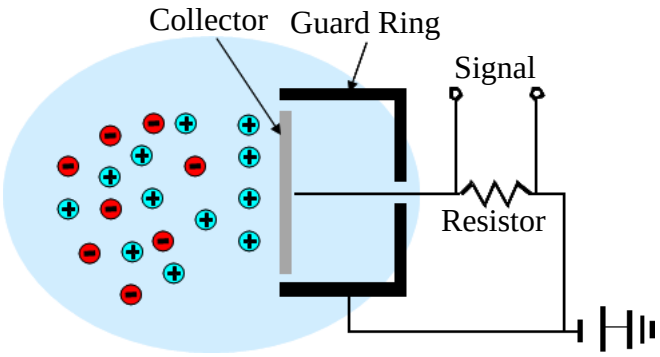

Figure 2.9 Schematic of a Faraday probe. The same voltage bias is applied to both the collector and the guard ring. The applied bias is negative with respect to the facility ground in order to repel electrons and collect only ion flux on the surface of the collector.

2.3.2 Probe Design

This section outlines the process that was followed to design the nude Faraday probe. Constraints were imposed on the following parameters to ensure an adequate Faraday probe design:

- Diameter of the collector
- Spacing between the collector and the guard ring
- Material of the probe
- Voltage bias

The Faraday probe can cause plasma perturbations, which can negatively affect plume measurements. A miniature probe design reduces the plasma perturbations and also allows for improved measurement resolution. To minimize edge effects around the collector, the sheath in front of the collector must be flat and uniform. This requires the spacing between the collector and the guard ring to be small to ensure an overlap of the collector and guard ring sheaths. The probe collector and guard rings must be made of a conducting material with a high melting point and low secondary electron emission from ion bombardment. Finally, the probe voltage bias, used to repel electrons, needs to be small in order not to alter ion trajectories and artificially increase ion collection.

Figures 2.10 and 2.11 represent drawings of the Faraday probe collector and guard ring respectively. The Faraday probe is designed with a collector diameter of 4.45mm and a guard ring diameter of 6.35mm. The dimensions were chosen because of manufacturing constraints, since smaller dimensions are more difficult and more expensive to machine. However, these dimensions are the smallest of any Faraday probe design described in the literature.

Figure 2.10 Drawing of the Faraday probe collector. The collector diameter is 4.45mm. The metallic rod attached to the back of the collector is used to apply a voltage bias and conduct current to the power supply. All dimensions are in millimeters.

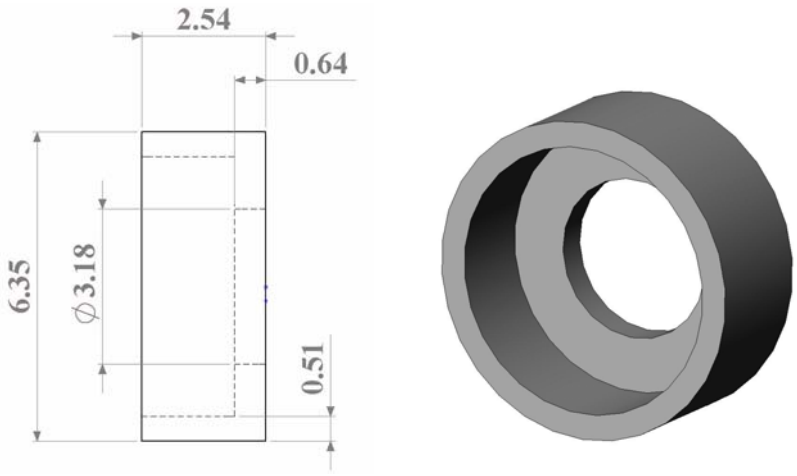

Figure 2.11 Drawing of the Faraday probe guard ring. The outer diameter of the guard ring is 6.35mm. All dimensions are in millimeters.

The plume Debye length is calculated to verify that the spacing between the collector and guard ring ensures an overlap of the sheaths. The spacing should be on the order of the

sheath thickness, which is 5 to 10 Debye lengths. The plume Debye length, λ_d, is calculated using

$$\lambda_d = \sqrt{\frac{\varepsilon_0 k T_e}{n_e e^2}} \tag{2.2}$$

where T_e is the electron temperature and n_e is the electron density. Table 2.1 shows estimates of the BHT-1500 plasma parameters used to calculate the Debye length at different distances from the thruster exit plane.

TABLE 2.1 Estimates of the BHT-1500 plasma parameters used to calculate the Debye length at various distances from the thruster exit plane.

	Distance From Thruster Exit Plane			
	0.25m	**0.50m**	**0.75m**	**1m**
T_e (eV)	3	3	2	2
n_e (m^{-3})[1]	1×10^{16}	2×10^{15}	1×10^{15}	6×10^{14}
λ_d (mm)	0.13	0.29	0.33	0.43

1. The electron density used in this table is the maximum electron density at the distance of interest. If the sheath thickness requirement is satisfied for the maximum electron density, it will be satisfied for all other electron densities at the distance of interest.

From Table 2.1, the Debye length varies from 0.13mm at a distance of 0.25m from the thruster exit to 0.43mm at 1m. Therefore, the sheath thickness lies between 0.65-1.3mm at 0.25m and 2.1-4.3mm at 1m. The spacing between the collector and guard ring is 0.45mm, which is less than 0.65mm, the sheath thickness at 0.25m. This ensure a flat uniform sheath over the collection area of the Faraday probe for measurements taken at distances equal or larger than 0.25m from the thruster exit.

The material of choice for both the guard ring and collector is 316 stainless steel due to its high melting point of 1700K, its ease in machining, and its relatively low cost compared to other metals used in Faraday probes, such as tungsten. Secondary electron emission from

ion bombardment of a stainless steel surface at energies less than 1keV is not a concern. For nickel, one of the components of stainless steel, the secondary electron yield due to Xe^+ bombardment at energies below 1keV is less than 0.02 electrons per ion [32].

To determine the appropriate voltage bias of the collector and guard ring, current density was measured at different voltage biases. Results show that current density levels off starting at a bias voltage of −10V [12]. Therefore, −20V was conservatively chosen as the probe bias. This voltage is applied to the collector and guard ring throughout this research.

2.3.3 Probe Construction

Once the guard ring and collector are machined, the steps illustrated in Figure 2.12 are followed to assemble the Faraday probe. These steps are summarized below:

1. The guard ring is inserted 1.0mm into a single-bore ceramic tube. The ceramic tube is made of 99.8% alumina and has an outer diameter of 3.18mm, an inner diameter of 1.58mm and a length of 25.4mm.
2. The guard ring is fixed on the alumina tube using a lock ring, a stainless steel low-compliance spring. The back face of the guard ring is spotwelded to the lock ring at four locations 90° apart.
3. A stainless steel wire with a 0.79mm diameter is wound around and spotwelded to the guard ring to provide voltage bias to the guard ring. The wire is then inserted into an alumina tube with an inner diameter of 0.79mm for electrical insulation from the plasma.
4. The collector is inserted into the alumina-guard ring combination. The stainless steel rod attached to the collector is slightly bent during insertion to cause friction with the inner wall of the alumina tube. This friction prevents the stainless steel rod from slipping inside the alumina tube once it is in place.
5. The collector is positioned inside the alumina tube. The collector face is flush with the front surface of the guard ring. The back of the collector is placed 0.92mm away from the front of the alumina tube. This gap is necessary to minimize the sputtered collector's stainless steel from depositing on the alumina. If sputtered stainless steel covers the alumina tube, it leads to an electrical short between the collector and the guard ring, which renders the Faraday probe ineffective.

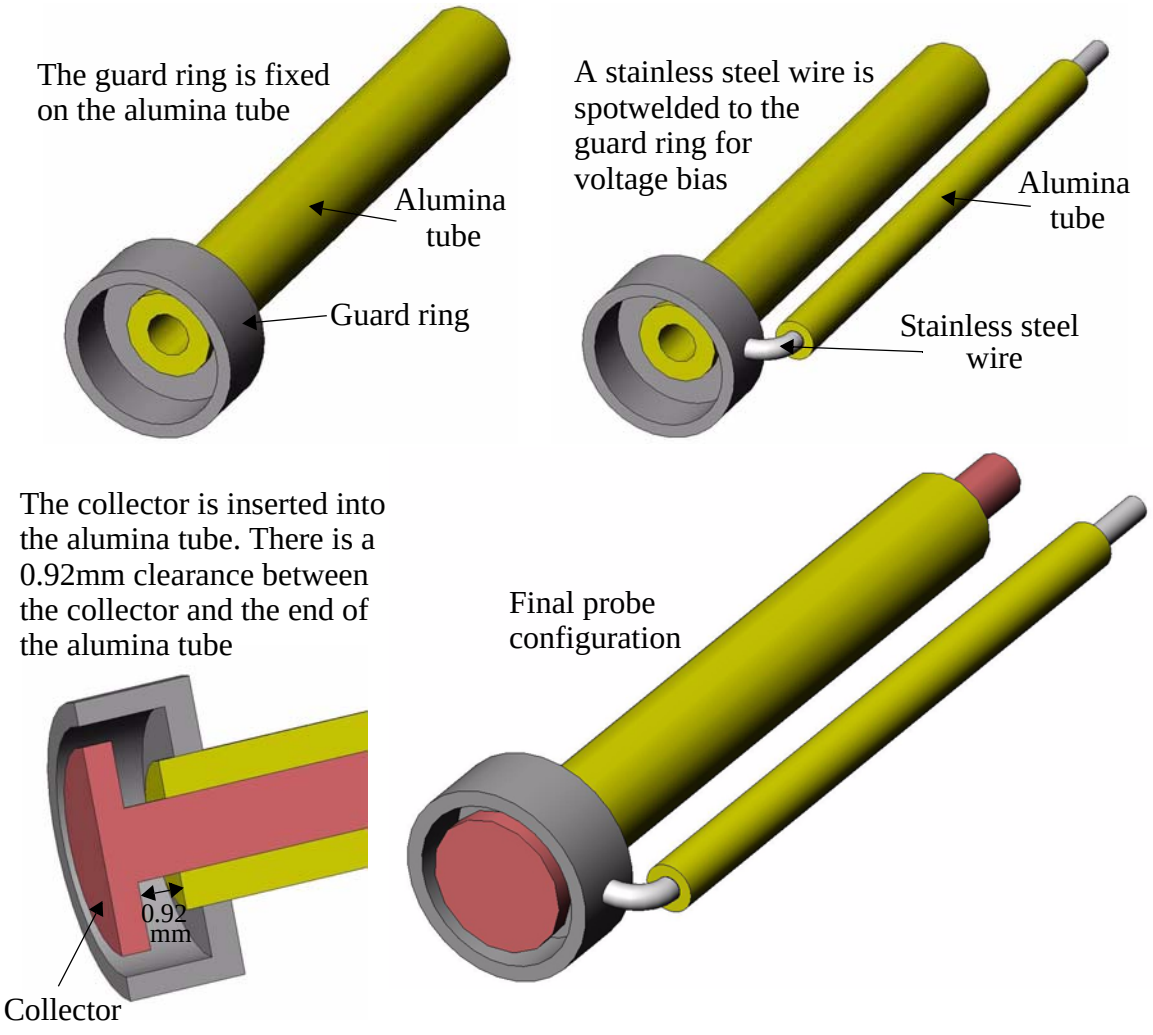

Figure 2.12 Illustration of the Faraday probe assembly process.

The resulting product is a Faraday probe that consists of a 4.45mm diameter stainless steel collector enclosed in a 6.35mm diameter stainless steel guard ring. Figure 2.13 is a picture of the Faraday probe.

Figure 2.13 Final Faraday probe design.

2.3.4 Design Verification

Before the Faraday probe is utilized to map the plume of the BHT-1500, it is cross-calibrated against a larger and well characterized Jet Propulsion Laboratory (JPL) Faraday probe [27]. The design verification experiment was conducted at the University of Michigan's Plasmadynamics and Electric Propulsion Laboratory (PEPL) by M. Walker. Results from the cross-calibration show that measurements obtained from both probes are nearly identical [12, 13]. Therefore, it can be concluded that the Faraday probe used in this research is reliable. The cross-calibration setup and comparison of MIT and JPL Faraday probe measurements are described in previous research [12, 13].

2.3.5 Probe Setup

The Faraday probe is mounted on the automated probe positioner inside the T8 vacuum chamber. Figure 2.14 is a picture of the experimental setup of the Faraday probe. The probe's collector is oriented to face the exit plane of the BHT-1500. The vertical height of the probe is set to bisect the plume, passing through its axis. A laser setup is used to align the probe, as shown in Figure 2.15. The probe is placed 1m downstream from the exit plane of the BHT-1500. In some cases, measurements are also taken at 0.50m and 0.75m downstream from the exit plane of the thruster. The probe is swept from –90° to 90° with respect to the thruster centerline in 3° increments through the plume. Looking downstream

from the thruster exit plane, angles become increasingly positive when the arm is moved clockwise, as shown in Figure 2.16.

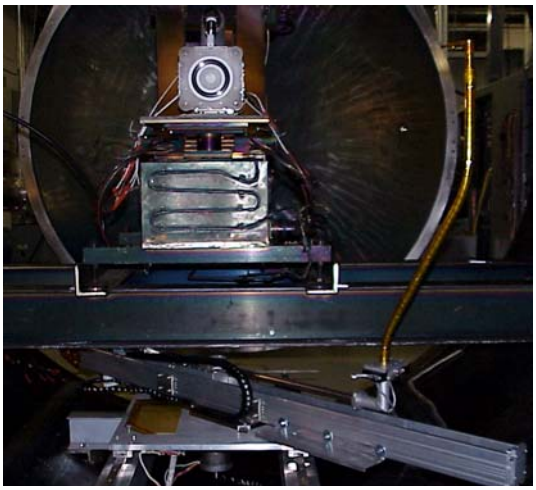

Figure 2.14 LEFT: Picture of the experimental setup of the Faraday probe inside the T8. The probe is mounted on the automated positioner facing the BHT-1500.

Figure 2.15 RIGHT: Laser Alignment setup. The laser is used to calibrate the height and the angular position of the Faraday probe inside the T8.

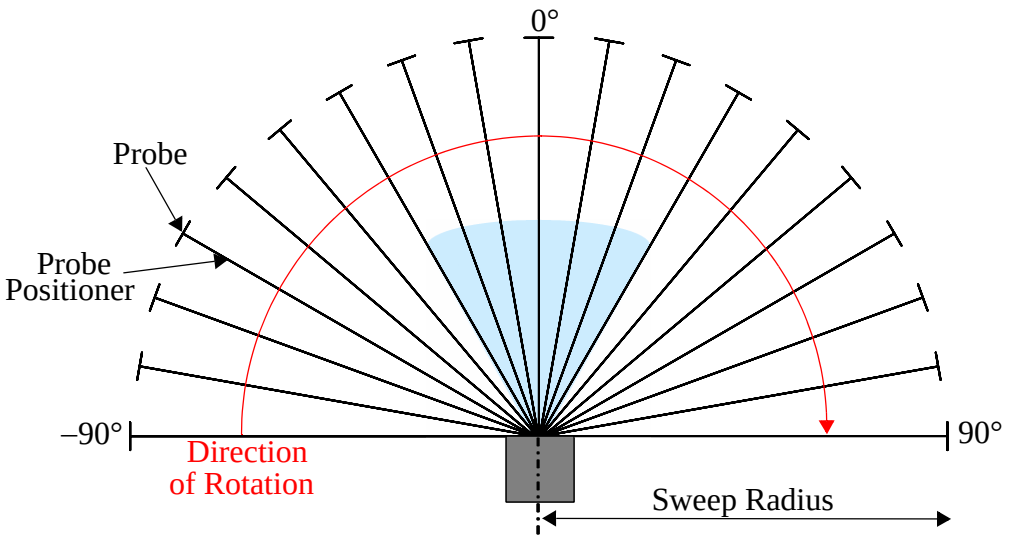

Figure 2.16 Top-view schematic of the probe setup.

Current drawn by the Faraday probe is determined by measuring the voltage drop across a 101.5Ω resistor, as shown in Figure 2.17. The voltage drop is acquired by a 22-bit HP34970A Agilent Data Logger and is stored with the probe's angular position in a file created by the same LabView program that commands the automated probe positioner.

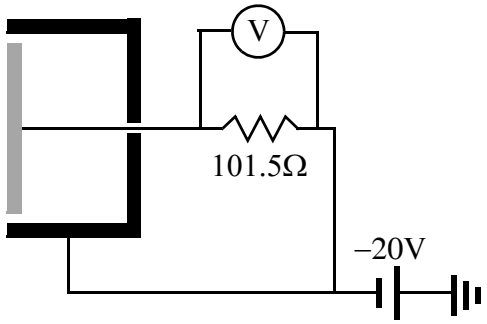

Figure 2.17 Electrical schematic of the Faraday probe.

2.3.6 Sample Measurements

Figures 2.18 and 2.19 portray typical Faraday probe measurements plotted in linear and logarithmic scales respectively. The figures represent the current density distribution at 1m from the BHT-1500 exit plane. The thruster is operating at a discharge voltage of 300V, discharge current of 2A, anode flow rate of 2.44mg/s, and background pressure of 6.58×10^{-6} Torr. The distribution is symmetric with respect to the centerline with "shoulders" at the wings and a double hump at the peak. The maximum current density occurs at the centerline, whereas the minimum current density occurs at the wings, with a maximum to minimum ratio of 75. The current density distribution is typically plotted in a logarithmic scale so that the structure of the distribution at high angles can be easily observed. The shoulders at the wings seen in the logarithmic scale are not displayed in the linear scale due to the high maximum to minimum current density ratio. The current density plotted in Figures 2.18 and 2.19 is an average of three measurements. The standard deviation of the average value for these measurements is smaller than 3%, indicating good reproducibility.

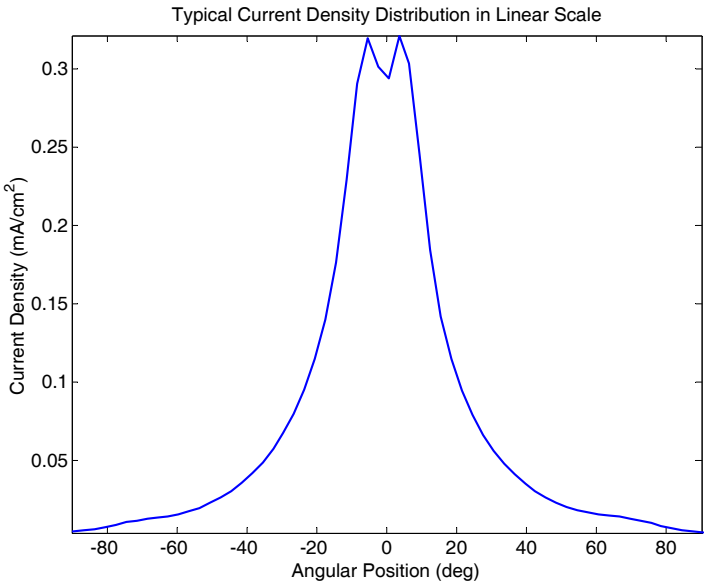

Figure 2.18 Typical current density distribution for the BHT-1500 plume. The current density is plotted on a linear scale. V_d = 300V, I_d = 2A, P = 6.58×10^{-6} Torr, $\dot{m}_a$ = 2.44mg/s and sweep radius = 1m.

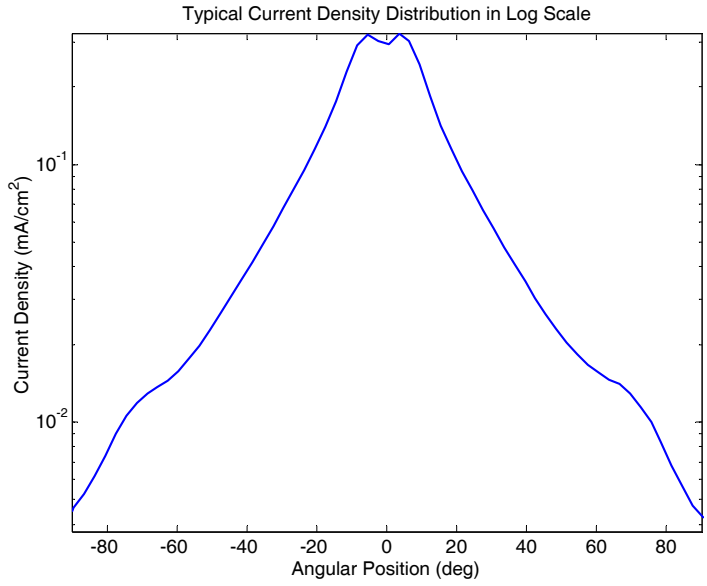

Figure 2.19 Typical current density distribution for the BHT-1500 plume. The current density is plotted on a logarithmic scale. V_d = 300V, I_d = 2A, P = 6.58×10^{-6} Torr, $\dot{m}_a$ = 2.44mg/s and sweep radius = 1m.

2.4 Retarding Potential Analyzer

2.4.1 Probe Description

A Retarding Potential Analyzer (RPA) is a diagnostic instrument that measures the ion energy distribution. It consists of a current collector shielded from the plasma by a series of biased grids. The RPA allows only ions with energy to charge ratios (E/q) higher than the retarding potential to reach the collector. Four grids are typically used in RPAs, of which the first grid is floated to reduce plasma perturbation, the second grid is negatively biased to repel electrons, the third grid is positively biased to repel only selected ions, and the fourth grid is negatively biased with respect to the collector to repel secondary electrons. The spacing between the grids is optimized to minimize space charging effects. Figure 2.20 shows a diagram of an RPA, as well as a schematic of the voltage bias applied to the grids. The figure also provides an illustration of the RPA concept.

Despite their ease of use, RPAs have several issues. For example, the internal pressure of the RPA may cause ions to collide before reaching the collector, thus leading to a decreased energy peak and a widened energy distribution towards lower ion energy. In addition, the RPA does not discriminate between singly charged and multiply-charged ions. Xenon Hall thruster plumes are generally composed of 89% Xe^{+}, 10% Xe^{2+} and 1% Xe^{3+} [33, 34, 35, 36]. A doubly charged ion born at the same potential as a singly charged ion is stopped by the same retarding potential as a singly charged ion. Therefore, in data reduction of RPA measurements, all collected ions are assumed to be singly charged.

2.4.2 Probe Design

Figure 2.21 shows a picture of the RPA used in this research. It is a new design originally based upon the University of Michigan's RPA described by Hofer [33]. The outer diameter of the RPA is 12.7mm with an aperture diameter of 6.35mm. A cross-section of the RPA is shown in Figure 2.22. The collector is placed 15.75mm away from the aperture, enabling a collimation angle of 22.8°, which ensures that only ions coming directly from near the exit

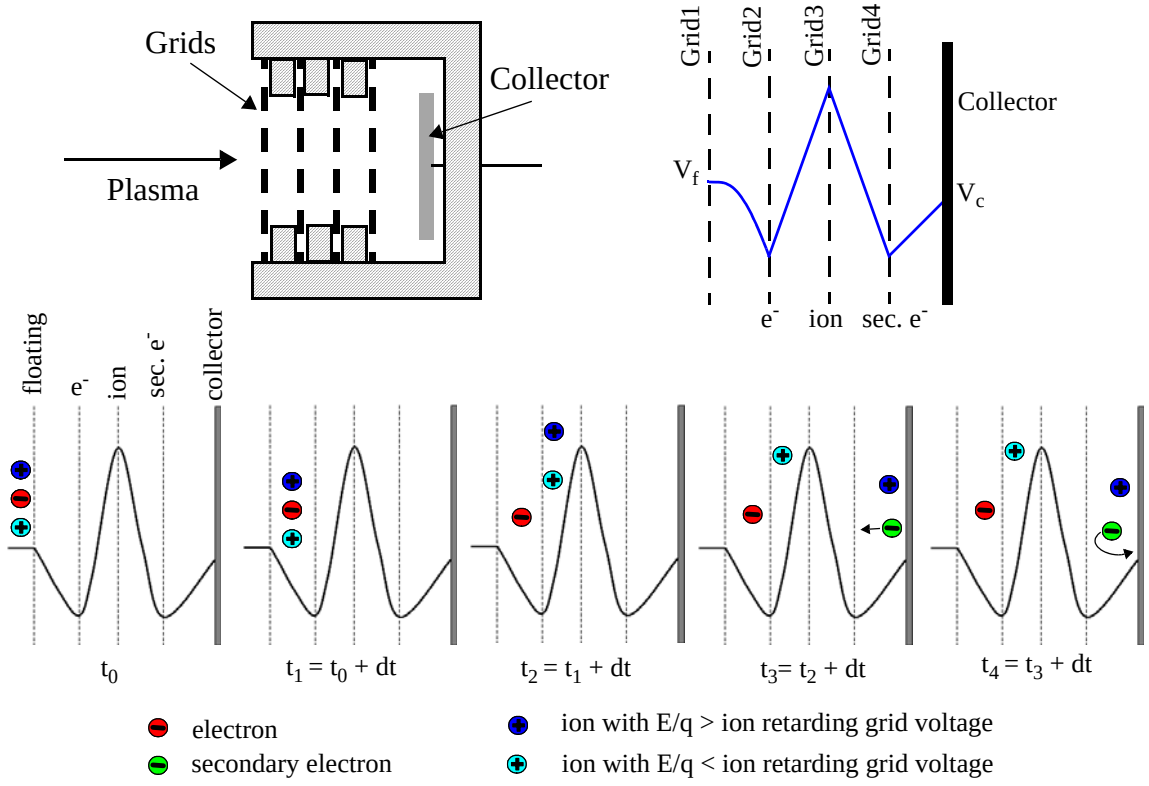

Figure 2.20 Schematic of a retarding potential analyzer and bias applied to grids. Diagram of RPA concept illustrates the effect of the grid bias on the plasma.

plane of the thruster are collected. Figure 2.23 is a cross-section schematic of the RPA that defines the collimation angle.

Three grids are used in this RPA. The first grid is floated to reduce plasma perturbation, the second grid is negatively biased to repel electrons, and the third grid is positively biased to retard ions. A secondary electron suppression grid is not utilized in this RPA design. In deciding to design the RPA with either three or four grids, it was important to have a design with a large open area to ensure an adequate signal to noise ratio. In addition, the secondary electron emission from ion bombardment of a stainless steel surface at energies less than 1keV is not a concern. As discussed in Section 2.3.2, the secondary electron yield due to Xe^+ bombardment at energies below 1keV is less than 0.02 electrons per ion [32].

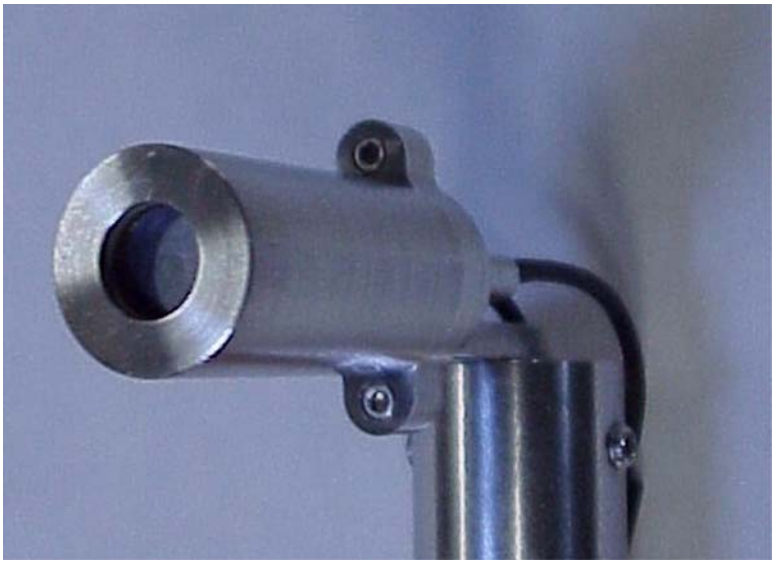

Figure 2.21 Picture of the retarding potential analyzer.

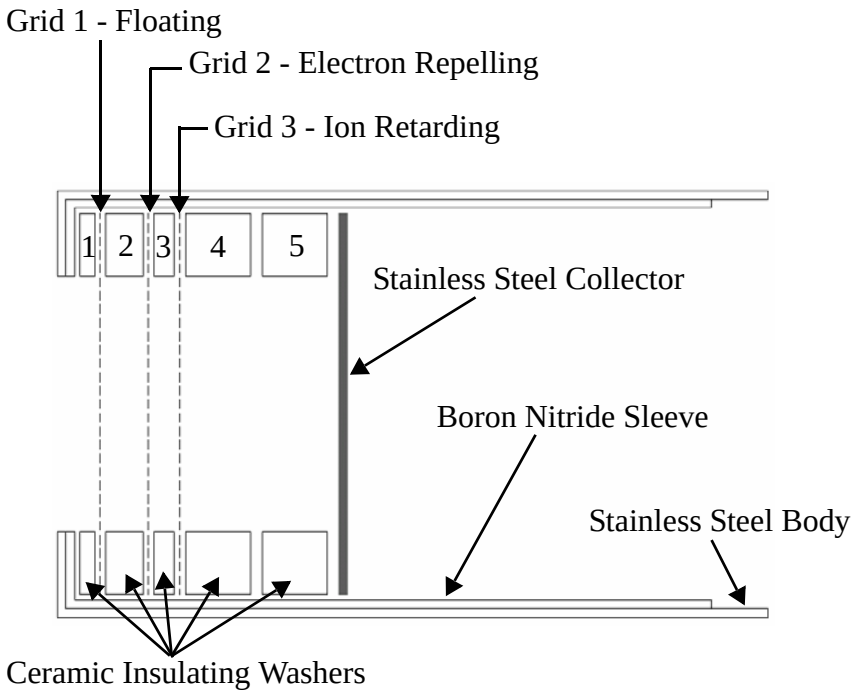

Figure 2.22 Cross-section schematic of the retarding potential analyzer [33].

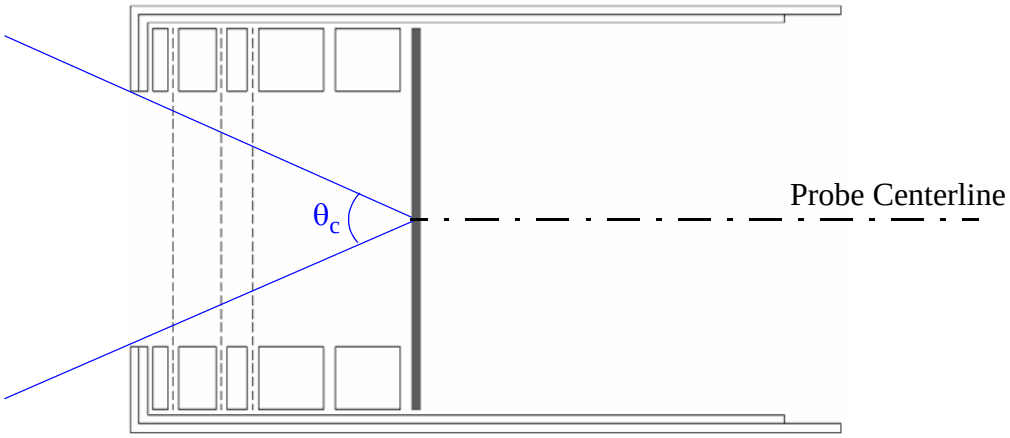

Figure 2.23 Schematic showing the collimation angle of the retarding potential analyzer, θ_c. The RPA has a collimation angle of 22.8°.

When designing an RPA, it is essential to properly size the grid openings. The grid openings must be smaller than the thickness of the sheath to ensure an effective grid bias. Figure 2.24 illustrates the influence of grid opening on the effectiveness of the grid bias. Since the plasma shields itself from external electrostatic fields, charged particles are not affected by the grid bias until they reach the sheath. If the sheath in front of the grid does not extend across the entire grid, plasma is able to escape through the grid openings, rendering the grid bias ineffective. As portrayed by Figure 2.24, for a negatively biased grid, only ions pass through the grid when the grid opening is smaller than the sheath thickness because the sheath extends across the opening. As charged particles reach the sheath, the grid potential is felt across the entire grid. When the grid opening is larger than the sheath thickness, the sheath does not extend across the opening. This creates a region within the grid opening where the grid bias is not felt by charged particles, allowing particles that should be repelled to pass through. The sheath thickness is on the order of 5-10 Debye lengths. Using Table 2.1, the grid opening must be smaller than 0.65mm in diameter. The grids used in this RPA are 35.6μm thick chemically etched Molybdenum. The grid opening is hexagonal with a width of 0.14mm and a 72% open area.

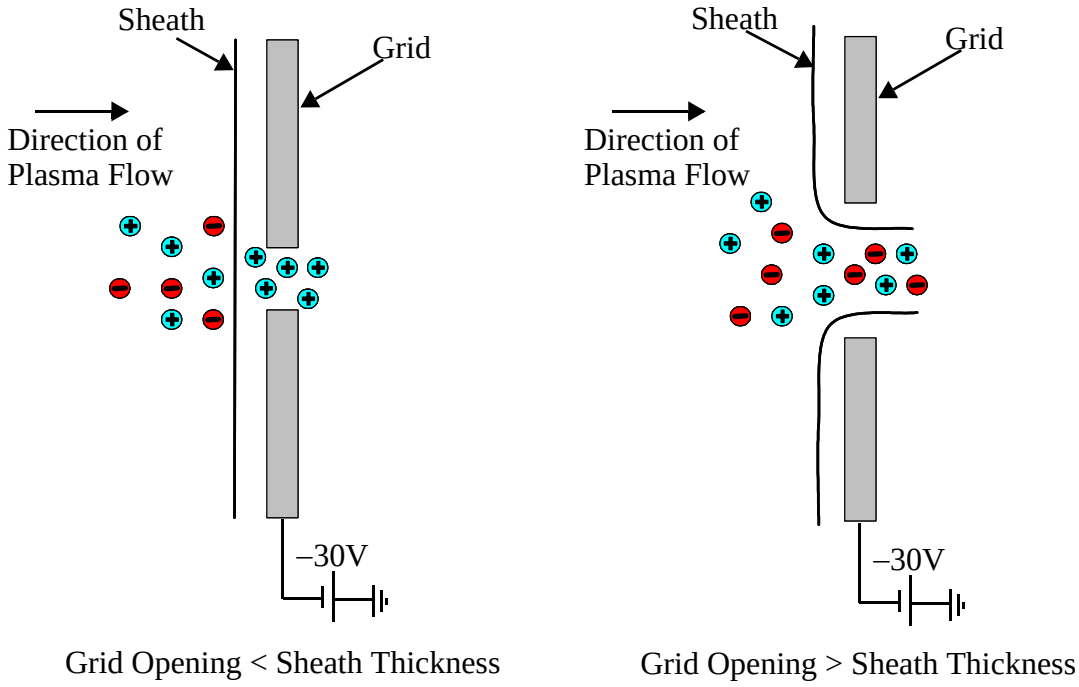

Figure 2.24 Schematic showing that effectiveness of the grid bias depends on the grid opening. The grid opening must be smaller than the sheath thickness. If the grid opening is larger than the sheath thickness, the sheath will not extend across the opening within the grid. This creates a region within the grid opening where the plasma can pass through uninfluenced by the grid bias. The illustration on the left shows proper sizing of the grid opening. For a negatively biased grid, only ions pass through. The illustration on the right shows a grid with a large opening compared to the sheath thickness. For a negatively biased grid, both ions and electrons pass through.

A major concern when designing an RPA is the space-charge limitation that can occur past the electron repelling grid. The charge density can reach a threshold beyond which no charge can be added. This occurs because the charge density can alter the potential between the grids, causing the ion retarding potential to be higher than the potential applied by the power supply. In this case, ions that should reach the collector are repelled, causing a shift in the ion energy distribution towards lower energies. Therefore it is important to determine the proper grid spacing to avoid space-charge limitation. This is especially critical for the spacing between the electron repelling and the ion retarding grids. The proper spacing between these grids can be determined by calculating the thickness of a sheath with a potential applied across it. Equating the ion Bohm flux to the Child-Langmuir flux gives

$$t_s = 1.02\lambda_d\left(\frac{eV}{kT_e}\right)^{3/4} \tag{2.3}$$

where t_s is the sheath thickness and V is the potential applied across the sheath [37]. Therefore, in order to avoid space charge limitation, the spacing between the electron repelling and the ion retarding grids must be smaller than t_s. The potential applied across the grids, V, at which space charge effects are greatest is 30V. It occurs when all ions are allowed to pass through the ion retarding grid. The Debye length, λ_d, is calculated from plasma density outside the RPA. Table 2.2 shows the maximum allowable spacing between the electron repelling and the ion retarding grids, t_{s_max}, at various distances from the thruster exit plane using the Debye lengths calculated in Table 2.1.

TABLE 2.2 Calculation of the maximum spacing between the electron repelling and the ion retarding grids to avoid space charge limitation. A potential difference, V, of 30V was used in this calculation because it is the potential at which the space charge effects are greatest.

	Distance From Thruster Exit Plane			
	0.25m	**0.50m**	**0.75m**	**1m**
T_e (eV)	3	3	2	2
λ_d (mm)	0.13	0.29	0.33	0.43
t_{s_max} (mm)	0.75	1.66	2.57	3.34

Using Table 2.2, 0.5mm was selected as the spacing between the electron repelling and the ion retarding grids.

2.4.3 Probe Construction

Figure 2.25 is a cross-section solid model drawing of the RPA. The RPA's grids and collector are enclosed in a 316 stainless steel outer casing, which is grounded to the facility tank. A Boron Nitride inner sleeve electrically isolates the collector and the grids from the outer casing. The grids and collector are electrically separated using glass-mica ceramic washers. The collector is made of 316 stainless steel. The electrical connections to the

grids and the collector are made by spot welding a 30 gauge copper wire coated with a Polyimide film. The wire, made by MWS Wire Industries, passes along the inner edge of the Boron Nitride sleeve and exits at the back of the RPA. A spring, placed between a glass-mica ceramic spacer and the RPA back cover, enables the washers, grids and collector to be anchored. The outer casing is attached to the back cover using a socket head cap screw and a hex nut.

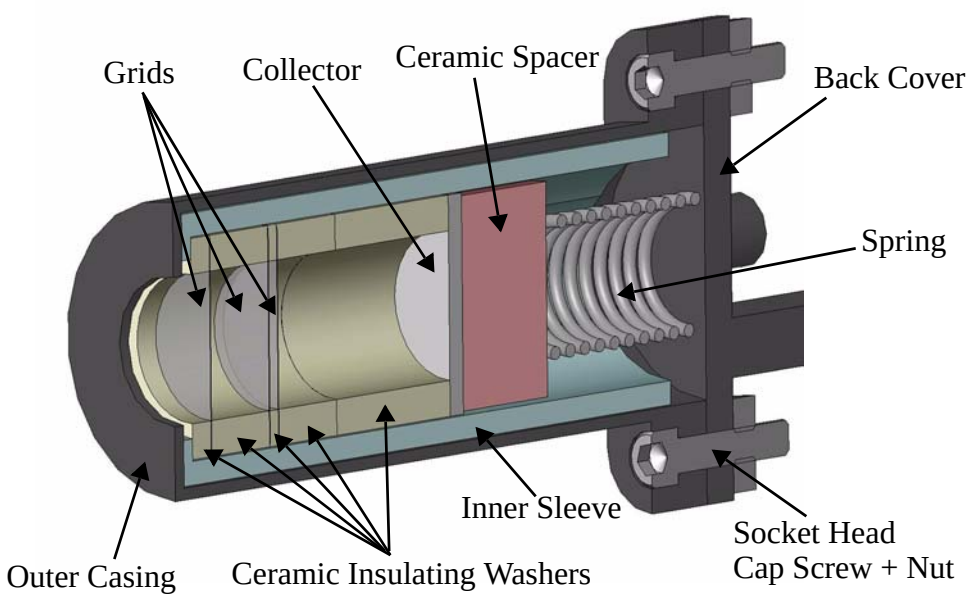

Figure 2.25 Cross-section of the retarding potential analyzer.

The resulting product is an RPA with an outer diameter of 12.7mm, an aperture diameter of 6.35mm and a collector placed 15.75mm away from the aperture. Table 2.3 summarizes the dimensions of the ceramic insulating washers.

TABLE 2.3 Dimensions of the ceramic insulating washers.

Washer[1]	1	2	3	4	5
Thickness (mm)	1.07	3.35	0.50	3.35	6.50
Inner Diameter (mm)	6.35	6.35	6.35	6.35	6.35

1. The numbering of the washers is the same as the one shown in Figure 2.22.

2.4.4 Probe Setup

The RPA is mounted on the same automated positioner system described in Section 2.2. The probe's collector is oriented to face the exit plane of the BHT-1500. The vertical height of the probe is set to bisect the plume, passing through its axis. A laser setup is used to align the probe. The probe is placed 1m downstream from the exit plane of the BHT-1500. The probe was swept from –90° to 0° with respect to the thruster centerline in 10° increments through the plume.

Figure 2.26 shows the electrical schematic of the RPA. The first grid is electrically isolated from the probe and the facility ground. The second grid, the electron repelling grid, is biased to –30V with respect to facility ground. The third grid, the ion retarding grid, is connected to a Keithley 2410 SourceMeter that can supply a potential up to 1100V. The potential applied to the third grid is varied from 0 to 1100V with respect to facility ground. Ions that overcome the retarding potential of the third grid are measured using a Keithley 6485 Picoammeter connected to the collector.

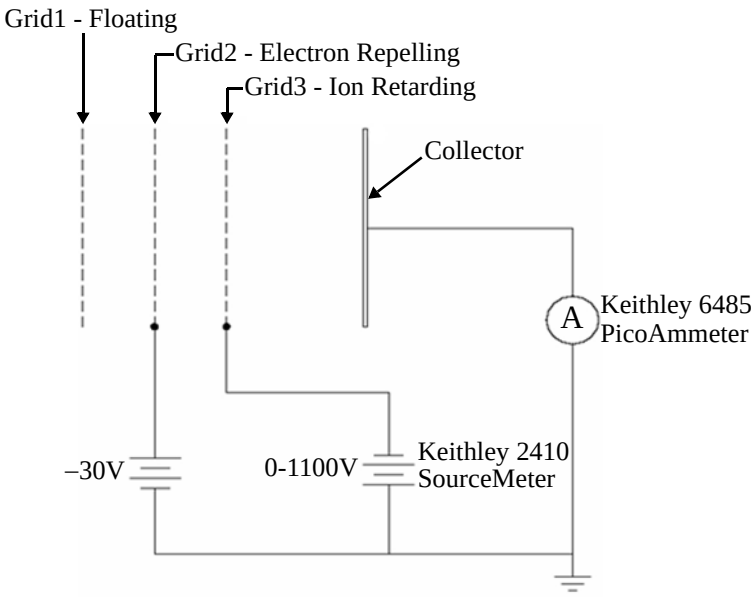

Figure 2.26 Electrical schematic of the retarding potential analyzer.

Two LabView programs are used for ion energy measurements. One program is used to position the probe. The second program, which is used to collect data, controls both the Keithley 2410 SourceMeter and the Keithley 6485 Picoammeter. The program sends a command to the SourceMeter to sweep the retarding voltage and simultaneously acquires the measured current from the PicoAmmeter.

2.4.5 Sample Measurements

The RPA measures the current drawn by the collector as a function of the potential applied to the ion retarding grid, yielding a current-voltage (I-V) curve. Figure 2.27 shows sample I-V curves for the probe positioned 1m away from the BHT-1500 at –90° and 0°. The I-V curves plotted in Figure 2.27 are an average of three measurements. The measurements are reproducible and the standard deviation of the average was calculated as less than 2%. The measurements are obtained for the thruster operating at a discharge voltage of 300V, a discharge current of 2A, an anode flow rate of 2.44mg/s, and a background pressure of 7.5×10^{-6} Torr.

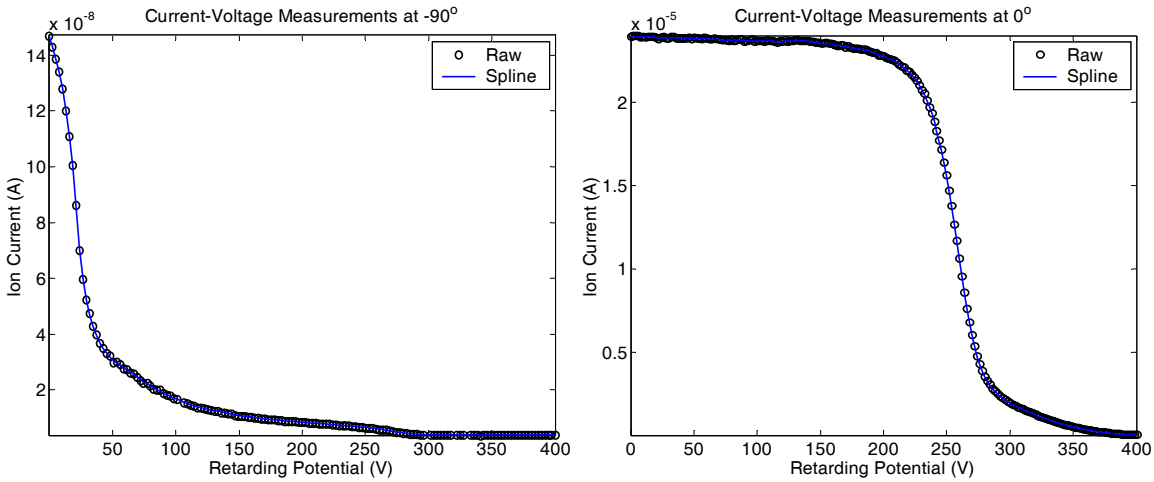

Figure 2.27 Sample raw I-V curves at V_d = 300V, I_d = 2A, P = 7.5×10^{-6} Torr and $\dot{m}_a$ = 2.44mg/s. A smoothing spline fit is applied to the raw data. The plot on the left represents measurements 1m downstream from the exit plane of the thruster at –90°. The plot on the right represents measurements 1m downstream from the exit plane of the thruster at 0°.

As seen in Figure 2.27, the current collected decreases with an increase in retarding potential because fewer ions are able to reach the collector. The goal of using an RPA is to determine the ion energy distribution. The following shows the mathematical equations that are used to convert collected current by the RPA into ion energy distribution. The current collected is related to the ion velocity distribution by

$$I(V) = A_c q_i n_i \int_{u(V)}^{\infty} u_i f(u_i) du_i \tag{2.4}$$

where A_c is the collection area, n_i is the ion density, q_i is the charge, V is the ion retarding potential, u_i is the ion velocity, and $f(u_i)$ is the ion velocity distribution function normalized to unity [37]. u_i is defined by

$$u_i = \sqrt{\frac{2q_i V}{m_i}} \tag{2.5}$$

where m_i is the ion mass. A change of variable is performed so that

$$du = \sqrt{\frac{q_i}{2m_i}} \frac{1}{\sqrt{V}} dV \tag{2.6}$$

$$f(u)du = f(V)dV \tag{2.7}$$

where $f(V)$ is the energy distribution function normalized to unity. Substituting Equations 2.5-2.7 into Equation 2.4, the current collected can be related to the ion energy distribution by

$$I(V) = A_c q_i n_i \sqrt{\frac{2q_i}{m_i}} \int_{V_{min}}^{\infty} \sqrt{V} f(V) dV \tag{2.8}$$

The derivative of the current with respect to the voltage yields the ion energy distribution as shown by Equation 2.9

$$\frac{dI}{dV} = -A_c q_i n_i \sqrt{\frac{2q_i V}{m_i}} f(V) \tag{2.9}$$

Figure 2.28 shows ion energy distributions derived from the I-V curves in Figure 2.27 using Equation 2.9. The I-V curves are first fitted with a smoothing spline algorithm and then numerically differentiated to produce ion energy distributions [38]. The spline is used to reduce numerical differentiation noise. The uncertainty due to the spline fit in the most-probable ion voltage, the voltage at the peak of the distribution, is estimated to be ±1%. A detailed description of the characteristics of the ion energy distribution is discussed in Chapter 3.

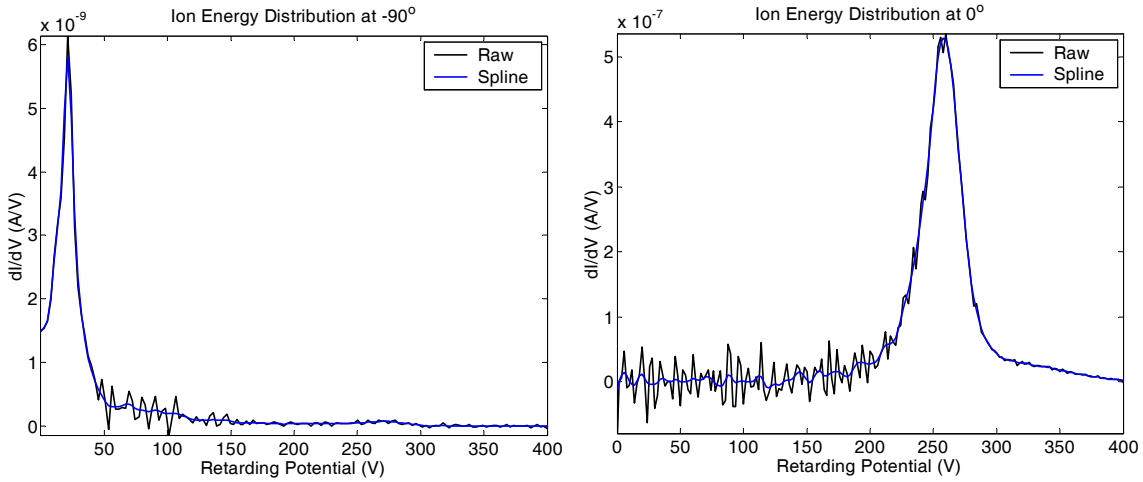

Figure 2.28 Comparison of ion energy distributions obtained from raw data and spline-fit data. The thruster is operated at V_d = 300V, I_d = 2A, P = 7.5×10^{-6} Torr and $\dot{m}_a$ = 2.44mg/s. The plot on the left represents measurements 1m downstream from the exit plane of the thruster at –90°. The plot on the right represents measurements 1m downstream from the exit plane of the thruster at 0°.

Chapter 3

DETERMINATION OF IN-ORBIT PLUME DIVERGENCE

The in-orbit plume is comprised of source ions, elastically scattered ions, charge exchange (CEX) ions, electrons and neutrals. The source ions are produced through electron impact ionization with neutrals. The elastically scattered and CEX ions are produced through source ion collisions with neutrals. The neutrals in the in-orbit plume originate from the anode and cathode of the thruster. The anode neutrals exist because the utilization efficiency of the anode propellant is always below 100%. The cathode neutrals exist because the cathode is a poor ionizer; only 10% of cathode flow is ionized. The laboratory plume includes, in addition to the in-orbit plume particles, elastically scattered and CEX ions produced through source ion collisions with tank neutrals. To determine the in-orbit plume characteristics from laboratory measurements, the contribution of the tank neutrals to the plasma plume needs to be removed.

This chapter outlines a simple and objective method to determine the in-orbit plume divergence from laboratory measurements. The chapter starts with a discussion of the factors causing plume divergence and covers a literature survey of the various methods that are currently used to determine the plume divergence. These methods are analyzed and critiqued. Finally, the effect of the discharge voltage on the plume divergence is investigated.

3.1 Causes of Plume Divergence

Hall thruster plumes have a wider plume divergence compared to other electric propulsion systems. Typical Hall thruster half-angle plume divergence values[1] in the literature range between 40-60° [39, 40, 41] compared to 20-30° for ion engines [42, 43]. Several factors cause ions entering the beam to diverge. They include the radial electric field, the location of the ionization region, and collisions. These factors are organized in this Section in two parts: the first part discusses the factors causing divergence inside the thruster channel and the second part discusses the factors affecting divergence in the plume.

3.1.1 Causes of Divergence Inside the Thruster Channel

Inside the thruster, ions are accelerated by the potential difference between the anode and cathode. The net ion velocity is expressed as

$$v_i = \sqrt{\frac{2eV_d}{m_i}} \tag{3.1}$$

Ions are also accelerated radially due to the potential drop in the pre-sheath and sheath inside the thruster channel. This radial potential drop is controlled by the electron temperature. Ions enter the sheath radially with the Bohm velocity,

$$v_{ir} = \sqrt{\frac{kT_e}{m_i}} \tag{3.2}$$

The plume divergence scales as the ratio of radial to net ion velocity. Using Equations 3.1 and 3.2, the half-angle plume divergence, θ_{div}, can be expressed roughly as the ratio of electron temperature to discharge voltage by

$$\sin\theta_{div} \approx \frac{v_{ir}}{v_i} = \sqrt{\frac{kT_e}{2eV_d}} \tag{3.3}$$

1. The method used to calculate the plume divergence is different for various thrusters. Section 3.2 discusses the techniques currently used to determine the plume divergence.

For a certain thruster operating discharge voltage, a low electron temperature is desired to obtain a small plume divergence; however, a low electron temperature would negatively affect the utilization efficiency, reducing thruster performance. Using a two-stage Hall thruster may mitigate the effect of electron temperature on plume divergence. In a two-stage Hall thruster, the ionization and acceleration regions are separated. The electron temperature is high in the ionization region and low in the acceleration region. Therefore, the radial potential drop across the channel of the acceleration region is small resulting in a potentially lower plume divergence. This is evident in ion engines where the ionization and acceleration regions are separated resulting in a low plume divergence compared to Hall thrusters.

There is also experimental evidence that points to the location of the ionization region as a potential factor affecting plume divergence. Raitses showed that a segmented Hall thruster with low-sputtering carbon-velvet electrodes produced a lower plume divergence than conventional non-segmented Hall thrusters [41]. The carbon-velvet electrodes, because of their low secondary electron emission, push the ionization region closer to the anode where the potential structure is flat, i.e. the electric potential contours are parallel to the thruster exit plane. The flat potential structure reduces the radial component of ion velocity, thereby reducing the plume divergence.

Reducing the plume divergence is not a trivial matter. There is a trade-off among thruster performance, thruster lifetime and plume divergence. As stated before, a low electron temperature reduces the radial potential drop, which results in a lower plume divergence. However, the cost of lowering the electron temperature is a low utilization efficiency, which harms thruster performance. Pushing the ionization region closer to the anode also reduces plume divergence. However, it can lead to higher wall losses and higher erosion of the channel material causing a reduced thruster lifetime. In general, when engineers design Hall thrusters, minimizing plume divergence is secondary to increasing thruster lifetime and performance.

3.1.2 Causes of Divergence in the Plume

An ion exiting the thruster can undergo a scattering collision with an electron, an ion, or a neutral, or it can charge exchange with a neutral. A mean free path analysis is performed in this section to examine the dominant collisions that cause plume divergence.

Coulombic Collisions

Ion-electron and ion-ion collisions are based on Coulomb interactions. In the case of ion-electron collisions, the mean free path of interest is the momentum loss mean free path, which is the length of successive ion collisions with electrons for the ion to change trajectory. An ion colliding with one electron will not change its trajectory because it is much heavier than the electron. The mean free path of ion-electron Coulomb collisions is

$$\lambda_{ie} = \frac{\bar{c}_e}{\nu_{ie}} \tag{3.4}$$

$\bar{c}_e$ is the mean thermal speed of electrons and is determined by

$$\bar{c}_e = \sqrt{\frac{8kT_e}{\pi m_e}} \tag{3.5}$$

ν_{ie}, the collision frequency of an ion colliding with Maxwellian electrons, is given by [44]

$$\nu_{ie} = \frac{m_e}{m_i}\frac{\sqrt{2}}{3\sqrt{\pi}} n_e \left(\frac{Ze^2}{4\pi\varepsilon_0}\right)^2 \frac{4\pi}{m_e^{1/2}(kT_e)^{3/2}} \ln\Lambda_e \tag{3.6}$$

For ion-ion collisions, the mean free path is determined by

$$\lambda_{ii} = \frac{v_i}{\nu_{ii}} \tag{3.7}$$

where v_i is the ion velocity and ν_{ii}, the ion-ion collision frequency, is given by [44]

$$\nu_{ii} = \frac{1}{3\sqrt{\pi}} n_e \left(\frac{Ze^2}{4\pi\varepsilon_0} \right)^2 \frac{4\pi}{m_i^{1/2} k T_i^{3/2}} \ln\Lambda_i \tag{3.8}$$

To calculate the mean free paths, we first estimate the electron density and the electron and ion temperatures. At the exit plane, the electron density can be estimated using

$$n_e = \eta_u \frac{\dot{m}_a}{m_i v_i A} \tag{3.9}$$

where η_u is the utilization efficiency, $\dot{m}_a$ is the propellant flow rate through the anode, and A is the thruster exit area. Downstream from the thruster exit, the plume expands spherically. Therefore, the electron density is assumed to fall as $1/r^2$. An electron temperature of 25eV is assumed at the thruster exit plane based on results of a Full PIC code simulating the BHT-1500 [14, 28, 45]. In the plume, the electron temperature tends to be in the 2-3eV range [12, 13]. Ions, on the other hand, are not thermalized in Hall thruster plumes and are assumed to be cold. For this calculation, an ion temperature of 1eV is used.

Table 3.1 shows the mean free path of Coulombic collisions at various distances with respect to the thruster exit. The table also includes estimates of the electron density and electron and ion temperatures used for the calculation of the mean free path.

TABLE 3.1 Mean free path of Coulombic collisions.

	Distance from Exit Plane		
	0m	**0.50m**	**1m**
T_e (eV)	25	3	2
T_i (eV)	1	1	1
n_e (m^{-3})[1]	1.65×10^{17}	3.25×10^{14}	8.13×10^{13}
λ_{ie} (m)	16×10^{6}	117×10^{6}	209×10^{6}
λ_{ii} (m)	2.2	1130	4519

1. The electron density at the thruster exit (0m) is calculated with Equation 3.9 using η_u of 0.9, v_i of 20,000m/s and $\dot{m}_a$ of 2.44mg/s.

As can be seen from Table 3.1, the ion-electron collision mean free path is very large compared to the features of interest. Therefore, ion-electron interactions do not contribute to plume divergence.

Despite that the mean free path of ion-ion collisions at the thruster exit is relatively small, they also do not contribute to plume divergence. The expression of ion-ion collision frequency in Equation 3.8 is derived for collisions occurring in the center of mass frame of reference where collisions are isotropic and the relative ion velocities at which they collide are assumed to be thermal. In the lab frame of reference, superimposing the center of mass velocity (which is axial and on the order of 300-1000V) to the particles' thermal velocities (on the order of few Volts) post collision yields ions that are mainly travelling axially. Therefore, ion-ion collisions lead to small angle deflections and are unlikely to cause plume divergence.

Elastic and CEX Collisions

The mean free path of ion-neutral collisions can be expressed as a function of the collision cross-section, σ, by

$$\lambda_{in} = \frac{1}{\sigma_{in} n_n} \tag{3.10}$$

where n_n is the neutral density. The general form of Equation 3.10 can be used for both elastic and charge exchange collisions by substituting the appropriate value of the collision cross-section. The Xe-Xe^+ elastic collision cross-section, σ_{sc}, is determined by

$$\sigma_{sc} = \frac{8.28072\times10^{-16}}{c_r} \tag{3.11}$$

where c_r is the relative velocity between a xenon neutral and a xenon ion [16, 46]. The Xe-Xe^+ charge exchange cross-section, σ_{cex}, is assumed to be approximately 5.4×10^{-19} m^2 [47]. In this analysis, the ion-neutral collisions are divided into ion collisions with tank neutrals and ion collisions with thruster neutrals (anode plus cathode neutrals).

The tank neutral density is assumed to be uniform inside the vacuum chamber. It is a function of the background pressure and is expressed using

$$n_{n,\,Tank} = 133.3\frac{P}{kT_n} \tag{3.12}$$

where P is the tank pressure in Torr and T_n is the neutral temperature in Kelvin. The density of thruster neutrals is the sum of anode and cathode neutral densities. As a rough estimate, we assume the cathode is internally mounted and that the cathode and anode neutrals expand in the same direction starting from the thruster exit, as shown in Figure 3.1.

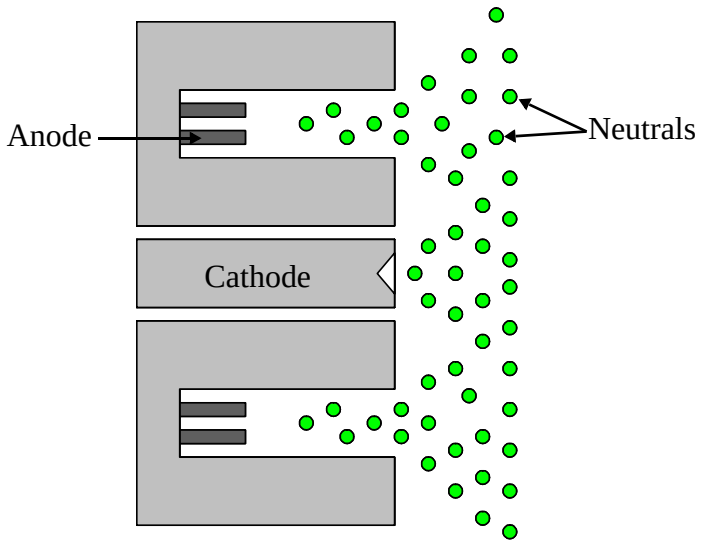

Figure 3.1 Schematic of neutral flow from the thruster. For simplicity, the calculation of the total neutral flow from the thruster assumes an internally mounted cathode and that the cathode and anode neutrals expand in the same direction. In reality, the cathode is mounted on top of the thruster as shown in Figure 2.1.

By continuity, the neutral density at the thruster exit is

$$n_{n,\,anode} = \frac{(1-\eta_u)\dot{m}_a}{m_i c_n A} \tag{3.13}$$

$$n_{n,\,cathode} = \frac{(1-\eta_u')\dot{m}_c}{m_i c_n A_{cathode}} \tag{3.14}$$

where c_n is the speed of neutrals, $\dot{m}_c$ is the flow through the cathode, $A_{cathode}$ is the cathode orifice area, and η_u' is the cathode utilization efficiency, which is estimated at 10%. Assuming that neutrals expand spherically and that the neutral density falls as $1/r^2$, we can calculate the neutral density at various distances with respect to the thruster exit. Table 3.2 provides estimates of the neutral density originating from the tank and the thruster.

TABLE 3.2 Ion-neutral mean free path for elastic scattering and CEX collisions.

	Distance from Exit Plane		
	0m	**0.50m**	**1m**
n_n [Tank][1] (m^{-3})	3.22×10^{17}	3.22×10^{17}	3.22×10^{17}
n_n [Thruster][2] (m^{-3})	2×10^{18}	7.63×10^{15}	1.91×10^{15}
λ_{in} [Tank] (m)	75	75	75
λ_{in} [Thruster] (m)	11.8	3167	12668
λ_{cex} [Tank] (m)	5.75	5.75	5.75
λ_{cex} [Thruster] (m)	0.93	243	970

1. The neutral density in the tank is based on a background pressure of 1×10^{-5} Torr.
2. The thruster neutral density includes both anode and cathode neutrals.

The results of the mean free path analysis of ion-neutral collisions are also presented in Table 3.2. Even though the mean free paths calculated in Table 3.2 are larger than the dimensions of interest, the small amount of charge exchange ions that are created may be important since they are accelerated sideways and backward due to the potential structure of the plume. These charge exchange ions tend to increase plume divergence and produce undesirable interactions at high angles. Comparing Table 3.1 with Table 3.2, ion-neutral collisions are more dominant than Coulombic interactions. Results of the mean free path analysis indicate that the dominant collisions in the plume are charge exchange collisions,

which are most likely to occur within two mid-channel diameter lengths of the thruster exit.

One important conclusion from this mean free path analysis is that near the thruster exit the CEX collisions of source ions with thruster neutrals is significantly higher than the CEX collisions of source ions with tank neutrals. Therefore, it is important that not all charge exchange ions are filtered out from laboratory measurements to obtain the in-orbit measurements. The mean free path analysis also shows that the laboratory plume can include significant interactions (depending on the background pressure) between source ions and tank neutrals. On the other hand, the in-orbit plume is collisionless past the thruster exit plane. Furthermore, at 1m, the laboratory plume is well formed except for the presence of collisions with background neutrals, which are not present in space. Hence, 1m plume measurements, after filtering the tank neutral effects, are representative of the true in-orbit plume.

3.2 Other Methods for Calculating Plume Divergence

The half-angle plume divergence, θ_{div}, is defined as the angle relative to the thruster centerline which contains 95% of the beam current. It is calculated using

$$0.95 I_b = 2\pi r^2 \int_0^{\theta_{div}} j(\theta) \sin\theta \, d\theta \tag{3.15}$$

where θ is the angle with respect to centerline, $j(\theta)$ is the measured current density, r is the distance from to the thruster exit where current density is measured, and I_b, the beam current, is calculated by

$$I_b = 2\pi r^2 \int_0^{\frac{\pi}{2}} j(\theta) \sin\theta \, d\theta \tag{3.16}$$

The measured current density, $j(\theta)$, includes measurements due to facility effects. Facility effects must be removed from the measured current density before Equation 3.15 is used to calculate the half-angle plume divergence. However, different methods exist to account for facility effects on the measured current density. These methods range from analytical manipulation of data to use of sophisticated probes to eliminate the effect of tank neutrals.

3.2.1 Analytical Methods

Method A

This method consists of extending the seemingly exponential portion of the current density distribution near the centerline to ±90° to obtain the corrected current density, as shown in Figure 3.2 [48].

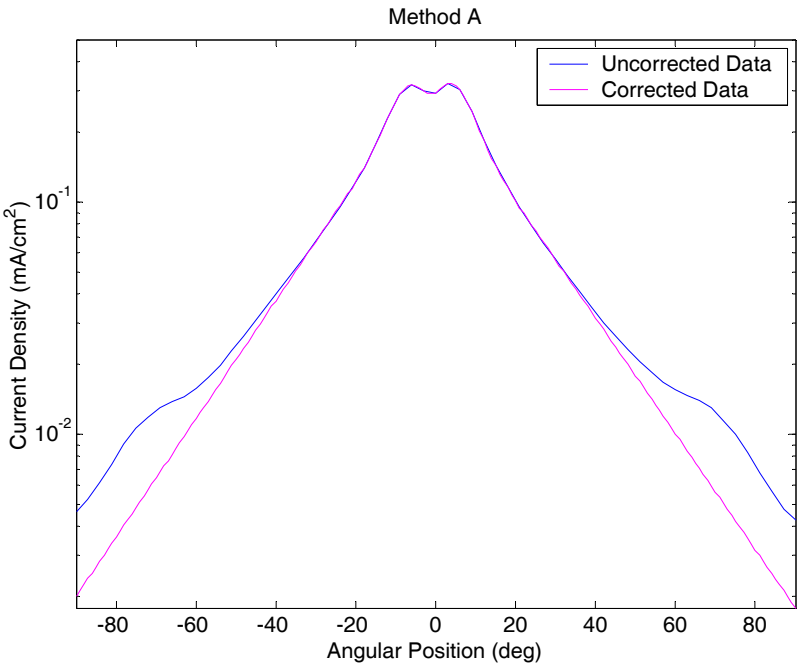

Figure 3.2 The uncorrected data curve represents current density measured with a Faraday probe at V_d = 300V, I_d = 2A, P = 6.58×10^{-6} Torr, $\dot{m}_a$ = 2.44mg/s and sweep radius = 1m. The corrected data curve represents the current density corrected for in-orbit conditions by extending the exponential portion of the current density in the 10-30° region to ±90°.

This method is subjective in the way the exponential fit is selected since the half-angle plume divergence depends on the extrapolation of the current density. For example, the 95% half-angle plume divergence for uncorrected data in Figure 3.2 is 76°. When using an exponential fit in the 10°-20° region of the current density, the 95% half-angle plume divergence is 58°, whereas a fit in the 10°-30° region produces a 95% half-angle plume divergence of 68°. This method also does not discriminate between effects caused by the anode/cathode neutrals and tank neutrals. However, when calculating the in-orbit plume divergence, only effects of the tank neutrals should be removed from the current density.

Method B

Another method that is used consists of correcting the measurements by subtracting the current density at 90° (with respect to thruster centerline) from the measurements at other angles [49]. Figure 3.3 shows a comparison between the measured and corrected current density.

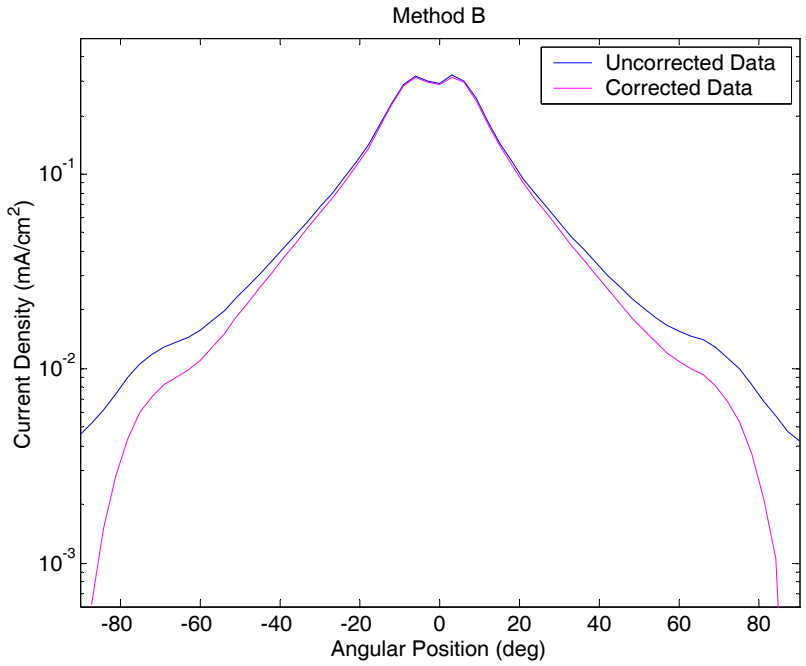

Figure 3.3 The uncorrected data curve represents current density measured with a Faraday probe at V_d = 300V, I_d = 2A, P = 6.58×10^{-6} Torr, $\dot{m}_a$ = 2.44mg/s and sweep radius = 1m. The corrected data are obtained by subtracting measured current density at 90° from the uncorrected data.

By using this method, one assumes that the current density due to scattered and charge exchange ions created through collisions with tank neutrals is the same for all angles. However, this assumption does not portray an accurate representation of the angular distribution of charge exchange ions. Numerical results suggest a “cylindrical dipole” type of distribution, centered about the 90° position [18, 19, 20].

Method C

A third method consists of using two Faraday probes to determine the in-orbit current density [50]. One Faraday probe is facing the exit plane of the thruster and the other probe is facing away from the thruster in the direction of plume expansion. The idea is that the probe facing away from the thruster only measures current density due to source ion collisions with tank neutrals. Subtracting measurements of the Faraday probe directed away from the thruster from measurements of the probe facing the thruster should theoretically yield the corrected current density for in-orbit conditions.

The BHT-1500 is used to measure current density with the Faraday probe facing the thruster and facing away from the thruster. This method is then used to determine the in-orbit current density. Figure 3.4 shows the measured current density taken with the probe facing the thruster (Forward Data) and away from the thruster (Backward Data). The corrected data in Figure 3.4 represent the in-orbit current density obtained using Method C. The Faraday probe measurements are obtained at two background pressures. Method C is then used to calculate the in-orbit current density based on measurements obtained at each background pressure, as shown in Figure 3.4.

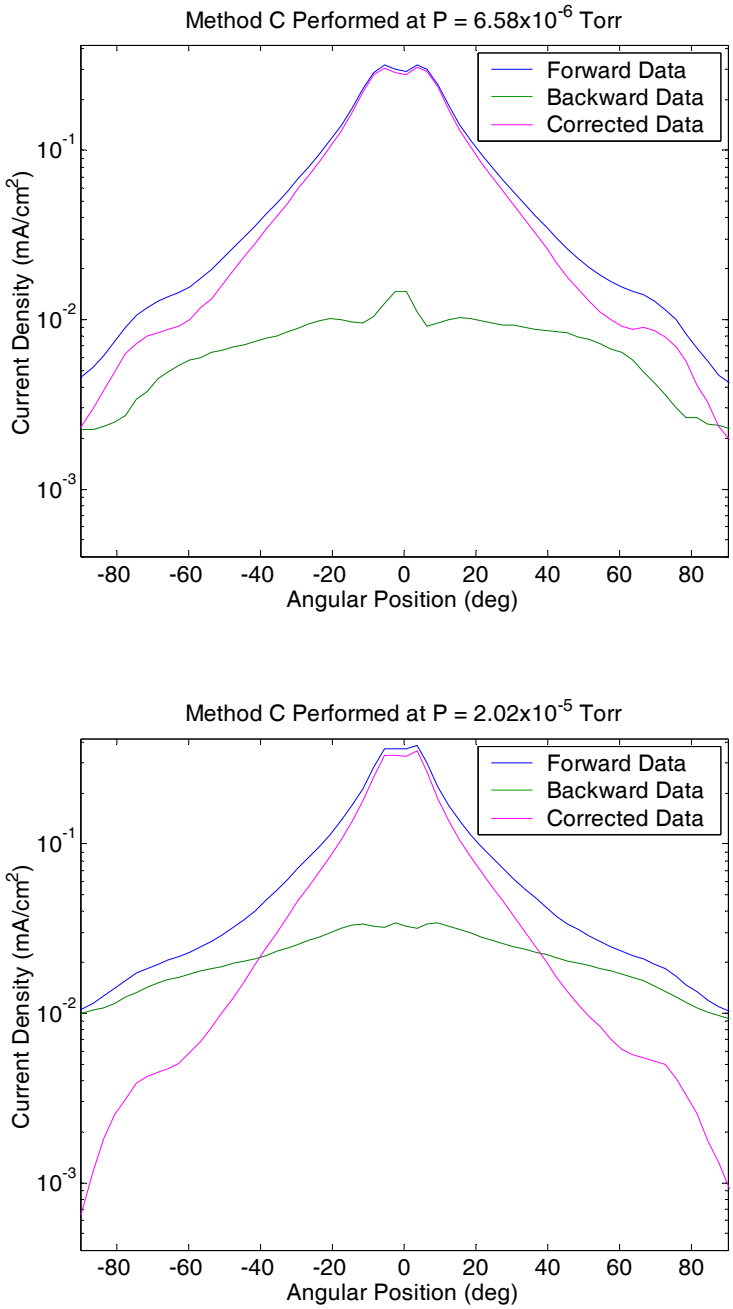

Figure 3.4 The forward data curve represents uncorrected current density measured with a Faraday probe facing the thruster exit plane; the backward data curve represents current density measured with a Faraday probe looking away from the thruster. The corrected data are the forward data minus the backward data. The measurements are obtained at V_d = 300V, I_d = 2A, $\dot{m}_a$ = 2.44mg/s and sweep radius = 1m. The plot on the top and the bottom show the correction method performed for P = 6.58×10^{-6} Torr and P = 2.02×10^{-5} Torr respectively.

The issue with this method is that the current density corrected from the two Faraday probe measurements depends on the background pressure. Figure 3.5 shows a comparison of the corrected current density obtained when Method C is used at background pressures of 6.58×10^{-6} Torr and 2.02×10^{-5} Torr. Figure 3.5 reveals that the corrected current densities do not match each other. Since the goal of the correction is to eliminate the effect of background neutrals, the corrected current density should not depend on what pressure the correction is made at. Therefore, this method cannot be relied upon to produce an accurate in-orbit current density.

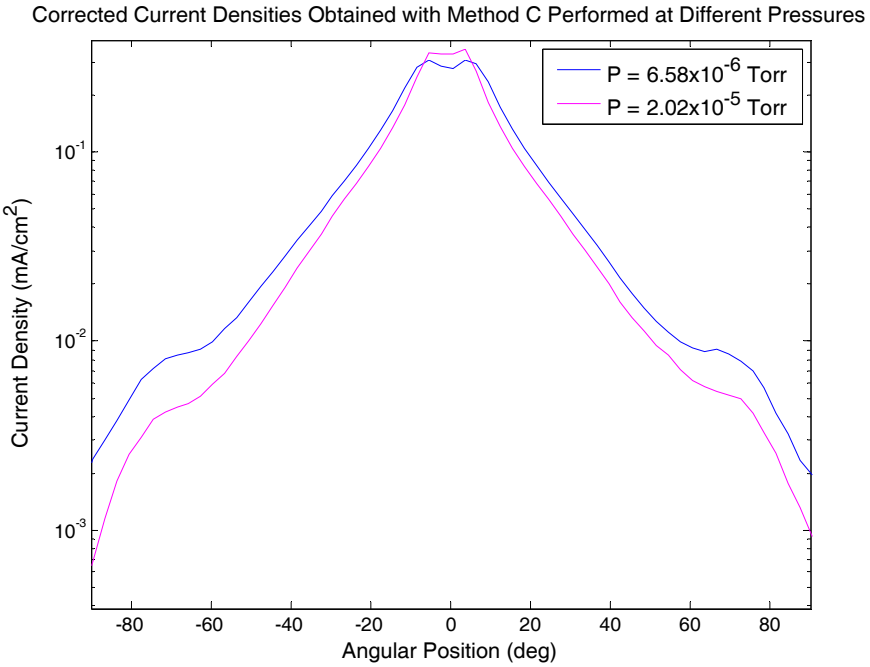

Figure 3.5 Corrected current density at V_d = 300V, $\dot{m}_a$ = 2.44mg/s and sweep radius = 1m. This figure shows that the correction made at 6.58×10^{-6} Torr does not match the correction made at 2.02×10^{-5} Torr, making this method unreliable for determining in-orbit current density and calculating plume divergence.

3.2.2 Experimental Methods

The three methods described earlier use a nude Faraday probe to measure current density and then analytically correct the measurements. Instead of using a nude Faraday probe, more sophisticated probes have been developed to eliminate the effect of tank neutrals without further data manipulation. These probes, shown in Figure 3.6, include a collimated Faraday probe [51], a single-screen gridded Faraday probe, a Retarding Potential Analyzer, and a magnetically filtered Faraday probe [52]. With the collimated Faraday probe, only ions coming directly from the thruster exit are collected by the probe. The collimation shields the probe's collector from ions arriving from outside the collector's line of site. The single-screen Faraday probe and the Retarding Potential Analyzer utilize a positively biased grid to repel low energy ions. The magnetically filtered Faraday probe uses a magnetic field that prevents low energy ions from reaching the collector.

All these probes have been successfully tested and have shown the ability to prevent low energy ions from reaching the collecting surface of the probe. However, filtering out low energy ions from the current density does not yield the in-orbit current density. When these probes remove low energy ions from the measurements, they do not discriminate between legitimate CEX ions that should be included in the measurements and CEX ions that should be excluded from the measurements. The legitimate CEX ions are due to interactions of source ions with anode and cathode neutrals whereas the CEX ions that should be removed are due to source ion interactions with tank neutrals. In addition, these probes do not remove elastically scattered ions from source ion collisions with tank neutrals. These elastically scattered ions may have higher energies compared to CEX ions and are able to bypass the filter of these probes and reach the surface of the collector.

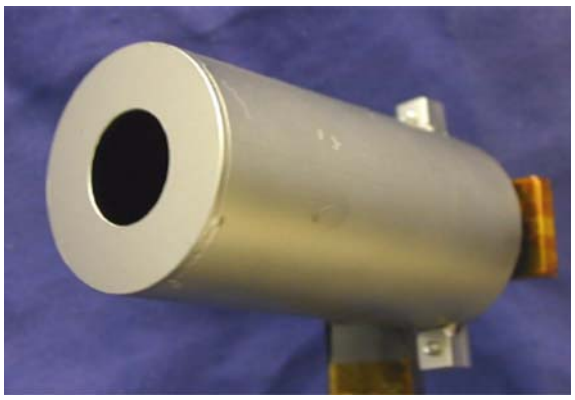

Collimated Faraday Probe [49]

Single-Screen Faraday Probe

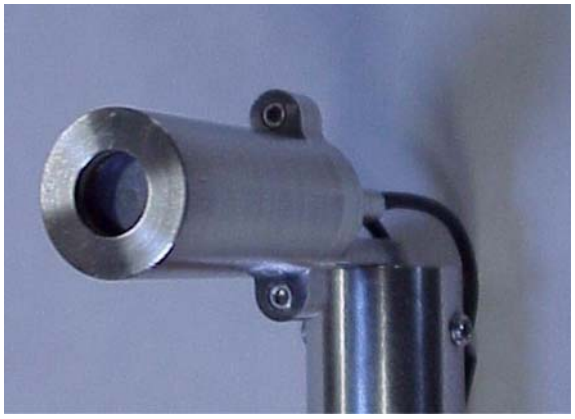

Retarding Potential Analyzer

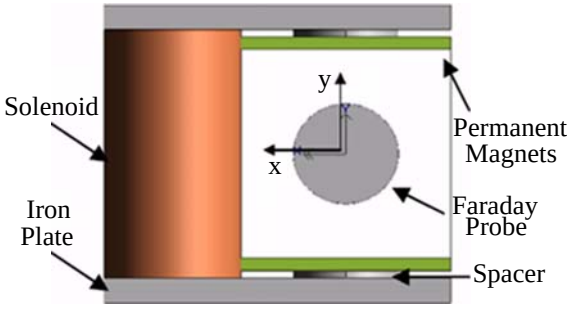

Magnetically Filtered Faraday Probe [50]

Figure 3.6 Pictures of different diagnostic instruments that are used to remove facility effects from plume measurements.

3.3 In-Orbit Extrapolation Method

In the present work, laboratory measurements were corrected for facility effects using an extrapolation technique. In order to properly filter out the effects of tank neutrals on the plume, these effects are first quantified. This is achieved by introducing xenon directly into the test facility to vary the partial pressure of tank neutrals, as explained in Section 2.2. Obtaining plume measurements at different background pressures enables us to determine how tank neutrals interact with thruster plume particles. Changes in background pressure only affect the population of scattered and CEX ions that are due to collisions with background neutrals. Results, discussed in detail in Section 3.3.1, show a linear relationship between current density and background pressure at each angular position. This linear relationship allows us to extrapolate the current density measurements to zero background pressure, the in-orbit condition. The in-orbit current density can then be used to determine the in-orbit plume divergence using Equation 3.15. The Faraday probe, described in Section 2.3, is used to measure the current density. The RPA, described in Section 2.4, is used to measure the ion energy distribution. Measurements from the Faraday probe were checked against RPA measurements to serve as a consistency check for the method. Measurements from both probes are also used to correlate changes of current density with changes in ion energy distribution due to an increase in background pressure. Finally, a new comprehensive way of reporting the plume divergence is proposed, which utilizes both Faraday probe and RPA measurements.

The Faraday probe and RPA measurements are taken during different testing periods with the BHT-1500 operating at discharge voltages of 300-1000V in 100V increments. The magnetic field is adjusted to minimize the discharge current at each discharge voltage. Both the Faraday probe and RPA are placed 1m downstream from the exit plane of the thruster. The Faraday probe is swept from –90° to 90° in 3° increments whereas the RPA is swept from –90° to 0° in 10° increments. Measurements shown below are taken with the thruster equipped with newly machined boron nitride exit rings (Grade AXO5). These measurements can serve as a database for plume conditions for a new thruster.

3.3.1 Current Density

Figure 3.7 portrays the effect of background pressure on current density for the BHT-1500 thruster plume at a discharge voltage of 300V, an anode flow rate of 2.44mg/s, and a sweep radius of 1m. Current density is measured at background pressures of 6.58×10^{-6} Torr, 8.51×10^{-6} Torr, 1.04×10^{-5} Torr, 1.55×10^{-5} Torr, and 2.02×10^{-5} Torr.

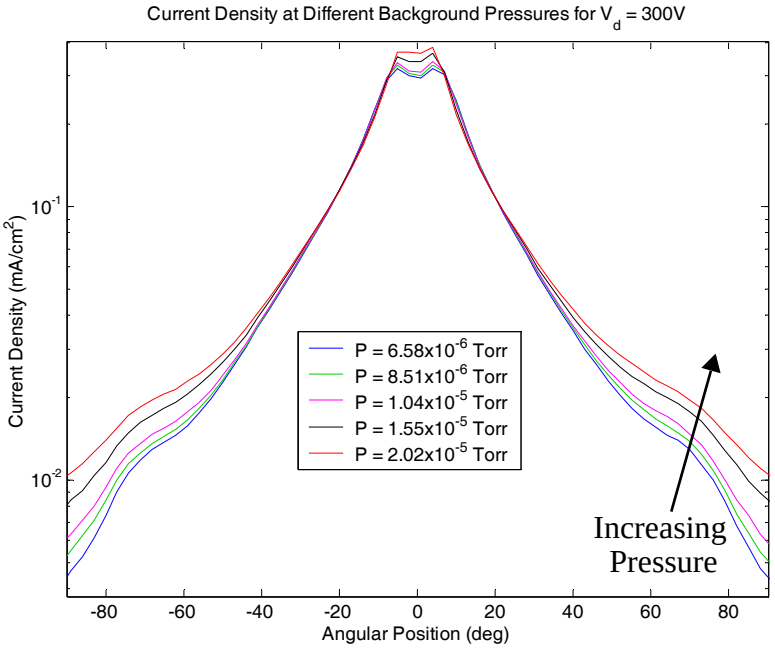

Figure 3.7 Effect of background pressure on current density. V_d = 300V, $\dot{m}_a$ = 2.44mg/s and sweep radius = 1m.

The current density distributions are symmetric with respect to the centerline with "shoulders" at the wings and a double hump at the peak. The double hump at the peak occurs because of the annular discharge channel. The magnetic field of the Hall thruster is designed to focus the annular discharge to a single beam. This leads to the angling of the plasma exhaust at the exit plane towards the centerline. This in turn causes plume crossing at the centerline, which produces a "swallow tail" plume configuration. There is also a slight asymmetry in the double hump of the current density distribution. This may be due

to a small asymmetry in the magnetic field or a non-uniform distribution of the xenon flow from the anode.

The shoulders at the wings of the current density distribution are explained by charge exchange collisions. An exchange of charge occurs when a fast moving ion collides with a slow moving neutral, causing the fast moving ion to become a fast moving neutral and the slow moving neutral to become a slow moving ion. The plasma potential in the plume is greatest at the centerline and lowest at the wings. The slow moving charge exchange ions do not have sufficient energy to overcome the plume potential hump at the centerline and are pushed to the side, creating an accumulation of charge exchange ions at the wings. The wings of the current density also contain elastically scattered ions and low energy source ions, which are born downstream from the ionization region. These low energy ions travel to large angles because their radial velocity is relatively high compared to their axial velocity. RPA measurements have shown that the wings of the current density distribution also contain a small population of source ions.

When charge exchange collisions occur, ions are removed from the middle of the beam and are redistributed to large angles. For example, if no collisions occur, an ion exiting the thruster at a 10° angle with respect to the centerline is collected at a 10° angle. If a charge exchange collision occurs, the resulting ion is collected at large angles due to the potential structure of the plume. If a charge exchange collision occurs with an ion exiting the thruster at a large angle, the resulting CEX ion is also collected at large angles.

With an increase in background pressure, the current density increases at the wings and decreases in the mid-angle region, as shown in Figure 3.7. The increase in background pressure leads to an increase in charge exchange collisions and ion-neutral elastic scattering. The charge exchange ions are pushed to the wings leading to the rise of the wings in the current density distribution at higher pressures. The decrease in current density in the mid-angle region is also attributed to collisions. Ions that were supposed to be collected in the mid-angle region were either charge exchanged or elastically scattered to large angles.

Figure 3.7 also shows that the current density at the centerline increases with background pressure. This is likely explained by the ionization of background neutrals after they penetrate the discharge cavity of the thruster. An increase in background pressure leads to an increase in the density of background neutrals. These background neutrals, which are unaffected by the electric and magnetic fields of the thruster, travel freely into the ionization region and are ionized. The ionized background neutrals act similarly to ions from the thruster by accelerating through the channel, traveling down the potential gradient, and leading to a higher current density at the centerline. The ionization of background neutrals should contribute to the current density at all angles but the effect is more noticeable at the centerline. This could be due to the geometrical configuration of the thruster. Background neutrals that are ionized close to the thruster wall, which tend to travel to large angles, are lost to the wall. On the other hand, neutrals that are ionized in the middle of the channel have a small radial velocity component and are therefore collected at the centerline. The current due to the ionization of background neutrals can be estimated using

$$I_{background} = en_n \frac{\bar{c}_n}{4} A \tag{3.17}$$

Assuming 100% ionization of background neutrals inside the discharge cavity, the current attributed to the ionization of background neutrals is calculated with Equation 3.17 to be 1.68mA for a pressure increase from 6.58×10^{-6} Torr to 8.51×10^{-6} Torr. However, the measured increase in current at the centerline is 4.04mA for the same pressure increase. The estimation is lower than the measured current increase at the centerline because only ionization of background neutrals at the thruster exit is considered. Ionization of background neutrals can also occur inside the thruster channel and in the vicinity of the thruster exit. In addition, an increase in background pressure enhances electron mobility towards the anode, which increases the discharge current. It is not known if an enhanced electron mobility leads to higher beam current, which would explain the increase in current density at the centerline. The increase in background pressure also leads to an increase in thrust, which is artificial, since ionization of background neutrals is significantly reduced in the

space environment. Depending on the background pressure, ionization of neutrals can contribute to up 1-2% of the total measured thrust.

When current density is plotted against background pressure at a constant observation angle, a clear linear relationship emerges, as shown in Figure 3.8. To demonstrate that the linear relationship is valid for any given angle, the Pearson product-moment correlation coefficient of the linear relationship (R^2 value) is calculated for any given angle. The Pearson product-moment correlation coefficient is a measure of the strength of the linear relationship between two random variables (in this case the two variables are current density and background pressure). An R^2 value of 1.0 indicates that current density and background pressure have a perfectly linear relationship. The calculated R^2 value is the 0.99-1.0 range for all angles, which confirms that the linear relationship between current density and background pressure is valid for any given angle. Figure 3.8 also displays the R^2 value of the linear relationship between current density and background pressure for 90°, 75°, 60°, 45°, 10°, and 0°.

Therefore, in order to obtain the in-orbit current density, the linear relationship is used to extrapolate measurements to zero pressure at each angular position. Figures 3.9-3.16 show the in-orbit current density (P = 0Torr) at discharge voltages of 300-1000V. The in-orbit current density still contains shoulders around 60° due to the accumulation of charge exchange ions created through source ion collisions with anode and cathode neutrals. It is interesting that the shoulders of the in-orbit current density become more pronounced as discharge voltage increases. Numerical simulation results discussed in Chapter 4 indicate that the shoulders also contain low energy source ions that are born at low potentials downstream from the ionization region. It is likely that the shoulders are more pronounced at high discharge voltages due to the increase in production of these low energy ions.

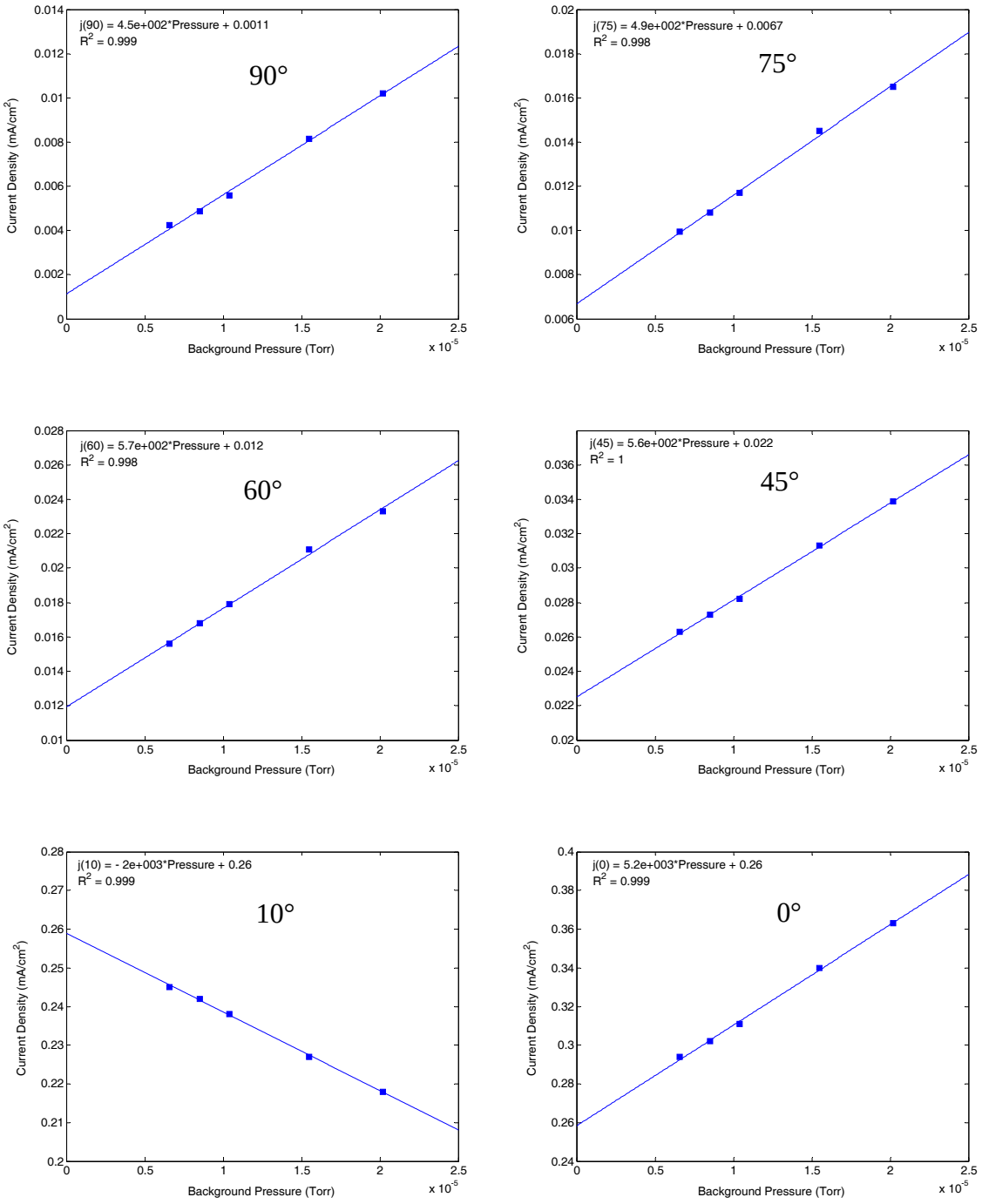

Figure 3.8 Effect of background pressure on current density at 90°, 75°, 60°, 45°, 10°, and 0°. V_d = 300V, $\dot{m}_a$ = 2.44mg/s and sweep radius = 1m. A linear relationship exits between current density and background pressure. Therefore, this linear relationship allows us to extrapolate the measurements to zero background pressure, the in-orbit condition.

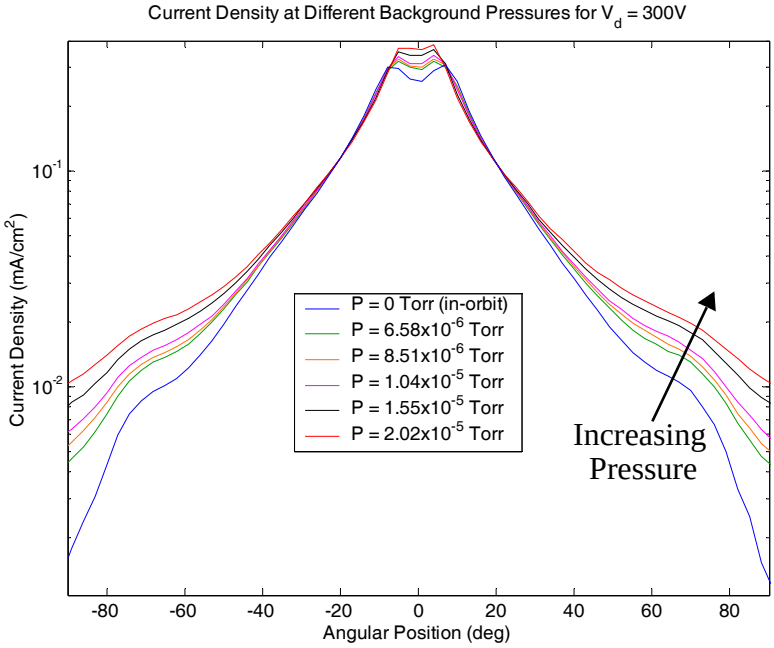

Figure 3.9 Effect of background pressure on current density. V_d = 300V, $\dot{m}_a$ = 2.44mg/s and sweep radius = 1m. The in-orbit (P=0) current density is calculated using the extrapolation method.

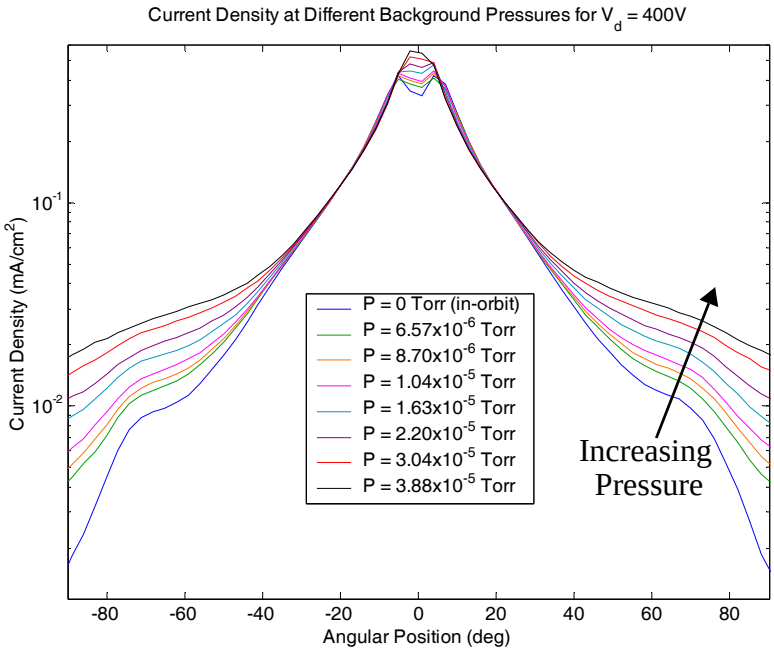

Figure 3.10 Effect of background pressure on current density. V_d = 400V, $\dot{m}_a$ = 2.44mg/s and sweep radius = 1m. The in-orbit (P=0) current density is calculated using the extrapolation method.

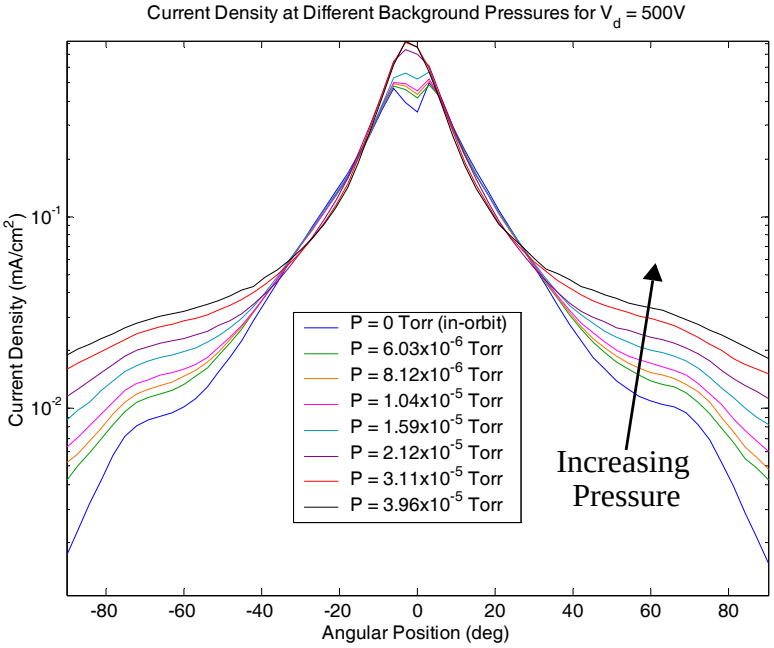

Figure 3.11 Effect of background pressure on current density. V_d = 500V, $\dot{m}_a$ = 2.44mg/s and sweep radius = 1m. The in-orbit (P=0) current density is calculated using the extrapolation method.

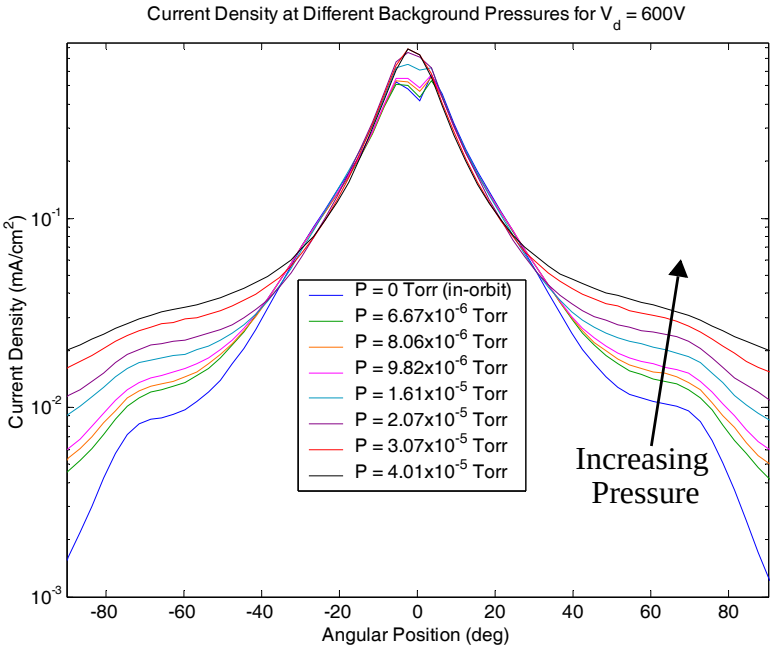

Figure 3.12 Effect of background pressure on current density. V_d = 600V, $\dot{m}_a$ = 2.44mg/s and sweep radius = 1m. The in-orbit (P=0) current density is calculated using the extrapolation method.

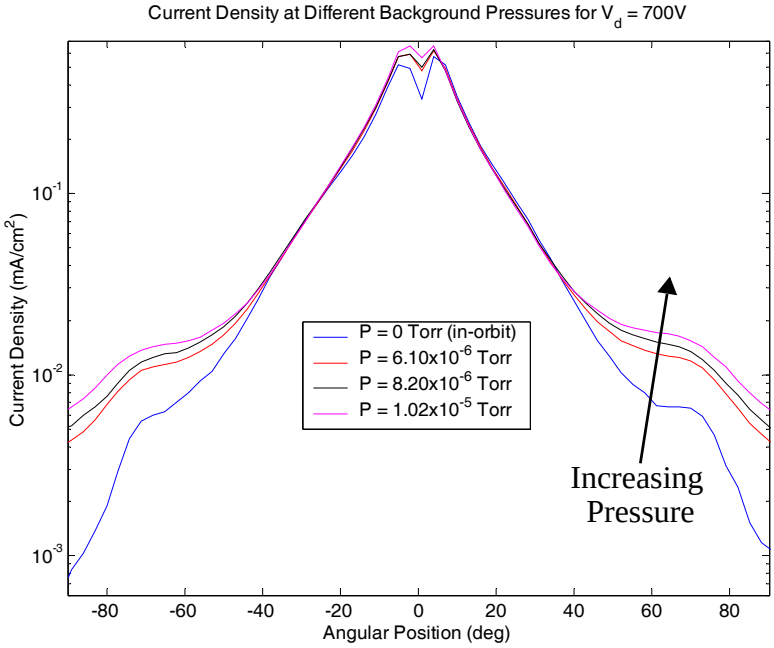

Figure 3.13 Effect of background pressure on current density. V_d = 700V, $\dot{m}_a$ = 2.44mg/s and sweep radius = 1m. The in-orbit (P=0) current density is calculated using the extrapolation method.

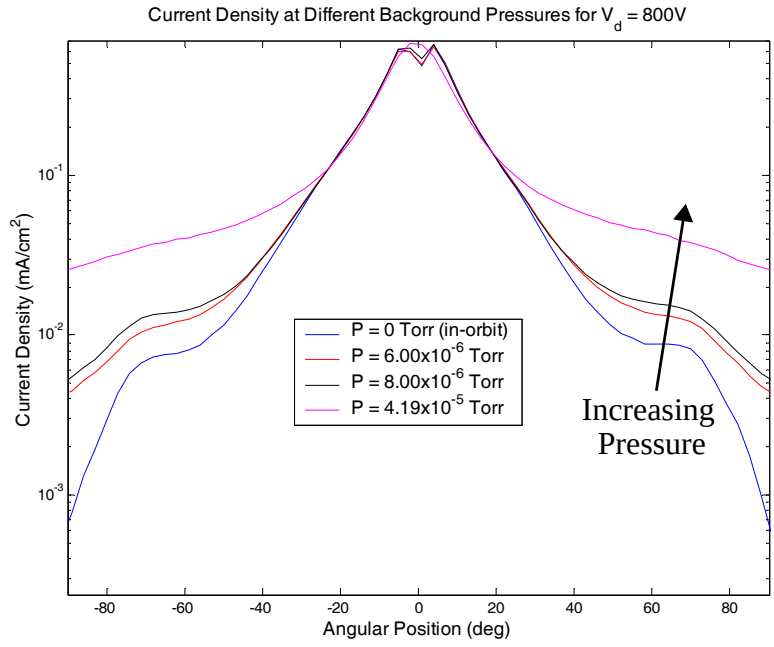

Figure 3.14 Effect of background pressure on current density. V_d = 800V, $\dot{m}_a$ = 2.44mg/s and sweep radius = 1m. The in-orbit (P=0) current density is calculated using the extrapolation method.

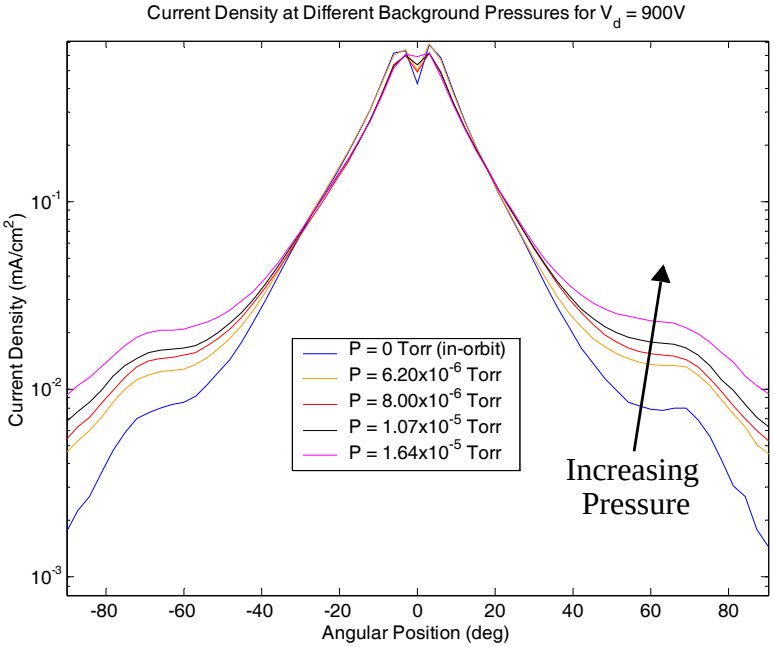

Figure 3.15 Effect of background pressure on current density. V_d = 900V, $\dot{m}_a$ = 2.44mg/s and sweep radius = 1m. The in-orbit (P=0) current density is calculated using the extrapolation method.

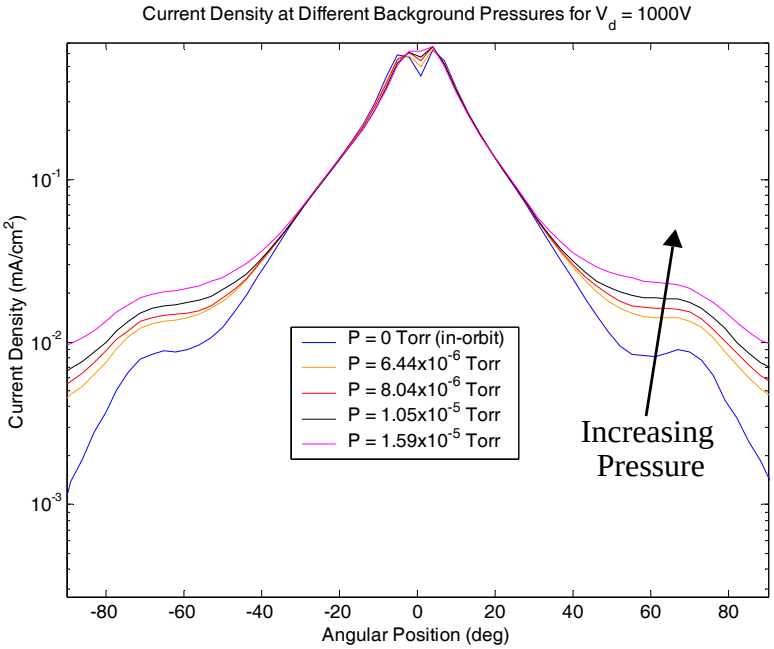

Figure 3.16 Effect of background pressure on current density. V_d = 1000V, $\dot{m}_a$ = 2.44mg/s and sweep radius = 1m. The in-orbit (P=0) current density is calculated using the extrapolation method.

3.3.2 Ion Energy Distribution

Figure 3.17 shows the ion energy distribution referenced with respect to facility ground for the BHT-1500 thruster plume at a discharge voltage of 300V, an anode flow rate of 2.44mg/s, and a sweep radius of 1m. The ion energy distribution is taken at angles of –90° to 0° in 10° increments for background pressures of 7.5×10^{-6} Torr and 2.0×10^{-5} Torr. At –90°, the ion energy distribution consists of only one population, low energy charge exchange ions, for which the peak of the distribution occurs at approximately 20V. At –80°, the ion energy distribution consists of mainly low energy charge exchange ions and a small population of source ions. An increase in change exchange ions occurs in the plume as the angle increases from –90° to –80°. At –70°, the ion energy distribution consists of low energy ions, source ions, and intermediate energy ions. The intermediate energy ions are likely source ions that have lost momentum due to elastic collisions and/or are source ions that are born downstream from the ionization region at potentials below the discharge potential. At –70°, the low energy charge exchange ion population decreases in favor of an increase in the source ion population. At –60°, the ion energy distribution consists of low energy ions, source ions and intermediate energy ions. At this angle, the plume crosses over from charge exchange ions dominant to source ions dominant. At –50° and –40°, the plume is dominated by source ions with a large population of intermediate energy ions. At angles of –30° and lower, the plume consists mainly of source ions. The peak of the source ion population increases as the RPA's angular position is rotated towards the centerline.

As shown in Figure 3.17, an increase in background pressure leads to an increase in the peak of low energy ions at –90° through –60°. Despite a greater than two times increase in background pressure, the population of low energy charge exchange ions does not double. This is because the RPA's collector is collimated, allowing only ions that are coming from near the exit plane of the thruster to be collected. The low energy ions that are collected by the RPA are mainly due to ions that underwent charge exchange collisions near the thruster exit. Based on the mean free path analysis performed in Section 3.1.2, these charge exchange collisions are dominated by collisions with anode and cathode neutrals.

Therefore, the collimation in the RPA is filtering out some of the tank neutral effects. In addition, an increase in background pressure leads charge exchange ions to shift towards a lower energy, as shown at –90° through –60° in Figure 3.17. An increase in background pressure increases electron-neutral collisions, which leads electrons to lose energy. The decrease in electron energy leads to lower plasma potentials in the plume. Since charge exchange ions acquire energy from the potential drop in the plume, their energy decreases with an increase in pressure. An increase in background pressure also leads to a decrease in the peak of the source ion population for angles between –70° through –10°. The decrease in the peak is due to an increase in ion-neutral elastic scattering and charge exchange collisions. This is consistent with current density measurements, which also show a decrease in current density in the mid-angle region with an increase in pressure. The net decrease in the source ion population does not translate into a net increase in the low energy population in the RPA measurements. This is likely due to collimation of the probe since ions resulting from charge exchange collisions that occur in the plume region (away from the thruster exit) are not collected by the RPA. At the centerline, the peak of the source ion population increases with pressure due to ionization of background neutrals, which is also consistent with the Faraday probe data.

Figures 3.18-3.24 are ion energy distributions for discharge voltages ranging from 400-1000V. For all measurements, the anode flow rate is 2.44mg/s and the sweep radius is 1m. The ion energy distribution is taken at angles of –90° to 0° in 10° increments for background pressures of 7.5×10^{-6} Torr and 2.0×10^{-5} Torr at all discharge voltages except 800V and 1000V, where measurements are taken only at 7.5×10^{-6} Torr. The observations that are made regarding the ion energy distribution at a discharge voltage of 300V also apply to other discharge voltages. The differences are the angle at which the source ions are detected and the angle at which the plume crosses over from charge exchange ion dominant to source ion dominant. A detailed discussion of the effect of discharge voltage on the ion energy distribution is presented in Section 3.4.2. This section is limited to the discussion of the facility effects on the ion energy distribution.

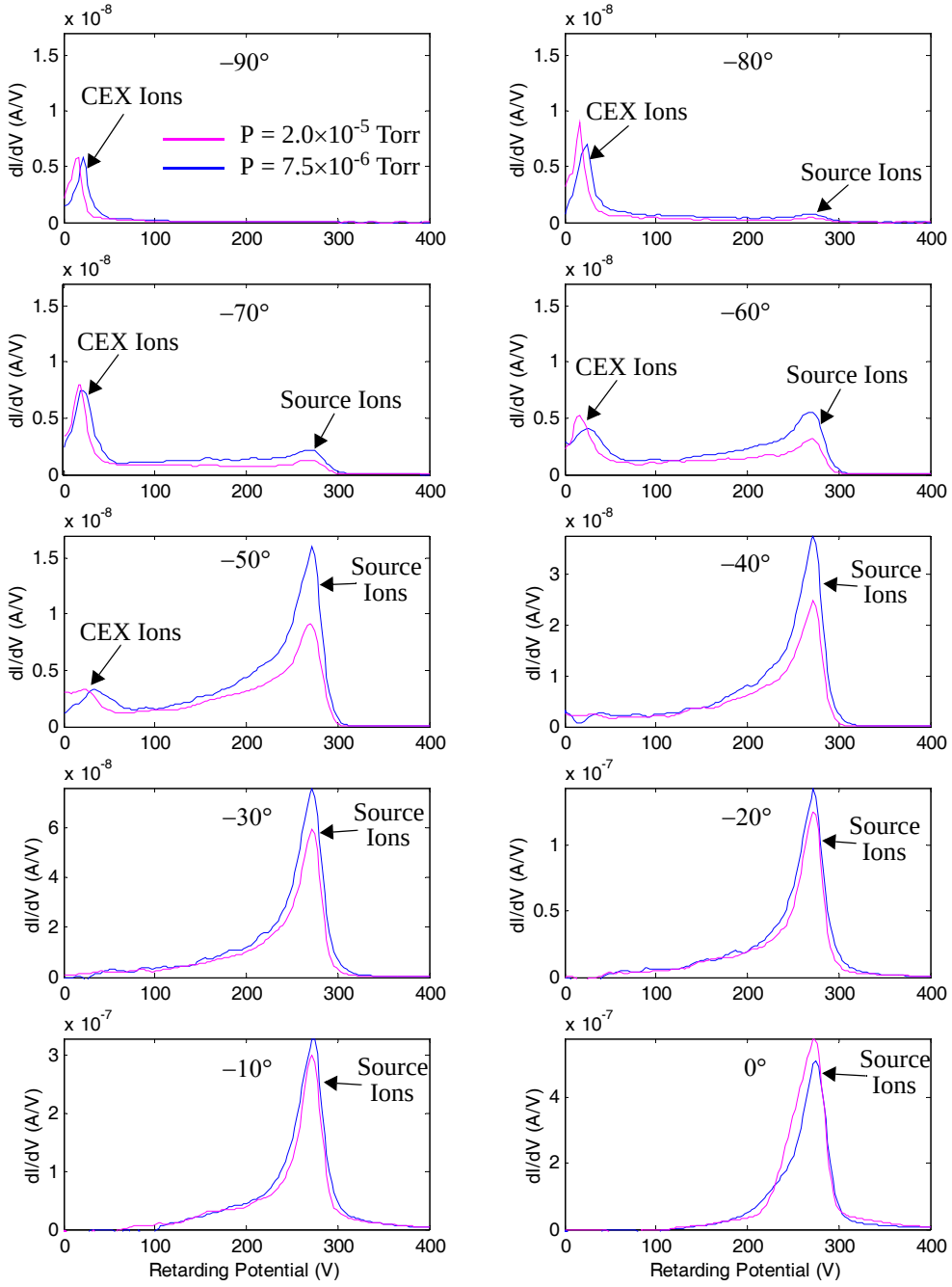

Figure 3.17 Effect of background pressure on ion energy distribution at angular positions of –90° to 0° in 10° increments. V_d = 300V, $\dot{m}_a$ = 2.44mg/s and sweep radius = 1m. Data are plotted on the same scale for angles between –90° and –50°. The retarding potential is referenced with respect to the facility ground whereas the discharge voltage is referenced with respect to the cathode potential, which is approximately –20V. To reference measurements with respect to the cathode potential, the ion energy distribution must be shifted to the right by 20V.

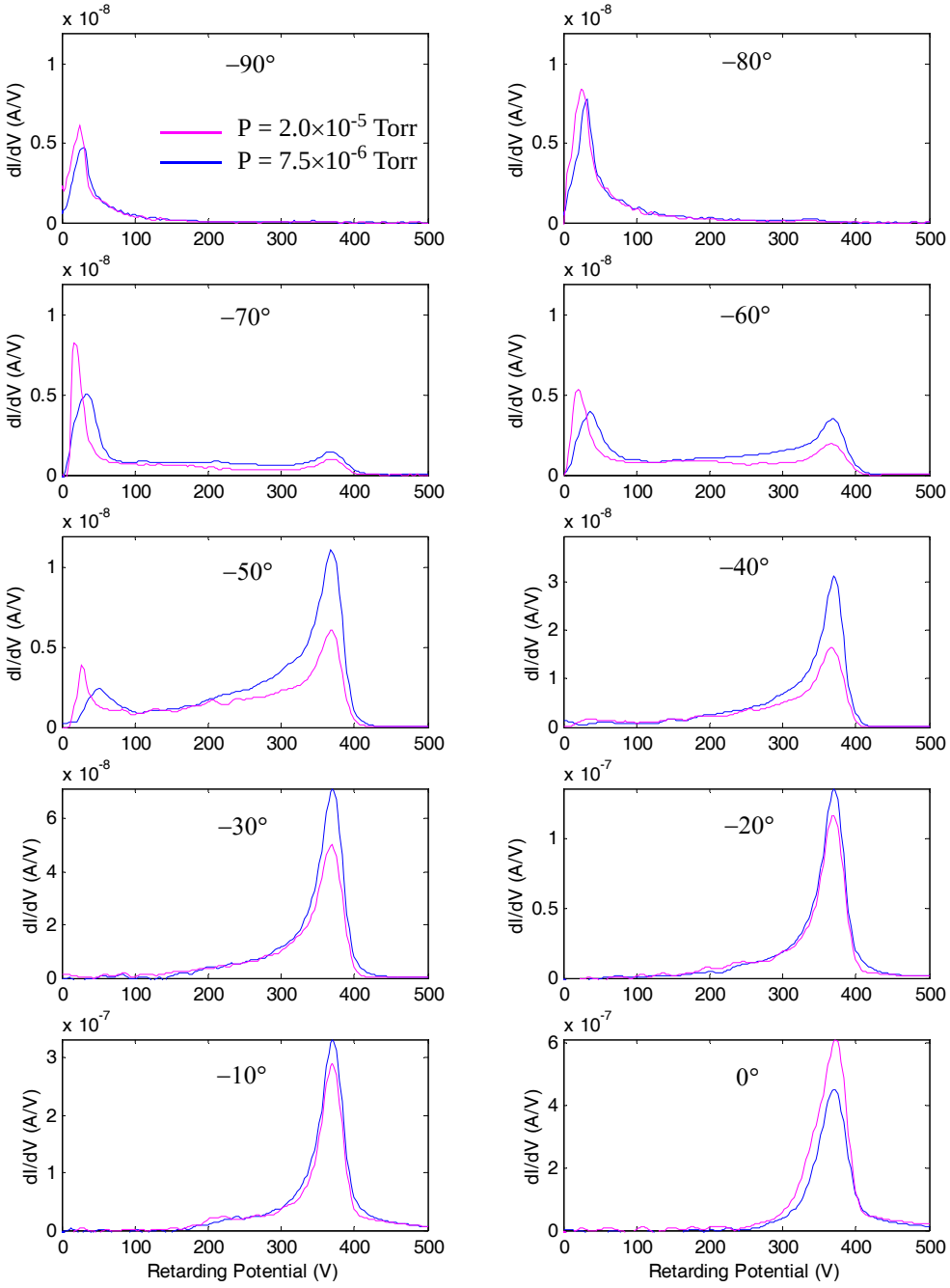

Figure 3.18 Effect of background pressure on ion energy distribution at angular positions of –90° to 0° in 10° increments. V_d = 400V, $\dot{m}_a$ = 2.44mg/s and sweep radius = 1m. Data are plotted on the same scale for angles between –90° and –50°. The retarding potential is referenced with respect to the facility ground whereas the discharge voltage is referenced with respect to the cathode potential, which is approximately –20V. To reference measurements with respect to the cathode potential, the ion energy distribution must be shifted to the right by 20V.

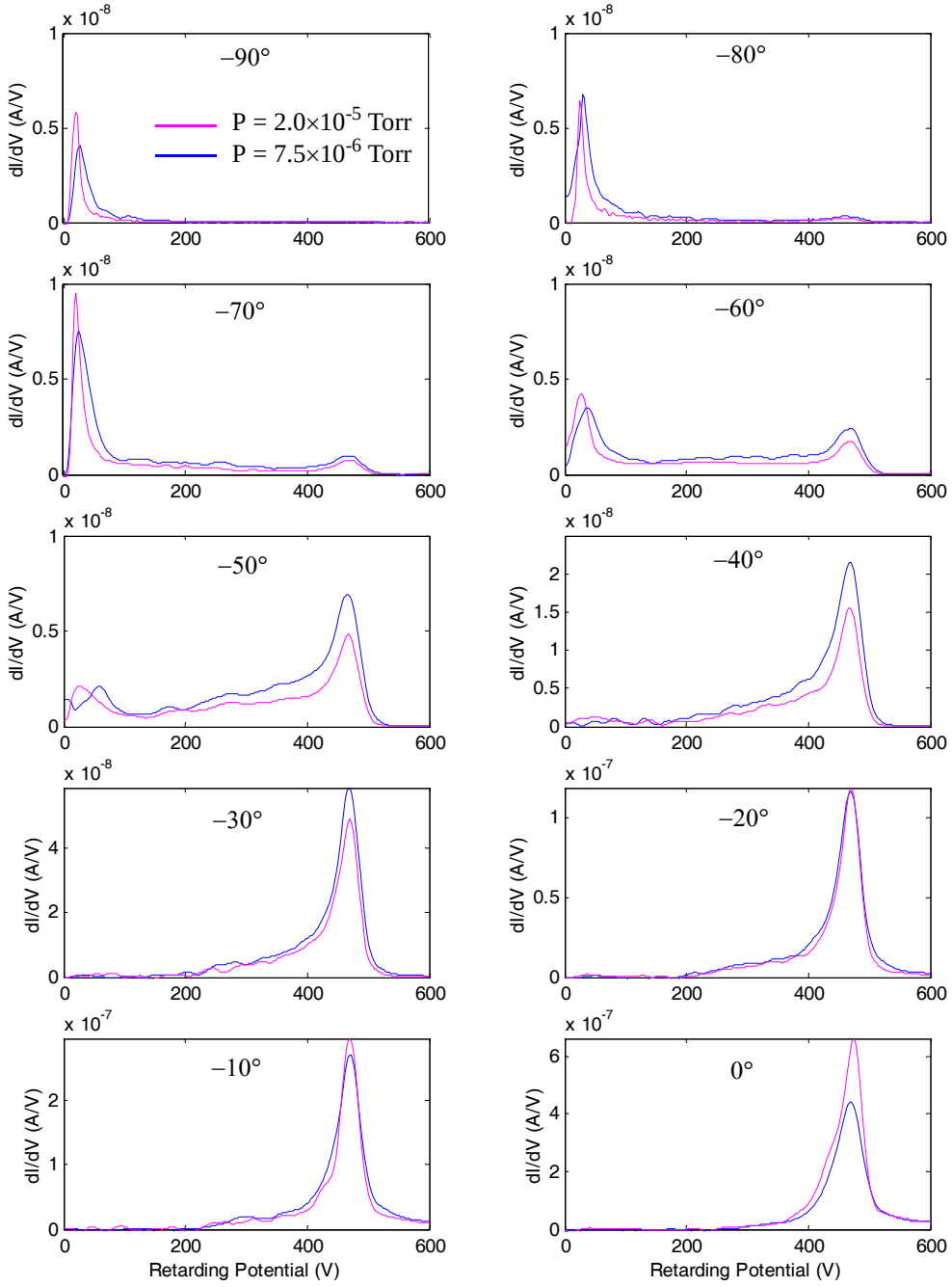

Figure 3.19 Effect of background pressure on ion energy distribution at angular positions of –90° to 0° in 10° increments. V_d = 500V, $\dot{m}_a$ = 2.44mg/s and sweep radius = 1m. Data are plotted on the same scale for angles between –90° and –50°. The retarding potential is referenced with respect to the facility ground whereas the discharge voltage is referenced with respect to the cathode potential, which is approximately –21V. To reference measurements with respect to the cathode potential, the ion energy distribution must be shifted to the right by 21V.

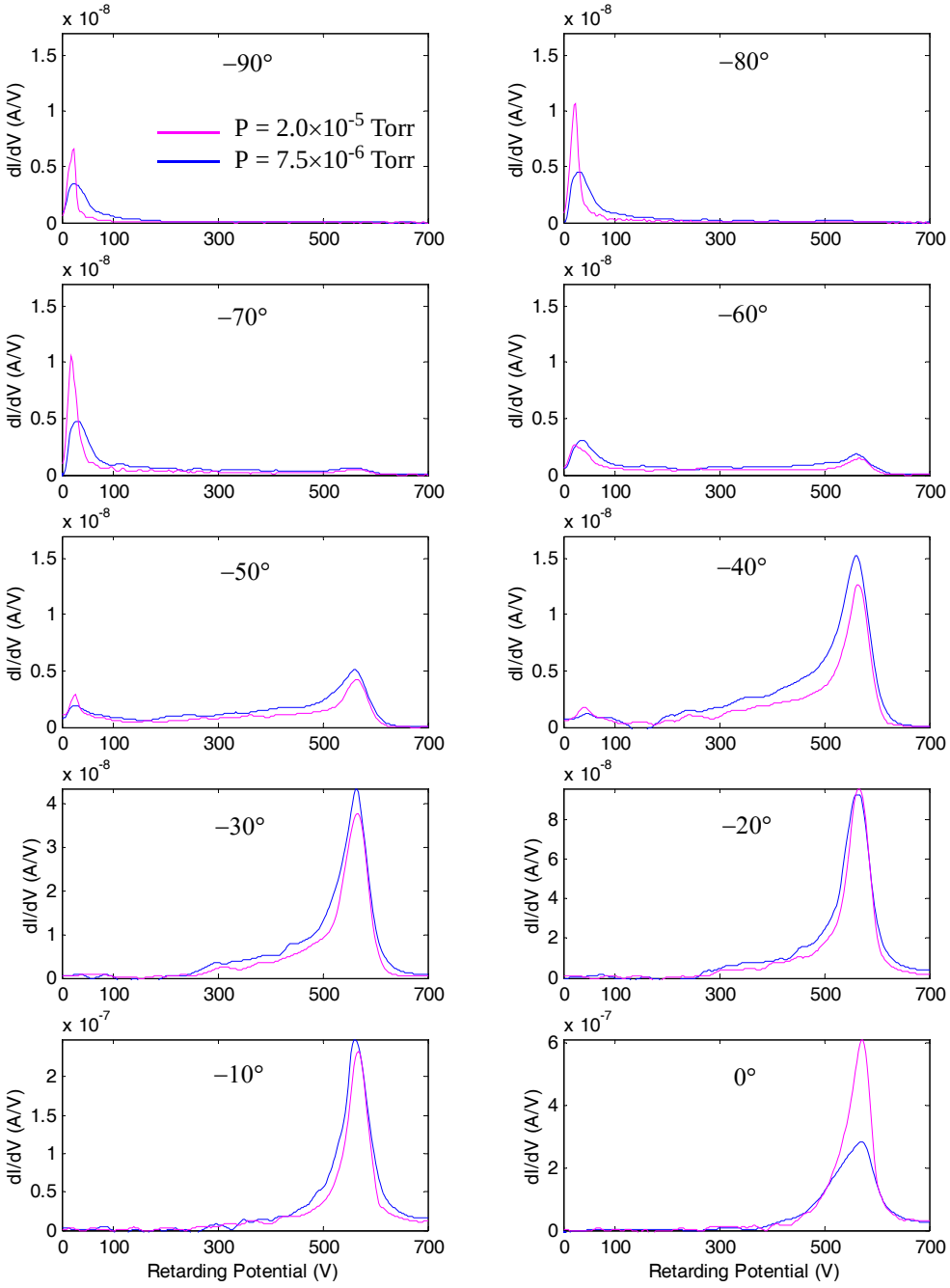

Figure 3.20 Effect of background pressure on ion energy distribution at angular positions of –90° to 0° in 10° increments. V_d = 600V, $\dot{m}_a$ = 2.44mg/s and sweep radius = 1m. Data are plotted on the same scale for angles between –90° and –40°. The retarding potential is referenced with respect to the facility ground whereas the discharge voltage is referenced with respect to the cathode potential, which is approximately –22V. To reference measurements with respect to the cathode potential, the ion energy distribution must be shifted to the right by 22V.

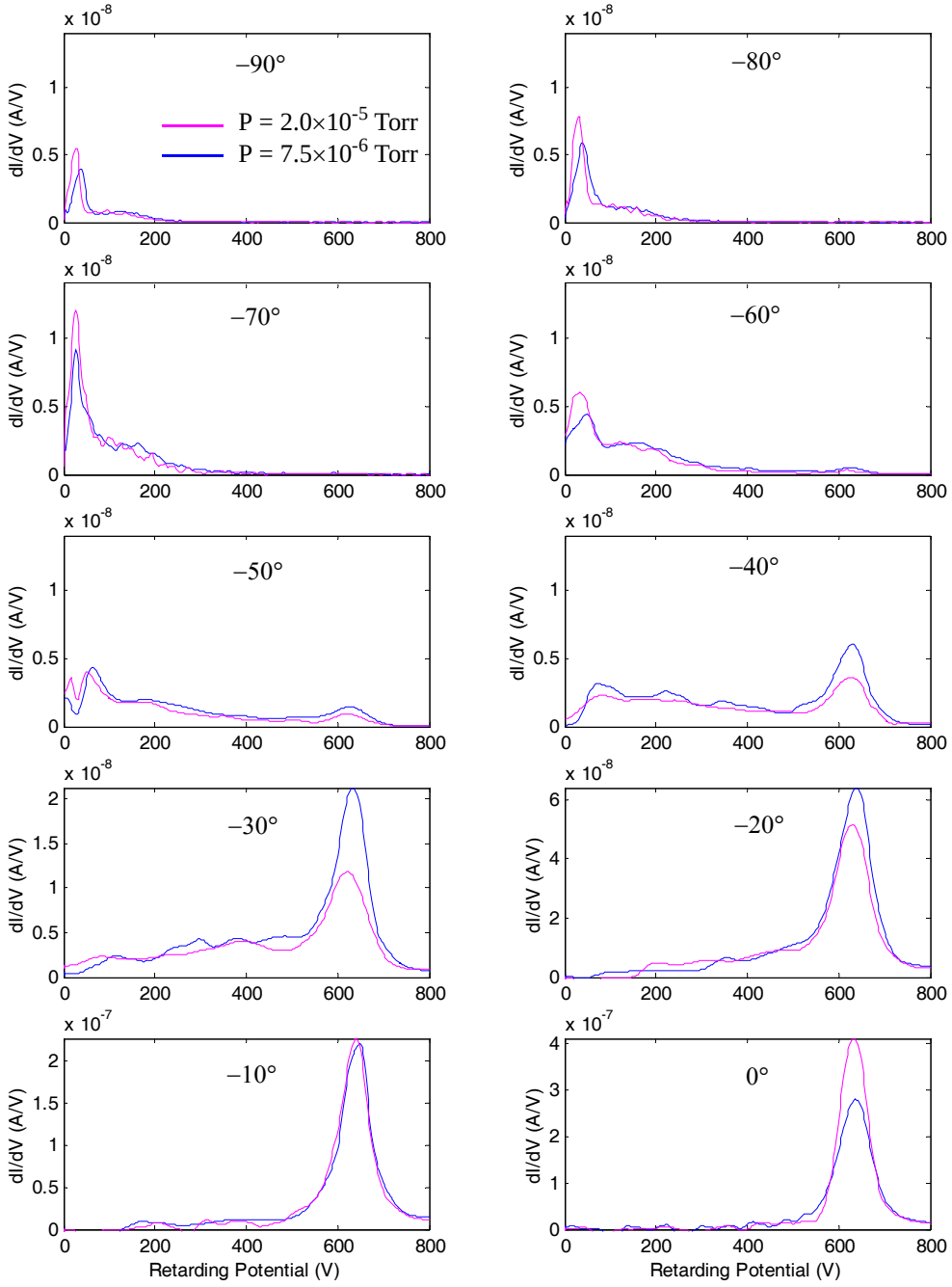

Figure 3.21 Effect of background pressure on ion energy distribution at angular positions of –90° to 0° in 10° increments. V_d = 700V, $\dot{m}_a$ = 2.44mg/s and sweep radius = 1m. Data are plotted on the same scale for angles between –90° and –40°. The retarding potential is referenced with respect to the facility ground whereas the discharge voltage is referenced with respect to the cathode potential, which is approximately –20V. To reference measurements with respect to the cathode potential, the ion energy distribution must be shifted to the right by 20V.

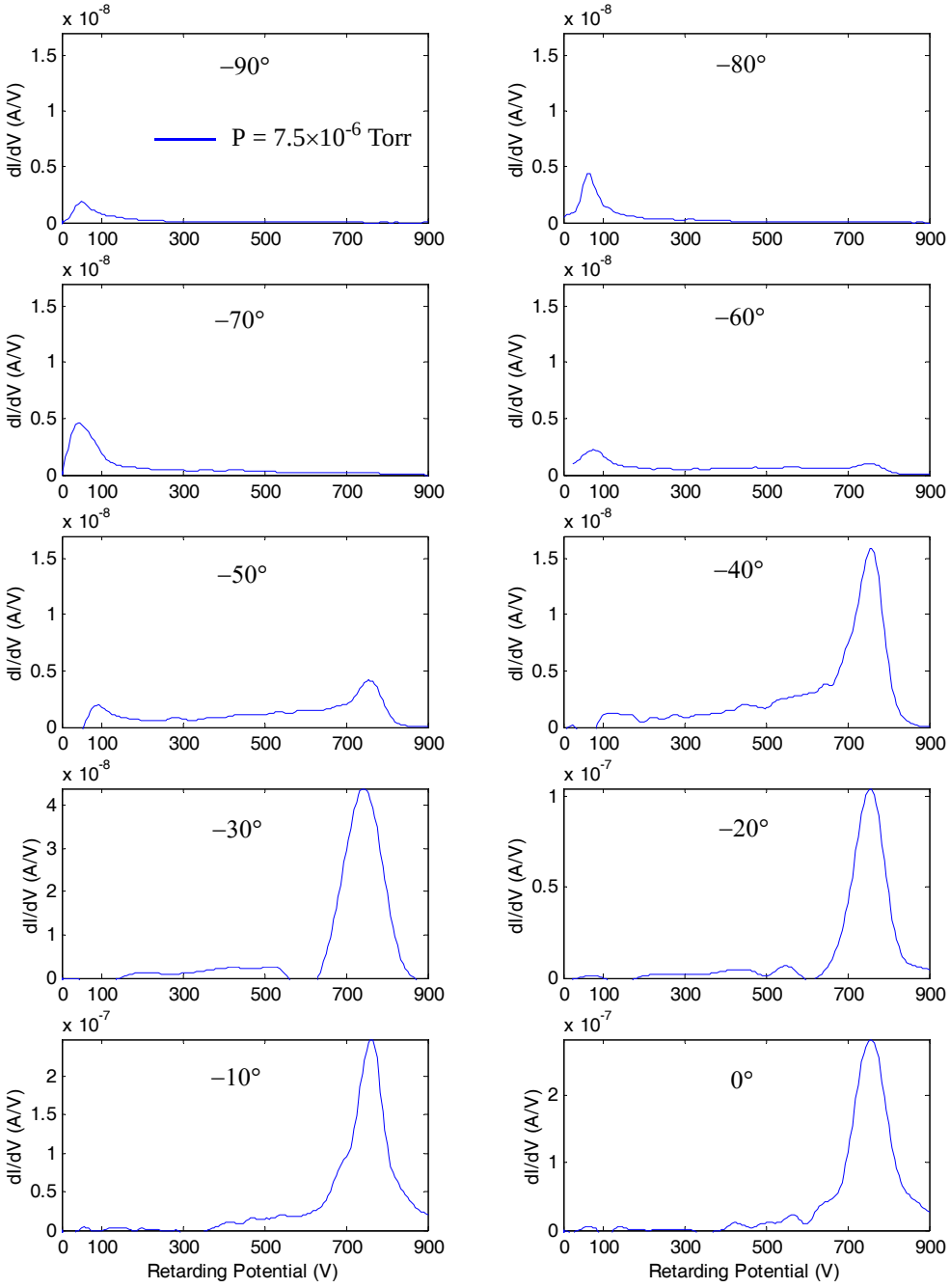

Figure 3.22 Ion energy distribution at angular positions of –90° to 0° in 10° increments. V_d = 800V, $\dot{m}_a$ = 2.44mg/s, sweep radius = 1m and P = 7.5×10^{-6} Torr. Data are plotted on the same scale for angles between –90° and –40°. The retarding potential is referenced with respect to the facility ground whereas the discharge voltage is referenced with respect to the cathode potential, which is approximately –22V. To reference measurements with respect to the cathode potential, the ion energy distribution must be shifted to the right by 22V.

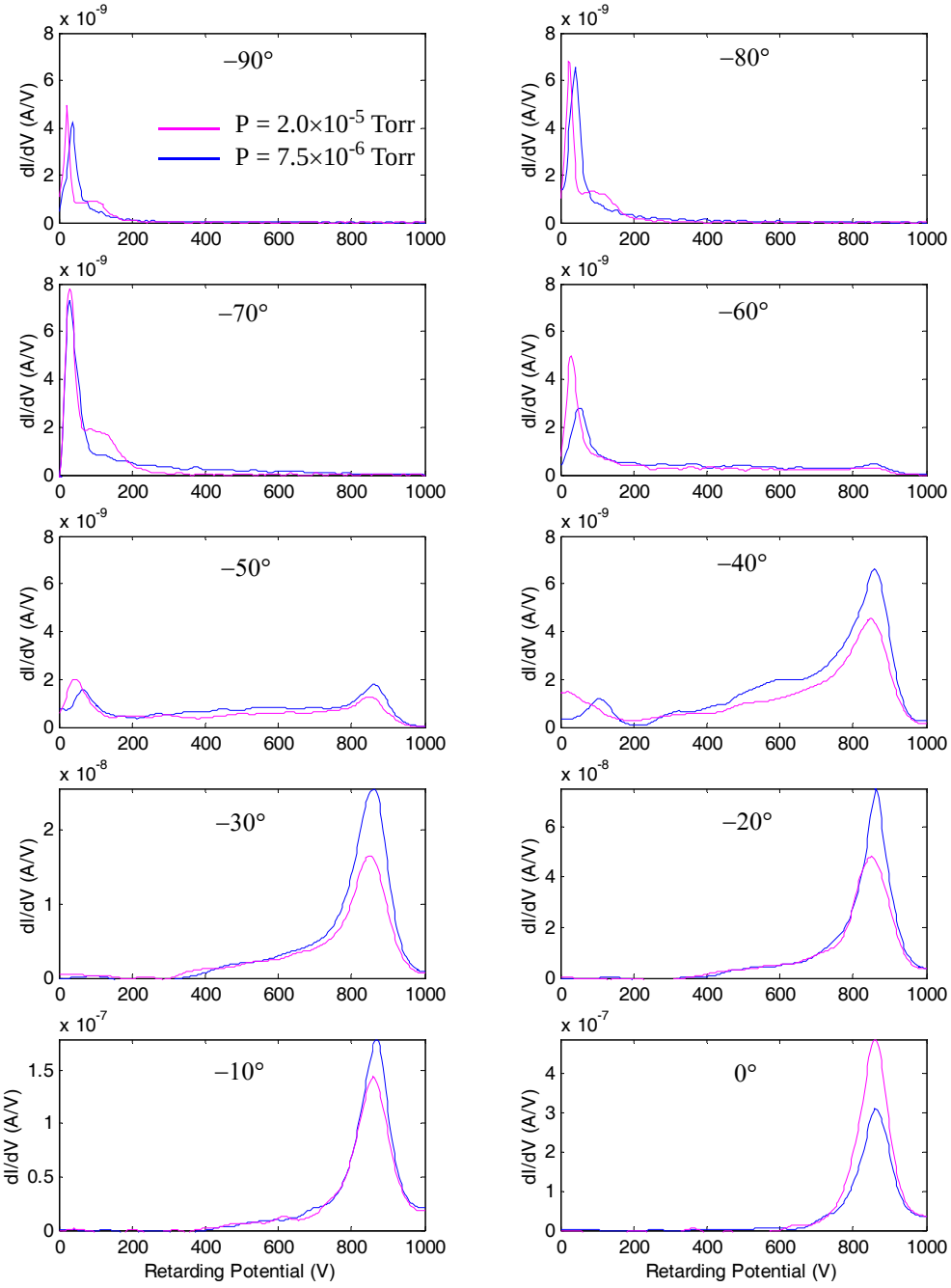

Figure 3.23 Effect of background pressure on ion energy distribution at angular positions of −90° to 0° in 10° increments. V_d = 900V, $\dot{m}_a$ = 2.44mg/s and sweep radius = 1m. Data are plotted on the same scale for angles between −90° and −40°. The retarding potential is referenced with respect to the facility ground whereas the discharge voltage is referenced with respect to the cathode potential, which is approximately −22V. To reference measurements with respect to the cathode potential, the ion energy distribution must be shifted to the right by 22V.

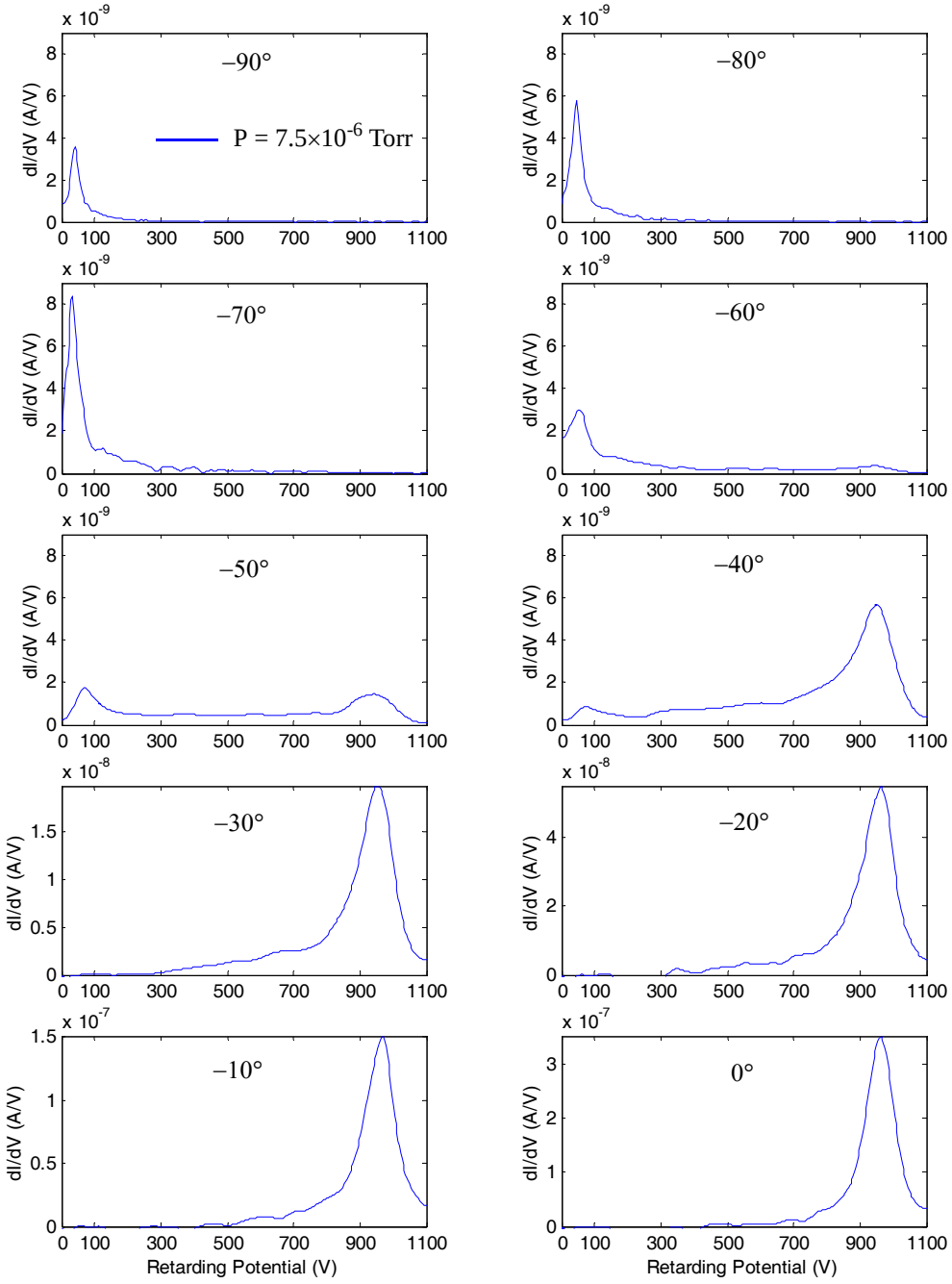

Figure 3.24 Ion energy distribution at angular positions of –90° to 0° in 10° increments. V_d = 1000V, $\dot{m}_a$ = 2.44mg/s, sweep radius = 1m and P = 7.5×10^{-6} Torr. Data are plotted on the same scale for angles between –90° and –40°. The retarding potential is referenced with respect to the facility ground whereas the discharge voltage is referenced with respect to the cathode potential, which is approximately –21V. To reference measurements with respect to the cathode potential, the ion energy distribution must be shifted to the right by 21V.

3.3.3 Experimental Consistency of the Extrapolation Method

Comparison of Faraday Probe and RPA Data

In this section, Faraday probe and RPA measurements are compared at background pressures of 7.5×10^{-6} Torr and 2.0×10^{-5} Torr. Faraday probe and RPA measurements are then corrected to in-orbit conditions using the linear extrapolation method and compared. A good agreement between the corrected Faraday probe and corrected RPA measurements serves as a consistency check for the extrapolation method.

To compare Faraday probe and RPA data, the RPA measurements are converted to current density. As discussed in Section 2.4.5, the RPA's raw measurements consist of current drawn by the collector as a function of the potential applied to the ion retarding grid. The total current drawn by the RPA corresponds to the current drawn with 0V applied to the ion retarding grid. This total current is divided by the effective collection area of the RPA to determine the current density. However, the RPA's effective collection area is difficult to calculate. The collimation of the RPA is a factor in determining the collection area because an ion entering the RPA at an angle with respect to the probe's centerline might be lost to the probe's walls. Therefore, an ion entering the probe is not guaranteed to reach the surface of the collector. The grids are also a factor in determining the RPA's effective collection area. The RPA contains three grids, each with a 72% open area fraction. The total open area fraction of the probe is also difficult to calculate because grid alignment is unknown. The probe's total area fraction can range from a maximum of 72% (if all the grids are perfectly aligned) to a minimum of (0.72^3) 37%. Instead of attempting to geometrically calculate the RPA's effective collection area, it is estimated using Faraday probe measurements by

$$A_{eff} = \frac{I_{rpa}}{j_{Faraday}} \tag{3.18}$$

For a particular background pressure, the current collected by the RPA at an angle of –30°, I_{rpa}, is divided by the current density measured with the Faraday probe at an angle –30°,

$j_{Faraday}$, to estimate the RPA's effective collection area, A_{eff}. This collection area is then used to convert RPA measurements at different angles to current density.

Figures 3.25 and 3.26 show a comparison of current density measured with the Faraday probe and current density derived from RPA data at background pressures of 7.5×10^{-6} Torr and 2.0×10^{-5} Torr respectively. The measurements are conducted at a discharge voltage of 300V, an anode flow rate of 2.44mg/s and a sweep radius of 1m. The RPA measures a smaller current density at the wings compared to the Faraday probe. This is due to collimation of the RPA, which filters out a portion of tank neutral effects.

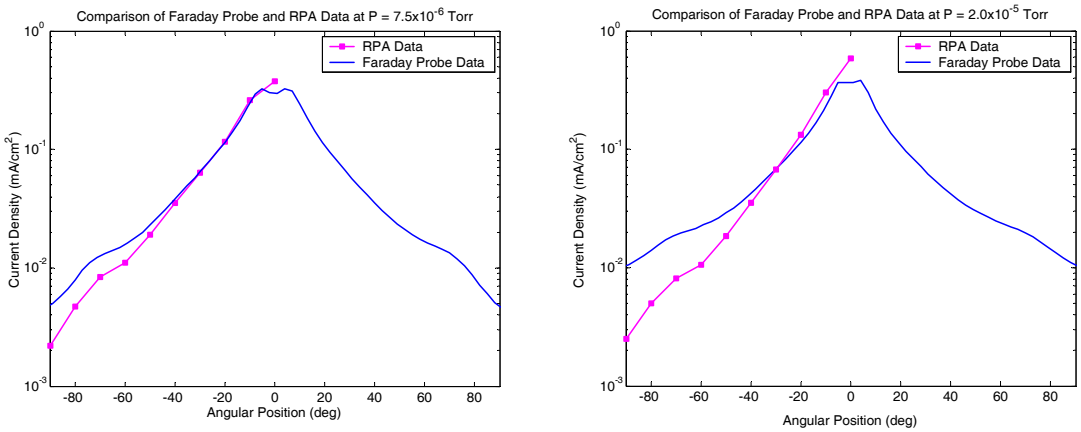

Figure 3.25 LEFT: Comparison of current density measured with the Faraday probe and current density calculated from RPA data. V_d = 300V, $\dot{m}_a$ = 2.44mg/s, sweep radius = 1m and P = 7.5×10^{-6} Torr.

Figure 3.26 RIGHT: Comparison of current density measured with the Faraday probe and current density calculated from RPA data. V_d = 300V, $\dot{m}_a$ = 2.44mg/s, sweep radius = 1m and P = 2.0×10^{-5} Torr.

The current density obtained from RPA data at the two background pressures is extrapolated to zero pressure. Figure 3.27 shows a comparison between the RPA data and Faraday Probe data extrapolated to zero pressure. The Faraday probe and RPA data are in agreement, which indicates that the extrapolation method is a valid tool to determine the in-orbit current density.

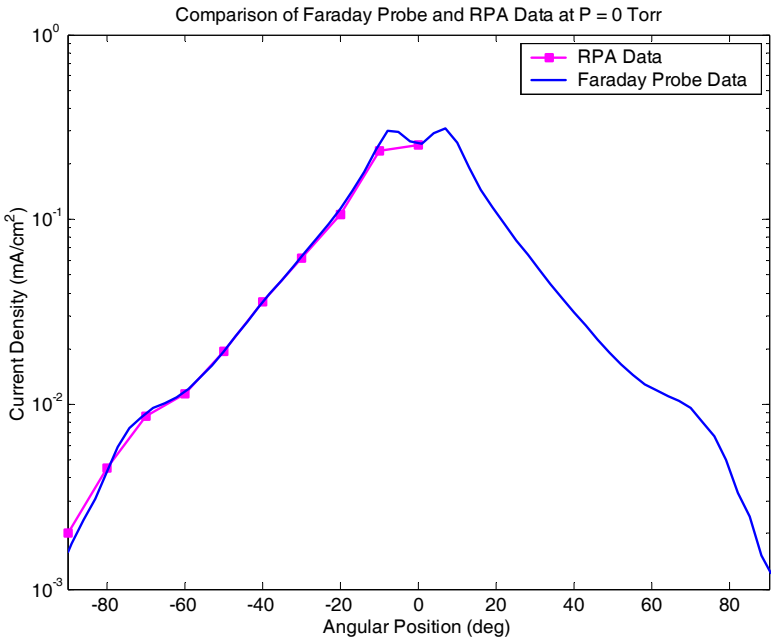

Figure 3.27 The Faraday probe and RPA measurements are corrected for in-orbit conditions and compared to each other. The Faraday probe and RPA data at zero pressure are in good agreement. V_d = 300V, $\dot{m}_a$ = 2.44mg/s, sweep radius = 1m and P = 0 Torr.

Based on the results in Figure 3.27, one can make the conclusion that the RPA alone can be used to determine both the in-orbit current density and the ion energy distribution. However, this is not the case. As explained earlier, the effective collection area of the RPA is estimated by using Faraday probe measurements. Without these measurements, it is difficult to convert RPA measurements into current density. The results in Figure 3.27 can be interpreted as follows:

1. A nude Faraday probe can be used to determine the in-orbit current density through a linear extrapolation of current densities measured at various background pressures.
2. The RPA can be used to provide the composition of the in-orbit plume, which means that the RPA can differentiate the plume ions into source ions, charge exchange ions, and elastically scattered ions.

As discussed earlier, the majority of ions collected by the RPA are coming directly from the exit face of the thruster. Based on the mean free path analysis performed in

Section 3.1.2, the charge exchange collisions that occur near the thruster exit are mainly due to collisions of source ions with anode and cathode neutrals. Therefore, the composition of the in-orbit plume is not different from the general composition of the plume in laboratory conditions as determined by the RPA. Using Figure 3.17, the composition of the in-orbit plume for a discharge voltage of 300V and anode flow rate of 2.44mg/s is:

1. At –90°, the plume consists of only one population, low energy charge exchange ions.
2. At –80°, the plume consists mainly of low energy ions and a small population of source ions.
3. At –70°, the plume is made of low energy ions, source ions, and intermediate energy ions.
4. At –60°, the plume consists of low energy ions, source ions and intermediate energy ions. At this angle, the plume crosses over from charge exchange ion dominant to source ion dominant.
5. At –50° and –40°, the plume is dominated by source ions with a large population of intermediate energy ions.
6. At angles of –30° and lower, the plume consists mainly of source ions.

In summary, the Faraday probe provides the shape of the in-orbit plume, while the RPA provides the composition of the in-orbit plume, and thus both probes should be used together.

Faraday Probe Measurements at Different Sweep Radii

Additional experimental measurements are obtained to further validate the extrapolation method. These measurements consist of taking Faraday probe data at sweep radii of 0.5m, 0.75m, and 1m. Facility effects influence current density measurements more as measurements are taken farther away from the thruster. For example, current density measurements at 1m are affected more by tank neutrals than current density measurements at 0.5m. This is true because ions exiting the thruster have a higher probability of collisions with tank neutrals as the traveling distance increases. If facility effects are removed, ions expand in the plume region (past the thruster exit) without collisions. The reason for this experiment is that comparison of measurements at various sweep radii for a particular

background pressure results in poor data agreement due to collision of source ions with tank neutrals. However, good agreement should result after current density at different sweep radii are corrected for in-orbit conditions using the extrapolation method. If this is found true, this experiment would further confirm the validity of the extrapolation method.

For each sweep radius, current density measurements are obtained at background pressures of 6.21×10^{-6} Torr, 1.07×10^{-5} Torr, 1.55×10^{-5} Torr and 2.15×10^{-5} Torr. At each background pressure, the current density measurements at 0.5m and 0.75m are scaled to current density at 1m. Assuming conical flow, current densities at two different sweep radii are related by

$$\frac{j(r_1)}{j(r_2)} = \left(\frac{r_2}{r_1}\right)^2 \tag{3.19}$$

The scaled current densities from sweep radii of 0.5m and 0.75m are compared to current density measurements at 1m. Figures 3.28-3.31 represent a comparison of scaled and measured current density. The data plotted in Figures 3.28-3.31 are not corrected for in-orbit conditions. As expected, the scaling relationship does not hold at the wings of the current density distribution, where effects of charge exchange collisions dominate. The difference in current densities between the scaled and measured data increases with background pressure. In addition, current density at the wings is higher at the larger sweep radius since collision of source ions with tank neutrals increases with distance. Therefore, some ions that are collected at the centerline at a sweep radius of 0.5m are deflected to the wings of the current density distribution at a sweep radius of 1m through either elastic scattering and/or charge exchange collisions.

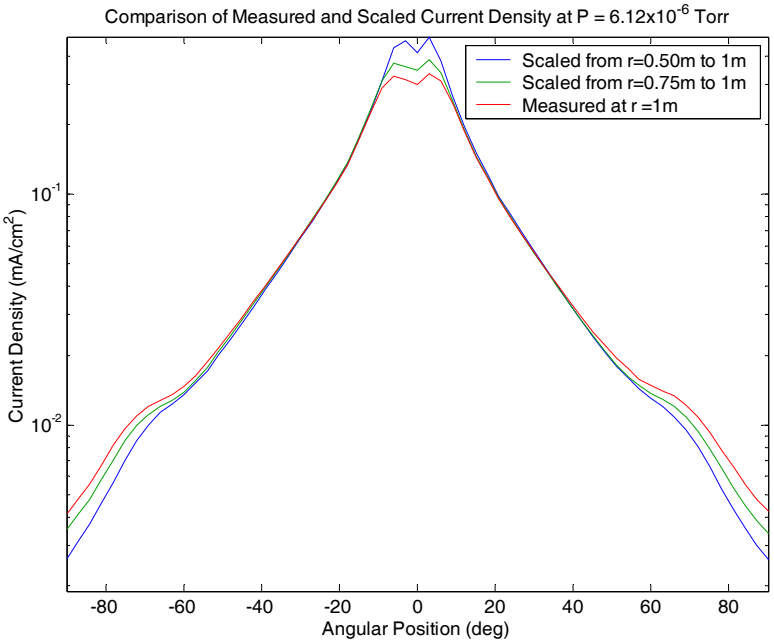

Figure 3.28 Comparison of scaled and measured current density at a background pressure of 6.26×10^{-6} Torr. V_d = 300V and $\dot{m}_a$ = 2.44mg/s.

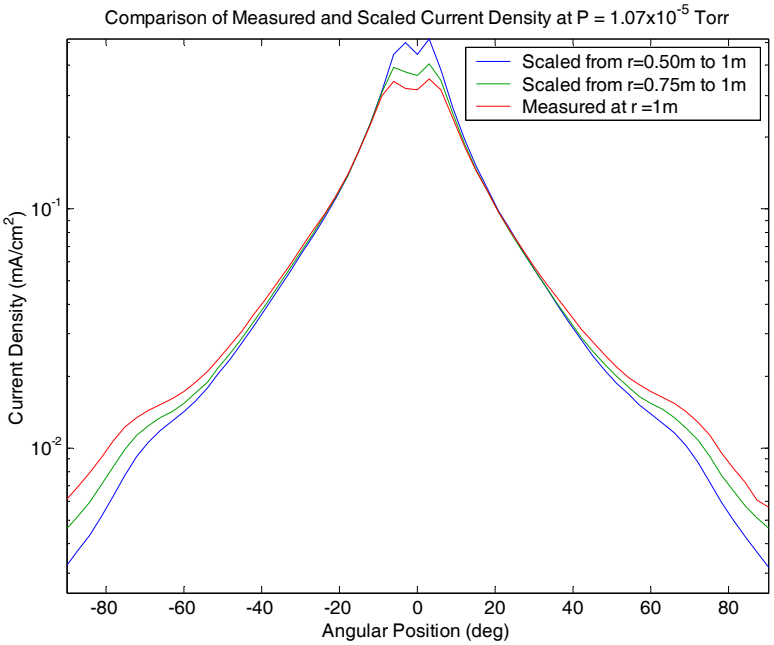

Figure 3.29 Comparison of scaled and measured current density at a background pressure of 1.07×10^{-5} Torr. V_d = 300V and $\dot{m}_a$ = 2.44mg/s.

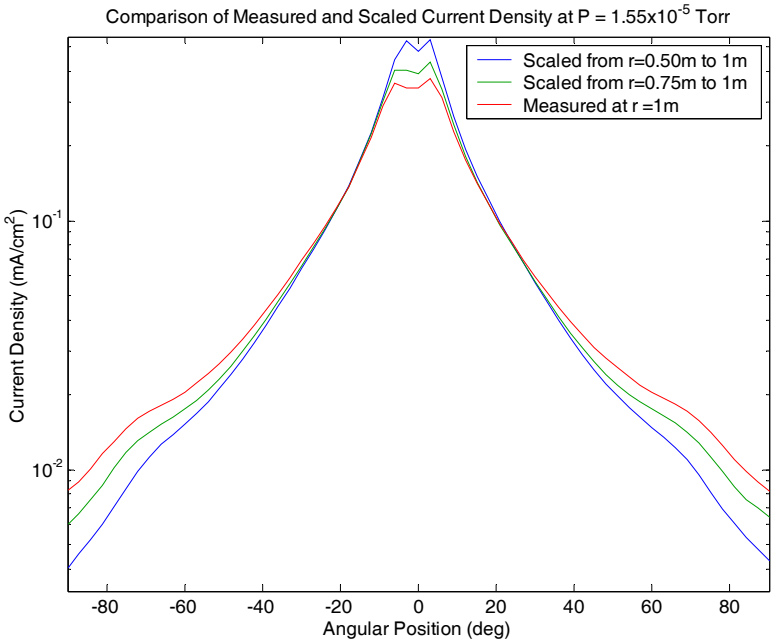

Figure 3.30 Comparison of scaled and measured current density at a background pressure of 1.55×10^{-5} Torr. V_d = 300V and $\dot{m}_a$ = 2.44mg/s.

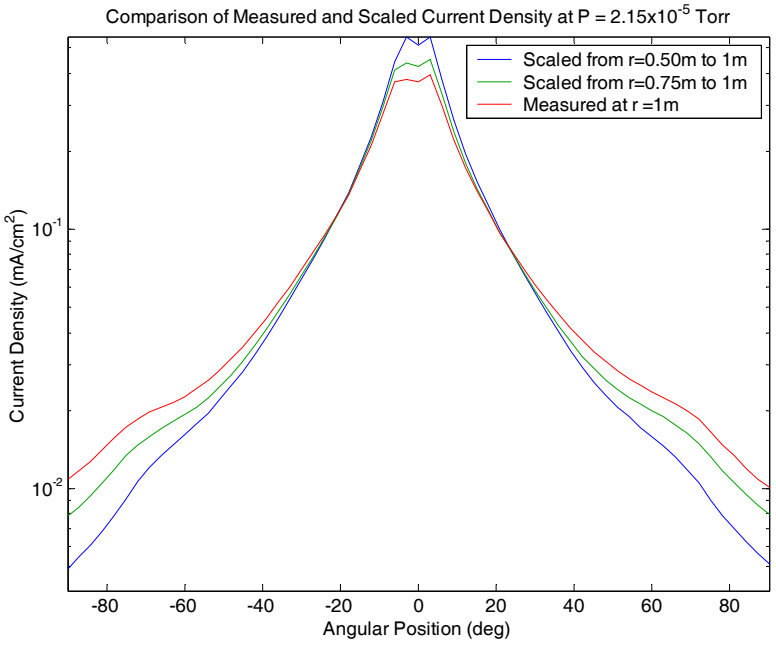

Figure 3.31 Comparison of scaled and measured current density at a background pressure of 2.15×10^{-5} Torr. V_d = 300V and $\dot{m}_a$ = 2.44mg/s.

Using the linear relationship between current density and background pressure, the in-orbit current density is calculated for each sweep radius. The in-orbit current density at 0.5m and 0.75m is scaled to current density at 1m using Equation 3.19 and then compared to in-orbit current density at 1m. Figure 3.32 shows the scaled in-orbit current density from 0.5m and 0.75m sweep radii measurements and the in-orbit measurements at 1m. The results show good agreement between scaled and measured data and prove the consistency of the extrapolation method.

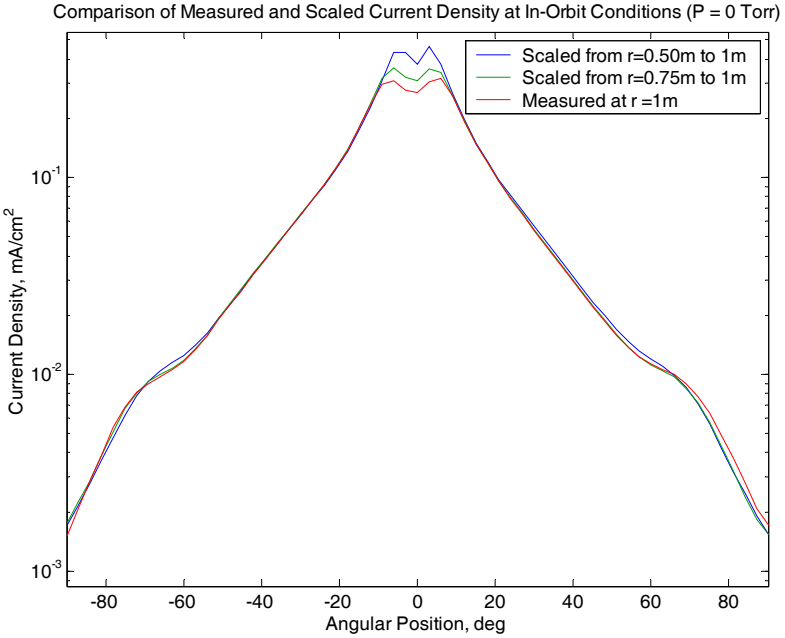

Figure 3.32 Comparison of the scaled in-orbit current density from 0.5m and 0.75m sweep radii measurements and the in-orbit measurements at 1m. V_d = 300V and $\dot{m}_a$ = 2.44mg/s

3.3.4 In-Orbit Plume Divergence

In Section 3.3.3, the extrapolation method of current density to in-orbit conditions proved to be a reliable and accurate method. Therefore, the in-orbit current density can be used to determine the 95% half-angle plume divergence. Using Equation 3.15, The 95% half-angle plume divergence of the BHT-1500 operating at a discharge voltage of 300V and an anode flow rate of 2.44mg/s is 70°. For North-South Station Keeping, where the solar arrays extend from the north and south face of the spacecraft, we would conclude that the thruster needs to be oriented by as much as 70° away from the north-south line. This is a very conservative estimate however, since based on RPA measurements, the 95% half-angle plume divergence includes both low and high energy ions. The low energy ions may not be harmful to the spacecraft and can be prevented from reaching the solar array using a thruster shield. Therefore, it is important to determine a broader definition of plume divergence that conveys information on the structure of the plume.

A more useful way of reporting the plume divergence is to state two angles: the 95% half-angle plume divergence and the 95% half-angle divergence of the source ion population. To obtain the latter, the contribution of the source ion population to the current density needs to be determined. This is achieved using RPA measurements. Figure 3.33 is a schematic of an ion energy distribution that is comprised of both CEX and source ions.

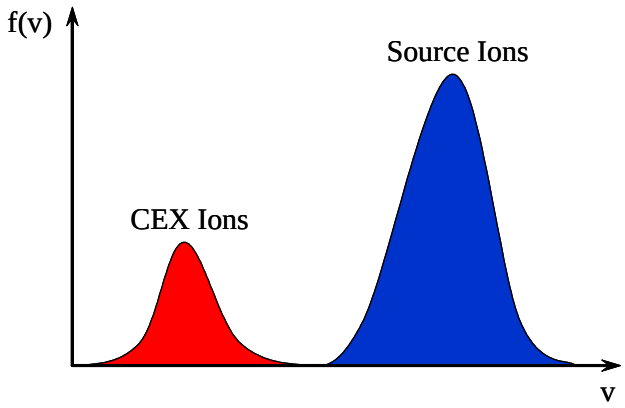

Figure 3.33 Schematic of an ion energy distribution. The blue portion of the ion energy distribution is integrated to calculate the current collected due to source ions.

For each angular position, the portion of the ion energy distribution that represents the distribution of the source ion population is integrated to calculate the current collected due to source ions. The current is then divided by the effective collection area of the RPA to obtain the current density.

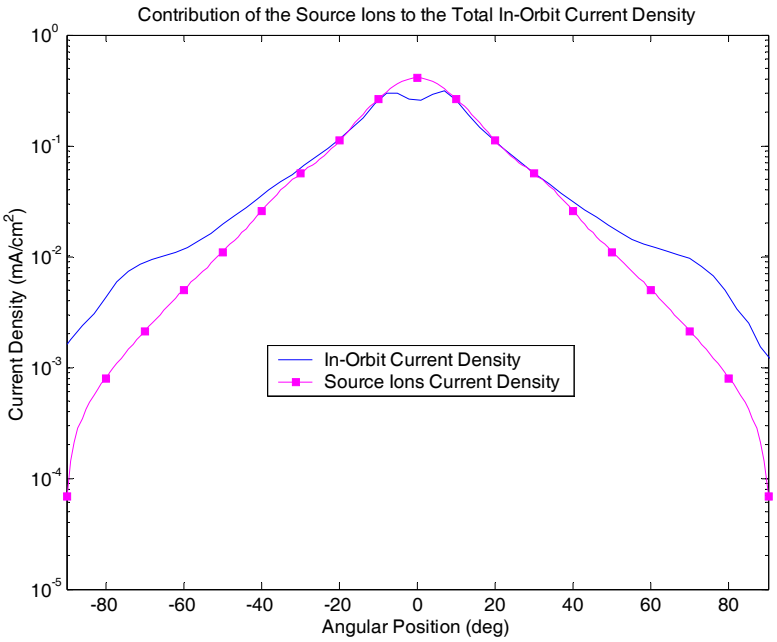

Figure 3.34 Plot of the in-orbit current density and the source ion current density. RPA measurements are used to determine the contribution of source ions to the total current density. V_d = 300V, $\dot{m}_a$ = 2.44mg/s and sweep radius = 1m.

Figure 3.34 shows the current density from only source ions. The difference between the in-orbit current density and source ion current density is due to charge exchange ions, elastically scattered ions and ions that are born at low potential downstream from the ionization region. The current density due to source ions is substituted into Equation 3.15 to determine the 95% half-angle plume divergence of the source ion population. For a discharge voltage of 300V and an anode flow rate of 2.44mg/s, the 95% half-angle divergence for source ions is 54.5°.

In summary, the plume divergence of a Hall thruster operating at a discharge voltage of 300V and an anode flow rate of 2.44mg/s should be stated as follows:

> "The 95% half-angle plume divergence is 70° with 95% of source ions contained within a 54.5° half-angle."

3.3.5 Comparison to Previous Methods

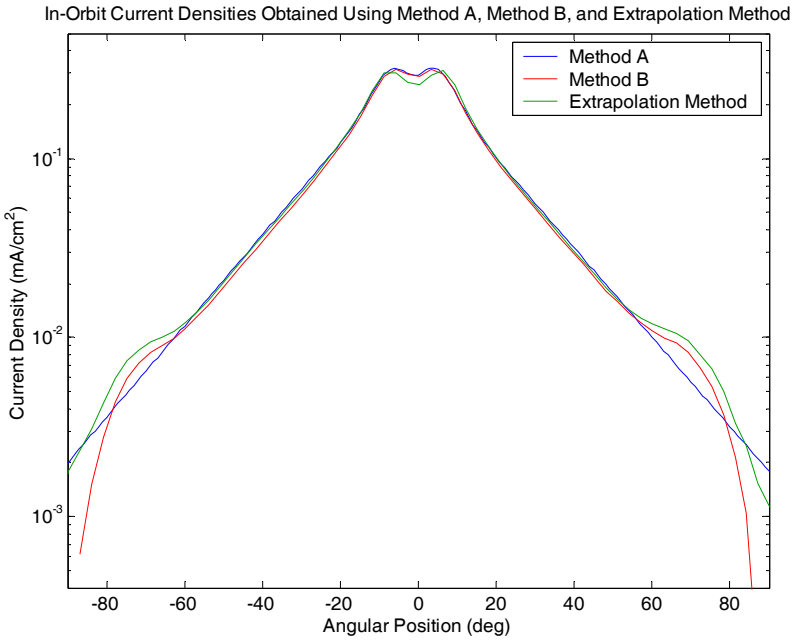

Figure 3.35 Comparison of in-orbit current densities obtained using method A, method B and the extrapolation method. V_d = 300V, $\dot{m}_a$ = 2.44mg/s and sweep radius = 1m.

Figure 3.35 compares the in-orbit current density obtained using the extrapolation method with current density obtained using Method A and Method B described in Section 3.2.1. The comparison is performed for a discharge voltage of 300V and an anode flow rate of 2.44mg/s. There is good agreement among the methods for angles lower than 50°. However, both methods A and B under-predict the current density at the wings compared to the extrapolation method. The 95% half-angle plume divergence for both methods A and B is 67° compared to 70° for the extrapolation method. Overall, methods A and B agree relatively well with the extrapolation method at this voltage. However, as explained in

Section 3.2.1, methods A and B are subjective in their correction for facility effects. The good agreement among methods may be merely related to data at one voltage. To illustrate this point, the in-orbit current densities obtained using Method A, Method B and the extrapolation method are plotted in Figure 3.36 for a discharge voltage of 500V. As illustrated in Figure 3.36, comparison of the in-orbit current densities shows that the difference in current densities is larger than for the 300V case. The 95% half-angle plume divergence is 61° for method A, 66.5° for method B, and 70° for the extrapolation method. Methods A and B under-predict the current density at the wings because they do not account for scattered and CEX ions produced through source ion collisions with anode and cathode neutrals. Therefore, to reliably obtain the in-orbit current density, the extrapolation method should be used.

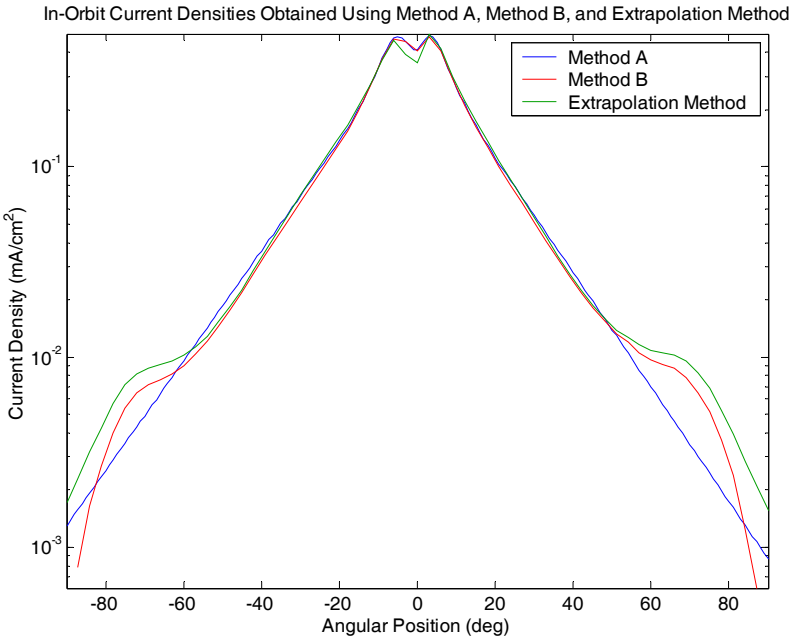

Figure 3.36 Comparison of in-orbit current densities obtained using method A, method B and the extrapolation method. V_d = 500V, $\dot{m}_a$ = 2.44mg/s and sweep radius = 1m.

3.4 Effect of Discharge Voltage on Plume Divergence

The effect of discharge voltage on uncorrected current density is first investigated. Then the extrapolation method, discussed in the previous section, is used to determine the effect of discharge voltage on in-orbit current density. Current density and ion energy distribution are subsequently used to correlate the effect of discharge voltage on plume divergence.

3.4.1 Current Density

Figure 3.37 portrays the effect of discharge voltage on current density uncorrected for facility pressure effects. All measurements are taken at a sweep radius of 1m and a background pressure of 6.5×10^{-6} Torr. The plots in Figure 3.37 are divided in two figures (Figures 3.38 and 3.39) to provide the reader with a better picture of the effect of discharge voltage on current density.

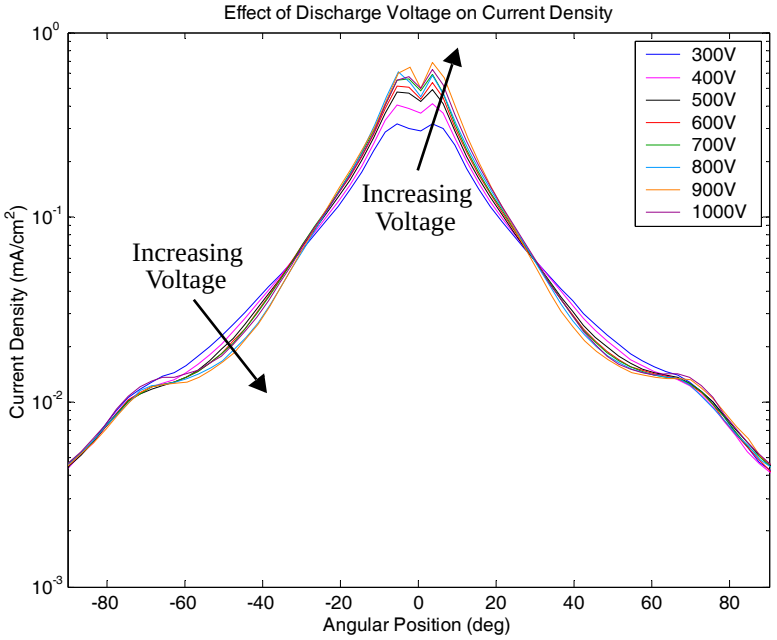

Figure 3.37 Effect of discharge voltage on current density. V_d = 300-1000V, $\dot{m}_a$ = 2.44mg/s, sweep radius = 1m and P = 6.5×10^{-6} Torr.

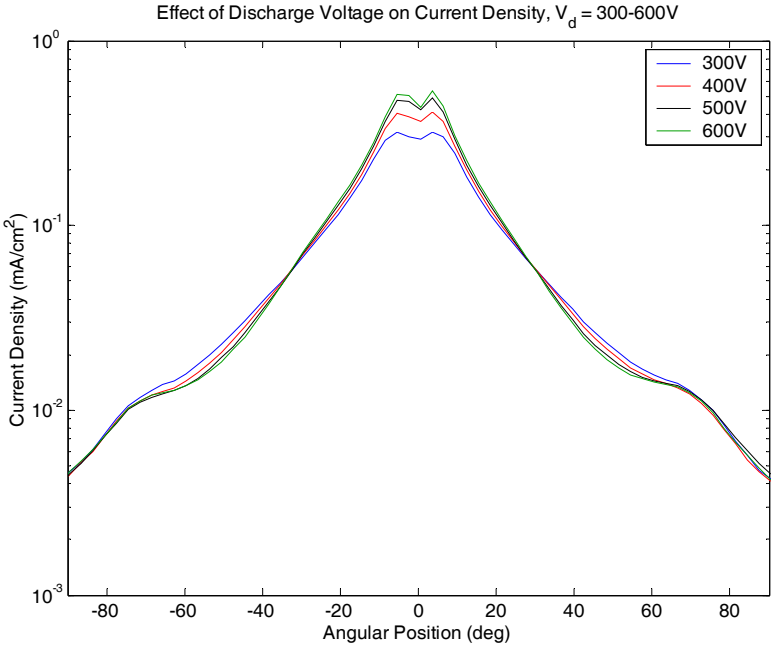

Figure 3.38 Effect of discharge voltage on current density. V_d = 300-600V, $\dot{m}_a$ = 2.44mg/s, sweep radius = 1m and P = 6.5×10^{-6} Torr.

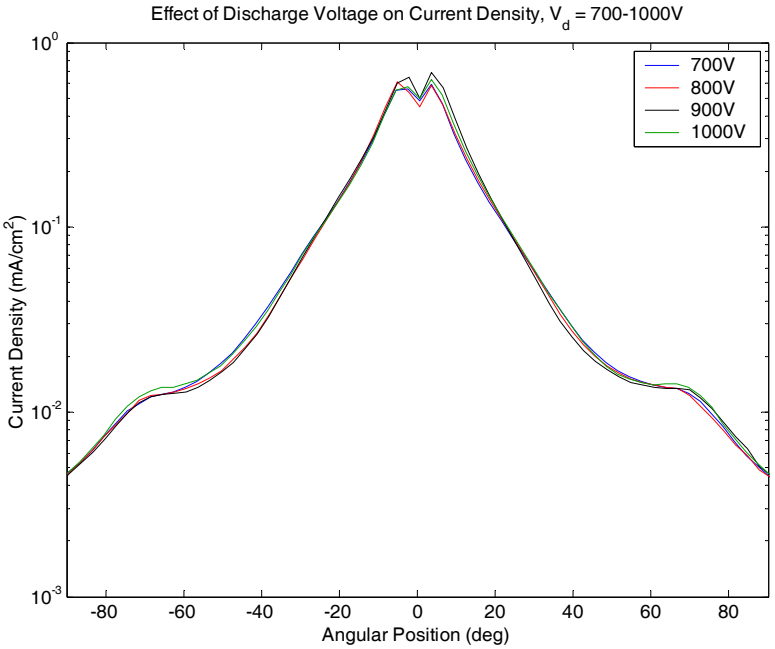

Figure 3.39 Effect of discharge voltage on current density. V_d = 700-1000V, $\dot{m}_a$ = 2.44mg/s, sweep radius = 1m and P = 6.5×10^{-6} Torr.

The discharge voltage does not affect the wings of the current density distributions. This is because the wings are mainly affected by the accumulation of charge exchange ions, the density of which depends upon the density of neutrals. As shown in Figure 3.37, the discharge voltage leads to narrowing of the current density. The current density decreases with discharge voltage for angles between 30° and 70° and increases for angles lower than 30°. This is an indication that the plume divergence decreases with discharge voltage. A detailed analysis of the effect of discharge voltage on plume divergence is discussed in Section 3.4.3. For angles lower than 30°, the increase in current density with discharge voltage is partly due to improved ion focusing. With an increase in discharge voltage, the axial component of the ion velocity increases faster than the radial component, which leads the ions to leave the thruster exit at smaller angles. The increase in current density with discharge voltage at the centerline is also due to an increase in utilization efficiency. The utilization efficiency is expressed by

$$\eta_u = \frac{T}{\dot{m}_a c} \tag{3.20}$$

where T is thrust and c is the beam exhaust speed that is expressed by

$$c = \sqrt{\frac{2eV_d}{m_i}} \tag{3.21}$$

Therefore, the utilization efficiency can be written as a function of discharge voltage,

$$\eta_u = \frac{T}{\dot{m}_a \sqrt{\frac{2eV_d}{m_i}}} \tag{3.22}$$

The thrust of the BHT-1500, T, is measured with the thrust stand described in Section 2.2 and is reported in several publications [14, 29]. Figure 3.40 shows the effect of discharge voltage on utilization efficiency of the BHT-1500. The utilization efficiency increases with discharge voltage, which helps explain the increase in current density with discharge voltage at the centerline.

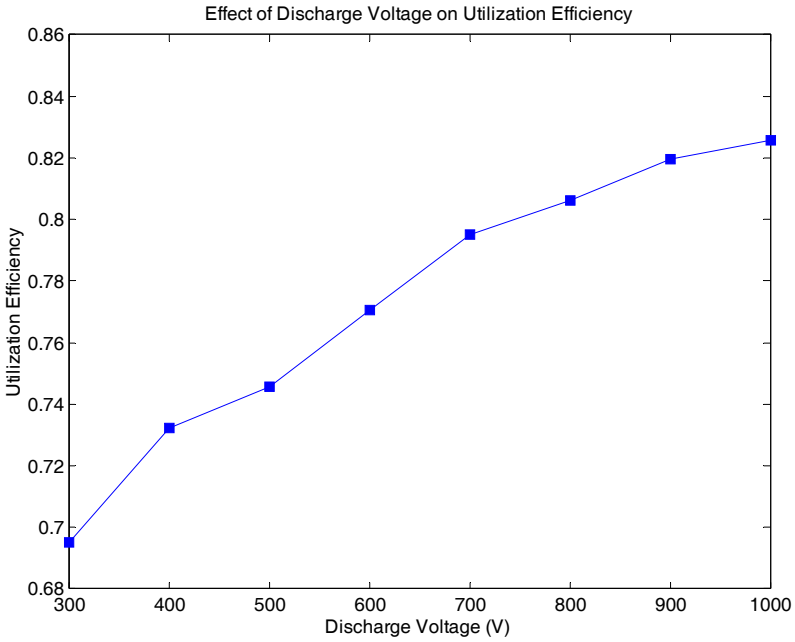

Figure 3.40 Effect of discharge voltage on utilization efficiency for the BHT-1500 operating at an anode flow rate of 2.44mg/s.

Using the extrapolation method, current density distributions at various discharge voltages are corrected for in-orbit conditions and are plotted in Figure 3.41. The effect of discharge voltage on the in-orbit current density is similar to the uncorrected current density except that the plume narrowing is more evident at higher discharge voltages at in-orbit conditions. Figure 3.42 shows the effect of discharge voltage on source ion current density distributions, which are derived from RPA measurements, as explained in Section 3.3.4. With an increase in discharge voltage, the source ion current density decreases for angles larger than 30° and increases for angles smaller than 30°. This indicates that as the discharge voltage increases, source ions are more focused toward the middle of the plume. Figure 3.42 shows clear evidence that the divergence of source ions decreases with voltage. The reason for this phenomenon is discussed in Section 3.4.3.

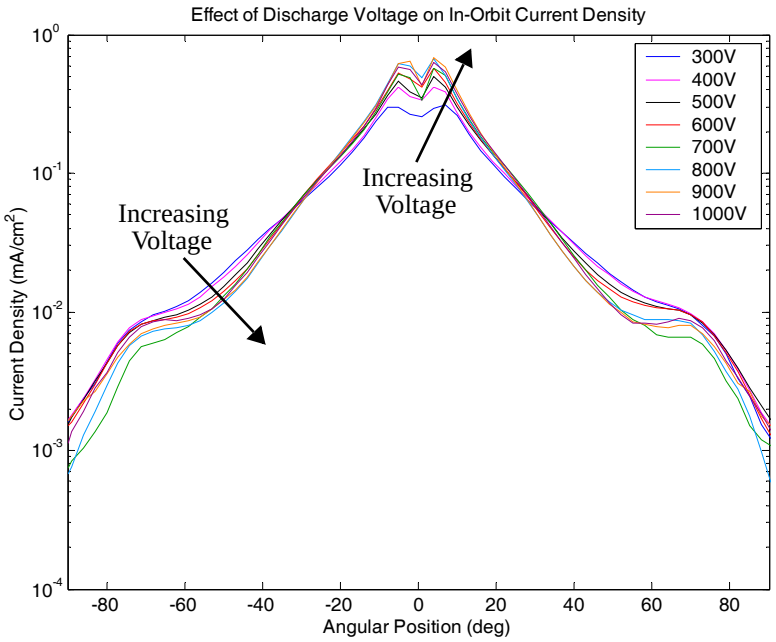

Figure 3.41 Effect of discharge voltage on in-orbit current density. V_d = 300-1000V, $\dot{m}_a$ = 2.44mg/s and sweep radius = 1m.

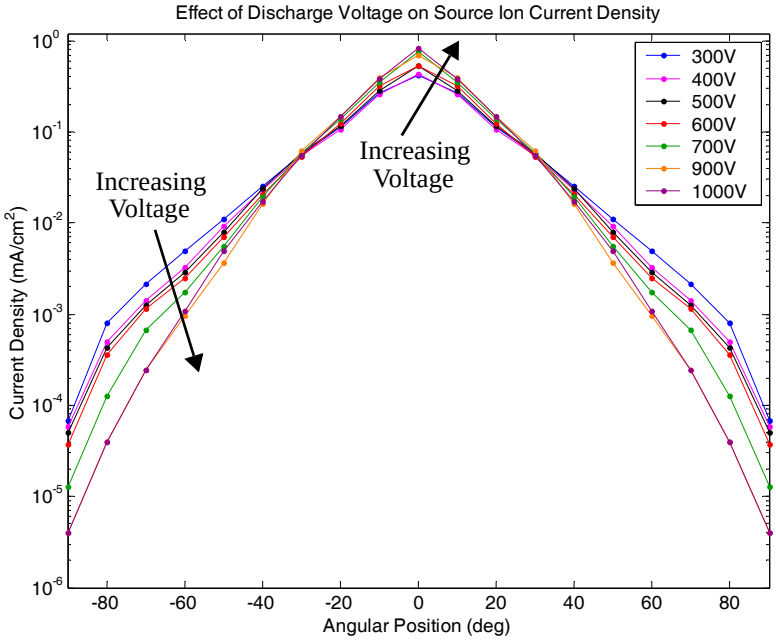

Figure 3.42 Effect of discharge voltage on source ion current density. V_d = 300-1000V, $\dot{m}_a$ = 2.44mg/s and sweep radius = 1m.

3.4.2 Ion Energy Distribution

Figures 3.43-3.47 show the effect of discharge voltage on the ion energy distribution at –90°, –80°, –70°, –60° and –50°. The measurements shown in Figures 3.43-3.47 are the same measurements in Figures 3.17-3.24, expect plotted differently. In Figures 3.43-3.47, ion energy distributions at various discharge voltages are grouped by angular position.

At each angular position, the energy of the charge exchange ion population does not change with discharge voltage. At –90°, the plume consists of only charge exchange ions for any given discharge voltage. The data plotted in Figures 3.43-3.47 show the following:

1. At –80° the primary source ion population progressively decreases as the discharge voltage increases from 300V to 600V. Source ions do not exist at this angle for discharge voltages higher than 600V.
2. At –70° the primary source ion population progressively decreases as the discharge voltage increases from 300V to 700V. Source ions do not exist at this angle for discharge voltages higher than 700V.
3. The angle at which the plume crosses over from charge exchange ion dominant to source ion dominant decreases with discharge voltage. For example, the crossover angle decreases from approximately –60° at V_d=300V to –50° at V_d=1000V.

These observations show that as the discharge voltage is increased, source ions are contained within smaller angles. This leads to the conclusion that the divergence of source ions decreases with an increase in discharge voltage.

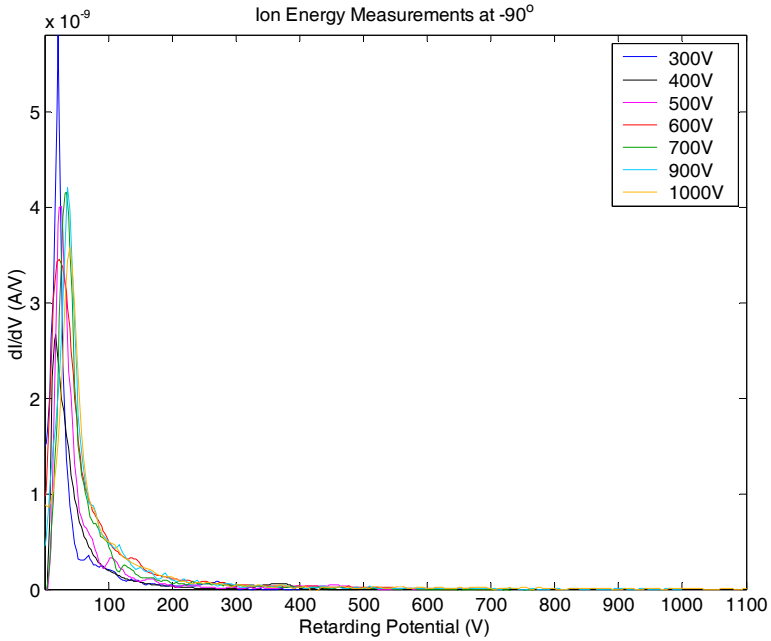

Figure 3.43 Effect of discharge voltage on the ion energy distribution at –90°. V_d = 300-1000V, $\dot{m}_a$ = 2.44mg/s, sweep radius = 1m and P = 7.5×10^{-6} Torr.

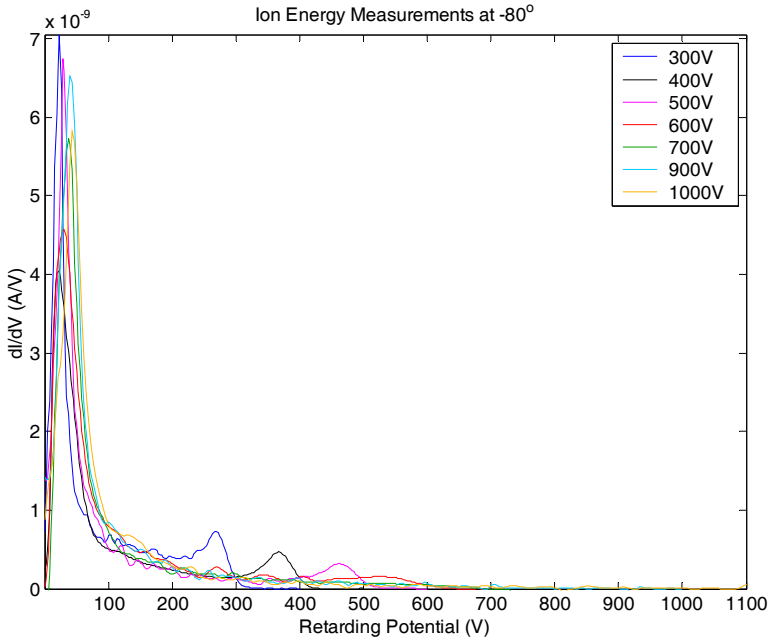

Figure 3.44 Effect of discharge voltage on the ion energy distribution at –80°. V_d = 300-1000V, $\dot{m}_a$ = 2.44mg/s, sweep radius = 1m and P = 7.5×10^{-6} Torr.

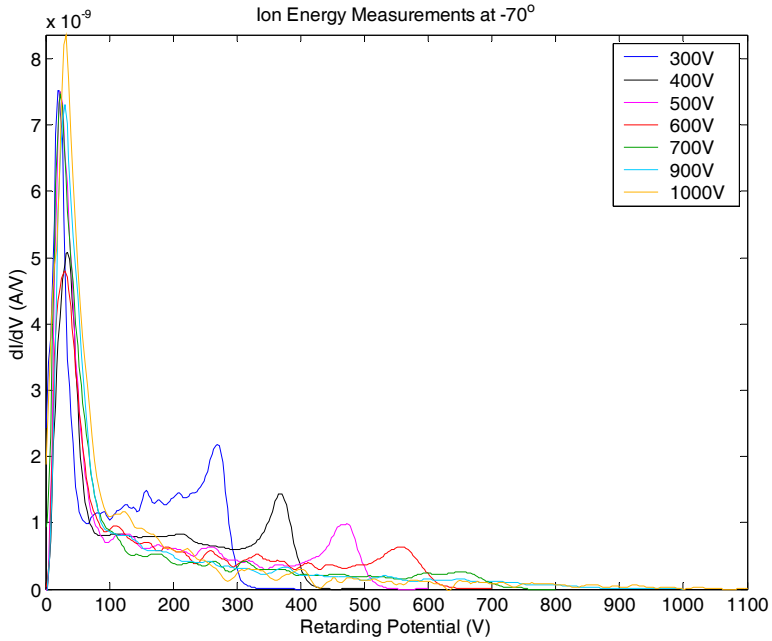

Figure 3.45 Effect of discharge voltage on the ion energy distribution at −70°. V_d = 300-1000V, $\dot{m}_a$ = 2.44mg/s, sweep radius = 1m and P = 7.5×10^{-6} Torr.

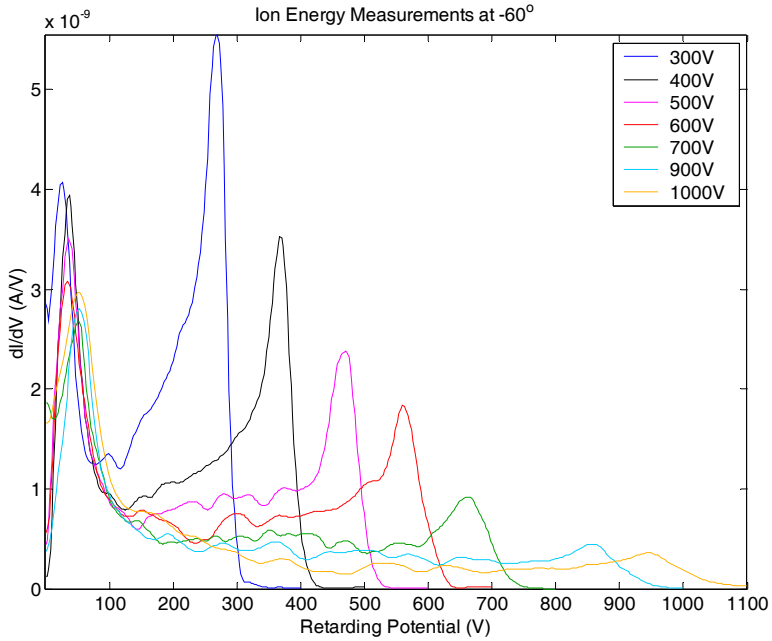

Figure 3.46 Effect of discharge voltage on the ion energy distribution at −60°. V_d = 300-1000V, $\dot{m}_a$ = 2.44mg/s, sweep radius = 1m and P = 7.5×10^{-6} Torr.

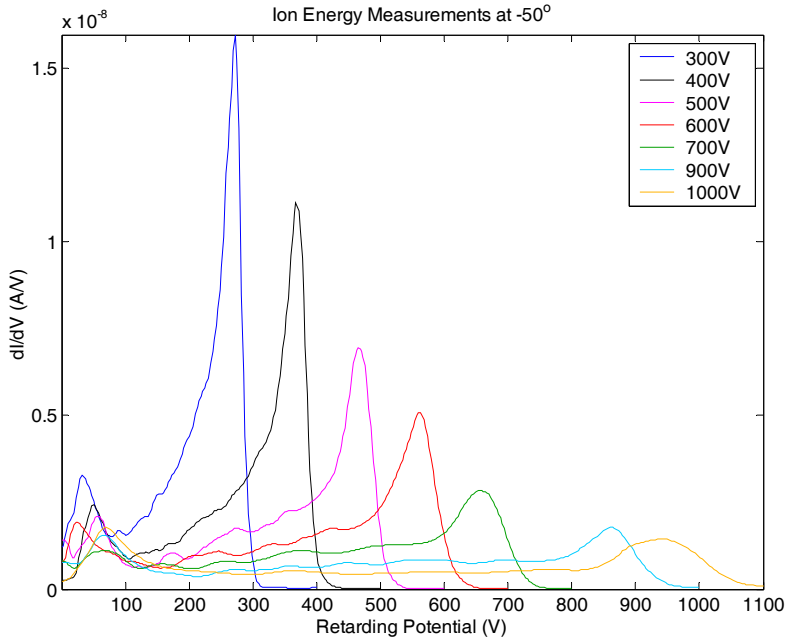

Figure 3.47 Effect of discharge voltage on the ion energy distribution at −50°. V_d = 300-1000V, $\dot{m}_a$ = 2.44mg/s, sweep radius = 1m and P = 7.5×10^{-6} Torr.

3.4.3 Plume Divergence

Using the in-orbit current density, the 95% half-angle plume divergence is approximately 70° regardless of the discharge voltage. As discussed earlier, the in-orbit current density includes charge exchange ions due to source ion collisions with anode and cathode neutrals. Charge exchange ions have an adverse effect on plume divergence and it is interesting to note that they also mask the effect of discharge voltage on plume divergence. Based on the results discussed in Sections 3.4.1 and 3.4.2, it is expected that plume divergence will decrease with an increase in discharge voltage. To determine the effect of discharge voltage on source ions, current densities plotted in Figure 3.42 are used to calculate the 95% half-angle plume divergence for source ions. Figure 3.48 shows the 95% half-angle plume divergence for source ions at various discharge voltages.

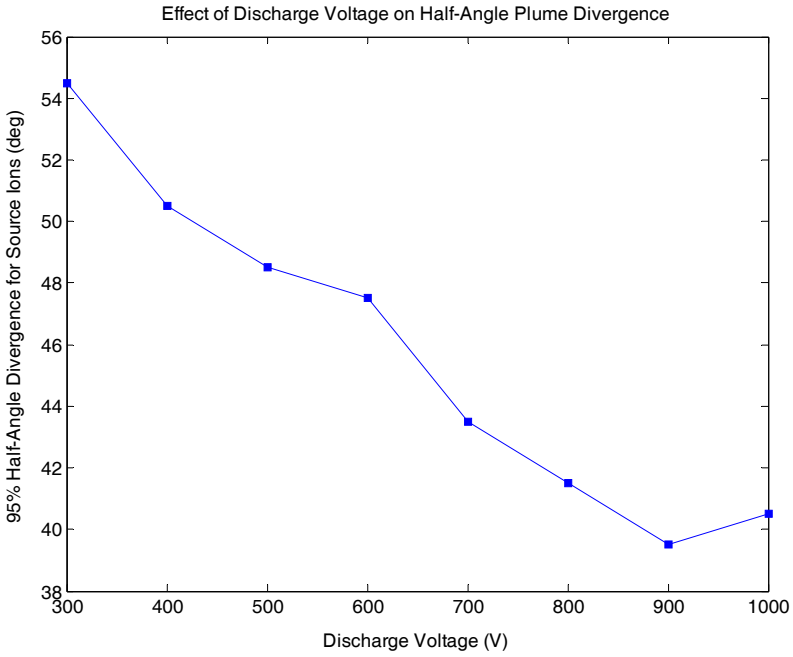

Figure 3.48 Effect of discharge voltage on the 95% half-angle divergence for source ions. V_d = 300-1000V and $\dot{m}_a$ = 2.44mg/s,

As shown in Figure 3.48, plume divergence decreases with an increase in discharge voltage. Equation 3.3 shows that plume divergence is proportional to the ratio of electron temperature and discharge voltage. Therefore, a decrease in plume divergence with voltage is likely due to discharge voltage increasing faster than an increase in electron temperature. Assuming a power law relationship between electron temperature and discharge voltage where

$$T_e \propto V_d^{\,n} \tag{3.23}$$

and substituting Equation 3.23 into Equation 3.3, the plume divergence is expressed as

$$\sin\theta_{div} \propto \frac{1}{V_d^{\frac{1-n}{2}}} \tag{3.24}$$

Plugging the experimental data in Figure 3.48 to solve for *n*, we obtain *n = 0.576*, and therefore, electron temperature and discharge voltage are related by

$$T_e \propto V_d^{0.576} \tag{3.25}$$

Equation 3.25 confirms that discharge voltage increases faster than electron temperature, which explains the decrease in plume divergence with discharge voltage.

Warner performed an electron power balance analysis on a Hall thruster discharge where electron temperature is related to discharge voltage [53]. One of the input parameters of the analysis is the fraction of electrons lost to the channel walls, which is calculated by a ratio of effective wall area and exit area. Assuming that electrons strike 25% of channel wall area, the area ratio is 0.3. Using the analytical expressions derived by Warner, the peak electron temperature inside the channel of the BHT-1500 is calculated for discharge voltages of 300-1000V. Figure 3.49 shows a plot of peak electron temperature versus discharge voltage.

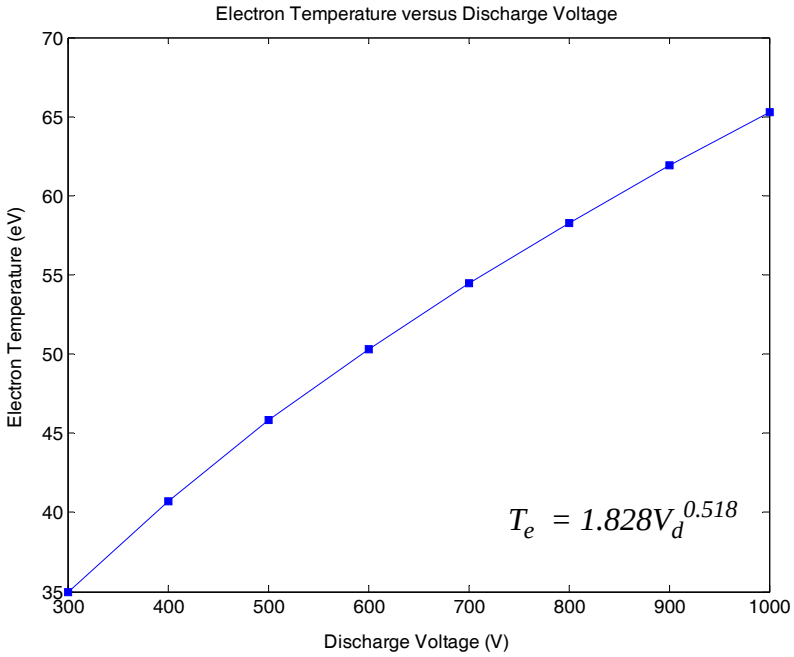

Figure 3.49 Plot of the predicted peak electron temperature versus discharge voltage for the BHT-1500 using an area ratio of 0.3.

Figure 3.49 shows that electron temperature and discharge voltage are related by

$$T_e = 1.828 V_d^{0.518} \tag{3.26}$$

Equation 3.26 shows that the dependence of electron temperature on discharge voltage is less than proportional, which is in agreement with the experimental data portrayed in Equation 3.25. The results of the analytical model performed by Warner confirm that discharge voltage increases more rapidly than electron temperature.

Chapter 4

NUMERICAL PLUME MODELING

The BHT-1500 plume is modeled using a numerical plume simulation developed at MIT [18, 19, 20]. The plume simulation is run at both laboratory and in-orbit conditions. Simulation results are compared to experimental measurements to determine the accuracy of the plume model and to provide recommendations for possible areas of improvement.

4.1 Roadmap of Numerical Modeling

Figure 4.1 is a schematic of the process that was followed to model the plume of the BHT-1500. The key elements required to model a Hall thruster plume are:

- Engine code
- Source model
- Plume simulation

The engine code outputs velocity distributions that represent the state of the plasma at the thruster exit. The source model is generated with the velocity distributions and is used with the plume simulation to model the BHT-1500 plume. Finally, results from the plume simulation are compared to experimental measurements.

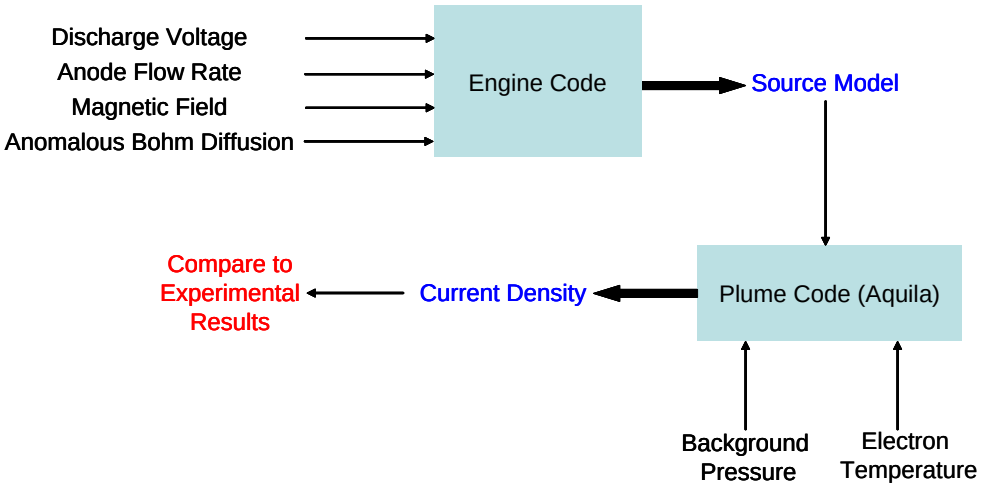

Figure 4.1 Flow diagram of the process that was followed to obtain numerical plume results and compare them to experimental measurements.

4.2 Engine Code

4.2.1 Code Description

The engine code is used to generate velocity distributions of single ions, double ions, and neutrals exiting the BHT-1500. The code used in this research is a full Particle-In-Cell (PIC) Monte Carlo Collision (MCC) simulation [28, 45]. It was developed at MIT by Szabo to model the discharge of a Hall thruster. The simulation is axisymmetric, capturing two dimensions in space and three dimensions in velocity (2D3V). The code models all species as particles. The species include electrons, neutrals, single ions, and double ions. The electric field is calculated by solving Poisson's equation starting from the charge distribution and boundary conditions. Anomalous electron diffusion is modeled in addition to the naturally occurring electron transport effects captured by classical diffusion and wall effects. The magnetic field is pre-calculated using a commercial software and is imposed on the simulation domain. Collisions are modeled using the MCC methodology. The type of collisions performed in the simulation include elastic and inelastic electron-neutral collisions, electron-ion ionizing collisions, ion-neutral scattering, and ion-neutral charge

exchange collisions. Coulombic collisions are implemented in the simulation but are not used in this work.

The code employs an artificial ion to electron mass ratio and an artificial permittivity to increase the computational speed of the simulation. The artificial permittivity increases the Debye length, which allows for coarser grids and longer time-steps. A methodology is implemented in the code to recover physical results. The full PIC simulation is described in length in several publications [28, 45].

The simulation domain, the grid, is a non-orthogonal mesh with a spacing that is roughly determined by the Debye length as modified by the artificial permittivity. Figure 4.2 shows the grid used to simulate the BHT-1500.

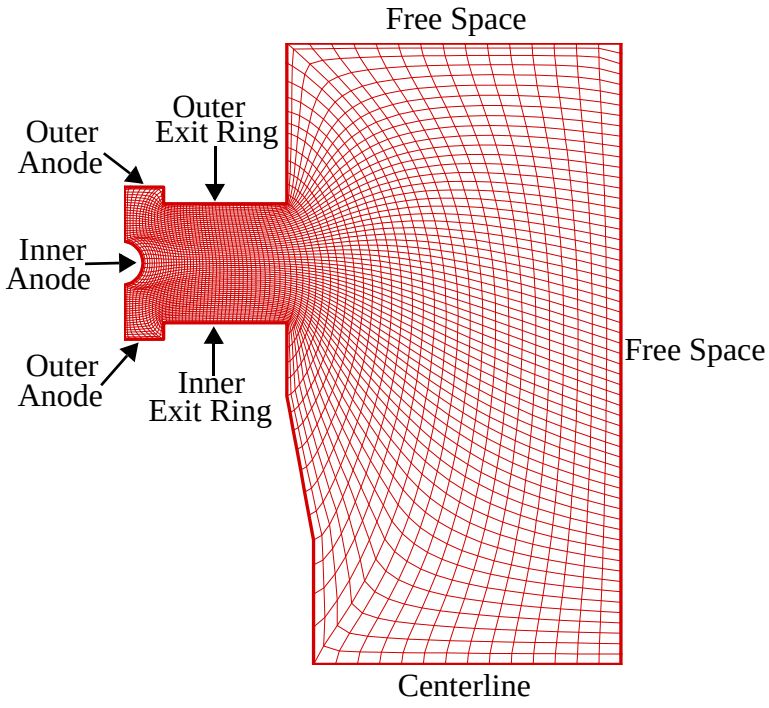

Figure 4.2 Computational grid for the BHT-1500.

The simulation can be set to run at various thruster operating conditions. The input parameters of the full PIC code include:

- Discharge voltage
- Anode flow rate
- Magnetic field
- Anomalous Bohm diffusion

The anomalous Bohm diffusion is numerically imposed on the simulation because classical diffusion alone does not predict discharge current accurately. Discharge current measurements tend to exceed the discharge current calculated using classical diffusion mechanisms. By imposing an anomalous electron transport, the electron collision frequency is artificially increased. The total electron collision frequency is

$$\nu_t = \nu_c + \nu_a \tag{4.1}$$

where ν_c is classical frequency. ν_a, the anomalous frequency, is determined by

$$\nu_a = \frac{\omega_{ce}}{\beta_a} \tag{4.2}$$

where ω_{ce} is the electron cyclotron frequency and β_a is the anomalous Hall parameter. A high β_a implies nearly classical behavior. The anomalous Bohm diffusion is modeled throughout the domain, except in a layer with a finite axial width encompassing all corresponding radial dimensions. The simulation allows for variation of the anomalous Hall parameter and the spacial location of the layer.

4.2.2 Code Performance

The performance of the BHT-1500 is numerically characterized and compared to experimental measurements. The simulation is performed for a discharge voltage of 300V and an anode flow rate of 2.44mg/s. The magnetic field is pre-calculated using a solenoid current of 2A. Experimentally, the BHT-1500 operates at a discharge voltage of 300V and an anode flow rate of 2.44mg/s in a minimum discharge current mode using a solenoid cur-

rent between 2A and 3A. The simulation is run with two different anomalous Hall parameter profiles to determine the profile that produces comparable results to the experimental measurements. Figure 4.3 illustrates the anomalous Hall parameter profiles that are imposed on the simulation.

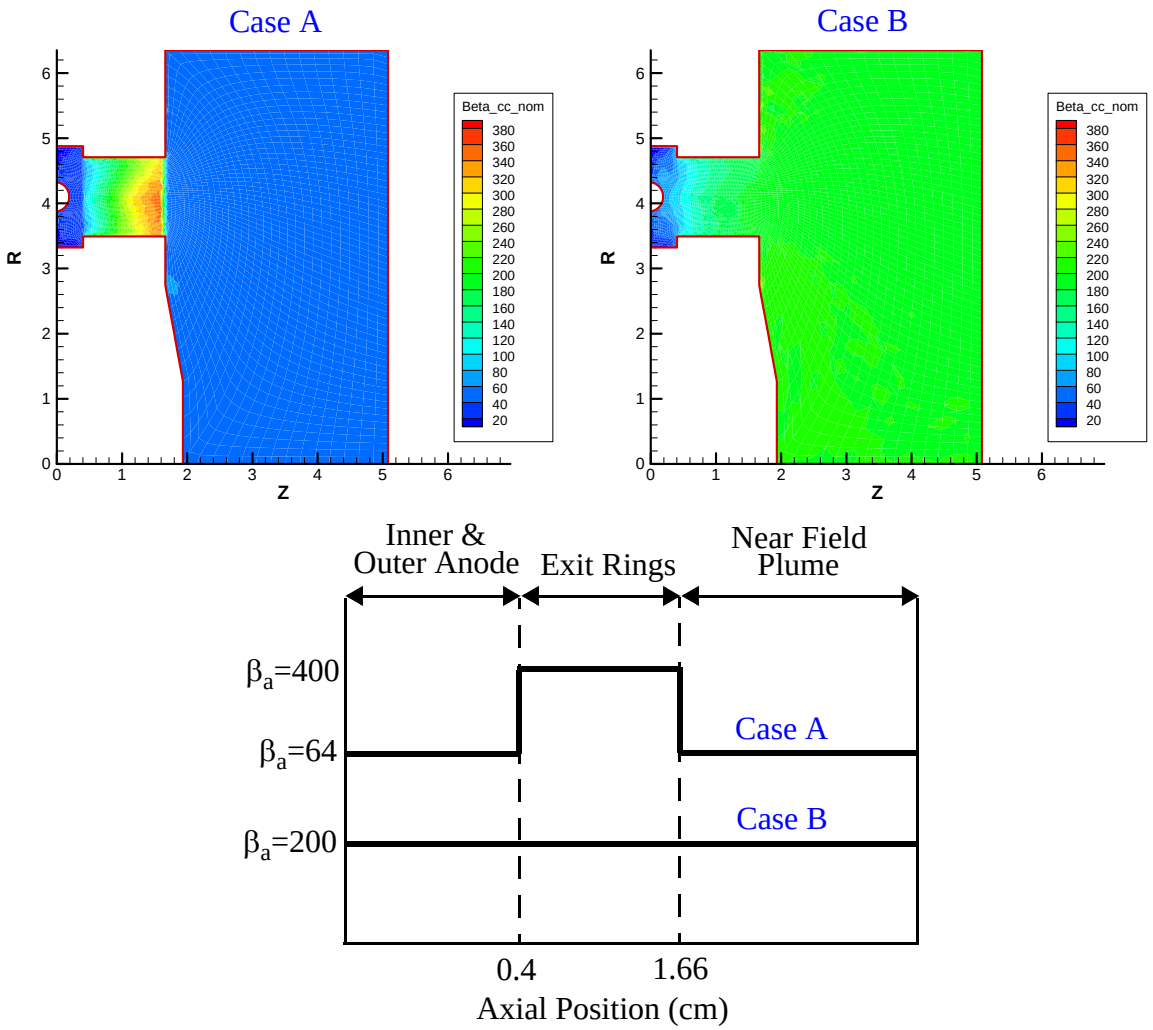

Figure 4.3 Profiles of the anomalous Hall parameters that are imposed on the simulation.

Case A consists of imposing a barrier layer along the entire length of the exit rings with an anomalous Hall parameter value of 400, which nearly suppresses anomalous transport. In case B, the anomalous Hall parameter is uniform in the entire simulation region with a value of 200.

For cases A and B, the simulation is started from a previously converged solution and is run for 200,000 iterations. The results are time-averaged over a discharge oscillation. Table 4.1 compares measured and predicted thruster performance obtained from both anomalous Hall parameter profiles.

TABLE 4.1 Results of the full PIC for different anomalous Hall parameter profiles at V_d = 300V and $\dot{m}_a$ = 2.44mg/s.

Case	Hall Parameter			I_d (A)	T (mN)	Efficiency
	Upstream	Between	Downstream			
A	64	400	64	1.93	35.7	45.3%
B	200	200	200	1.53	32.5	47.5%
Experimental	N/A	N/A	N/A	1.98	35.6	43.6%

Results presented in Table 4.1 show that the anomalous Hall parameter profile in case A predicts a thruster performance that is in agreement with experimental measurements. This shows that the full PIC simulation can accurately predict the performance of the BHT-1500 and therefore can be used to generate velocity distributions that represent the state of the plasma exiting the thruster. In this research, the source model is generated for both anomalous Hall parameter profiles to understand the effect of electron transport on the plume.

4.3 Source Model

Szabo implemented algorithms in the engine code to generate velocity distribution functions for single ions, double ions and neutrals crossing a user specified sampling plane. The velocity distributions of the charged species are corrected to account for the non-zero electric potential at the sampling plane and are time-averaged over a discharge oscillation. The velocity distributions are then processed to generate a source model. This section covers two different methods that are used to generate a source model. The first method, used in previous work [18, 19, 20, 54, 55], generates a source model that produces poor agreement between plume simulation results and experimental measurements. Based on those

results, a new source model was developed to improve comparison with experimental data.

4.3.1 Previous Source Model

Figure 4.4 shows the computational grid of the BHT-1500 and the location of the sampling plane.

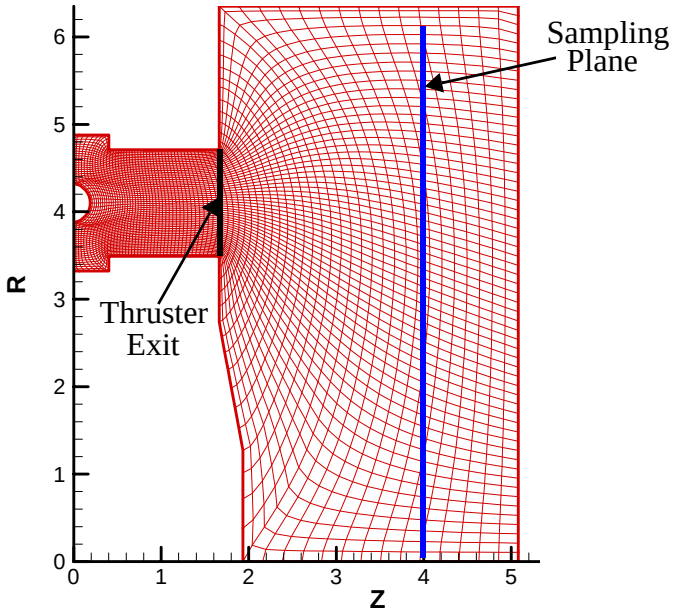

Figure 4.4 Computational grid of the BHT-1500. Dimensions of the R and Z axes are in centimeters. The sampling plane is placed at z = 4cm because the potential due to the engine falls off by the time ions reach this axial location.

The plume simulation does not model electron-impact ionization and it also does not model ions falling through the potential produced by the thruster. To capture these effects into the source model, the sampling plane axial location is selected at z = 4cm. At this location, the space potential due to the engine has mostly fallen off by the time ions reach this axial position. The radial location of the sampling plane extends from the centerline to r = 6cm. The sampling plane is divided into 61 radial bins. As a particle crosses a radial bin, the axial, radial, and azimuthal velocities are recorded. Single ions, double ions, and

neutrals are sampled separately. The single and double ions are each divided into four populations: near-side and far-side source ions, and near-side and far-side charge exchange ions. The near-side population represents particles that are generated within the computational grid. The far-side population represents particles that crossed the thruster centerline from the opposite side of the annular channel. The neutrals are divided into two populations: source neutrals and charge exchange neutrals. The source neutrals represent the portion of the propellant that was not ionized. The charge exchange neutrals represent ions that underwent charge exchange collisions and transformed into fast neutrals. In total, the full PIC simulation generates axial, radial, and azimuthal velocity distributions at 61 radial positions for 10 populations.

The source model serves as a link between the engine code and the plume simulation. The velocity distributions generated by the engine code are converted into input parameters for the plume simulation. For each species - single ions, double ions, and neutrals -, the plume simulation requires the total flux versus radius. In addition, the plume simulation requires information about each population of the species in the form of:

- Fraction of total flux versus radius
- Average axial velocity versus radius
- Average radial velocity versus radius
- Average azimuthal velocity versus radius
- Average axial temperature over the sampling plane
- Average radial temperature over the sampling plane
- Average azimuthal temperature over the sampling plane

All input parameters are extracted from the velocity distribution functions. The density, average velocity, and flux of each population at a radial position are determined by

$$n(r) = \sum f(v_z) = \sum f(v_r) = \sum f(v_\phi) \tag{4.3}$$

$$\bar{v}_z(r) = \frac{\sum f(v_z) v_z}{n(r)},\ \bar{v}_r(r) = \frac{\sum f(v_r) v_r}{n(r)},\ \bar{v}_\phi(r) = \frac{\sum f(v_\phi) v_\phi}{n(r)} \tag{4.4}$$

$$flux(r) = n(r)\sqrt{\bar{v}_z^2 + \bar{v}_r^2 + \bar{v}_\phi^2} \tag{4.5}$$

where *f(v)* is the velocity distribution function generated for each population. At each radial position, the flux of the populations belonging to a particular species is added to determine the total flux of that species. The flux fraction of each population is then calculated by dividing the flux of the individual population by the total flux of the species it corresponds to. Finally, for each population, a Maxwellian distribution is fit to the velocity distribution at each radial position to determine the temperature for each radius. Since the plume simulation only requires one temperature for each population, the temperature is averaged over the sampling plane. The process is performed for axial, radial and azimuthal velocity distributions to obtain average axial, radial and azimuthal temperatures respectively.

The main input parameters for the source model are plotted in Figures 4.5-4.7, which are grouped by species. Tables 4.2-4.4 summarize the temperatures for the different populations. The input parameters plotted in Figures 4.5-4.7 and the temperatures shown in Tables 4.2-4.4 are extracted from the full PIC simulation run with the anomalous Hall parameter profile in case A. The input parameters extracted from the full PIC simulation run for case B have similar trends to the results plotted for case A. Input parameters obtained from cases A and B are referred to as source models A and B respectively.

The results of source model A show that the flow is composed of 83% single ions, 7% double ions and 10% neutrals. For source model B, the flow is composed of 79% single ions, 5% double ions and 16% neutrals. As expected, the charged species are dominated by the near-side source population. The charge exchange single and double ion populations represent a small percentage of the total species flow. However, it is important to include them in the source model because they represent the flow that affects large angles of the plume measurements. The source and charge exchange velocities are similar for both single and double ions. This occurs because in the engine code charge exchange ions are produced near the anode and are accelerated by the same potential difference as the

source ions. The velocity of the far-side population for single and double ions is dominated by radial motion. This is consistent since the far-side ions need a large radial velocity component to cross the thruster centerline. As seen in Figures 4.5 and 4.6, the far-side single and double ions do not exist past r = 4cm. This discontinuity is likely due to thruster geometrical constraints. Far-side ions that would have been collected at the radial sampling plane past r = 4cm have a high radial velocity and were likely lost to the channel walls.

It is interesting to note that neutrals are dominated by charge exchange neutrals in the channel region of the thruster. Outside the channel region, source neutrals dominate. The axial velocity of the charge exchange neutrals is lower than originally expected. However, the axial velocity is consistent because charge exchange collisions occur near the anode before ions are accelerated by the full thruster potential. When charge exchange collisions occur, ions that transform into neutrals only have approximately 20eV of energy.

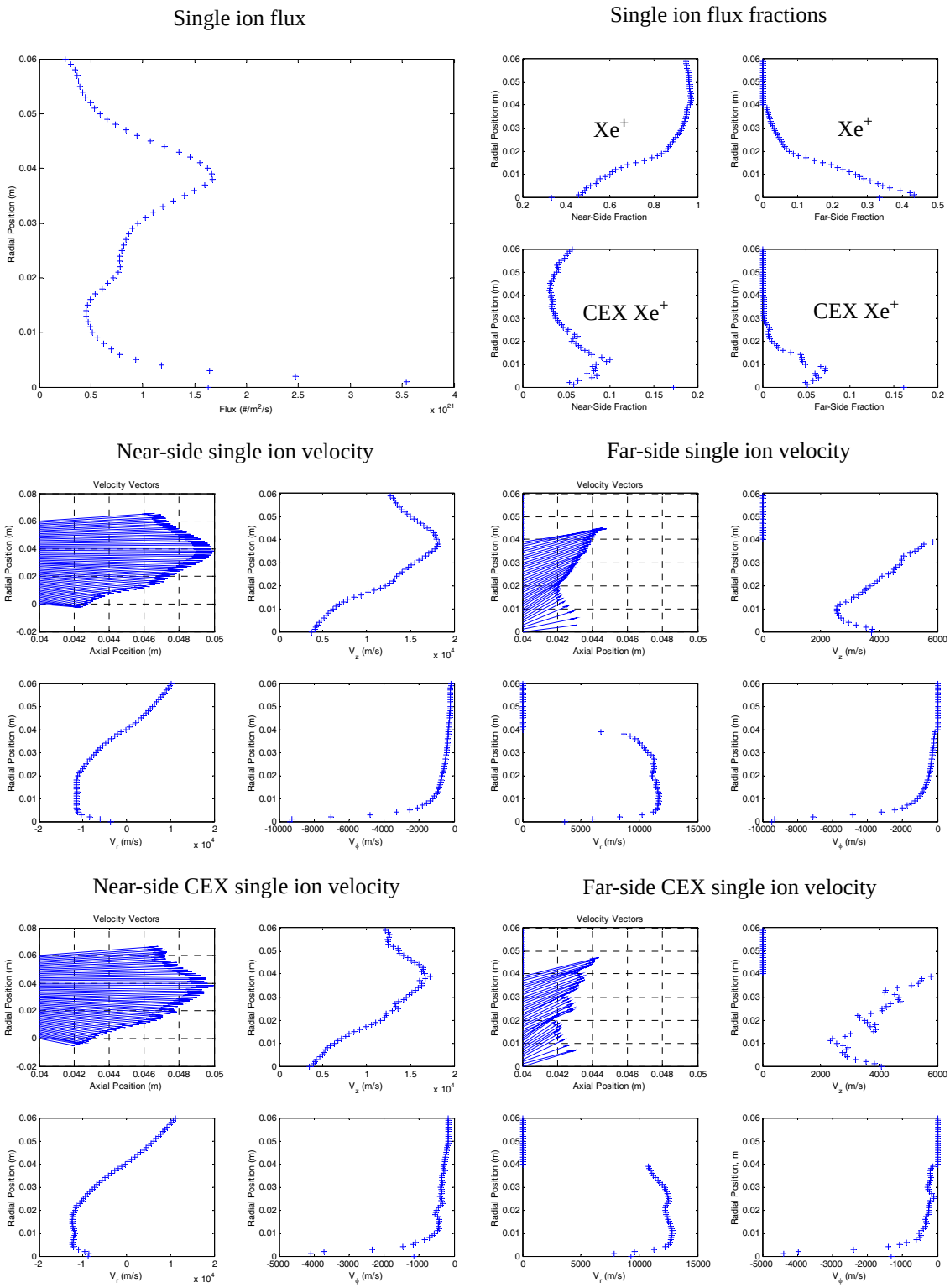

Figure 4.5 Single ion input parameters. v_z, v_r and v_ϕ are axial, radial and azimuthal velocities respectively. V_d = 300V and $\dot{m}_a$ = 2.44mg/s.

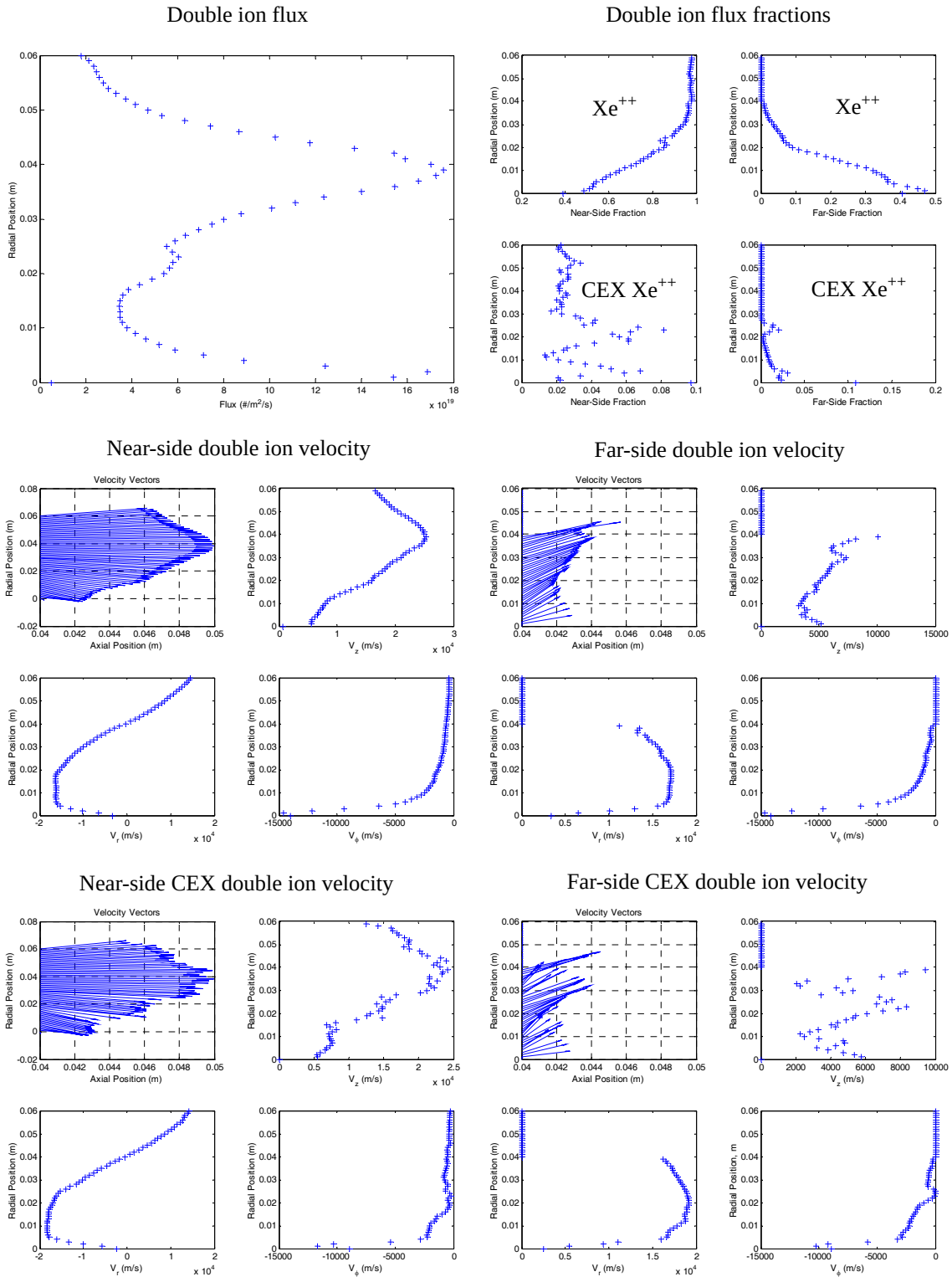

Figure 4.6 Double ion input parameters. v_z, v_r and v_ϕ are axial, radial and azimuthal velocities respectively. V_d = 300V and $\dot{m}_a$ = 2.44mg/s.

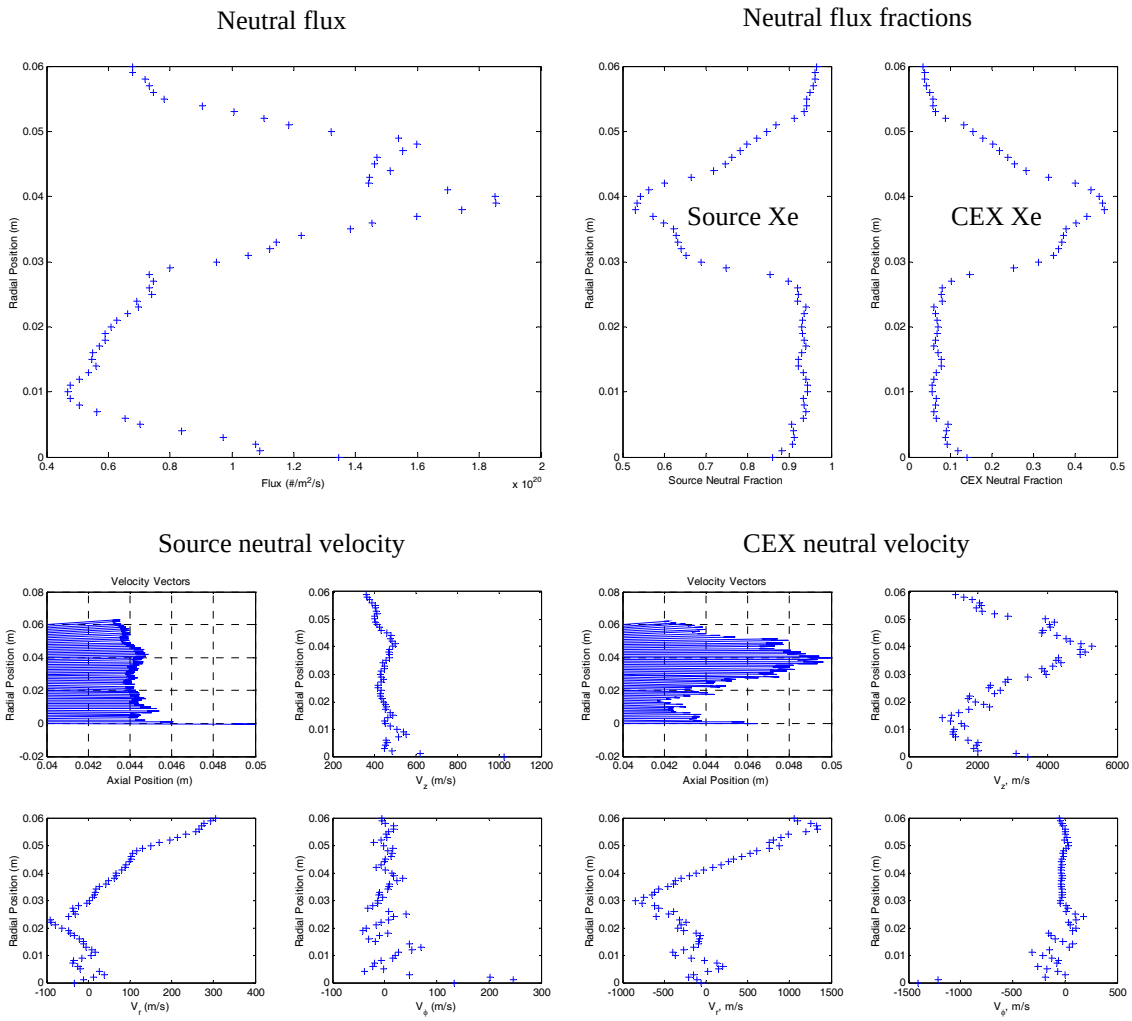

Figure 4.7 Neutral input parameters. v_z, v_r and v_ϕ are axial, radial and azimuthal velocities respectively. Source neutrals represent neutral propellant that did not ionize. CEX neutrals represent ions that transformed into neutrals through charge exchange collisions. V_d = 300V and $\dot{m}_a$ = 2.44mg/s.

TABLE 4.2 Source model temperatures in eV for single ions.

	Source		CEX	
	Near-side	**Far-side**	**Near-side**	**Far-side**
Axial	0.59	2.30	1.41	2.28
Radial	0.25	2.09	0.30	2.10
Azimuthal	0.02	0.05	0.04	0.06

TABLE 4.3 Source model temperatures in eV for double ions.

	Source		CEX	
	Near-side	**Far-side**	**Near-side**	**Far-side**
Axial	1.64	3.78	1.65	0.72
Radial	0.78	3.84	0.62	0.06
Azimuthal	0.04	0.15	0.05	0.04

TABLE 4.4 Source model temperatures in eV for neutrals.

	Source	**CEX**
Axial	0.02	0.7
Radial	0.04	0.08
Azimuthal	0.05	0.04

Using inputs from the previous source model, the plume simulation in essence reconstructs the velocity distributions for single ions, double ions, and neutrals as Maxwellian distributions at each radial position. Figure 4.8 shows a comparison at r = 3.1cm between an axial velocity distribution generated for near-side single ions by the full PIC code and a Maxwellian distribution by which near-side single ions are injected into the plume simulation.

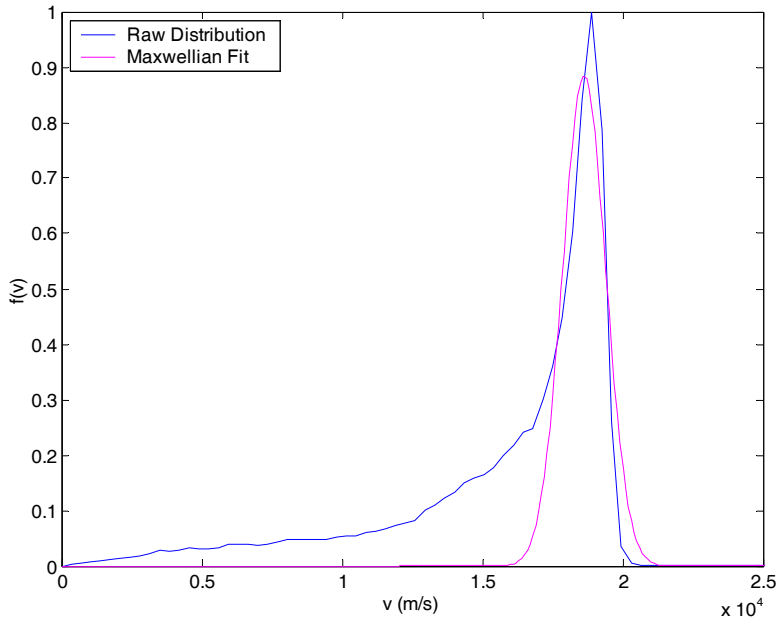

Figure 4.8 Comparison between an axial velocity distribution and a Maxwellian fit to the distribution. The raw distribution is a normalized axial velocity distribution for the near-side single ions generated by the full PIC code at r = 3.1cm. The Maxwellian fit is the distribution by which the near-side single ions are injected into the plume simulation at r = 3.1cm.

Figure 4.8 shows that a significant portion of the original distribution is discarded when using a Maxwellian fit. The Mawellian distribution provides a good fit for the high energy ions but it does not include low energy ions. This means that when velocity distributions are converted into Maxwellian distributions, low energy ions are not injected into the plume simulation. Low energy ions play an important role in plume expansion. As discussed in Chapter 3, low energy ions are pushed by the plume potential to the side and are

measured at high angles with respect to the thruster centerline. Therefore, in order to properly model the plume expansion at high angles, it is important to include all particles that were created in the engine code.

4.3.2 New Source Model

To resolve this issue, the code of the plume simulation is changed to allow the source model to pass velocity distributions into the plume simulation. Therefore, the velocity distributions that are generated with the full PIC code are used as the new source model without any processing. The change in the plume code rendered the new source model simpler than the previous one. For example, in the previous source model, each species - single ions, double ions, and neutrals - are divided into populations. With the new source model, dividing the species into separate populations is not necessary. For each species, the input parameters of the new source model are:

- Total flux versus radius
- Axial velocity distribution versus radius
- Radial velocity distribution versus radius
- Azimuthal velocity distribution versus radius

As mentioned earlier, the full PIC simulation generates axial, radial, and azimuthal velocity distributions at 61 radial positions for 10 populations. For the new source model, the velocity distributions of the populations from each species are consolidated to yield the axial, radial, and azimuthal velocity distributions versus radius for each species. The total flux versus radius of each species is calculated similarly to the method described in the previous source model.

Another issue of concern in the previous source model is addressed in the new source model. Figure 4.9 illustrates ion flux lines generated by the full PIC code. The previous source model is generated from particles crossing a sampling plane that is placed at z = 4cm and extends from the thruster centerline to r = 6cm. As shown in Figure 4.9, ion flux at large angles is not captured by the radial sampling plane. To capture all ions exiting the thruster, a cylindrical section. Figure 4.10 shows the BHT-1500 computational grid with a radial sampling plane placed at z = 4cm and extending from the centerline to r = 6cm, and a cylindrical sampling section placed at r = 6cm and extending from z = 2cm to z = 4cm. The radial sampling plane is divided into 61 bins and the cylindrical sampling section is divided into 20 bins. In total, for each species, axial, radial, and azimuthal velocity distributions are generated for 61 radial positions and 20 axial positions.

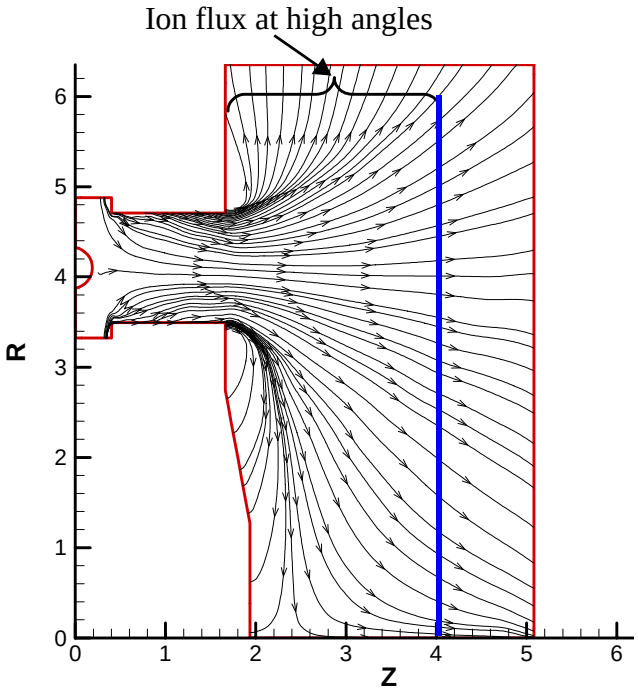

Figure 4.9 Ion flux lines. Ion flux at high angles is not captured by the sampling plane in the previous source model.

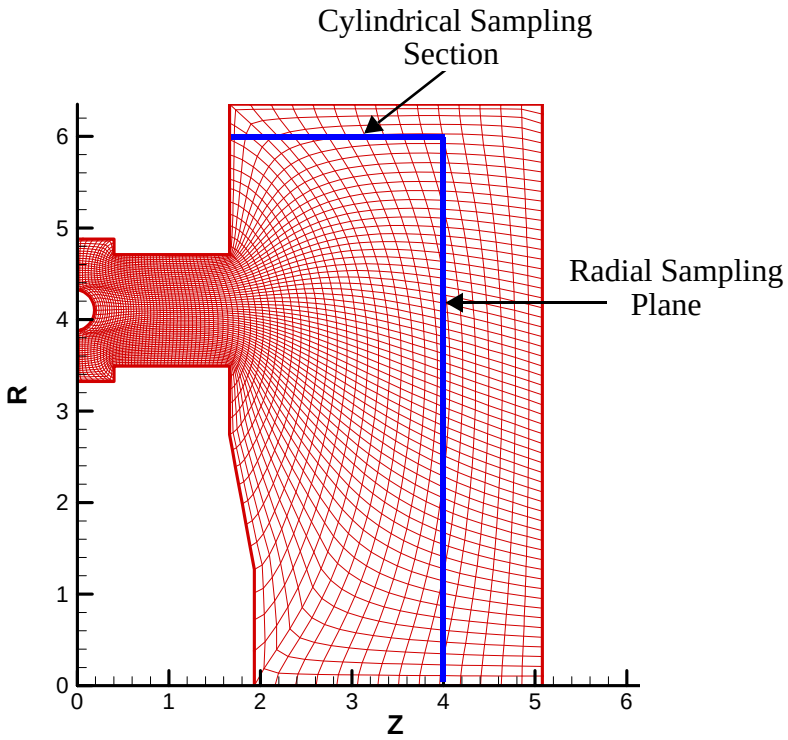

Figure 4.10 Radial sampling plane and a cylindrical sampling section are used to generate the new source model.

The plume simulation allows particles to be injected from only one planar surface. To address this issue, the axial, radial, and azimuthal velocity distributions generated for each species at the 20 axial positions are projected onto the radial plane placed at z = 4cm. Figure 4.11 shows a schematic of the geometrical parameters to explain the method used to project the velocity distributions onto the radial sampling plane.

For a velocity distribution, *f(v)*, generated at $z = z_1$, particles cross the cylindrical sampling section at an average angle α_1 determined by

$$\tan\alpha_1 = \frac{\bar{v}_r}{\bar{v}_z} \tag{4.6}$$

where $\bar{v}_z$ and $\bar{v}_r$ are average axial and radial velocities obtained from the velocity distribution at $z = z_1$ using Equation 4.4. The position, r_1, at which particles cross the radial sampling plane on average is calculated by

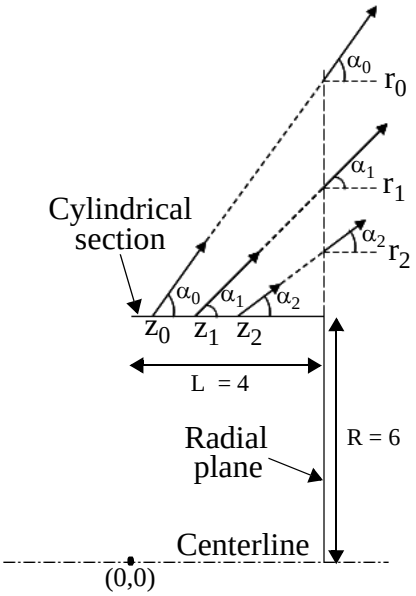

Figure 4.11 Geometrical parameters used to explain the method of projecting distribution functions generated from particles crossing the cylindrical section onto the radial plane.

$$r_1 = (L - z_1)\tan\alpha_1 + R \tag{4.7}$$

then, the velocity distribution at $r = r_1$ is

$$f(v)\big|_{r = r_1} = f(v)\big|_{z = z_1} \tag{4.8}$$

For the source model, we need to know the velocity distribution and the flux. The flux of particles crossing the radial plane at $r = r_1$ is smaller than the flux at $z = z_1$. Using a *1/r* relationship, the flux at $r = r_1$ is determined by

$$flux\big|_{r = r_1} = flux\big|_{z = z_1} \frac{\sin\alpha\cos\alpha}{\sin\alpha\cos\alpha - (L - z_1)\dfrac{d\alpha}{dz}} \frac{R}{r_1} \tag{4.9}$$

where $flux\big|_{z = z_1}$ is the flux obtained from the velocity distribution at $z = z_1$ using Equation 4.5. The term $\dfrac{d\alpha}{dz}$ at $r = r_1$ is calculated by

$$\left.\frac{d\alpha}{dz}\right|_{r = r_1} = \frac{\alpha_2 - \alpha_0}{z_2 - z_0} \tag{4.10}$$

Using Equations 4.8 and 4.9, all velocity distributions for each species generated from particles crossing the cylindrical section are projected onto the radial sampling plane.

In summary, the new source model is generated from particles crossing a radial sampling plane and a cylindrical sampling section. The velocity distributions for particles crossing the cylindrical section are projected onto a radial plane at z = 4cm. This allows us to obtain velocity distributions of all particles exiting the thruster along a radial plane. For each species, the inputs of the new source model consist of total flux and axial, radial, and azimuthal velocity distribution functions.

4.4 Aquila

A hybrid-PIC simulation developed at MIT is used to model plume expansion of the BHT-1500 [18, 19, 20, 55]. The plume simulation called Aquila models ions and neutrals as particles whereas electrons are modeled as a fluid. Aquila uses the source model to inject particles into the simulation domain. The plume simulation is discussed in detail in several publications [18, 19, 20, 55]. This section provides an overview of Aquila's major components.

4.4.1 Grid

The simulation uses a 3D unstructured tetrahedral grid. The grid is generated using GridEx, a NASA Langley griding package developed for computational fluid dynamics [56]. A parasolid format of the simulated domain is read into GridEx, which then generates surface and volume meshes. Figure 4.12 shows the simulated vacuum tank geometry used in this work. The simulated vacuum tank is 2.4m in diameter, which is the same as the diameter of the Busek T8 vacuum tank. The length of the simulated vacuum tank is 2.5m. The small red cylinder inside the tank, shown in Figure 4.12, represents the Hall thruster. A grid line source is used in GridEx to obtain better grid refinement in the dense region of the plasma. The line source extends from the face of the thruster out to 1.5m. Figure 4.13 is a cross-section of the simulation grid, which shows a fine grid in front of the thruster exit and a coarse grid at large angles with respect to the thruster centerline. Aquila injects all particles from a user specified thruster face. Figure 4.14 shows the grid resolution of the thruster face from which all particles are injected into the simulation domain.

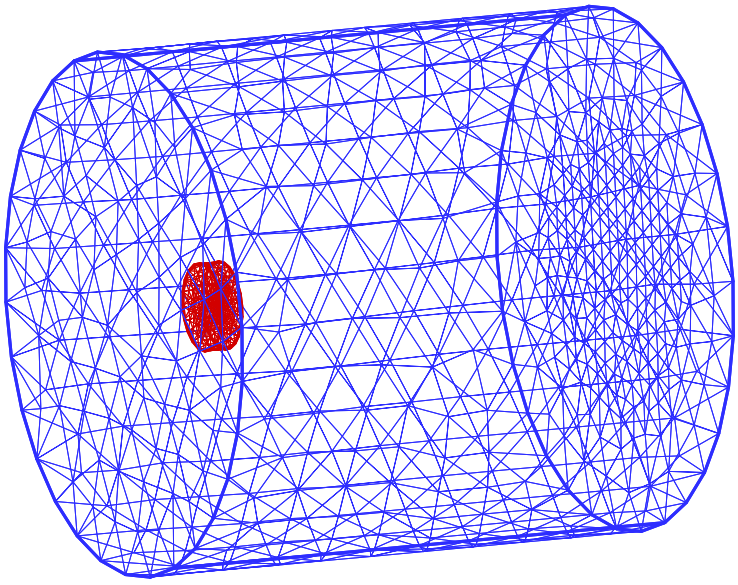

Figure 4.12 3D view of the simulated vacuum tank.

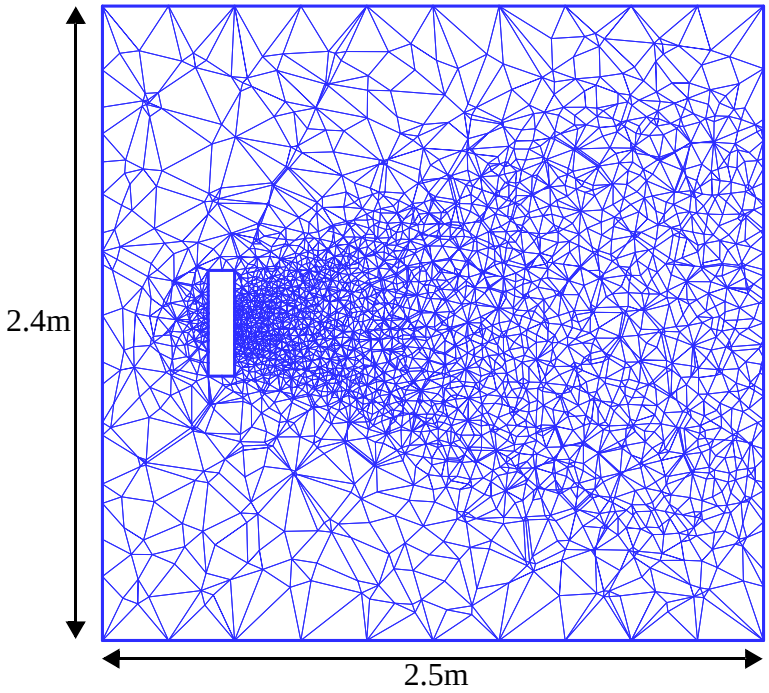

Figure 4.13 Cross-section of simulation grid.

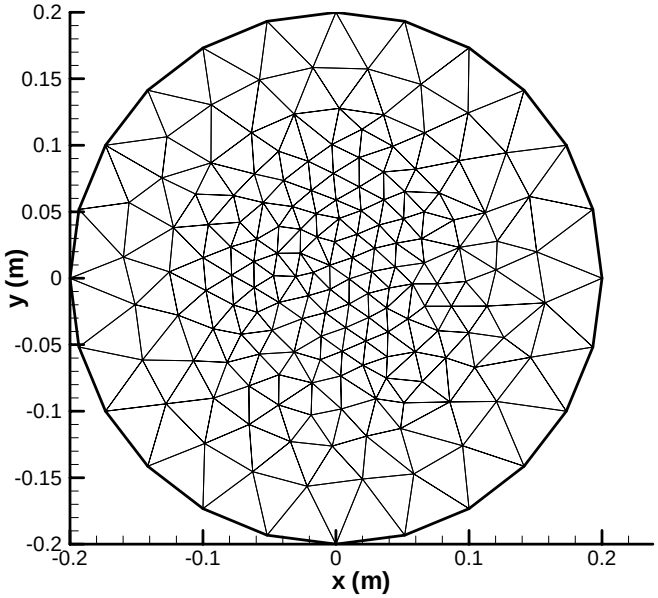

Figure 4.14 Grid resolution of thruster face. All particles are injected into the simulation domain of Aquila from the thruster face.

4.4.2 Potential Solver

By assuming quasi-neutrality, the electric field is calculated using a modified form of the common Boltzmann law. Neglecting collisional, magnetic, and inertial effects, the electron momentum balance is

$$\nabla(n_e k T_e) = e n_e \nabla\phi \tag{4.11}$$

Since $\frac{\nabla n_e}{n_e} \gg \frac{\nabla T_e}{T_e}$, Equation 4.11 becomes

$$k T_e \nabla(n_e) \approx e n_e \nabla\phi \tag{4.12}$$

Experimental results suggest that a polytropic relationship exists between electron density and electron temperature [12, 13]. The relationship can be written as

$$\frac{T_e}{T_{eo}} = \left(\frac{n_e}{n_{eo}}\right)^{\gamma - 1} \tag{4.13}$$

where γ falls roughly between ($\gamma = 1$) for an isothermal expansion and ($\gamma = 5/3$) for an adiabatic expansion. Using Equations 4.12 and 4.13, the potential is calculated by

$$\phi = \phi_o + \frac{k T_{eo}}{e} \frac{1 - \left(\frac{n_e}{n_{eo}}\right)^{\gamma - 1}}{\gamma - 1} \tag{4.14}$$

where n_e is calculated by tracking the particles and weighting them to the grid nodes. To solve Equation 4.14, the simulation requires a reference potential, ϕ_o, a reference electron temperature, T_{eo}, and a value for γ. These values are generally selected using existing experimental plume data. The plume simulation is also capable of solving the potential where quasi-neutrality breaks down. In these cases, the electric field is calculated by solving Poisson's equation. Further details on the capabilities of Aquila's potential solver can be found in several publications [18, 19, 20, 55].

4.4.3 Collision Model

Collisions are modeled using the Monte Carlo Collision (MCC) methodology. The type of collisions performed in the simulation include:

- Elastic Xe-Xe collisions
- Elastic Xe-Xe^{+} collisions
- Elastic Xe-Xe^{++} collisions
- Charge exchange Xe-Xe^{+} collisions
- Charge exchange Xe-Xe^{++} collisions

Aquila is also equipped with a No-Time-Counter Direct Simulation Monte Carlo (DSMC) method. The DSMC method requires that all particles of the same species have the same weighting [18]. This method is not used in this research because background neutrals and engine neutrals are modeled with different weightings.

4.5 Aquila Results

Aquila is run for 6,000 iterations with a timestep of 1×10^{-7}s. Averaged results are taken between iterations 4,000 and 6,000. The simulation injects particles at a flow rate of 2.44mg/s. Particle species weightings are chosen so as to inject 100 particles for engine neutrals and 250 particles for single and double ions at each timestep. The background pressure is simulated by uniformly initializing neutral particles at 300°K throughout the simulation domain. The particle weighting of background neutrals is selected so that 300,000 particles for neutrals are initialized. The pressure is maintained by balancing mass flow injected by the thruster to mass lost to the tank walls. The mass flow lost is scaled by changing the sticking coefficient of the walls. The sticking coefficient is set to 1 when the plume simulation is run at zero pressure. Ions and neutrals striking the surfaces of the tank are reflected as neutrals with an energy accommodation coefficient of 0.95 for ions and 0.65 for neutrals. The potential solver uses a polytropic relationship between electron temperature and electron density with $\gamma = 1.3$, $\phi_o = 0$, and $T_{eo} = 3$eV. The refer-

ence potential, ϕ_o, and reference electron temperature, T_{eo}, are imposed at the centerline 25cm away from the thruster face.

When the engine code was run to generate the source model, the thruster exit rings were modeled with a secondary electron emission yield of a ceramic corresponding to Borosil ($BN\text{-}SiO_2$) Grade M. Therefore, for accurate comparison, the plume simulation results in this chapter are plotted against experimental measurements taken with the same exit ring material.

4.5.1 Comparison of Source Models

Figure 4.15 shows plume simulation results of current density obtained with the previous and new source models. The simulation results are also compared to measured current density to determine the accuracy of the source models. For this comparison, both previous and new source models are generated from the full PIC engine code setup with an anomalous Hall parameter profile that consists of a barrier imposed inside the entire length of the channel (Case A). The plume simulation results and experimental data are plotted for a discharge voltage of 300V, an anode flow rate of 2.44mg/s, a background pressure of 2.35×10^{-5} Torr, and a sweep radius of 1m.

The simulation results obtained with the previous source model underpredict the current density at the wings where low energy charge exchange ions dominate. The poor agreement at the wings was originally blamed on Aquila's collision model [55]. It was thought that Aquila's collision model did not generate sufficient charge exchange ions to populate the wings of the current density. Since the current density obtained with the new source model matches the experimental results using the same collision model, Aquila's collision model cannot be the source of the discrepancy. Therefore, the discrepancy is caused by deficiencies in the previous source model. As explained in Section 4.3.1, the method used to generate the previous source model discards some of the low energy ions created in the full PIC simulation when the velocity distributions are fit with Maxwellian distributions.

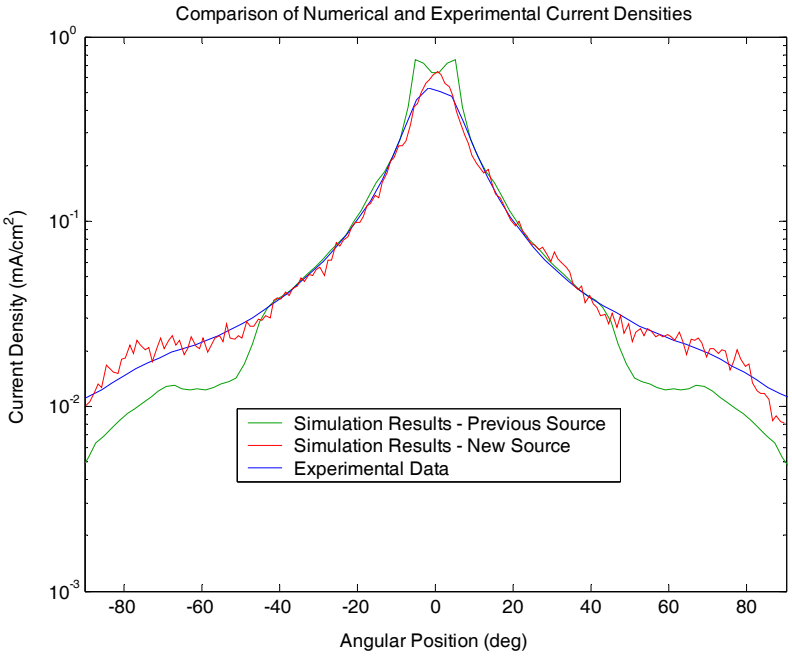

Figure 4.15 Current density from the previous and new source model compared to experimental results. The simulation results are obtained from source models generated for the anomalous Hall parameter profile depicted in case A. V_d = 300V, $\dot{m}_a$ = 2.44mg/s, P = 2.35×10^{-5} Torr and sweep radius = 1m.

Figure 4.15 also shows that deficiencies in the previous source model are identified and addressed when generating the new source model. Therefore, the method used to generate the new source model, which is described in Section 4.3.2, produces a source model that can be reliably used with Aquila to model plume expansion.

4.5.2 New Source Model Results

Using the method of generating a source model outlined in Section 4.3.2, two source models are generated from the full PIC engine code running at a discharge voltage of 300V and a flow rate of 2.44mg/s. Source model A is generated for an anomalous Hall parameter profile that consists of a barrier imposed inside the entire length of the channel (Case A) and source model B is generated for a uniform anomalous Hall parameter in the entire simulation region (Case B). This section presents results obtained with Aquila using inputs from the both source models at a simulated background pressure of 2.35×10^{-5} Torr.

Figures 4.16-4.25 show contour plots of simulated plasma plume properties of the BHT-l500 at a background pressure of 2.35×10^{-5} Torr. Plume properties generated from source models A and B have the same trends. The electron temperature and plasma potential are highest at the middle of the plume and lowest at the wings following the polytropic relationship between electron temperature and electron density. Ions modeled in Aquila are classified into three populations: source ions, charge exchange ions and elastically scattered ions. The source ions are ions that do not undergo any collisions in the plume. As expected, source ions expand in the middle of the plume and form a jet. A small population of source ions travel to high angles away from the centerline and backstream to the wall behind the thruster. These source ions are likely low energy ions that were pushed by the plume potential to large angles. Low energy ions are either born at low potentials or undergo charge exchange collisions in a low potential region of the engine code. The resulting ions from the latter effect are also labeled source ions by Aquila until they undergo collisions in the plume simulation domain. The contour plot of charge exchange ions shows that they are found throughout the plume with a roughly equal probability at all angles. The density of elastically scattered ions is small compared to the other ion populations. The elastically scattered ions are mainly created in the middle of the plume where the electron density is highest.

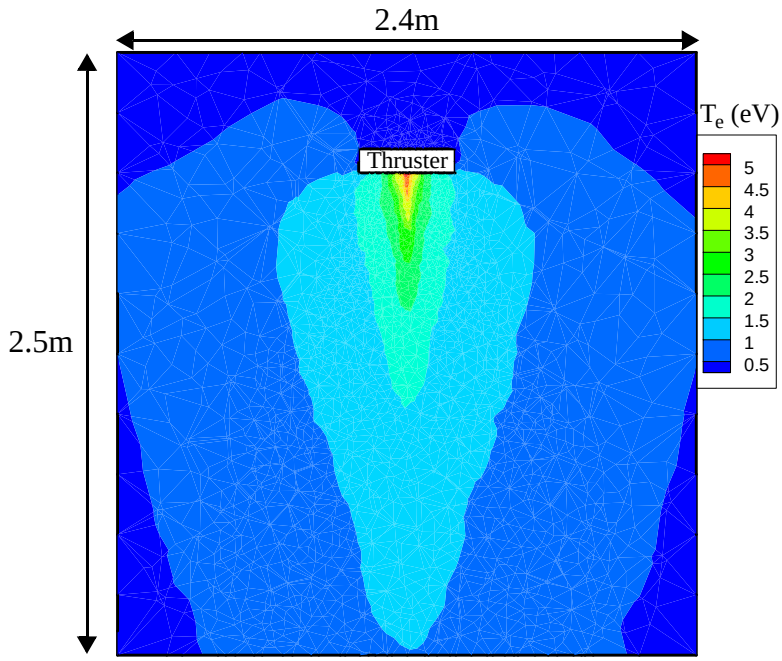

Figure 4.16 Contour plot of electron temperature obtained with Aquila using source model A. T_e is in eV. V_d = 300V, $\dot{m}_a$ = 2.44mg/s and P = 2.35×10^{-5} Torr.

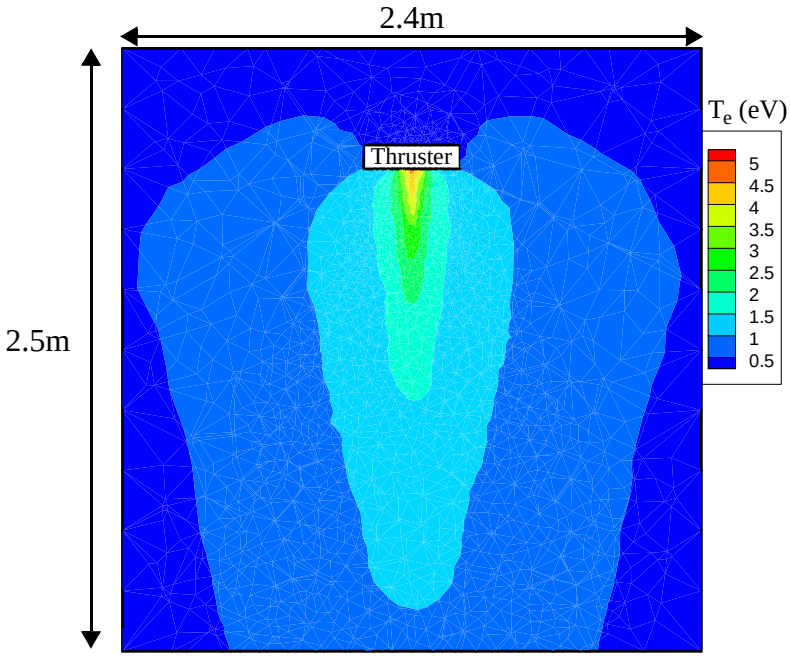

Figure 4.17 Contour plot of electron temperature obtained with Aquila using source model B. T_e is in eV. V_d = 300V, $\dot{m}_a$ = 2.44mg/s and P = 2.35×10^{-5} Torr.

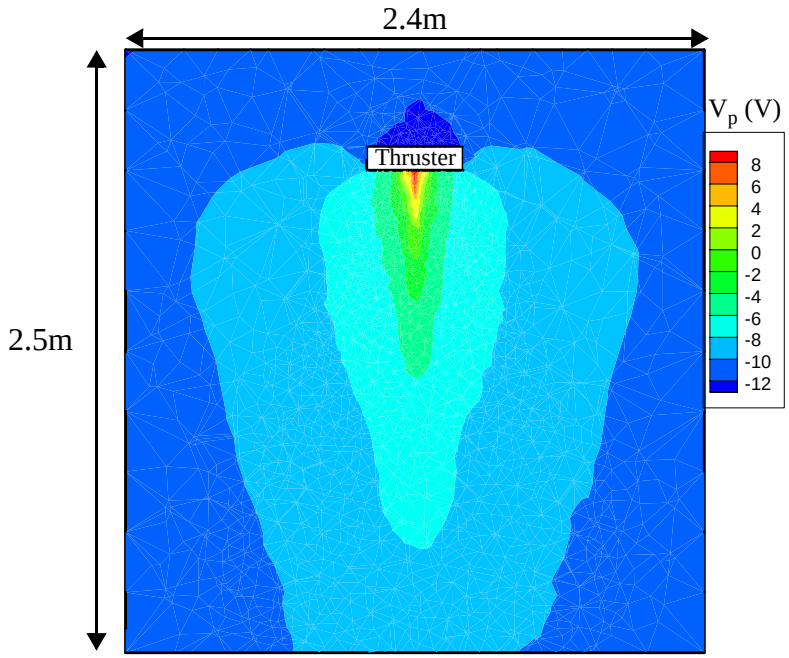

Figure 4.18 Contour plot of plasma potential obtained with Aquila using source model A. V_d = 300V, $\dot{m}_a$ = 2.44mg/s and P = 2.35×10^{-5} Torr.

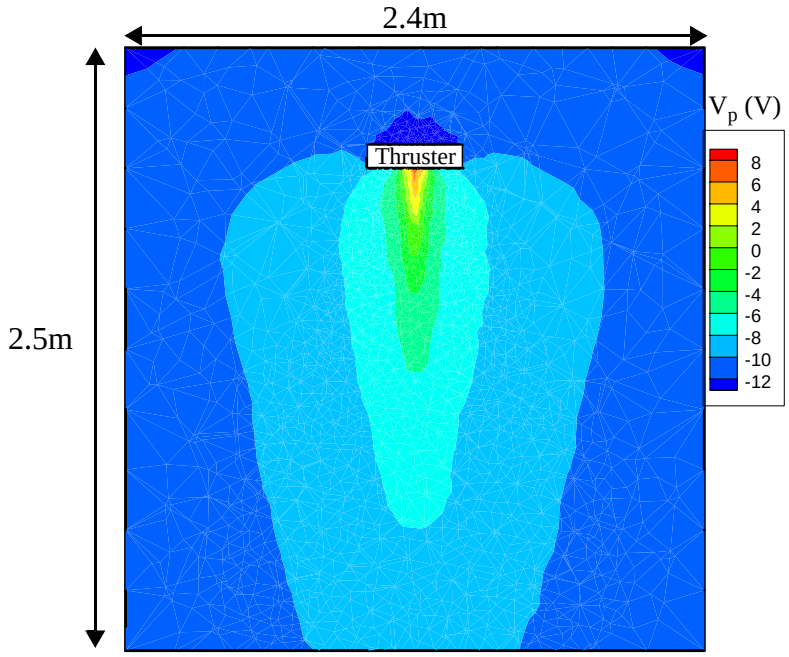

Figure 4.19 Contour plot of plasma potential obtained with Aquila using source model B. V_d = 300V, $\dot{m}_a$ = 2.44mg/s and P = 2.35×10^{-5} Torr.

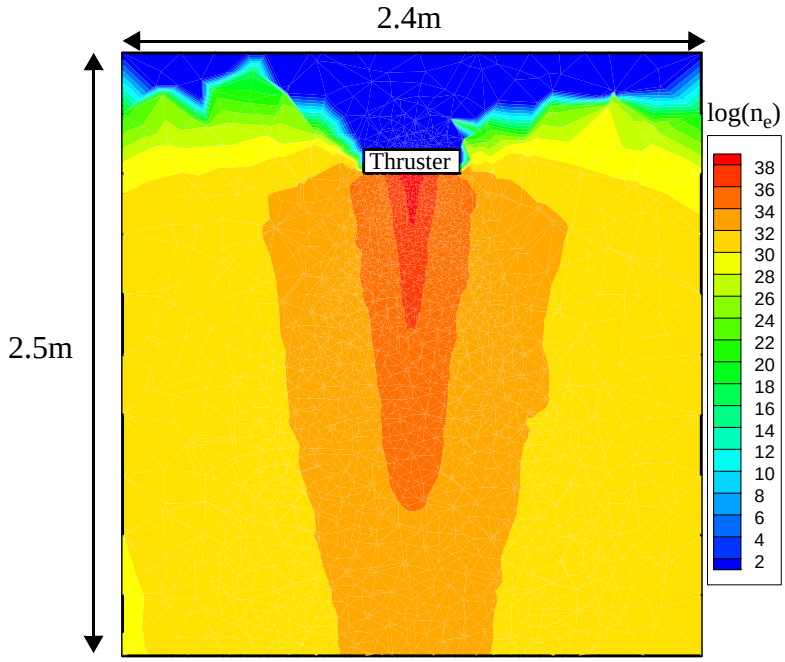

Figure 4.20 Logarithmic contour plot of the density of source ions obtained with Aquila using source model A. The source ions include both source single and double ions. V_d = 300V, $\dot{m}_a$ = 2.44mg/s and P = 2.35×10^{-5} Torr.

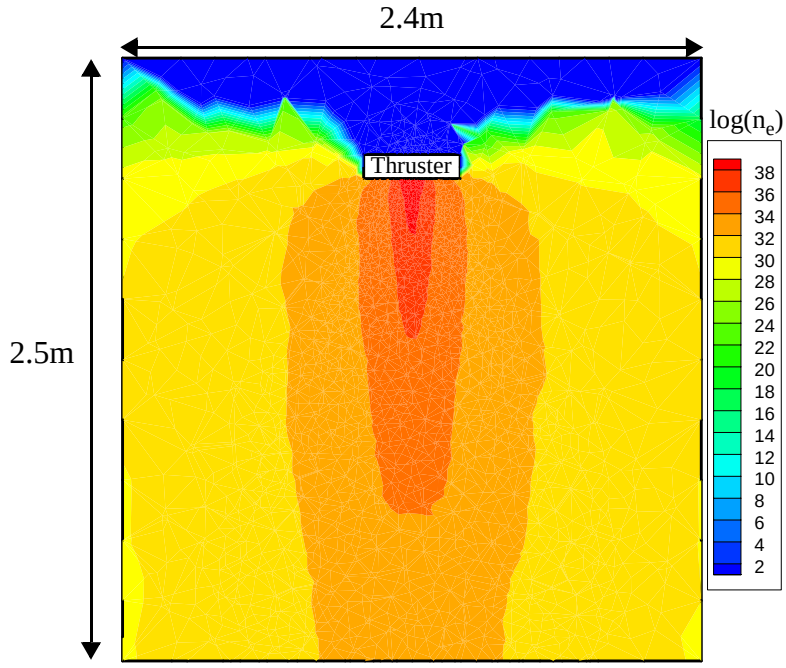

Figure 4.21 Logarithmic contour plot of the density of source ions obtained with Aquila using source model B. The Source ions include both source single and double ions. V_d = 300V, $\dot{m}_a$ = 2.44mg/s and P = 2.35×10^{-5} Torr.

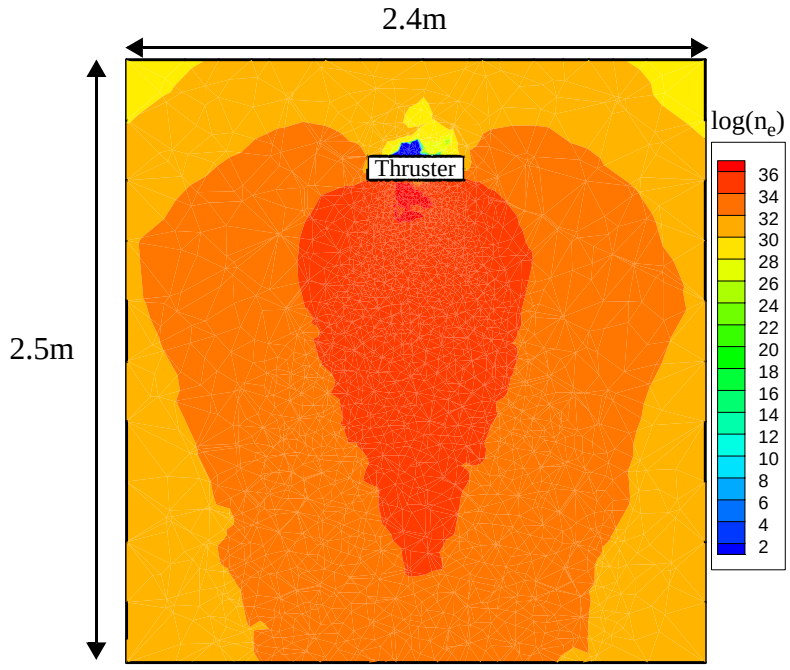

Figure 4.22 Logarithmic contour plot of the density of charge exchange ions obtained with Aquila using source model A. The plotted charge exchange ions include ions produced through collisions with tank and engine neutrals. V_d = 300V, $\dot{m}_a$ = 2.44mg/s and P = 2.35×10^{-5} Torr.

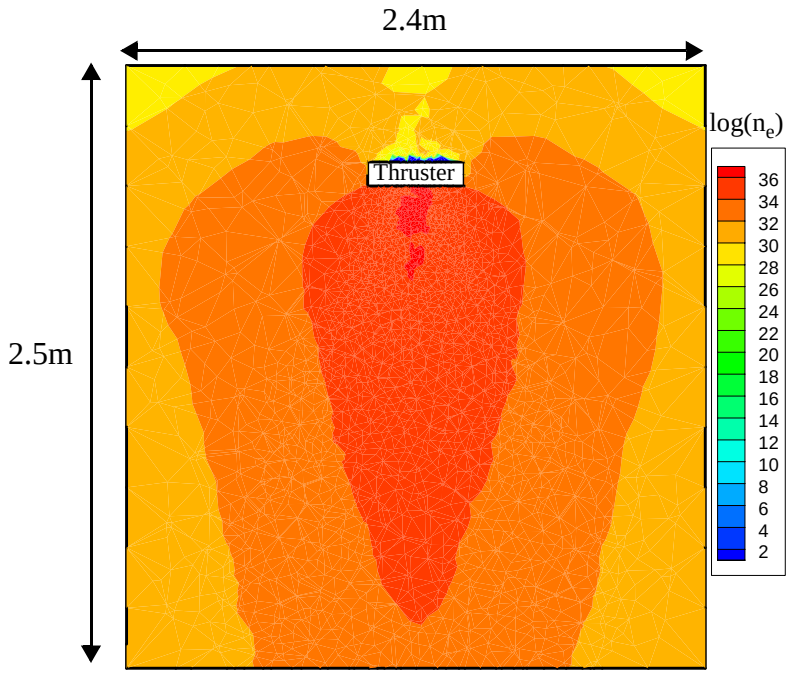

Figure 4.23 Logarithmic contour plot of the density of charge exchange ions obtained with Aquila using source model B. The plotted charge exchange ions include ions produced through collisions with tank and engine neutrals. V_d = 300V, $\dot{m}_a$ = 2.44mg/s and P = 2.35×10^{-5} Torr.

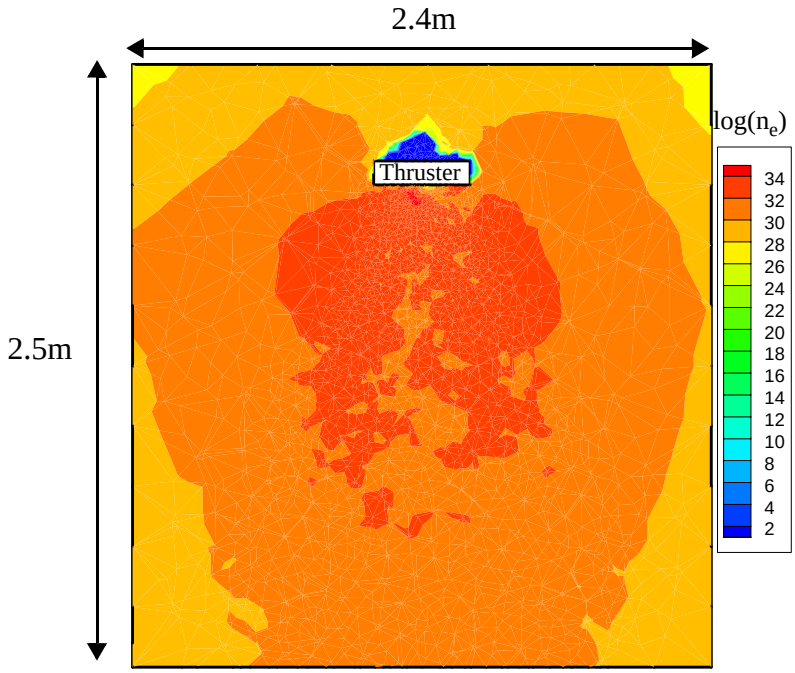

Figure 4.24 Logarithmic contour plot of the density of elastically scattered ions obtained with Aquila using source model A. The plotted elastically scattered ions include ions produced through collisions with tank and engine neutrals. V_d = 300V, $\dot{m}_a$ = 2.44mg/s and P = 2.35×10^{-5} Torr.

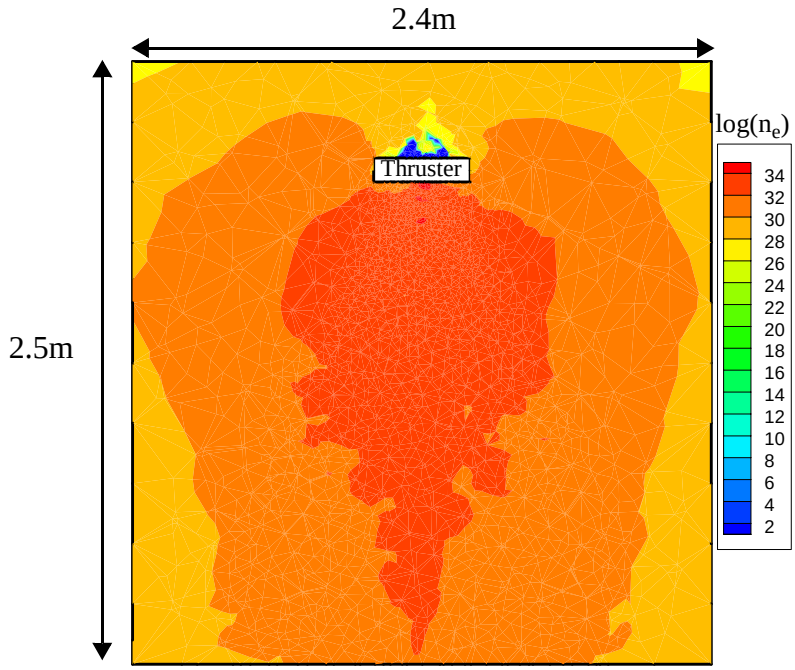

Figure 4.25 Logarithmic contour plot of the density of elastically scattered ions obtained with Aquila using source model B. The plotted elastically scattered ions include ions produced through collisions with tank and engine neutrals. V_d = 300V, $\dot{m}_a$ = 2.44mg/s and P = 2.35×10^{-5} Torr.

Figures 4.26-4.27 show current density obtained from source models A and B respectively at a simulated background pressure of 2.35×10^{-5} Torr. The current density is broken up into current densities from source ions, charge exchange ions and elastically scattered ions. As shown in the mean free path analysis performed in Section 3.1.2, the plume is mainly collisionless. This explains the total current density being composed mainly of source ions, ions that did not undergo any collisions. The source ion current density distribution contains shoulders at the wings. The shoulders are an accumulation of low energy ions generated by the engine code through either ionization at low potentials or charge exchange collisions. As discussed earlier, these ions are labeled as source ions by Aquila until they undergo collisions in the plume simulation domain. Charge exchange current density is approximately constant at all angles. At large angles, the contribution of charge exchange ions is important, whereas the contribution of elastic scattered ions to the current density remains negligible. This is consistent as the mean free path for charge exchange collisions is smaller than that for elastic collisions, as shown in Section 3.1.2.

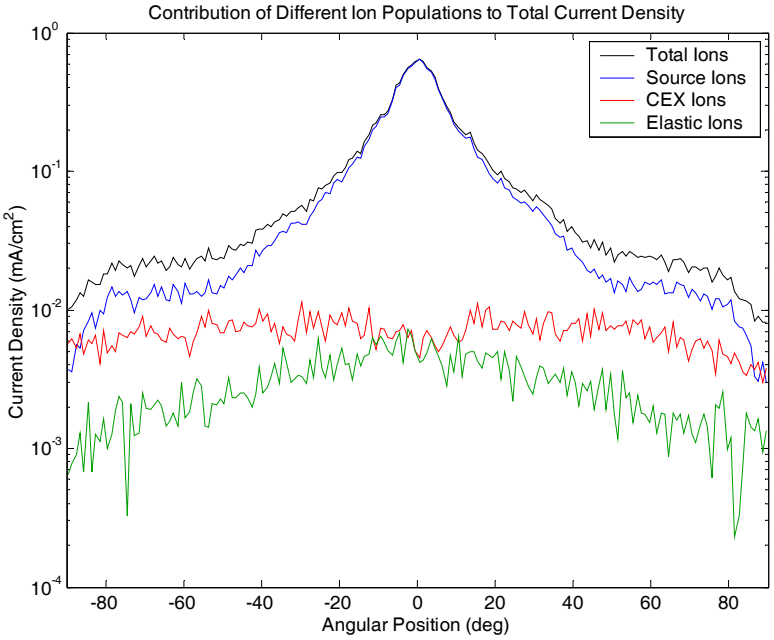

Figure 4.26 Current density distribution of different ion populations obtained with Aquila using source model A. V_d = 300V, $\dot{m}_a$ = 2.44mg/s, P = 2.35×10^{-5} Torr and sweep radius = 1m.

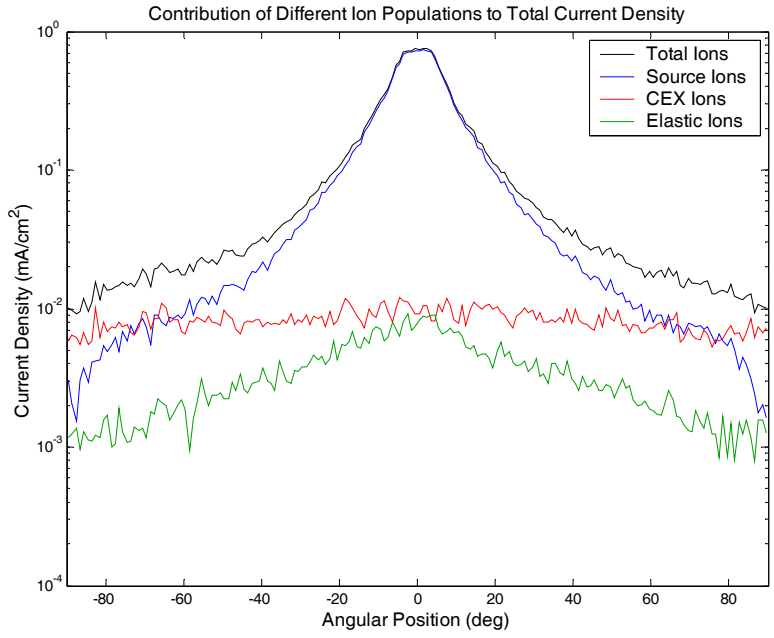

Figure 4.27 Current density distribution of different ion populations obtained with Aquila using source model B. V_d = 300V, $\dot{m}_a$ = 2.44mg/s, P = 2.35×10^{-5} Torr and sweep radius = 1m.

4.5.3 Comparison of New Source Model to Experimental Data

Aquila current density results at background pressures of 0 Torr and 2.35×10^{-5} Torr are compared to extrapolated current density to zero pressure and measured current density at 2.35×10^{-5} Torr respectively. The beam current calculated with Aquila's current density is smaller than the beam current calculated with the measured current density. At each background pressure, Aquila's current density is multiplied by a scaling factor so that the beam current obtained with Aquila's current density matches the experimental beam current. The experimental data are compared to simulated current density obtained from both source models A and B.

Figures 4.28-4.29 show a comparison between experimental data and scaled simulated current density obtained from source model A at background pressures of 2.35×10^{-5} Torr and 0 Torr respectively. The scaled simulated current density matches experimental current density at a background pressure of 2.35×10^{-5} Torr. However, there is relatively poor agreement between simulation and experimental data for perfect vacuum conditions.

Figures 4.30-4.31 show a comparison between experimental data and scaled simulated current density obtained from source model B at background pressures of 2.35×10^{-5} Torr and 0 Torr respectively. There is relatively poor agreement between simulation and experimental data at a background pressure of 2.35×10^{-5} Torr. On the other hand, the scaled simulated current density at 0 Torr matches the extrapolated current density for zero pressure.

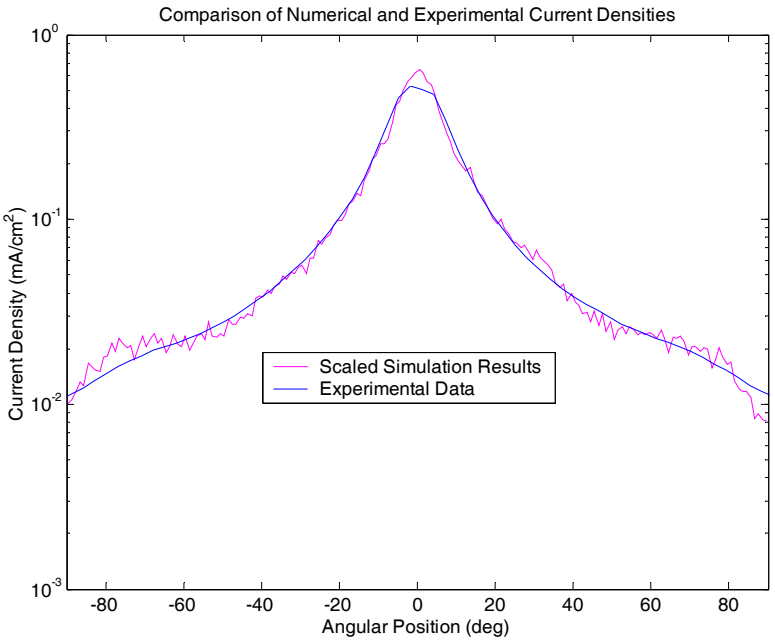

Figure 4.28 Simulated current density obtained with Aquila using source model A compared to experimental data. V_d = 300V, $\dot{m}_a$ = 2.44mg/s, P = 2.35×10^{-5} Torr and sweep radius = 1m.

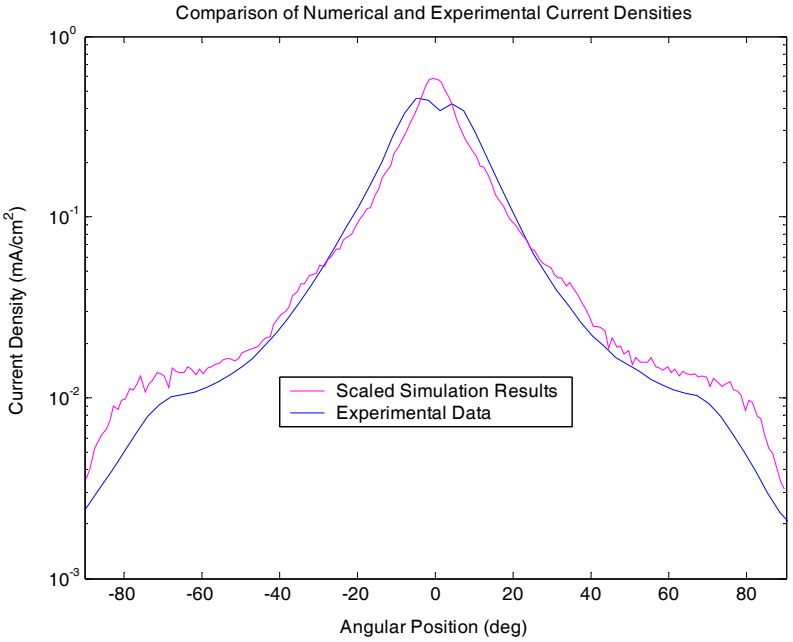

Figure 4.29 Simulated current density obtained with Aquila using source model A compared to experimental data. V_d = 300V, $\dot{m}_a$ = 2.44mg/s, P = 0 Torr and sweep radius = 1m.

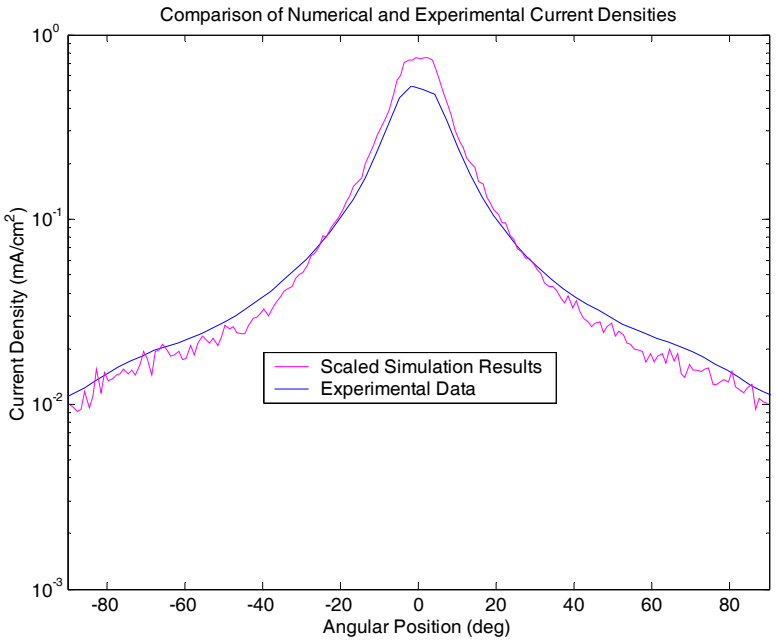

Figure 4.30 Simulated current density obtained with Aquila using source model B compared to experimental data. V_d = 300V, $\dot{m}_a$ = 2.44mg/s, P = 2.35×10^{-5} Torr and sweep radius = 1m.

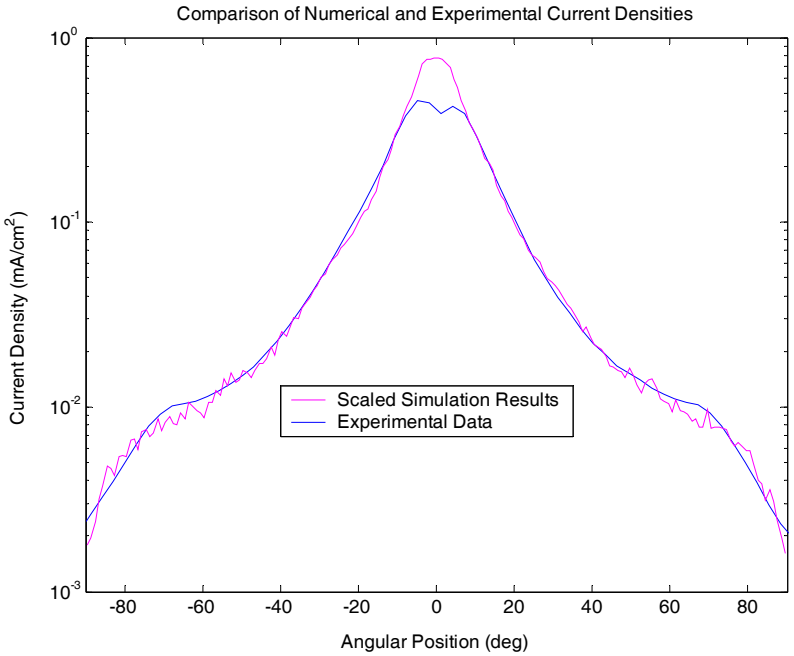

Figure 4.31 Simulated current density obtained with Aquila using source model B compared to experimental data. V_d = 300V, $\dot{m}_a$ = 2.44mg/s, P = 0 Torr and sweep radius = 1m.

Ideally, for one source model, the simulated and measured current density should agree at all background pressures. However, these results imply that simulated and measured current density agree at different pressures only if the source model changes with pressure. The difference in source models stems from the different anomalous Hall parameter profiles. In principal, this might indicate that anomalous transport is a function of background pressure. Anomalous transport might change with background pressure because background neutrals enhance electron mobility towards the anode. It should be noted that when the source models were originally generated, the engine code did not include a model for background pressure. A model for background pressure was subsequently included in the engine code so that a source model could be generated for the same background pressure used in Aquila. For example, to model plume expansion with Aquila at a background pressure of 2.35×10^{-5} Torr, the source model is generated with the engine code that includes a background neutral density corresponding to a pressure of 2.35×10^{-5} Torr. A comparison of source models generated with and without a background pressure model in the engine code showed no effect of background pressure on the source models. This result likely means that anomalous transport does not change with background pressure, which implies that only one source model should be used to match current density at all background pressures.

The reason simulation and experimental data do not match at all pressures for one source model is probably due to deficiencies in Aquila's collision model. In Chapter 5, an analytical model is used to estimate the current density from source ion collisions with tank neutrals. Results of the analytical model show that Aquila underpredicts current density from source ion collision with tank neutrals.

The good agreement between plume simulation and experimental results for source model A at 2.35×10^{-5} Torr could also be a coincidence. The engine code may have overpredicted the ion flux. This led to simulated current density at 0 Torr to be larger than the current density extrapolated to zero pressure. At 2.35×10^{-5} Torr, the overpredicted flux coupled

with deficiencies in Aquila's collision model led to the coincidental match of simulation and experimental data.

For source model B, the ion flux is probably accurately modeled, which leads to a good match between simulation and experimental data at 0 Torr. At 2.35×10^{-5} Torr, because of deficiencies in the collision model, ions in the middle of the plume do not undergo enough collisions that would reduce current density in the mid-angle region and increase it at large angles.

To illustrate that Aquila's collision model is the source of the discrepancy between simulation and experimental data at 2.35×10^{-5} Torr for source model B, the cross-section of charge exchange and elastic scattering ion-neutral collisions is doubled. Figures 4.32 and 4.33 show a comparison between simulation and experimental data at 2.35×10^{-5} Torr and 0 Torr respectively for source model B with the collision cross-section doubled.

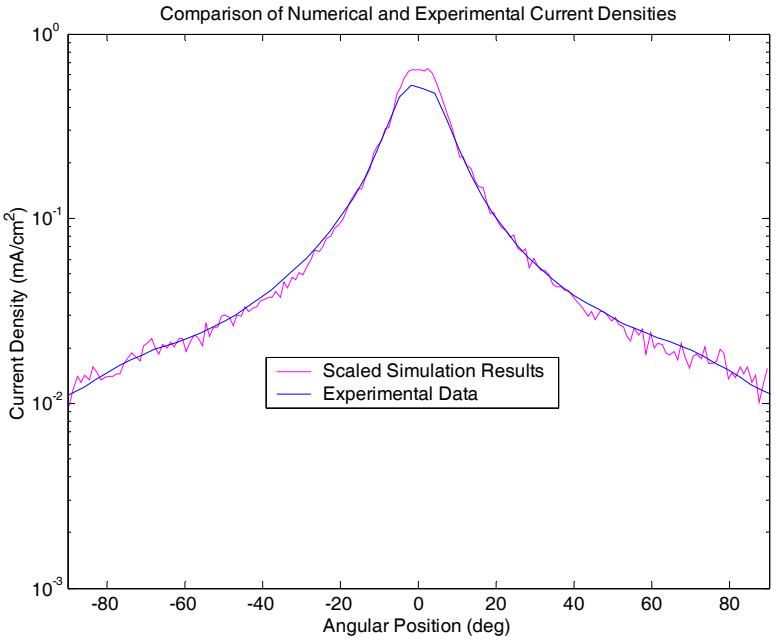

Figure 4.32 Simulated current density obtained with Aquila using source model B compared to experimental data. V_d = 300V, $\dot{m}_a$ = 2.44mg/s, P = 2.35×10^{-5} Torr and sweep radius = 1m. The cross-section of charge exchange and elastic scattering ion-neutral collisions is doubled compared to the case in Figure 4.30.

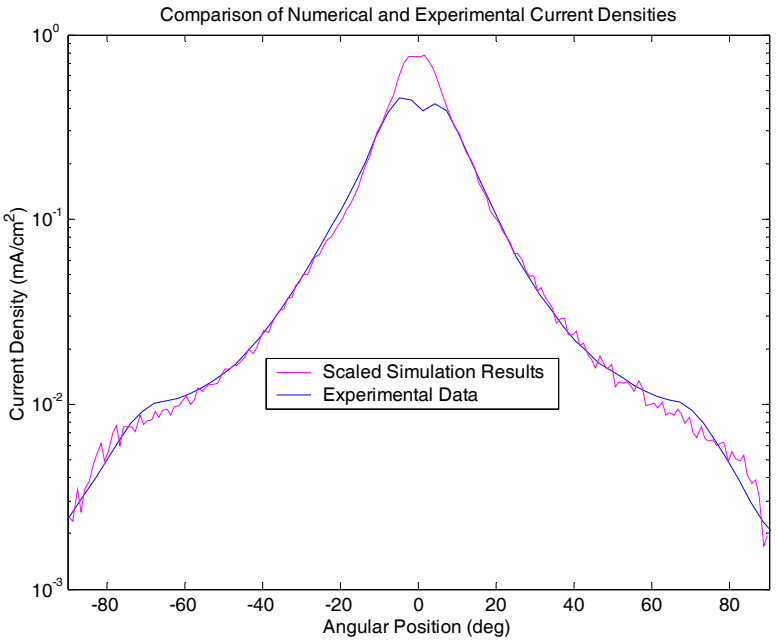

Figure 4.33 Simulated current density obtained with Aquila using source model B compared to experimental data. V_d = 300V, $\dot{m}_a$ = 2.44mg/s, P = 0 Torr and sweep radius = 1m. The cross-section of charge exchange and elastic scattering ion-neutral collisions is doubled compared to the case in Figure 4.31.

As shown in Figures 4.32 and 4.33, there is good agreement between simulation and experimental data at both pressures. The agreement at 2.35×10^{-5} Torr in Figure 4.32 between simulation and experimental data, however, does not indicate that the collision cross-section should be doubled in the simulation. This figure merely relates that the statistics of collisions in the numerical plume simulation may be inadequate. There are likely statistical issues in the collision model that do not account for all collisions. At 0 Torr, doubling the collision cross-section does not have any significant effect on the simulated current density. This is consistent because at 0 Torr the plume is nearly collisionless.

4.5.4 Discussion

Two statements can be deduced from the comparison between Aquila's new source model results and experimental data:

1. Aquila's collision model may have deficiencies that lead to a smaller than expected current density from source ion collisions with tank neutrals.
2. The full PIC engine code generates a good source model when the anomalous Hall parameter is uniform in the entire simulation region (source model B).

The second statement infers that the full PIC engine code should be trusted only for a uniform anomalous Hall parameter (Case B). However, thruster performance is better predicted with an anomalous Hall parameter profile that consists of a barrier imposed inside the entire length of the channel (Case A), as shown in Table 4.1. On the one hand, one Bohm condition produces good thruster exit plane conditions and poor thruster performance, whereas another Bohm condition produces the exact opposite effect. This presents a dilemma concerning which Bohm condition to trust. Unfortunately, this can only be answered with an accurate anomalous transport model. The anomalous transport in Hall thrusters is still not well understood and is the subject of many studies. Fox is in the process of implementing a semi-empirical Quench model where plasma shear effects reduce anomalous transport in the ionization layer [57]. The Quench model should serve as a better substitute to the crude implementation of Bohm layers inside the thruster discharge channel.

Internal probe measurements can also serve to help answer which Bohm condition should be used with the full PIC. For example, measurements such as electron temperature and plasma potential inside the thruster channel should be compared against the simulation to determine if the simulation physics are properly modeled. Comparing thrust and discharge current obtained with the simulation and the experiment is insufficient to conclude that the engine code is accurate.

Chapter 5

ANALYTICAL PLUME MODELS

This chapter contains analytical estimates for current density due to source ion collisions with tank and engine neutrals. This includes estimates for both charge exchange and elastic scattering current densities. The total contribution of ion-neutral collisions is compared to experimental and numerical results. Finally, a self-similar solution of current density is compared to extrapolated current density to zero pressure to determine the model's validity.

5.1 Analytical Estimate of Current Density from Source Ion Collisions with Tank Neutrals

In this section, a simple model is used to estimate the current density from source ion collisions with tank neutrals for a Hall thruster plume expanding inside a vacuum tank [58]. The current resulting from ion-neutral collisions is determined by

$$I_{in} = \int_0^L eR_{in}A(x)dx \tag{5.1}$$

where L is the length of the vacuum tank and A is the cross-sectional area of the plume. R_{in} is the rate of ion-neutral collisions per unit volume and is given by

$$R_{in} = n_n n_i v_i \sigma_{in} \tag{5.2}$$

where σ_{in} is the ion-neutral collision cross-section. Substituting Equation 5.2 into Equation 5.1, the current is expressed as

$$I_{in} = \int_0^L e n_n n_i v_i \sigma_{in} A(x) dx \tag{5.3}$$

The beam current, I_b, is calculated by

$$I_b = e n_i v_i A \tag{5.4}$$

Therefore, Equation 5.3 can be rewritten as

$$I_{in} = \int_0^L n_n \sigma_{in} I_b dx \tag{5.5}$$

Figure 5.1 is a schematic of the plume showing geometrical parameters used in the analytical model of current density from source ion collisions with tank neutrals. For approximation, we assume in this analysis that the beam is a line at $\theta = 0$. After collisions, the emission of ions is evenly distributed along the beam of the plume.

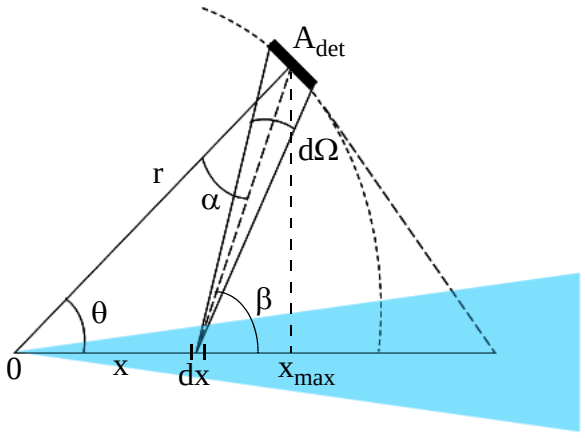

Figure 5.1 Schematic of a Hall thruster plume showing geometrical parameters used in the analytical model of current density from source ion collisions with tank neutrals.

The emission from an element dx at x, which is received at the detector is

$$A_{det} d(j_{in}) = I_b \sigma_{in} n_n dx g(\beta) d\Omega \tag{5.6}$$

where g(β) is the fraction emitted into a unit solid angle, $d\Omega$. For example, if emission is fully isotropic, then g(β) is 1/4π. g(β) must satisfy

$$\int_0^{\pi} g(\beta) 2\pi \sin\beta d\beta = 1 \tag{5.7}$$

where β is

$$\beta = \theta + \alpha \tag{5.8}$$

The solid angle $d\Omega$ can be expressed as

$$d\Omega = \frac{A_{det} \cos\alpha}{r^2} \frac{\sin^2(\theta + \alpha)}{\sin^2\theta} \tag{5.9}$$

Substituting Equation 5.9 into Equation 5.6, cancelling A_{det}, and integrating the expression, we obtain

$$j_{in} = \frac{I_b \sigma_{in} n_n}{r^2 \sin^2\theta} \int_0^{x_{max}} g(\theta + \alpha) \cos\alpha \sin^2(\theta + \alpha) dx \tag{5.10}$$

The choice of x_{max} shown in Figure 5.1 is due to the fact that emission is assumed to be only forward. To solve Equation 5.10, we first need to relate x and α. The general relationship between x and α follows from

$$\frac{r}{\sin(\theta + \alpha)} = \frac{x}{\sin\alpha} \tag{5.11}$$

Therefore, the differential element, dx, can be expressed in terms of α by

$$dx = r\frac{\sin\theta}{\sin^2(\theta+\alpha)}d\alpha \tag{5.12}$$

Substituting Equation 5.12 into Equation 5.10, the current density from ion-neutral collisions is determined by

$$j_{in} = \frac{I_b\sigma_{in}n_n}{r\sin\theta}\int_0^{\left(\frac{\pi}{2}-\theta\right)} g(\theta+\alpha)\cos\alpha\, d\alpha \tag{5.13}$$

where g depends on the type of ion-neutral collisions. Since source ions can undergo either charge exchange or elastic collisions with neutrals, the current density from ion-neutral collisions can be either charge exchange current density or elastic scattering current density.

5.1.1 Charge Exchange Current Density

Based on Figures 4.26 and 4.27, the charge exchange current density is approximately constant for angles between –90° and 90°. Assuming a charge exchange distribution where emission is isotropic in the plane perpendicular to collisions, g can be written as

$$g(\beta) = \begin{cases} g_o\delta\left(\beta-\frac{\pi}{2}\right) & \beta \le \frac{\pi}{2} \\ 0 & \beta > \frac{\pi}{2} \end{cases} \tag{5.14}$$

Substituting Equation 5.14 into Equation 5.7, we obtain

$$g_o = \frac{1}{2\pi} \tag{5.15}$$

Using Equations 5.13-5.15, the charge exchange current density is

$$j_{cex} = \frac{I_b \sigma_{cex} n_n}{2\pi r \sin\theta} \int_0^{\left(\frac{\pi}{2}-\theta\right)} \delta\left(\beta - \frac{\pi}{2}\right) \cos\alpha \, d\alpha \tag{5.16}$$

Performing the integral, Equation 5.16 simplifies to

$$j_{cex} = \frac{I_b \sigma_{cex} n_n}{2\pi r \sin\theta} \cos\left(\frac{\pi}{2} - \theta\right) \tag{5.17}$$

The final expression for charge exchange current density from source ion collisions with tank neutrals is

$$j_{cex} = \frac{I_b \sigma_{cex} n_n}{2\pi r} \tag{5.18}$$

Note that the expression of charge exchange current density is independent of angle, which is similar to what is observed in numerical results shown in Figures 4.26 and 4.27.

5.1.2 Elastic Scattering Current Density

Assuming hard sphere collisions of source ions with stationary neutrals, the distribution of scattering collisions in the laboratory frame of reference is [59]

$$g(\beta) = \begin{cases} \frac{\cos\beta}{\pi} & \beta \le \frac{\pi}{2} \\ 0 & \beta > \frac{\pi}{2} \end{cases} \tag{5.19}$$

Substituting Equation 5.19 into Equation 5.13, the current density from ion-neutral elastic scattering is

$$j_{sc} = \frac{I_b \sigma_{sc} n_n}{\pi r \sin\theta} \int_0^{\left(\frac{\pi}{2}-\theta\right)} \cos(\theta + \alpha) \cos\alpha \, d\alpha \tag{5.20}$$

Since hard sphere collisions are assumed, $\sigma_{sc} = \pi D^2$, where D is the molecular diameter of xenon. Performing the integral in Equation 5.20, the final expression is

$$j_{sc} = \frac{I_b D^2 n_n}{2r}\left(\frac{\pi}{2} - \theta\right)\cot\theta \tag{5.21}$$

5.1.3 Comparison to Experimental and Numerical Results

The charge exchange current density obtained in Equation 5.18 is added to the elastic scattering current density obtained in Equation 5.21 to determine the total current density from source ion collisions with tank neutrals. Results of the analytical model are compared to experimental and numerical results at r = 1m.

For the BHT-1500 operating at V_d = 300V and $\dot{m}_a$ = 2.44mg/s, the beam current, I_b, is 1.64A. This is determined using source ion current density obtained with RPA measurements, as shown in Figure 3.34. The charge exchange collision cross-section, σ_{cex}, is approximately 5.4×10^{-19} m^2 [47] and the molecular diameter of xenon at room temperature, D, is approximately 3.42×10^{-8} cm [16, 64].

Comparison to Experimental Results

Experimentally, the current density from source ion collisions with tank neutrals at a particular tank pressure is determined by subtracting the extrapolated current density to zero pressure from the current density measurements at the pressure of interest. Figure 5.2 shows a comparison between the analytical model and experimental data at background pressures of 6.58×10^{-6} Torr, 8.51×10^{-6} Torr, 1.04×10^{-5} Torr, 1.55×10^{-5} Torr, and 2.02×10^{-5} Torr. The analytical calculation is performed for angles between –90° and –60° because they represent the angles where the effect of tank neutrals on the current density distribution is most visible.

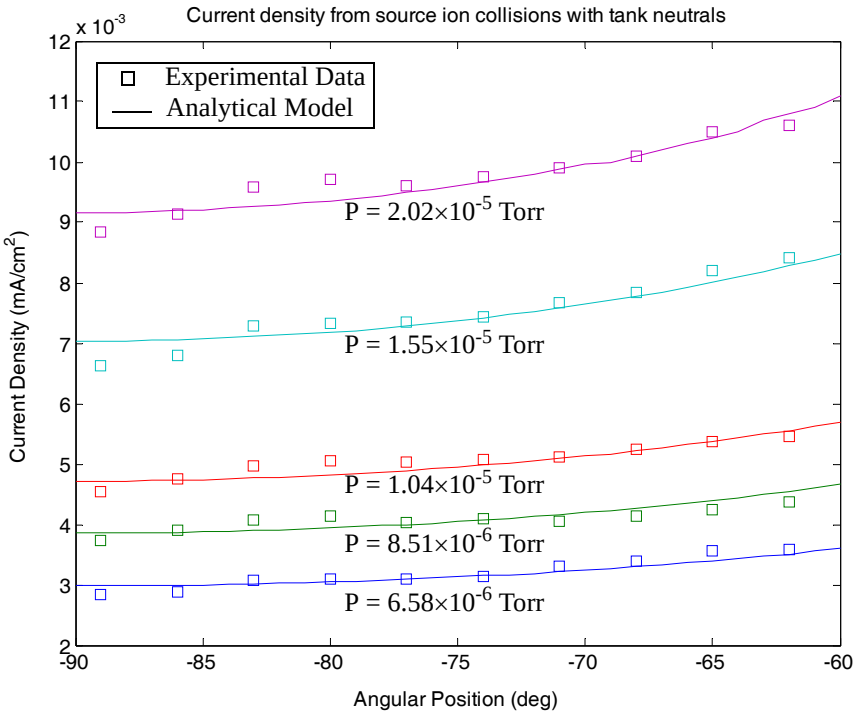

Figure 5.2 Comparison of current density from source ion collisions with tank neutrals obtained from both analytical model and experimental data. In the plot, the experimental data are represented by squares and the analytical model is represented by solid lines. The comparison between experimental data and the analytical model is performed at different background pressures. A set of squares and a line plotted using the same color represent a comparison performed at the same background pressure.

Figure 5.2 shows that the analytical model matches experimental results. The analytical model can then be used to predict the in-orbit current density without need for pressure variation. However, it should be noted that the expression can only be used for angles between 90° and 60° where charge exchange and elastically scattered ions dominate. Subtracting the analytical estimate from the measured current density in the 90-60° region provides the in-orbit current density at the wings. In the region between centerline and 60°, either methods A or B described in Chapter 3 can be used to obtain the in-orbit current density since they produce comparable results to the extrapolation method in that region as shown by Figure 3.35. Therefore, the in-orbit current density for all angles is determined. However, the author believes that the extrapolation method should always be used to determine the in-orbit current density since it is more robust. The method

described in this section should be used in the event measurements of current density are only available at one background pressure.

Comparison to Numerical Results

The analytical model is also compared to numerical simulation results obtained with Aquila using source models A and B. The simulated current density from source ion collisions with tank neutrals at a particular tank pressure is determined by subtracting the simulated current density at zero pressure from the simulated current density at the background pressure of interest. Figure 5.3 shows a comparison of analytical and numerical model predictions at a background pressure of 2.35×10^{-5} Torr.

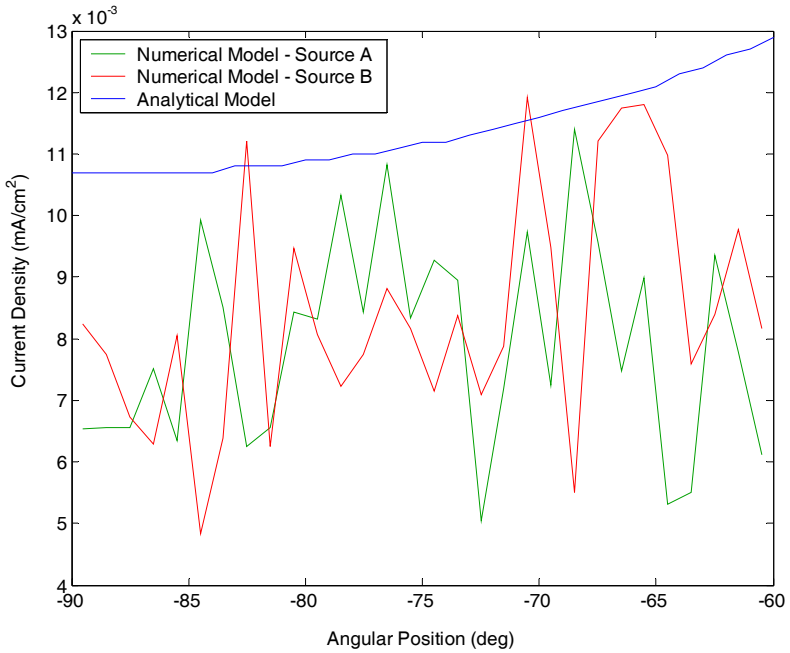

Figure 5.3 Comparison of current density from source ion collisions with tank neutrals obtained from analytical and numerical models. The results of the numerical model are produced with Aquila using source models A and B. The comparison is performed at a background pressure of 2.35×10^{-5} Torr.

Figure 5.3 shows that the numerical results with Aquila using source models A and B underpredict the current density from source ion collisions with tank neutrals. This com-

parison indicates deficiencies in modeling the high angle region where collisions of source ions with tank neutrals greatly affect the current density distribution. The deficiency is likely due to inadequacies in Aquila's collision model, as discussed in Chapter 4. From the "spikiness" of the numerical results, the likely problem is an insufficient number of "numerical collisions", somehow biasing the statistics down.

5.2 Analytical Estimate of Current Density from Source Ion Collisions with Engine Neutrals

Since the utilization efficiency of a Hall thruster never reaches 100%, a fraction of the propellant is ejected as neutrals and can undergo collisions with source ions. Similarly to the analysis performed for collisions with tank neutrals, the current resulting from ion and engine neutral collisions is determined by Equation 5.5. The expression in Equation 5.5 applies for both charge exchange and elastic scattering. Since ion-neutral collisions are relatively rare events in the plume, the beam current remains independent of *x*. In addition, the collision cross-section is a function of ion energy, which is assumed to remain constant in the plume region. Therefore, Equation 5.5 can rewritten as

$$I_{in} = \sigma_{in} I_b \int_0^L n_n dx \tag{5.22}$$

To solve Equation 5.22, the expression of engine neutral density as function of *x* is first determined. The formulation of engine neutral density is done using a crude model that needs further refinement. However, as shown later, the model performs relatively well when compared to the experimental results. The rate of neutral ejection by the thruster is determined by

$$\dot{m}_n = (1 - \eta_u)\dot{m}_a \tag{5.23}$$

From continuity, the anode flow rate, $\dot{m}_a$, is

$$\dot{m}_a = m_i c_n A n_n \tag{5.24}$$

where is c_n is thermal speed of neutrals defined by

$$c_n = \sqrt{\frac{5}{3}\frac{kT_w}{m_n}} \tag{5.25}$$

The ionized portion of the flow is

$$\dot{m}_i = \eta_u \dot{m}_a = \frac{m_i}{e} I_b \tag{5.26}$$

Using Equations 5.23-5.26, the engine neutral density can be written as

$$n_n(x) = \frac{1-\eta_u}{\eta_u} \frac{I_b}{ec_n A(x)} \tag{5.27}$$

Figure 5.4 is a schematic of a Hall thruster showing geometrical parameters used in this analysis.

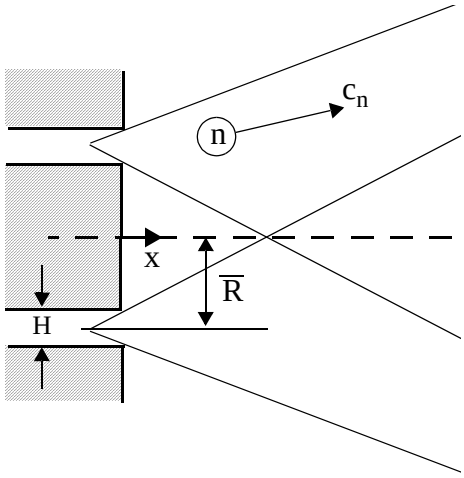

Figure 5.4 Schematic of a Hall thruster cross-section defining geometrical parameters that are used in the analytical estimation of current density from source ion collision with engine neutrals.

At the thruster exit plane ($x = 0$), the plume cross-sectional area is

$$A(0) = 2\pi\bar{R}H \tag{5.28}$$

where is $\overline{R}$ and H are the mid-channel radius and height of the thruster's discharge channel respectively. Downstream the thruster exit, $A(x)$ increases quadratically with x. Assuming the jet expands from a virtual origin at $x = -H$, $A(x)$ can be expressed by

$$A(x) = A(0)\left(1 + \frac{x}{H}\right)^2 \tag{5.29}$$

Therefore, we can rewrite the engine neutral density as

$$n_n \approx \frac{1-\eta_u}{\eta_u}\frac{1}{2\pi\bar{R}Hec_n}\frac{I_b}{\left(1+\frac{x}{H}\right)^2} \tag{5.30}$$

When Equation 5.30 is substituted in Equation 5.22, L is set to ∞. This is a reasonable assumption because the majority of source ion collisions with engine neutrals occur near the engine. Therefore, the current produced from source ion collisions with engine neutrals is expressed by

$$I_{in} \approx \frac{1-\eta_u}{\eta_u}\frac{I_b^2\sigma_{in}}{2\pi\bar{R}ec_n} \tag{5.31}$$

Assuming the resulting ions after collisions issue uniformly from a small region into the forward hemisphere, the current density at a distance r is given by

$$j_{in} = \frac{I_{in}}{2\pi r^2} \tag{5.32}$$

Substituting Equation 5.31 into Equation 5.32, the expression for current density due to source ion collisions with engine neutrals is

$$j_{in} = \frac{1-\eta_u}{\eta_u}\left(\frac{I_b}{2\pi r}\right)^2 \frac{\sigma_{in}}{\overline{R}ec_n} \tag{5.33}$$

As discussed earlier, collisions of source ions with neutrals can result in either charge exchange or elastically scattered ions. Therefore, Equation 5.33 can be written for both type of collisions. The charge exchange current density from engine neutrals is

$$j_{cex} = \frac{1-\eta_u}{\eta_u}\left(\frac{I_b}{2\pi r}\right)^2 \frac{\sigma_{cex}}{\overline{R}ec_n} \tag{5.34}$$

The elastic scattering current density is

$$j_{sc} = \frac{1-\eta_u}{\eta_u}\left(\frac{I_b}{2\pi r}\right)^2 \frac{\sigma_{sc}}{\overline{R}ec_n} \tag{5.35}$$

For the BHT-1500 operating at V_d = 300V and $\dot{m}_a$ = 2.44mg/s, I_b is 1.64A, c_n is 235m/s and η_u is 0.7. The thermal speed of neutrals, c_n, is calculated with Equation 5.25 using a wall temperature of 250°C, which is the measured exit ring temperature at V_d = 300V as shown in Figure A.19 of Appendix A. The utilization efficiency, η_u, is determined from the analysis performed in Section 3.4.1. The mid-channel radius of the thruster, $\overline{R}$, is 41mm. The charge exchange collision cross-section, σ_{cex}, is approximately 5.4×10^{-19} m^2 and the elastic scattering collision cross-section, σ_{sc}, is approximately 4.5×10^{-20} m^2 [16, 46, 47]. Using Equation 5.34, the charge exchange current density at 1m due to collisions with engine neutrals is

$$j_{cex} = 1.02 \times 10^{-3}\, mA/cm^2 \tag{5.36}$$

The elastically scattered current density at 1m due to collisions with engine neutrals is

$$j_{sc} = 8.52 \times 10^{-5}\, mA/cm^2 \tag{5.37}$$

Therefore, the total current at 1 m from collisions with engine neutrals is

$$j = 1.11 \times 10^{-3}\, mA/cm^2 \tag{5.38}$$

Source ion collisions with engine neutrals are dominated by charge exchange collisions, as shown by Equations 5.36 and 5.37. This estimated current density does not account for cathode neutrals. These neutrals should increase the result in Equation 5.38 by approximately 20%.

The extrapolated current density to zero pressure at 300V gives a current density of 1.77×10^{-3} mA/cm^2 at –90°, where RPA measurements show that the plume is composed of only charge exchange ions. Therefore, the zero pressure current density at –90° solely represents charge exchange current density from engine neutrals. This shows that the analytical model is in good agreement with the experimental results.

The simulated zero pressure current density at 300V gives a current density of 3.59×10^{-3} mA/cm^2 and 1.79×10^{-3} mA/cm^2 at –90° for source models A and B respectively. The results of source model B are in agreement with the analytical calculation whereas the results of source model A overpredict the current density at –90°. Based on the results in the previous section, Aquila's collision model is found to underpredict collisions of source ions with neutrals. The fact that the results of source model A show an overprediction of current density at –90° does not mean that Aquila overpredicts collisions of source ions with engine neutrals. Since collisions of source ions with engine neutrals also occur in the engine code, it is likely that the discrepancy in the results of source model A originate in the engine code.

5.3 Self-Similar Plume Model

Self-similar solutions were developed for a plasma jet expanding without collisions from a nozzle into a vacuum by A. Korsun and E. Tverdokhlebova [60]. The solutions were later rederived by M. Martinez-Sanchez [61]. The self-similar model provides analytical solutions to current density. A detailed derivation of the self-similar solutions is described in a previous publication [12]. Experimental results are compared to the model to determine its validity.

The self-similar solution of current density is

$$j = \frac{j_c}{\cos^3\theta\left(1 + \dfrac{\tan^2\theta}{\tan^2\theta_{1/2}}\right)^{1+\gamma/2}} \tag{5.39}$$

where j_c is the current density at the centerline and $\theta_{1/2}$ is the angle at which the plasma density falls to half the centerline value. Rearranging a few terms in Equation 5.39, we obtain

$$\left(\frac{j_c}{j\cos^3\theta}\right)^{2/(2+\gamma)} = \frac{1}{\tan^2\theta_{1/2}}\tan^2\theta + 1 \tag{5.40}$$

It should be noted that the model does not determine the value of $\theta_{1/2}$. Equation 5.40 indicates that a plot of $\left(\dfrac{j_c}{j\cos^3\theta}\right)^{2/(2+\gamma)}$ versus $\tan^2\theta$ yields a straight line whose slope is $\dfrac{1}{\tan^2\theta_{1/2}}$. Therefore, when measured current density data are plotted in the form expressed in Equation 5.40, a linear relationship would validate the model and provide a value for $\theta_{1/2}$.

The self-similar model does not account for collisional effects. Therefore, to validate the model, extrapolated current density data for zero pressure (the in-orbit current density) are the appropriate data to use in Equation 5.40.

Figures 5.5 and 5.6 show extrapolated current density for zero pressure plotted in the form expressed in Equation 5.40 using γ values of 1.3 and 1.67 respectively. A γ value of 1.67 represents an adiabatic expansion of electrons, whereas a γ value of 1.3 is usually the experimental value relating electron temperature and electron density as shown by Equation 4.13. This value falls halfway between an isothermal expansion ($\gamma = 1$) and adiabatic expansion ($\gamma = 1.67$). Figure 5.5 is plotted for angles between 0° and 75° whereas Figure 5.6 is plotted for angles between 0° and 65°. At angles larger than 65°, the plume is composed of mainly charge exchange ions, which are not accounted for in this model. The data are plotted for a discharge voltage of 300V, an anode flow rate of 2.44mg/s and a sweep radius of 1m.

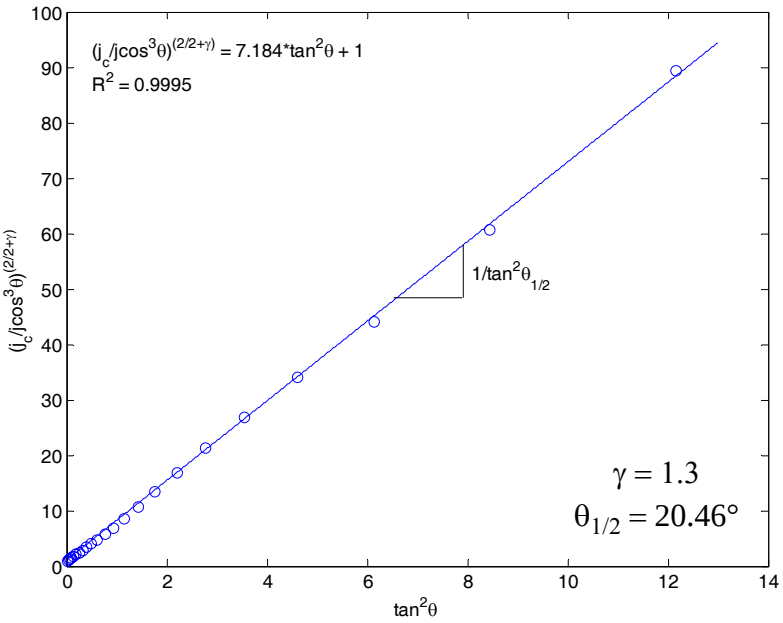

Figure 5.5 Extrapolated current density for zero pressure is plotted in the form expressed in Equation 5.40 using a γ value of 1.3. The small circles represent the data and the line represents the linear fit to the data. V_d = 300V, $\dot{m}_a$ = 2.44mg/s and sweep radius = 1m.

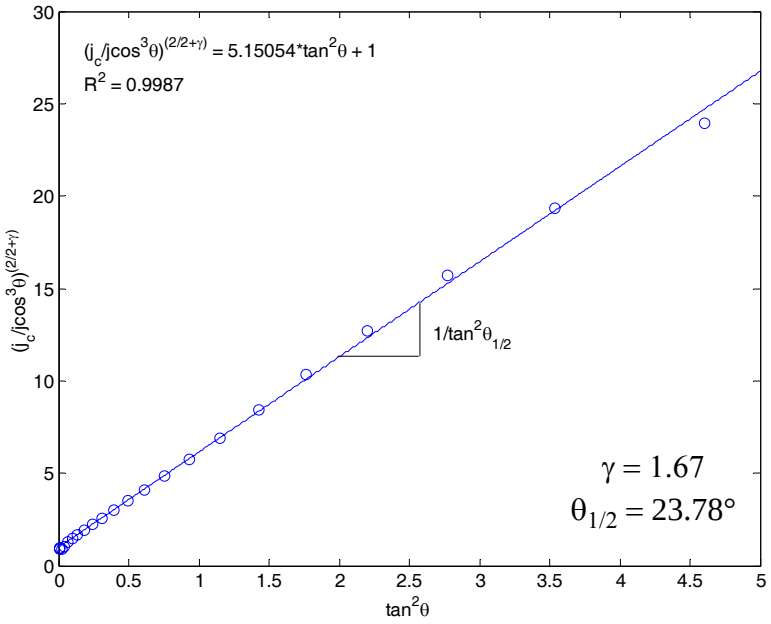

Figure 5.6 Extrapolated current density for zero pressure is plotted in the form expressed in Equation 5.40 using a γ value of 1.67. The small circles represent the data and the line represents the linear fit to the data. V_d = 300V, $\dot{m}_a$ = 2.44mg/s and sweep radius = 1m.

Figures 5.5 and 5.6 show a linear relationship between the plotted parameters, indicating good agreement between measurements and the self-similar plume model. The slope of the linear relationship is $\frac{1}{\tan^2\theta_{1/2}}$. For $\gamma = 1.3$, the slope is 7.184, which corresponds to $\theta_{1/2} = 20.46°$. In the case of $\gamma = 1.67$, the slope is 5.150, which corresponds to $\theta_{1/2} = 23.78°$.

The self-similar model also predicts a solution for the value of current density at the centerline and is given by

$$j_c = \frac{\gamma}{2\pi r^2}\frac{I_b}{\tan^2\theta_{1/2}} \tag{5.41}$$

Substituting $\gamma = 1.3$, $\theta_{1/2} = 20.46°$, $r = 1$m, and $I_b = 1.64$A into Equation 5.41, the self-similar predicted value of current density at the centerline is 0.244mA/cm^2. For $\gamma = 1.67$, $\theta_{1/2} = 23.78°$, the self-similar predicted value of current density at the centerline is 0.224mA/cm^2. The experimental current density for zero pressure at the centerline for the same thruster operating conditions is 0.260mA/cm^2, indicating good agreement with the self-similar plume model solution.

The experimental value of current density at the centerline is used in Equation 5.39 to calculate the self-similar solution of current density for all other angles. Figures 5.7 and 5.8 show a comparison between the extrapolated current density for zero pressure and the self-similar solution of current density for γ values of 1.3 and 1.67 respectively.

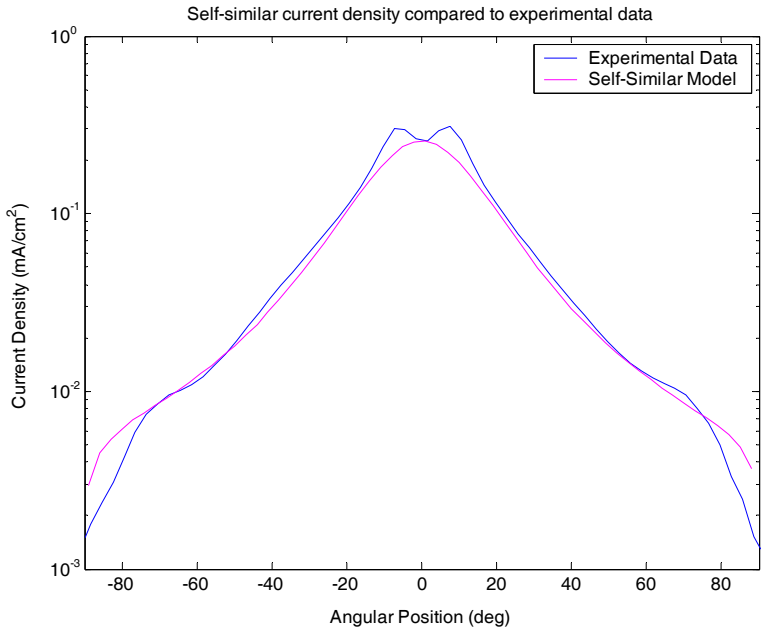

Figure 5.7 Comparison of current density obtained using the self-similar model to extrapolated current density for zero pressure. V_d = 300V, $\dot{m}_a$ = 2.44mg/s, sweep radius = 1m, γ = 1.3 and $\theta_{1/2}$ = 20.46°.

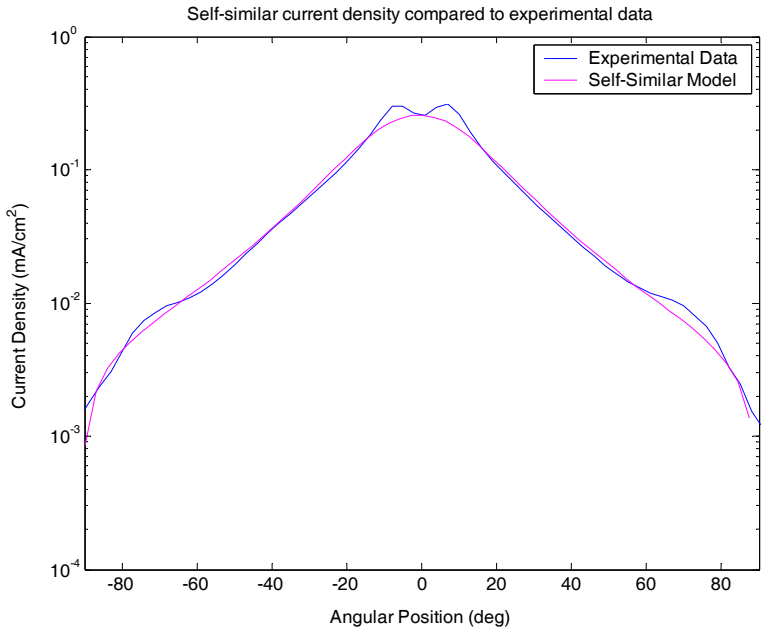

Figure 5.8 Comparison of current density obtained using the self-similar model to extrapolated current density for zero pressure. V_d = 300V, $\dot{m}_a$ = 2.44mg/s, sweep radius = 1m, γ = 1.67 and $\theta_{1/2}$ = 23.78°.

Figures 5.7 and 5.8 show good agreement between the model and the “in-orbit” current density. Therefore, the model can reliably predict the current density profile for “in-orbit” conditions. However, the model cannot be substituted for experimental measurements since it requires the value of $\theta_{1/2}$, which can only be determined experimentally. At angles higher than 70° where collisions dominate the plume, the model does not match experimental data because collisions are ignored in the model. It is interesting that the model predicts shoulders at high angles similarly to experimental data. Since the self-similar plume solution of current density models only source ion expansion, it might be inferred from these results that the shoulders in the measured current density contain mainly source ions. However, RPA measurements show that the shoulders of the current density are dominated by charge exchange ions, which are not included in the self-similar model. The message inferred by the model at high angles is not well understood.

Overall, the self-similar model agrees well with the experimental data at different values of γ. This means that ions are unaffected by the thermal expansion of electrons, which is expected because ions travel in the plume with a hypersonic speed. Since a γ value of 1.67 fits the experimental data better than a γ value of 1.3, it is likely that electrons expand in the plume adiabatically. This is not unreasonable since ionization and excitation of neutrals through electron impact is negligible in the region where the model and experimental data are compared.

Chapter 6

CONCLUSIONS AND RECOMMENDATIONS

Extensive plume measurements were taken on the BHT-1500 with the objective of establishing a method to determine the in-orbit plume divergence from data taken in laboratory conditions. Experimental measurements were also used to cross-calibrate a numerical plume simulation. In addition, analytical plume models were utilized to confirm the experimental findings. This chapter highlights the significant conclusions and contributions of this thesis and provides recommendations for future work.

6.1 Summary of Results and Contributions

6.1.1 Experimental Results

Facility Effects

Current density is measured at different background pressures. An increase in background pressure increases the current density at the wings and centerline. The increase in current density at the wings is due to an increase in production of charge exchange ions. The increase in current density at the centerline is partly due to ionization of background neutrals. It can also be due to an increase in utilization efficiency from enhanced electron mobility towards the anode.

The ion energy distribution is also measured at different background pressures. Experimental measurements show that ions in the plume can be divided into three populations:

source ions, charge exchange ions and intermediate energy ions. The source ions are born at a potential corresponding to the discharge potential. The low energy ions have energies on the order of 20eV. The intermediate energy ions either lost energy through elastic collisions or are born at low potentials. The plume is dominated by charge exchange ions for angles larger than 60°. Since the RPA is collimated, an increase in pressure illustrates that the majority of charge exchange ions measured with the probe are due to collisions with engine neutrals. For angles larger than 40°, the plume is dominated by source ions.

In-Orbit Extrapolation Method

Variation of background pressure leads to a clear technique to obtain the in-orbit current density. The current density is found to increase linearly with background pressure for any given angle. This relationship is used to extrapolate the current density to zero background pressure, the in-orbit condition. An experimental consistency check of the extrapolation method reveals that the method is both reliable and accurate. The in-orbit plume divergence is derived from both the in-orbit current density and the ion energy distribution. The half-angle plume divergence is reported as two angles: the 95% half-angle plume divergence and the 95% half-angle divergence of the source ion population. This is a comprehensive method of reporting the half-angle plume divergence because it provides information about the composition of the plume. When compared to the extrapolation method, conventional methods [48, 49, 50] underpredict current density at the wings because they do not account for charge exchange collisions with engine neutrals.

The experimental measurements obtained in this thesis show that charge exchange ions play a significant role in current density and ion energy distributions, even though only a small fraction of the ion beam undergoes collisions. Therefore, the effects of charge exchange ions should not be ignored. This is especially important for space operation, where charge exchange plasma can backstream to the spacecraft. Using the extrapolation method, all particles that exist in space conditions, including charge exchange ions, are accounted for.

Discharge Voltage Effect

Plume measurements are taken at various discharge voltages. An increase in discharge voltage leads to an increase in utilization efficiency. This translates into an increase in current density at the centerline. In the mid-angle region of the plume, the current density decreases with an increase in discharge voltage. There is no significant effect of discharge voltage on the shoulders of the current density. Overall, an increase in discharge voltage narrows the current density distribution, indicating that plume divergence decreases with an increase in discharge voltage. This is also confirmed through studying the effect of discharge voltage on the ion energy distribution. The decrease in plume divergence with discharge voltage indicates that the dependence of electron temperature on discharge voltage is less than proportional. This conclusion is supported by a power balance analysis performed by Warner [53].

Magnetic Field Effect

Experimental characterization of the BHT-1500 shows that the thruster can be operated in two modes depending on the magnetic field setting, as discussed in Appendix A. The modes are referred to as the jet and collimated modes. Plume measurements show that the two modes have drastically different current density and ion energy distributions. Thruster performance is higher in the jet mode, however, plume measurements indicate that source ions have a smaller divergence in the collimated mode. Temperature measurements show that the thruster walls are hotter in the collimated mode, indicating higher wall losses, which can result in higher erosion.

6.1.2 Numerical Results

Numerical results are obtained with Aquila using two different methods of generating a source model. The new source model utilizes velocity distributions generated by the 2D3V full PIC engine code, whereas the previous source model uses Maxwellian distributions constructed from average properties of the velocity distributions. Comparison of Aquila's results obtained with the two source models illustrates that plume simulation results are sensitive to the input parameters of the source model.

Results generated using the previous source model underpredict the current density at the wings because the input parameters of this source model inadvertently ignore low energy ions. On the other hand, results generated using the new source model are comparable to the experimental measurements. Therefore, velocity distributions generated by the 2D3V full PIC engine code should be used instead of average velocities to produce a source model.

In addition, using velocity distributions from the 2D3V full PIC engine code, source models A and B were generated by modifying the anomalous electron transport. Source model A is obtained by imposing a barrier layer along the entire length of the exit rings with an anomalous Hall parameter value of 400. Source model B is obtained using a uniform anomalous Hall parameter value of 200 in the entire simulation domain. At zero background pressure, Aquila's results, generated using source model B, exhibit good agreement when compared to extrapolated current density to zero pressure. At the uniform anomalous Hall parameter condition, the full PIC engine code predicts poor thruster performance. However, there is experimental evidence that points to the existence of a low anomalous transport layer in the discharge channel [62]. Therefore, in theory, the extrapolated current density should be in agreement with Aquila's results obtained with source model A, which is not the case. Thus, it is difficult to draw a conclusion based on these results, and more work on anomalous diffusion should be performed in order to identify the source of the discrepancy.

At a non-zero background pressure, Aquila underpredicts collisions of source ions with tank neutrals. This finding is confirmed using analytical models, discussed in Chapter 5. However, this deficiency in Aquila's collision model would not explain the discrepancy at zero pressure discussed earlier because collisions are almost negligible at this pressure.

6.1.3 Analytical Results

Analytical expressions derived for charge exchange and elastic scattering current density from source ion collisions with background and engine neutrals are consistent with experimental data. Therefore, if current density measurements are obtained at one background pressure, we can use the analytical expressions to derive the in-orbit current density. In the 90°-60° region, the in-orbit current density at the wings can be obtained by subtracting the estimate of current density from source ion collisions with tank neutrals from the measured current density. In the region between the centerline and 60°, we can use either methods A or B described in Chapter 3 to obtain the in-orbit current density since they are comparable to the extrapolation method in that region as shown by Figure 3.35. By "stitching" current densities in the regions of 90°-60° and 60°-0°, we obtain the current density at all angles.

In addition, a self-similar solution of current density is compared to extrapolated current density to zero pressure and exhibits good agreement, thereby validating the self-similar model of current density. However, the model cannot be substituted for experimental measurements since it requires the value of $\theta_{1/2}$, which can only be determined experimentally. Results of the comparison also indicate that electrons expand in the plume adiabatically, which is not unreasonable since ionization and excitation of neutrals through electron impact is negligible in the region where the model and experimental data are compared.

6.2 Recommendations

6.2.1 Experimental Work

The purpose of the extrapolation method is to provide the electric propulsion community with an objective approach to calculate the in-orbit current density. This method should eliminate the variation of data across different facilities. It would be interesting to test the same thruster in different facilities and obtain the in-orbit current density using the extrapolation method. The in-orbit current density should remain the same regardless of the facility.

There are several topics of interest in the Hall thruster community. For example, miniaturization of Hall thrusters is an active area of research [53]. It is thought that smaller thrusters have higher plume divergence. Therefore, it is recommended to investigate the effect of Hall thruster scaling on plume divergence. Another topic that is actively discussed concerns thruster lifetime [63]. Erosion of the thruster exit rings is the main life limiting factor of Hall thrusters. A trade-off may exist between exit ring material and plume divergence. Therefore, as thrusters are equipped with materials that have low sputtering yield to increase lifetime, it is recommended to study the effect of the exit ring material on plume divergence.

One of the observations made in this thesis is that plume divergence decreases with an increase in discharge voltage since electron temperature does not increase proportionally with discharge voltage. This may be due to secondary electron emission by the walls of the exit rings, which has a “cooling” effect on the bulk electron temperature. Thrusters equipped with metallic walls have a negligible secondary electron emission and therefore there is no cooling effect. In these type of thrusters, the electron temperature might increase proportionally with discharge voltage thereby increasing plume divergence with voltage. Thus, it would be of interest to measure the plume divergence for thrusters with ceramic and metallic walls and determine the trends of plume divergence as a function of discharge voltage.

6.2.2 Numerical Work

The continued development of an accurate plume simulation is very important for modeling the interaction of the thruster plume with the host spacecraft. However, in order to trust the plume simulation, it needs to accurately predict plasma plume parameters such as current density and ion energy distribution. Aquila produces reasonable results to current density, but there are still a few issues that need to be examined. For example, the discrepancy of the collision model needs to be investigated and resolved.

In addition, ion energy measurements were not obtained with Aquila. A simulated retarding potential analyzer needs to be incorporated into Aquila to obtain these measurements. For accurate comparison with the experimental ion energy distribution, the simulated retarding potential analyzer must have an identical collimation angle as the laboratory retarding potential analyzer. Comparison of ion energy measurements should provide more insight on the accuracy of Aquila in modeling plume expansion.

As discussed in Chapter 4, Aquila allows particles to be injected from only one planar surface. Therefore, velocity distributions that were generated for particles crossing the cylindrical sampling section were projected onto the radial plane. It is recommended that Aquila is modified to accept velocity distributions from more than one surface. In addition, the simulation should allow these surfaces to be non-planar.

Furthermore, Aquila relies on input parameters from the engine code. Therefore, it is important that the engine code is also modeled properly. As discussed earlier, the anomalous electron transport is not well understood. Current efforts include using a semi-empirical Quench model where plasma shear effects reduce anomalous transport in the ionization layer [57].

Finally, the plume simulation ignores near-field effects such as the magnetic field. These effects should be included in the plume simulation. It may be that we should eliminate the source model altogether (eliminate the link between engine code and plume code) and

write an end-to-end model, which consists of one code modeling both the thruster discharge and the plume.

REFERENCES

[1] Goebel, D., M. Martinez-Lavin, T. Bond, and A. King, "Performance of XIPS Electric Propulsion in On-orbit Station Keeping of the Boeing 702 Spacecraft," AIAA-2002-4348, 38th AIAA/ASME/SAE/ASEE Joint Propulsion Conference and Exhibit, Indianapolis, IN, July 7-10, 2002.

[2] Pidgeon, D., R. Corey, B. Sauer, and M. Day, "Two Years On-Orbit Performance of SPT-100 Electric Propulsion," AIAA-2006-5353, 24th AIAA International Communications Satellite Systems Conference, San Diego, CA, June 11-14, 2006.

[3] de Grys, K., C. Rayburn, F. Wilson, J. Fisher, L. Werthman, and V. Khayms, "BPT-4000 Multi-Mode 4.5 KW Hall Thruster Qualification Status," AIAA-2003-4552, 42nd AIAA/ASME/SAE/ASEE Joint Propulsion Conference and Exhibit, Sacramento, CA, July 9-12, 2006.

[4] Polk, E. J., R. Kakuda, J. Anderson, J. Brophy, V. Rawlin, M. Patterson, J. Sovey, and J. Hamley, "Performance of the NSTAR ion propulsion system on the Deep Space One mission," AIAA-2001-965, 39th Aerospace Sciences Meeting and Exhibit, Reno, NV, January 8-11, 2001.

[5] Brophy, J., M. Marcucci, J. Gates, C. Garner, B. Nakazono, and G. Ganapathi, "Status of the Dawn Ion Propulsion System," AIAA-2004-3433, 40th AIAA/ASME/SAE/ASEE Joint Propulsion Conference and Exhibit, Fort Lauderdale, FL, July 11-14, 2004.

[6] Milligan, D., O. Camino, and D. Gestal, "SMART-1 Electric Propulsion: An Operational Perspective," AIAA-2006-5767, 9th International Conference on Space Operations, Rome, Italy, June 19-23, 2006.

[7] Brown, C. O., and E. Pinsley. "Further Experimental Investigations of a Cesium Hall-Current Accelerator." *AIAA Journal*, 3(5), May 1965.

[8] Janes, G. S., and R. Lowder. "Anomalous Electron Diffusion and Ion Acceleration in a Low-Density Plasma." *Physics of Fluids*, 9. P.1115, 1966.

[9] Morozov, A. I., Yu. Esipchuk, and A. Kapulkin. "Azimuthally Asymmetric Modes and Anomalous Conductivity in Closed Electron Drift Accelerators." *Soviet Physics Technical Physics*, 18, P.615, 1973.

[10] Kim, V., G. Popov, B. Arkhipov, V. Myrashko, O. Gorshkov, A. Koroteyev, V. Garkusha, A. Semenkin, and S. Tverdokhlebov, "Electric Propulsion Activity in Russia," IEPC-2001-05, 27th International Electric Propulsion Conference, Pasa-

dena, CA, October 2001.

[11] Hruby, V., J. Monheiser, B. Pote, P. Rostler, J. Kolencik, and C. Freeman, "Development of Low Power Hall Thrusters," AIAA-1999-3534, 30th AIAA Plasmadynamics and Lasers Conference, Norfolk, VA, June 28-July 1, 1999.

[12] Azziz, Y., Instrument Development and Plasma Measurements on a 200-Watt Hall Thruster Plume, S.M. Thesis, Massachusetts Institute of Technology, September 2003.

[13] Azziz, Y., and M. Martinez-Sanchez, "Plasma Measurements on a 200-Watt Hall Thruster Plume," IEPC-2003-140, 28th International Electric Propulsion Conference, Toulouse, France, March 17-21, 2003.

[14] Szabo, J., Y. Azziz, and M. Martinez-Sanchez, "Characterization of a High Specific Impulse Xenon Hall Effect Thruster," IEPC-2005-324, 29th International Electric Propulsion Conference, Princeton, NJ, October 31 - November 4, 2005.

[15] Samanta Roy, R. I., Numerical Simulation of Ion Thruster Plume Backflow for Spacecraft Contamination Assessment, Ph.D. Thesis, Massachusetts Institute of Technology, June 1995.

[16] Oh, D. Y., Computational Modeling of Expanding Plasma Plumes in Space Using a PIC-DSMC Algorithm, Sc.D. Thesis, Massachusetts Institute of Technology, February 1997.

[17] Gavryushin, V. M., and V. Kim. "Effect of the Characteristics of a Magnetic Field on the Parameters of an Ion Current at the Output of an Accelerator with Closed Electron Drift." *Soviet Physics Technical Physics*, 26(4):505-505, April 1981.

[18] Santi, M. M., Hall Thruster Plume Simulation Using a Hybrid-PIC Algorithm, S.M. Thesis, Massachusetts Institute of Technology, September 2003.

[19] Cheng, S., M. Santi, M. Celik, M. Martinez-Sanchez, and J. Peraire. "Hybrid PIC-DSMC simulation of a Hall thruster plume on unstructured grids." *Computer Physics Communications*, 164(2004):73-79, 2004.

[20] Cheng, S., and M. Martinez-Sanchez, "Comparison of Numerical Simulation to Hall Thruster Plume Shield Experiment," AIAA-2005-3635, 40th AIAA/ASME/SAE/ASEE Joint Propulsion Conference and Exhibit, Fort Lauderdale, FL, July 11-14, 2004.

[21] King, L., and A. Gallimore. "Mass Spectral Measurements in the Plume of an SPT-100 Hall Thruster." *Journal of Propulsion and Power*, 16(6):1086-1092, 2000.

[22] Sang-Wook, K., and A. Gallimore. "Plume Study of a 1.35-kW SPT-100 Using an

ExB Probe." *Journal of Spacecraft and Rockets*, 39(6):904-909, 2002.

[23] Absalamov, S. K., V. Andreev, T. Colbert, et al, "Measurement of Plasma Parameters in the Stationary Plasma Thruster (SPT-100) Plume and its Effect on Spacecraft Components," AIAA-1992-3156, 28th AIAA/ASME/SAE/ASEE Joint Propulsion Conference and Exhibit, Nashville, TN, July 6-8, 1992.

[24] Manzella, D. H., M. Sankovic, "Hall Thruster Ion Beam Characterization," AIAA-1995-2927, 31st AIAA/ASME/SAE/ASEE Joint Propulsion Conference and Exhibit, San Diego, CA, July 10-12, 1995.

[25] Walker, M., Effects of Facility Backpressure on the Performance and Plume of a Hall Thruster, Ph.D. Thesis, University of Michigan, 2005.

[26] Walker, M. L. R., A. Victor, R. Hofer, and A. Gallimore. "Effect of Backpressure on Ion Current Density Measurements in Hall Thruster Plumes." *Journal of Propulsion and Power*, 21(3):408-415, 2005.

[27] Walker, M. L. R., R. Hofer, and A. Gallimore, "The Effects of Nude Faraday Probe Design and Vacuum Facility Backpressure on the Measured Ion Current Density Profile of Hall Thruster Plumes," AIAA-2002-4253 38th AIAA/ASME/SAE/ASEE Joint Propulsion Conference and Exhibit, Indianapolis, IN, July 7-10 2002.

[28] Szabo, J., Fully Kinetic Numerical Modeling of a Plasma Thruster, Ph.D. Thesis, Massachusetts Institute of Technology, February 2001.

[29] Busek Company, "A High Isp Hall Thruster for Advanced In-Space Propulsion," SBIR Final Report NAS3-01124, Natick, MA, February, 2005.

[30] Haag, T., "Design of a Thrust Stand for High Power Electric Propulsion Devices," AIAA-1989-2829, 25th Joint Propulsion Conference, Monterey, CA, July 10-12, 1989.

[31] Haag, T. and M. Osborn, "RHETT/EPDM Performance Characterization," IEPC-1997-107, 25th International Electric Propulsion Conference, Cleveland, OH, August 24-28, 1997.

[32] Carlston, C., G. D. Magnuson, P. Mahadevan, D. E. Harrison. "Electron Ejection from Single Crystals Due to 1- to 10-keV Noble-Gas Ion Bombardment." *Physical Review*, 139(3A):729-736, 1965.

[33] Hofer, R., J. Haas, and A. Gallimore, "Ion Voltage Diagnostics in the Far-Field Plume of a High-Specific Impulse Hall Thruster," AIAA-2003-4556, 39th Joint Propulsion Conference, Huntsville, AL, July 20-23, 2003.

[34] Hofer, R., A. Gallimore, "Ion Species Fractions in the Far-Field Plume of a High-Specific Impulse Hall Thruster," AIAA-2003-5001, 39th Joint Propulsion Conference, Huntsville, AL, July 20-23, 2003.

[35] Gulczinski, F. S., Examination of the Structure and Evolution of Ion Energy Properties of a 5 kW Class Laboratory Hall Effect Thruster at Various Operational Conditions, Ph.D. Thesis, University of Michigan, 1999.

[36] King, L. B., Transport-property and Mass Spectral Measurements in the Plasma Exhaust Plume of a Hall-effect Space Propulsion System, Ph.D. Thesis, University of Michigan, 1998.

[37] Hutchinson, I. H., *Principles of Plasma Diagnostics*, Cambridge University Press, Cambridge, 1987.

[38] Reinsch, C. "Smoothing by Spline Functions." *Numerische Mathematic*, 10:177-183, 1967.

[39] Hofer, R. and R. Jankovsky, "The Influence of Current Density and Magnetic Field Topography in Optimizing the Performance, Divergence, and Plasma Oscillations of High Specific Impulse Hall Thrusters," IEPC-2003-142, 28th International Electric Propulsion Conference, Toulouse, France, March 17-21, 2003.

[40] McVey, J., E. Britt, S. Engelman, F. Gulczinski, E. Beiting, and J. Pollard, "Characteristics of the T-220HT Hall-Effect Thruster," AIAA 2003-5158, 39th Joint Propulsion Conference, Huntsville, AL, July 20-23, 2003.

[41] Raitses, Y., D. Staack, A. Dunaevsky, and N. Fisch. "Operation of a Segmented Hall Thruster with Low-Sputtering Carbon-Velvet Electrodes." *Journal of Applied Physics*, 99, 036103, February 2006.

[42] Myers, R., E. Pencil, V. Rawlin, M. Kussmaul, and K. Oden, "NSTAR ion thruster plume impacts assessment," AIAA-1995-2827, 31st Joint Propulsion Conference, San Diego, CA, July 10-12, 1995.

[43] Samanta Roy, R., D. Hastings, and N. Gatsonis, "Modeling of Ion Thruster Plume Contamination," AIAA-1994-3138, 30th Joint Propulsion Conference, Indianapolis, IN, June 27-29, 1994.

[44] Hutchinson, I. H., *8.613J Introduction to Plasma Physics class notes*, Massachusetts Institute of Technology, Fall 2001.

[45] Szabo, J., N. Warner, M. Martinez-Sanchez, and O. Batishchev, "A Full Particle-In-Cell Simulation Methodology for Axisymmetric Hall Effect Thruster Discharges," submitted to the AIAA Journal of Propulsion and Power, March, 2007.

[46] Banks, P. "Collision Frequencies and Energy Transfer - Ions."*Planetary and Space Science*, 14:1105-1122, 1966.

[47] Miller, J., S. Pullins, D. Levandier, Y. Chiu, and R. Dressler. "Xenon Charge Exchange Cross-Sections for Electrostatic Thruster Models." *Journal of Applied Physics*, 91(3):984-991, 2002.

[48] McVey, J., E. Britt, S. Engelman, F. Gulczinski, E. Beiting, and J. Pollard, "Characteristics of the T-220HT Hall-Effect Thruster," AIAA-2003-5158, 39th Joint Propulsion Conference, Huntsville, AL, July 20-23, 2003.

[49] Raitses, Y., D. Staack, A. Dunaevsky, L. Dorf, and N. Fisch, "Preliminary Results of Plasma Flow Measurements in a 2kW Segmented Hall Thruster," IEPC-2003-0139, 28th International Electric Propulsion Conference, Toulouse, France, March 17-21, 2003.

[50] King, L., A. Gallimore, and C. Marrese. "Transport-Property Measurements in the Plume of an SPT-100 Hall Thruster," *Journal of Propulsion and Power*, 14(3):327-335, 1998.

[51] Hofer, R., M. Walker, A. Gallimore, "A Comparison of nude and collimated Faraday Probes for Use with Hall Thrusters," IEPC-2001-20, 27th International Electric Propulsion Conference, Pasadena, CA, October 14-19, 2001.

[52] Rovey, J., M. Walker, A. Gallimore, and P. Peterson, "Evaluation of a Magnetically-Filtered Faraday Probe for Measuring the Ion Current Density Profile of a Hall Thruster," AIAA-2004-3948, 40th Joint Propulsion Conference, Fort Lauderdale, FL, July 11-14, 2004.

[53] Warner, N., Theoretical and Experimental Investigation of Hall Thruster Miniaturization, Ph.D. Thesis, Massachusetts Institute of Technology, June 2007.

[54] Cheng, S. Y., Computational Modeling of a Hall Thruster Plasma Plume in a Vacuum Tank, S.M. Thesis, Massachusetts Institute of Technology, February 2002.

[55] Celik, M., M. Santi, S. Cheng, M. Martinez-Sanchez, and J. Peraire, "Hybrid-PIC Simulation of a Hall Thruster Plume on an Unstructured Grid with DSMC Collisions," 28th International Electric Propulsion Conference, Toulouse, France, March 17-21, 2003.

[56] Jones, W. T., "An Open Framework for Unstructured Grid Generation," AIAA-2002-3192, 32nd AIAA Fluid Dynamics Conference and Exhibit, St. Louis, MO, 2002.

[57] Fox, J., Advances in Fully-Kinetic PIC Simulations of a Near-Vacuum Hall Thruster and Other Plasma Systems, Ph.D. Thesis, Massachusetts Institute of Technology,

September 2007.

[58] Martinez-Sanchez, M., *16.522 Space Propulsion class notes*, Massachusetts Institute of Technology, Spring 2002.

[59] McDaniel, E., *Collision Phenomena in Ionized Gases*, John Wiley & Sons Inc., New York, 1964.

[60] Korsun, A. G., and E. Tverdokhlebova, "The Characteristics of the EP Exhaust Plume in Space," AIAA-1997-3065 33rd AIAA/ASME/SAE/ASEE Joint Propulsion Conference and Exhibit, Seattle, WA, July 1997.

[61] Martinez-Sanchez, M., Personal Communication, May 2003.

[62] Cappelli, M. A., N. B. Meezan, and N. Gascon, "Transport Physics in Hall Plasma Thrusters," AIAA-2002-0485, 40th AIAA Aerospace Sciences Meeting and Exhibit, Reno, NV, January 2002.

[63] Cheng, S. Y., Modeling of Hall Thruster Lifetime and Erosion Mechanisms, Ph.D. Thesis, Massachusetts Institute of Technology, June 2007.

[64] Lide, D. R., *CRC Handbook of Chemistry and Physics 75th ed.*, CRC Press, Boca Raton, 1994.

Appendix A

MAGNETIC FIELD EFFECT ON THE BHT-1500 PLUME

Appendix A covers additional experimental characterization of the BHT-1500 plume. For the same discharge voltage and anode flow rate, it was observed that the thruster can be operated in two different modes. The two modes, which are controlled by the thruster's magnetic field, are differentiated by monitoring the amplitude of discharge oscillations and the thruster's plume structure. Measurements of current density and ion energy obtained with the thruster running in each mode are compared in order to correlate visual observations of the plume structure with plume data. Temperature measurements of the thruster's outer exit ring are also taken to help explain the effect of magnetic field on thruster discharge and plume structure.

A.1 Plume Structure

A.1.1 Jet Mode

After a discharge is established at a particular operating voltage and anode flow rate, the solenoid current controlling the thruster's magnetic field is adjusted to run the thruster in a stable mode. To maximize thrust efficiency, the magnetic field is adjusted to minimize discharge current. In the minimum discharge current setting, the plume is in a "jet mode" where the inner core jet is much larger, longer and brighter and the surrounding plasma is significantly reduced. A noticeable "spike" can be seen in the middle of the plume stretching from the thruster exit plane to approximately 20cm downstream. The discharge oscil-

lations exhibit a “breathing mode.” The frequency of discharge oscillations ranges from 25-30kHz and the amplitude of oscillations ranges from 1.2-3A. Figures A.1 and A.2 show a picture of the thruster plume and a snapshot of the discharge oscillations respectively for the BHT-1500 operating in the jet mode. All measurements discussed in Chapters 3-6 were obtained with the thruster operating in the jet mode.

A.1.2 Collimated Mode

In an effort to reduce the amplitude of discharge oscillations for the BHT-1500 operating at a particular discharge voltage and anode flow rate, the solenoid current controlling the thruster’s magnetic field is adjusted. It was observed that when the thruster is operating in jet mode, reducing the solenoid current decreases the amplitude of the discharge oscillations. The plume structure also drastically changes. In this mode, there is no spike in the middle of the beam. The color of the beam is sharper on the outside. The plasma is cylindrical and converges to a jet approximately 20cm away from the thruster exit plane. This mode is referred to as the “collimated mode.” The thruster performance in the collimated mode is lower than in the jet mode. For example, at a discharge voltage of 400V and an anode flow rate of 2.44mg/s, thrust decreases by 5% when the thruster is operated in the collimated mode compared to the jet mode. The thruster performance is not thoroughly characterized in this research, however, the 5% drop in measured thrust is also observed at a discharge voltage of 500V. Figures A.3 and A.4 show a picture of the thruster plume and a snapshot of the discharge oscillations respectively for the BHT-1500 operating in the collimated mode.

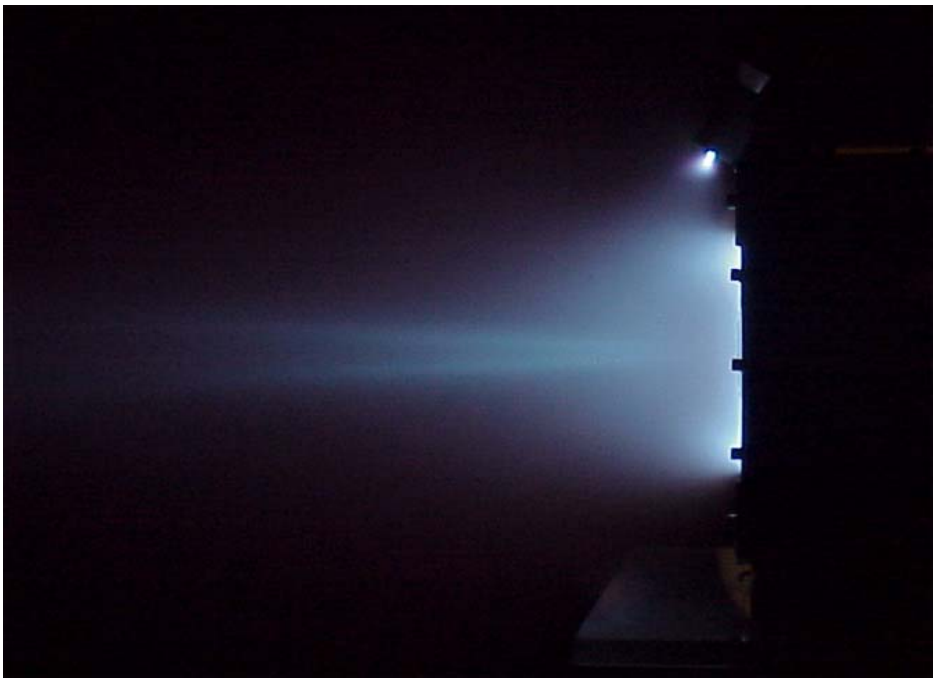

Figure A.1 Picture of the BHT-1500 operating in jet mode.

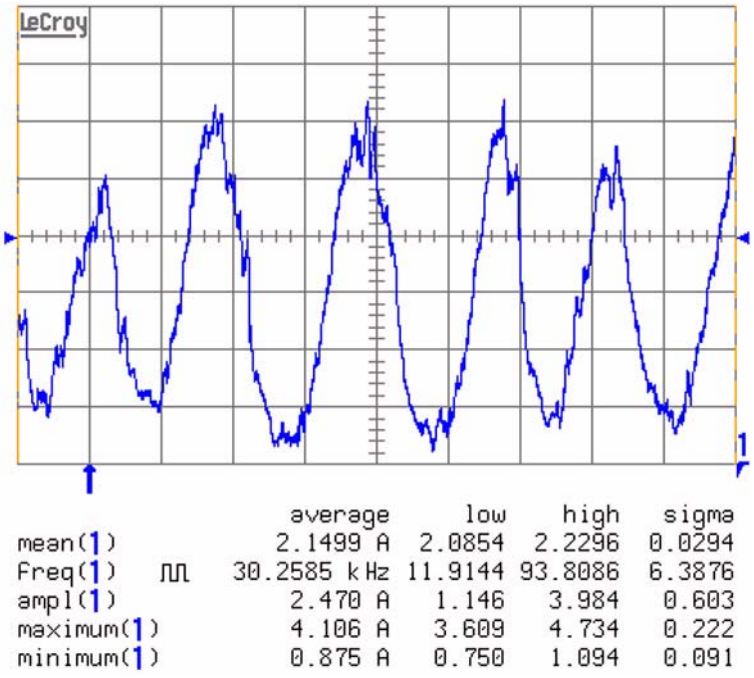

Figure A.2 Discharge oscillations of the thruster operating in jet mode. V_d = 500V and $\dot{m}_a$ = 2.44mg/s.

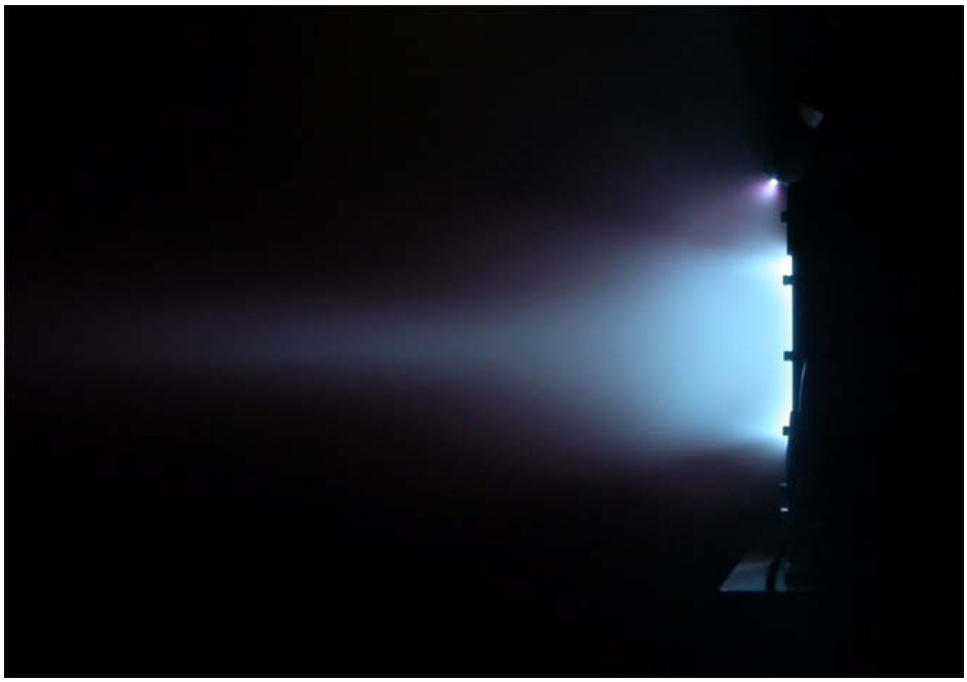

Figure A.3 Picture of the BHT-1500 operating in collimated mode.

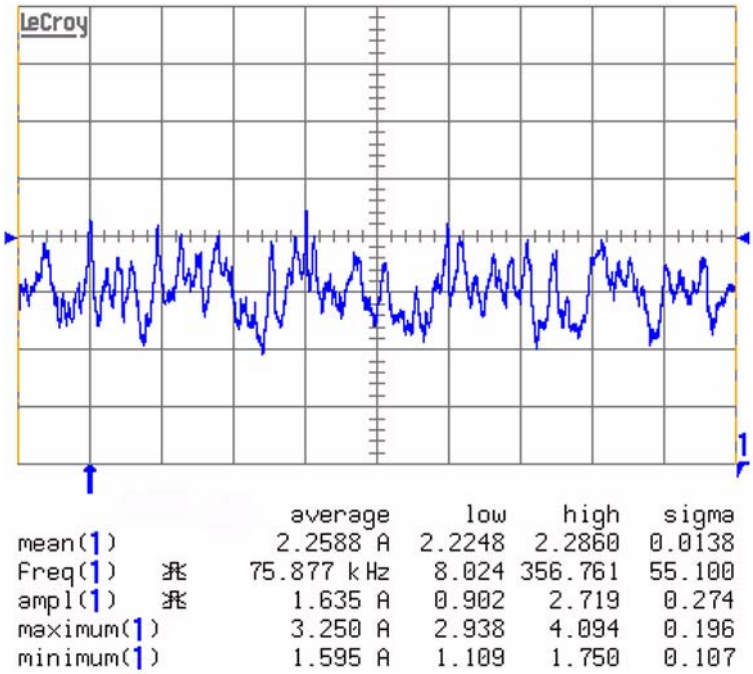

Figure A.4 Discharge oscillations of the thruster operating in collimated mode. V_d = 500V and $\dot{m}_a$ = 2.44mg/s.

It is important to note that the collimated mode is only observed after the thruster is warmed up for over an hour. Attempts to run the thruster in the collimated mode at the start of the thruster were unsuccessful. Furthermore, the thruster is operated in jet and collimated modes for voltages ranging from 400-1000V. At a discharge voltage of 300V, the thruster operates only in jet mode. Finally, it should also be noted that when the thruster is operating in jet mode, the thruster oscillations can be reduced by increasing the magnetic field, which does not result in the thruster switching from the jet to the collimated mode. To ensure that the thruster is operating in the collimated mode, the plume structure should be visually inspected and the thruster's oscillations should be monitored.

A.2 Plume Measurements

Measurements shown in this appendix are taken with the thruster equipped with Borosil (BN-SiO_2) Grade M exit rings. It should be noted that the thruster equipped with Boron Nitride (BN) Grade AX05 exit rings is also able to operate in both the jet and collimated modes. Plume characterization of the two modes is performed with a Faraday probe and an RPA. Both probes are placed 1m downstream from the exit plane of the thruster. The Faraday probe is swept from –90° to 90° in 3° increments whereas the RPA is swept from –90° to 0° in 10° increments.

A.2.1 Current Density

Figures A.5-A.11 compare current densities obtained with the thruster operating in jet and collimated modes for discharge voltages of 400-1000V. For all measurements, the anode flow rate is 2.44mg/s, the sweep radius is 1m, and the background pressure is 7×10^{-6} Torr. As shown in the figures, the "jet mode" current density is different than the "collimated mode" current density. In the jet mode, the current density distribution is smoother with no local minimum in the shoulders. In the collimated mode, the shoulders are more pronounced stretching from 40-70°. The beam of the collimated mode is narrower than in the jet mode, as indicated by comparison of current density for angles between centerline and 40°.

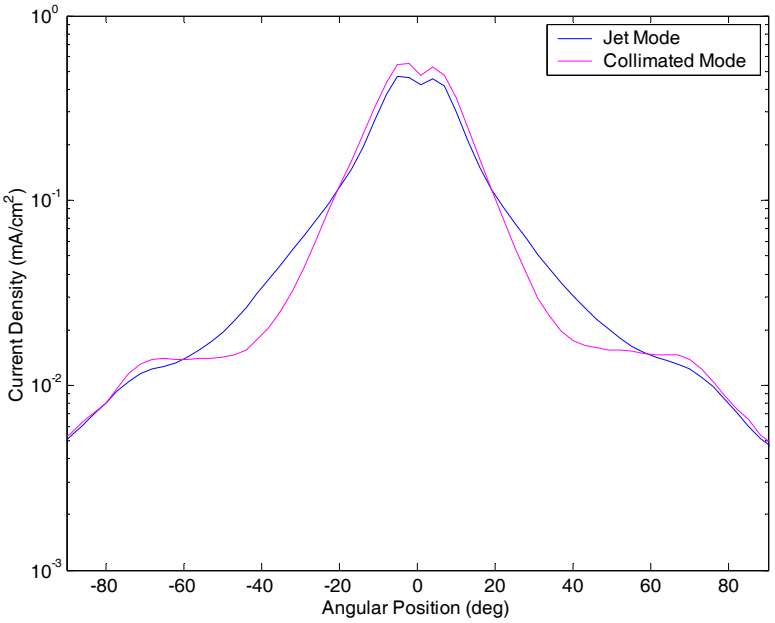

Figure A.5 Comparison of current densities obtained with the thruster operating in jet and collimated modes. V_d = 400V, $\dot{m}_a$ = 2.44mg/s, P = 7×10^{-6} Torr and sweep radius = 1m.

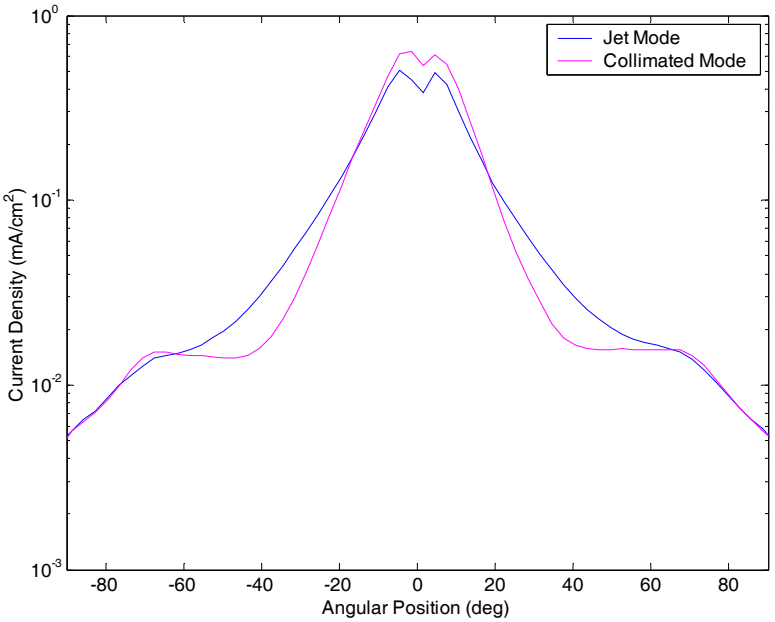

Figure A.6 Comparison of current densities obtained with the thruster operating in jet and collimated modes. V_d = 500V, $\dot{m}_a$ = 2.44mg/s, P = 7×10^{-6} Torr and sweep radius = 1m.

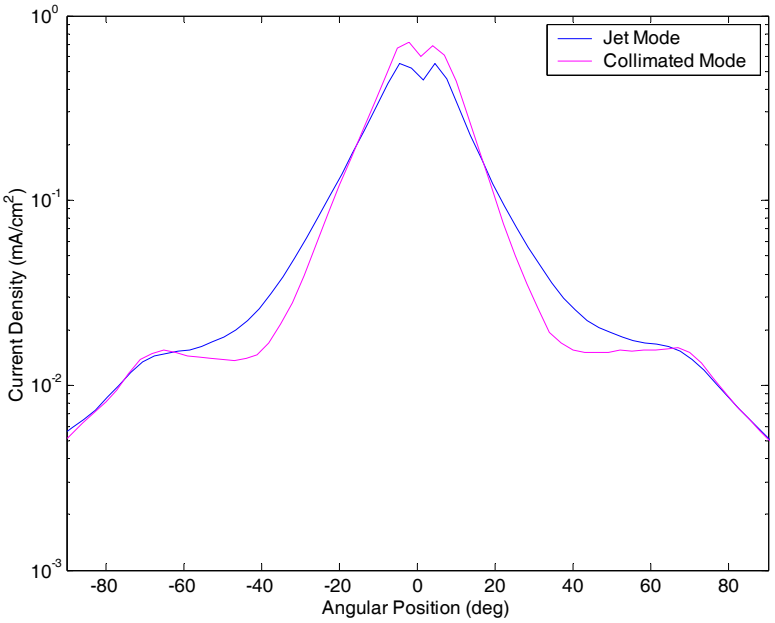

Figure A.7 Comparison of current densities obtained with the thruster operating in jet and collimated modes. V_d = 600V, $\dot{m}_a$ = 2.44mg/s, P = 7×10^{-6} Torr and sweep radius = 1m.

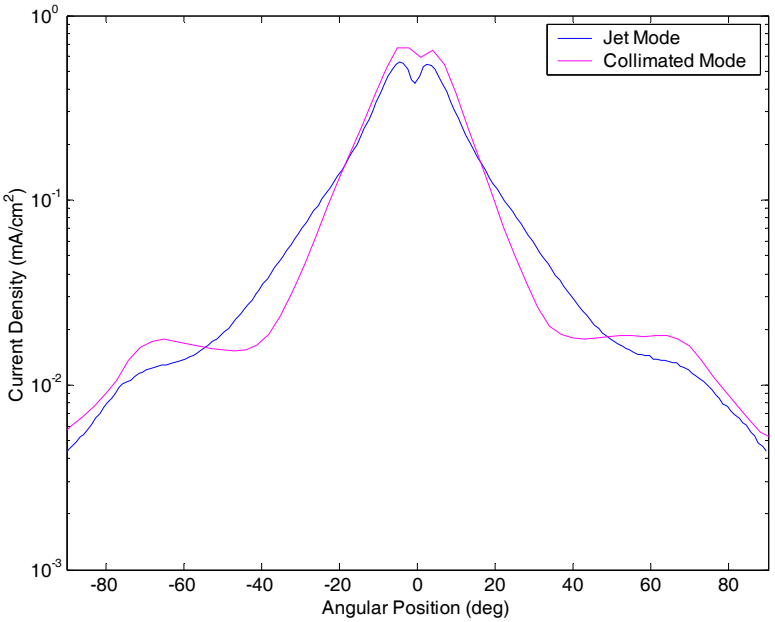

Figure A.8 Comparison of current densities obtained with the thruster operating in jet and collimated modes. V_d = 700V, $\dot{m}_a$ = 2.44mg/s, P = 7×10^{-6} Torr and sweep radius = 1m.

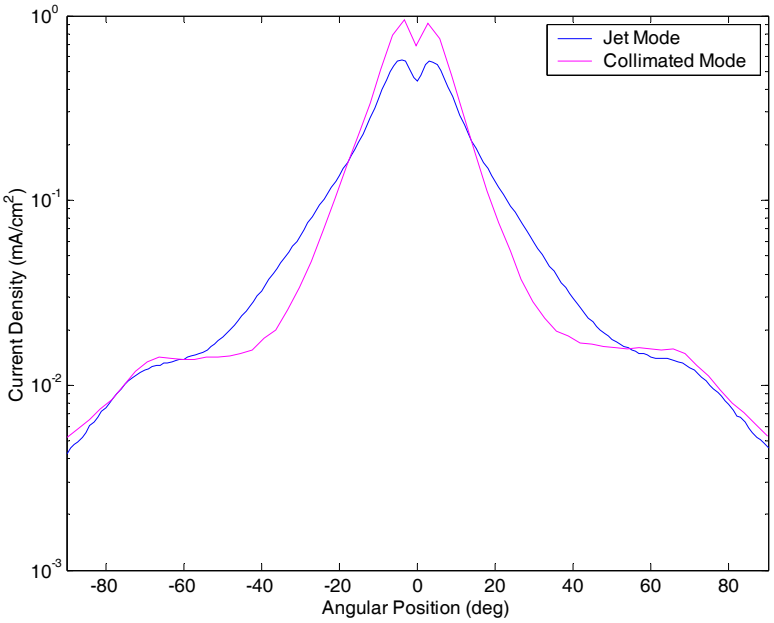

Figure A.9 Comparison of current densities obtained with the thruster operating in jet and collimated modes. V_d = 800V, $\dot{m}_a$ = 2.44mg/s, P = 7×10^{-6} Torr and sweep radius = 1m.

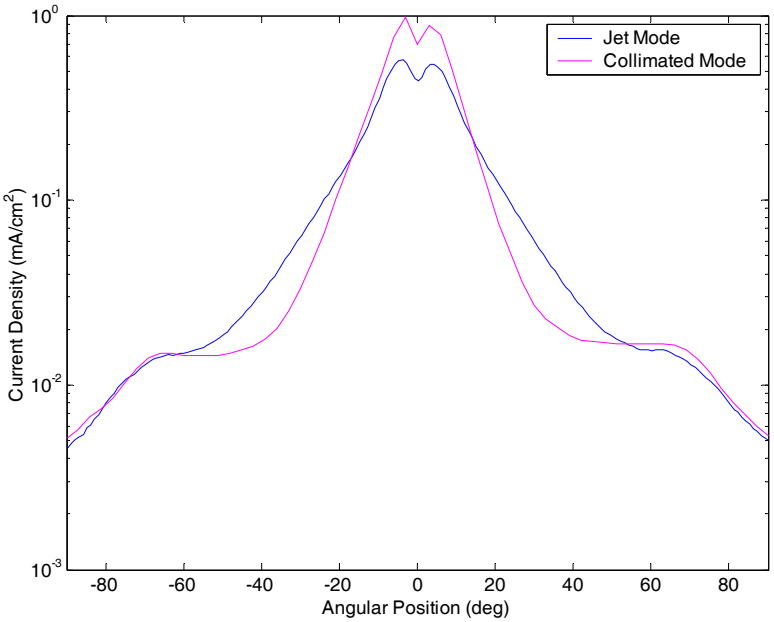

Figure A.10 Comparison of current densities obtained with the thruster operating in jet and collimated modes. V_d = 900V, $\dot{m}_a$ = 2.44mg/s, P = 7×10^{-6} Torr and sweep radius = 1m.

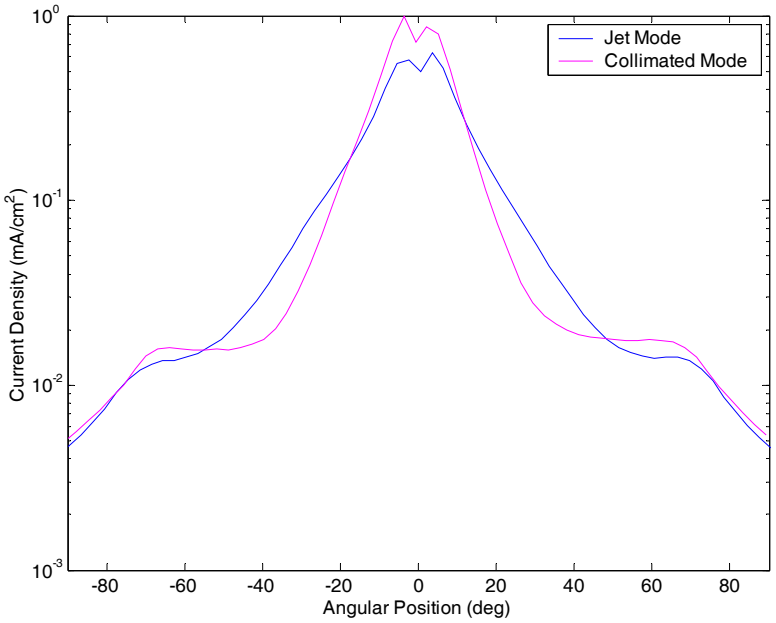

Figure A.11 Comparison of current densities obtained with the thruster operating in jet and collimated modes. V_d = 1000V, $\dot{m}_a$ = 2.44mg/s, P = 7×10^{-6} Torr and sweep radius = 1m.

A.2.2 Ion Energy Distribution

The ion energy distribution provides insight into the structure of the ion beam at each mode. Figures A.12-A.15 compare ion energy distributions obtained with the thruster operating in jet and collimated modes for discharge voltages of 400-700V. Similarly to Faraday probe measurements, RPA measurements are also taken at an anode flow rate of 2.44mg/s, a sweep radius of 1m, and a background pressure of 7×10^{-6} Torr. The structure of the ion energy distribution in jet mode is discussed in Chapter 3. This section covers the ion energy distribution for the collimated mode and highlights the difference in energy distribution for the two modes.

In the collimated mode, the structure of the ion energy distribution at large angles consists of two low energy peaks, which likely indicate two different low energy populations. The reason for the two peaks is not well understood. A possible explanation is that ions undergo charge exchange collisions in the plume and inside the acceleration region of the

thruster. The charge exchange ions created in the plume when the thruster is running in collimated mode have similar energies to the ones created in jet mode. The other low energy population is made up of ions born at higher potentials inside the discharge channel. In the mid-angle region, the plume is composed of source ions and intermediate energy ions. The energy distributions obtained at angles of −40° and −30° show that the plume is made of ions that have higher energies than “conventional” charge exchange ions. These ions can be a combination of elastic scattering ions, charge exchange ions inside the thruster channel, or source ions born at low potentials. At angles between centerline and −20°, the plume is made up of only source ions.

Comparing the jet mode to the collimated mode, source ions are contained within a smaller angle, which means the plume is narrower. This is also observed with Faraday probe measurements. The shoulders of the current density in the collimated mode consist of only low energy ions whereas source ions exist in the shoulders of the jet mode current density. For angles between centerline and −20°, the peak of source ion distribution in the collimated mode is higher than in the jet mode. This is also consistent with Faraday probe measurements since the current density for angles between centerline and −20° in the collimated mode is higher than for the jet mode.

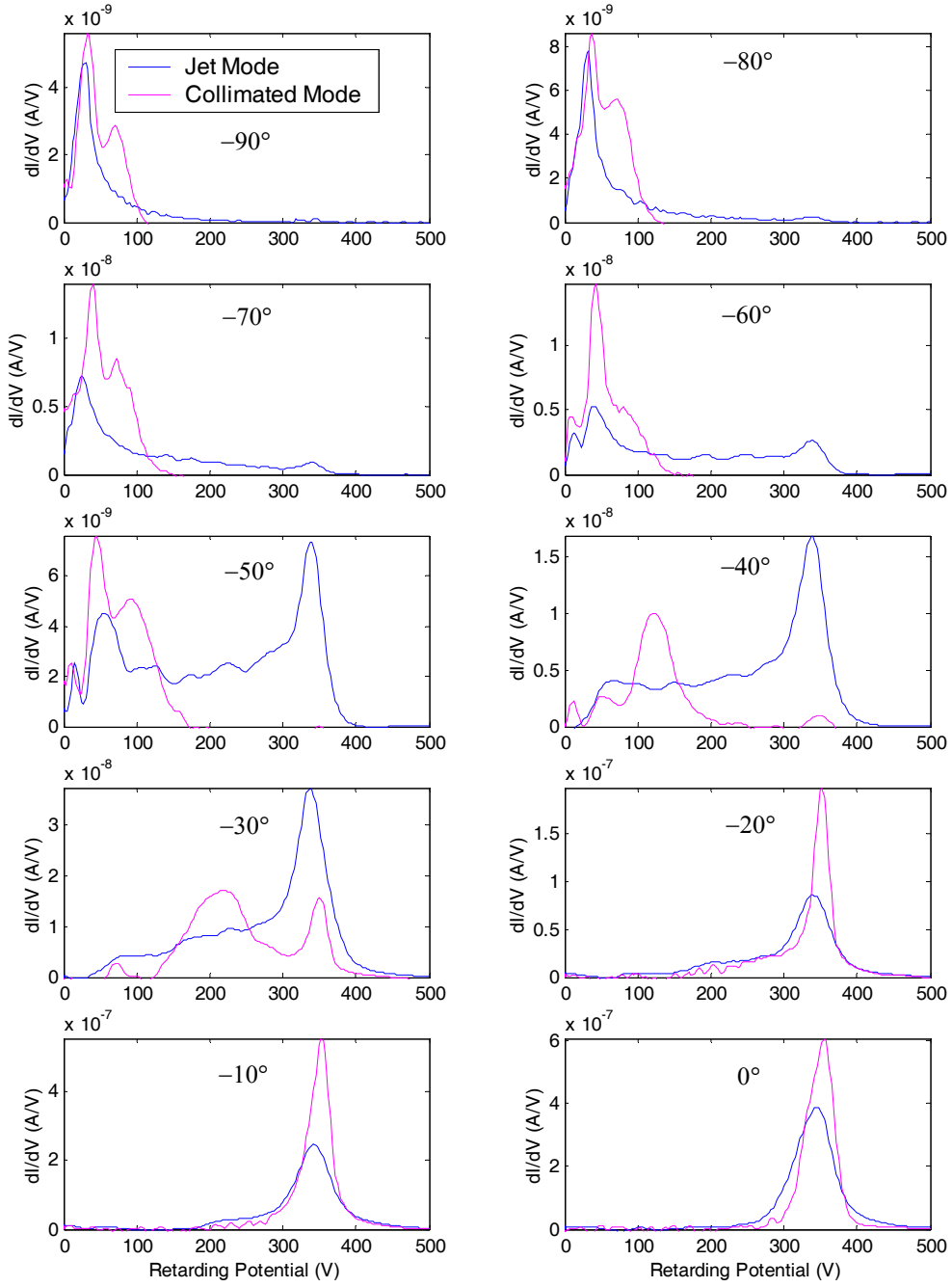

Figure A.12 Comparison of ion energy distributions obtained with the thruster operating in jet and collimated modes. V_d = 400V, $\dot{m}_a$ = 2.44mg/s, P = 7×10^{-6} Torr and sweep radius = 1m. The retarding potential is referenced with respect to the facility ground whereas the discharge voltage is referenced with respect to the cathode potential, which is approximately –20V.

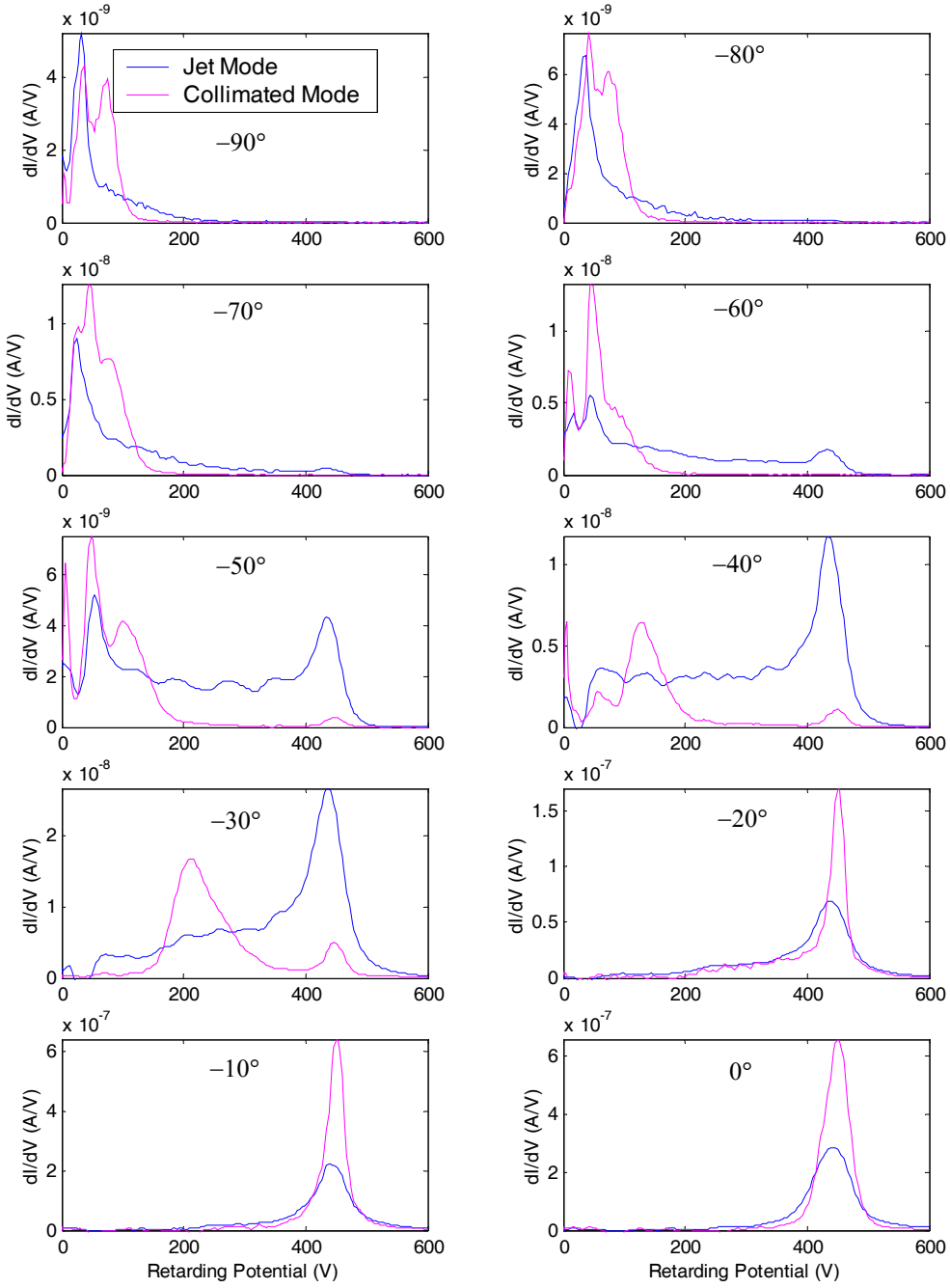

Figure A.13 Comparison of ion energy distributions obtained with the thruster operating in jet and collimated modes. V_d = 500V, $\dot{m}_a$ = 2.44mg/s, P = 7×10^{-6} Torr and sweep radius = 1m. The retarding potential is referenced with respect to the facility ground whereas the discharge voltage is referenced with respect to the cathode potential, which is approximately –21V.

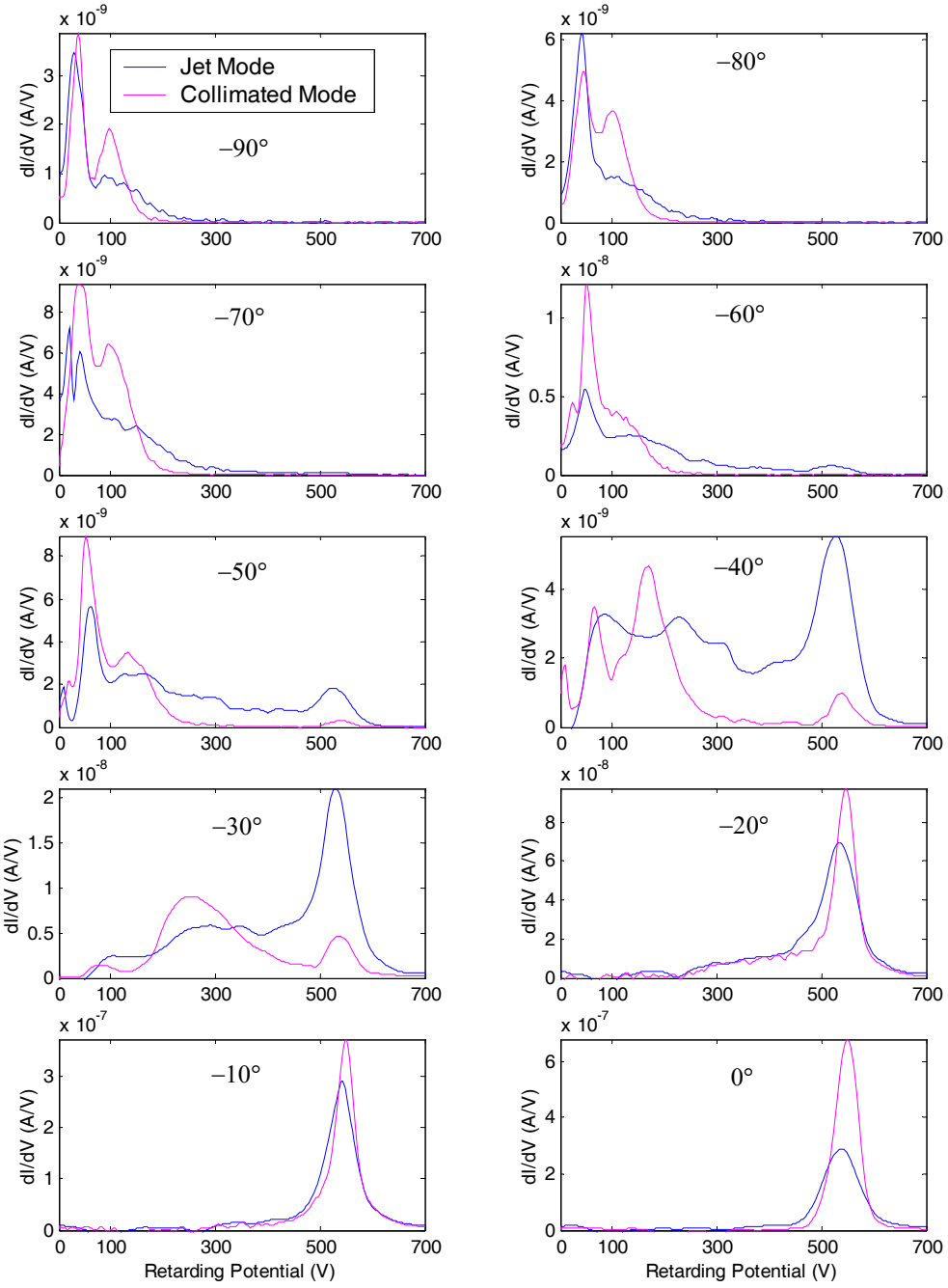

Figure A.14 Comparison of ion energy distributions obtained with the thruster operating in jet and collimated modes. V_d = 600V, $\dot{m}_a$ = 2.44mg/s, P = 7×10^{-6} Torr and sweep radius = 1m. The retarding potential is referenced with respect to the facility ground whereas the discharge voltage is referenced with respect to the cathode potential, which is approximately –22V.

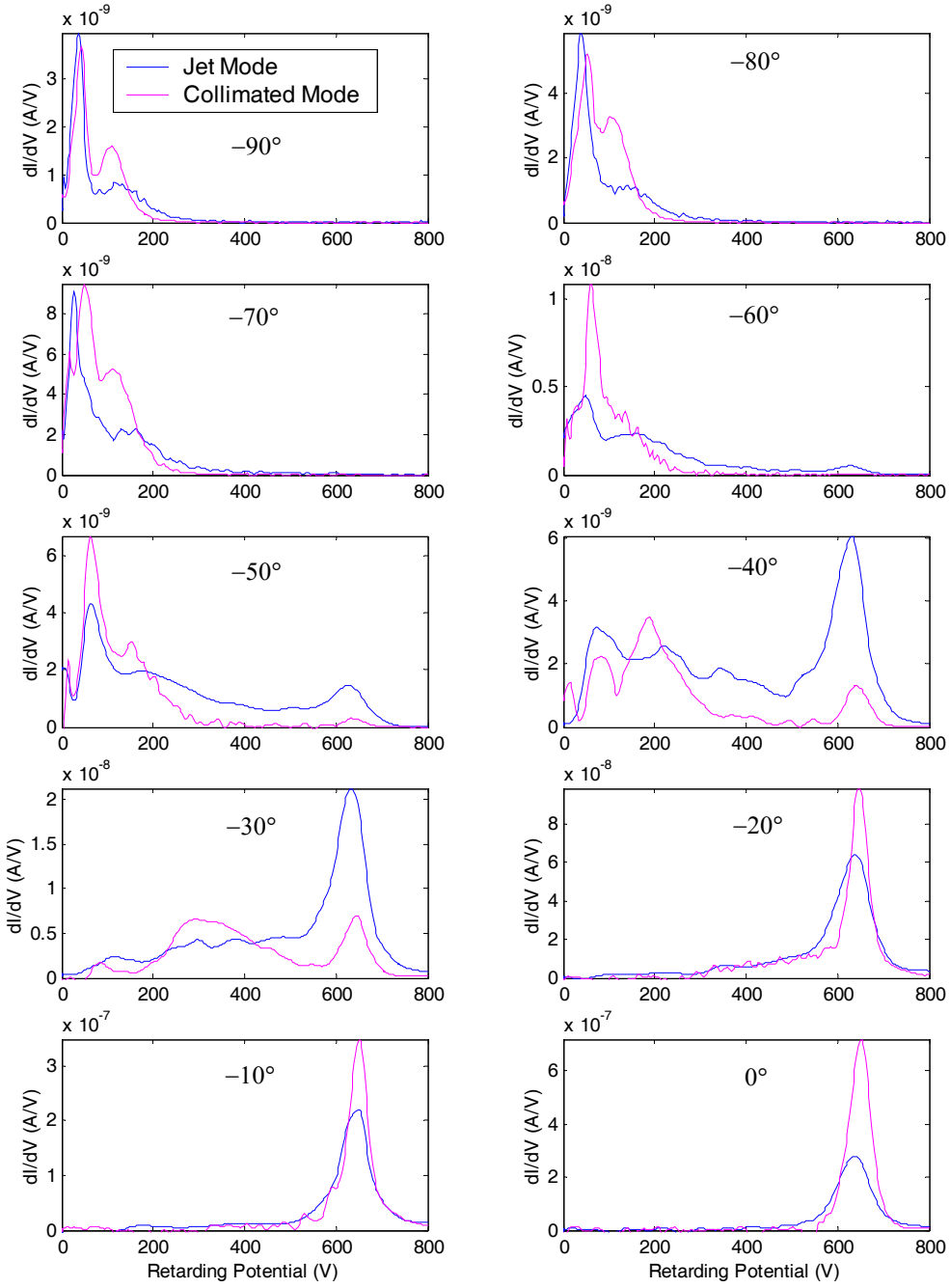

Figure A.15 Comparison of ion energy distributions obtained with the thruster operating in jet and collimated modes. V_d = 700V, $\dot{m}_a$ = 2.44mg/s, P = 7×10^{-6} Torr and sweep radius = 1m. The retarding potential is referenced with respect to the facility ground whereas the discharge voltage is referenced with respect to the cathode potential, which is approximately –20V.

A.2.3 Discussion

As mentioned earlier, the thruster can operate in the collimated mode only after it reaches a thermal steady state. As the thruster warms up, the permeability of the magnetic core decreases, which can affect both the magnitude and the shape of the magnetic field. The topology of the magnetic field for the two modes is likely different. The effect of the magnetic field topology in shaping the plume is currently not well understood. A possible explanation for the change in plume shape with changes in magnetic field topology is that the magnetic field changes the position of the ionization region. It is believed that the ionization region is closer to the anode in the collimated than the jet mode, as shown in Figure A.16.

Based on this hypothesis, ion loss to the thruster walls should be greater for the collimated than the jet mode. As ions are lost to the wall, they are reflected as neutrals, creating a "cloud" of neutrals near the walls. Some of these neutrals can either become ionized or undergo charge exchange collisions downstream from the ionization region. They are then accelerated with a potential that is smaller than the full discharge voltage. These newly created ions have energies smaller than the source ions and are measured with the RPA as separate ion populations. The term collimated is used to describe this mode because it is thought that a portion of the beam is lost to the walls. It is believed that the beam is narrower in the collimated mode not because the magnetic field focuses the ions towards the centerline but because ions traveling to large angles are lost to the walls.

In the jet mode, the ionization region likely occurs closer to the thruster exit. Inside the discharge cavity, ions travelling to large angles are able to exit the thruster without being lost to the walls. The thrust measured in this mode is higher than in the collimated mode, which likely verifies that more ions leave the thruster exit in the jet mode that in the collimated mode.

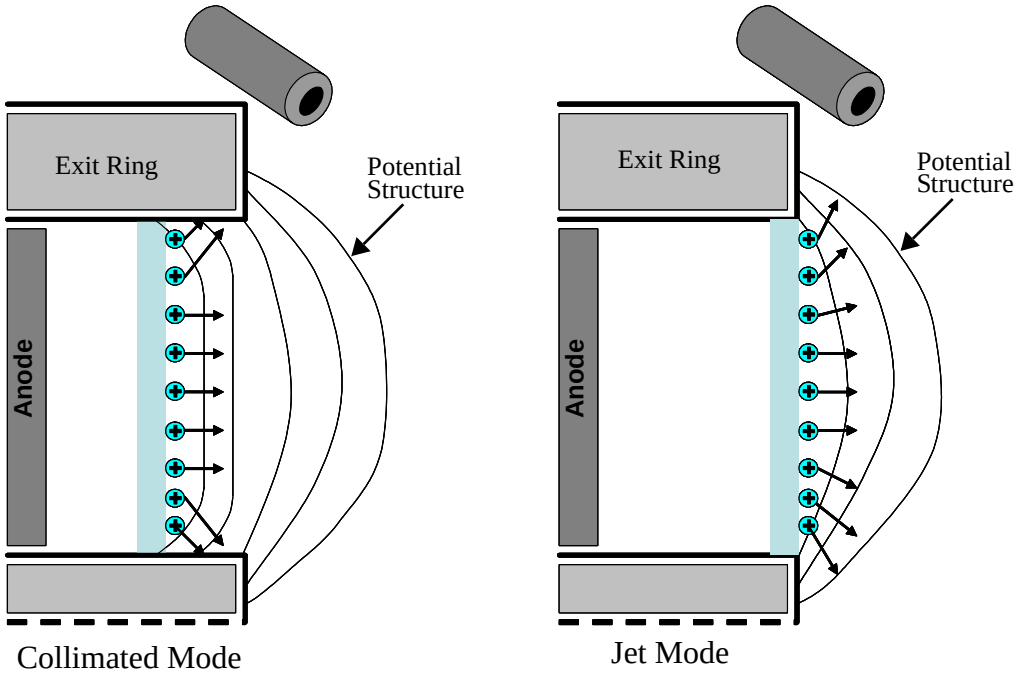

Figure A.16 Schematic of the ionization region in collimated and jet modes. The ionization region is thought to be closer to the anode for the collimated mode, which results in greater ion loss to the thruster walls.

A.3 Thermal Measurements

To verify that ion loss to the thruster walls is greater for the collimated mode than for the jet mode, the outer exit ring of the thruster is equipped with a thermocouple to measure its temperature. The idea is that greater ion loss to the thruster walls yields higher wall temperatures. Thus, it is expected that the temperature of the outer exit ring is higher when the thruster is operating in collimated mode rather than jet mode. Figure A.17 shows a schematic of the thermocouple setup. The thermocouple used is a type K capable of measuring temperatures up to 1250°C. Data obtained with the thermocouple is acquired by a 22-bit HP34970A Agilent data logger.

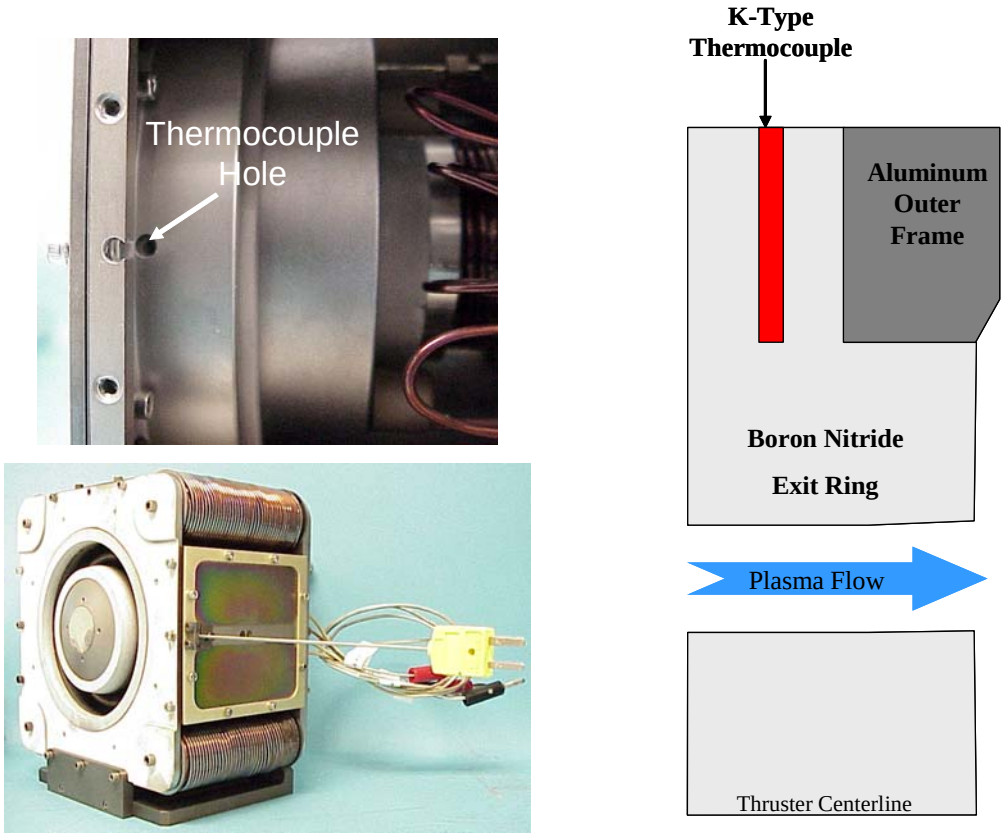

Figure A.17 Schematic of the thermocouple setup used to measure the outer exit ring temperature.

Figure A.18 shows temperature measurements obtained as the thruster's discharge voltage is increased from 300-800V in 100V increments. The thruster is run in both collimated and jet modes starting from a discharge voltage of 400V. The measurements show that the temperature of the exit rings increases with voltage. This occurs because an increase in discharge voltage, while maintaining a constant flow rate, increases the thruster's power, which translates into an increase in power of ions lost to the thruster walls.

The measurements in Figure A.18 are divided into several plots representing temperature measurements at each discharge voltage. The measurements plotted in Figure A.19 show that the thruster reaches a thermal steady state after 2 hours of operation. Furthermore, Figures A.19-A.24 depict that the exit ring temperature is higher in the case of the thruster running in the collimated mode than in the jet mode for all discharge voltages. It can be inferred from these results that ion loss to the thruster walls is greater for the collimated mode than the jet mode. As explained earlier, one possible reason that ion loss is greater for the collimated mode is that the ionization region is upstream, as shown in Figure A.16, which increases the likelihood of ions hitting the thruster channel walls.

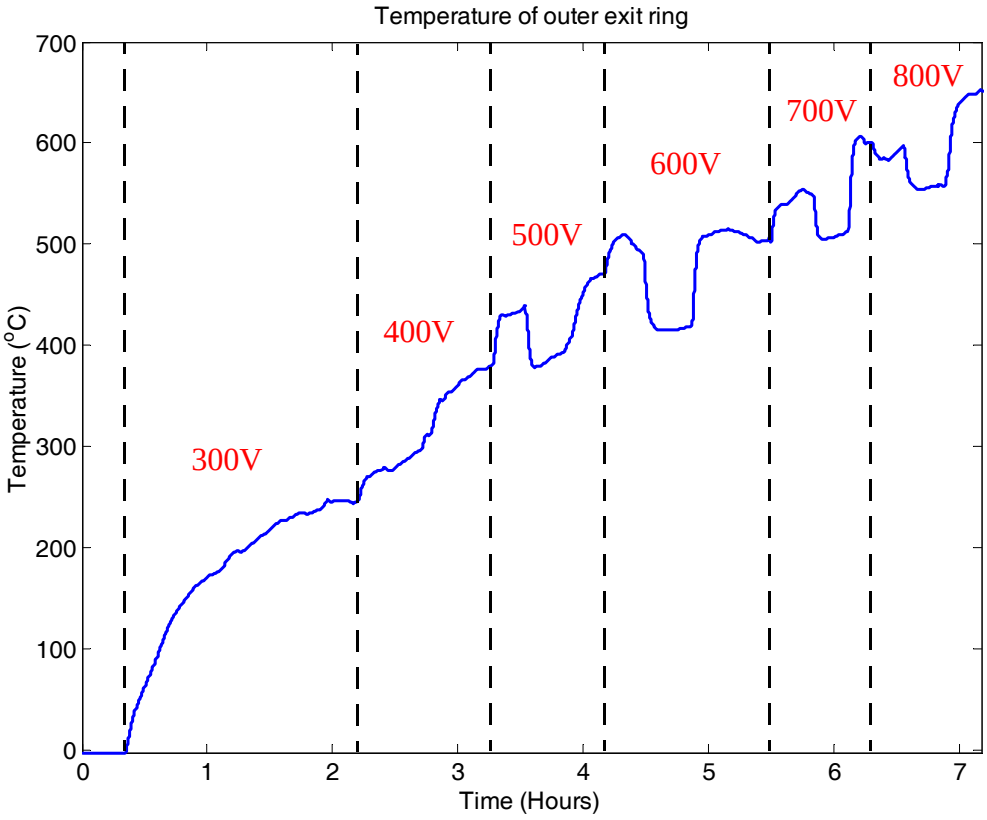

Figure A.18 Outer exit ring temperature measurements. The thruster's discharge voltage is increased from 300-800V in 100V increments. The thruster is operated in collimated and jet modes starting from a discharge voltage of 400V. During these measurements, the anode flow rate is kept constant at 2.44mg/s. The data plotted in this figure are divided into several plots representing temperature measurements at each discharge voltage and show when the thruster is operating in jet and collimated modes.

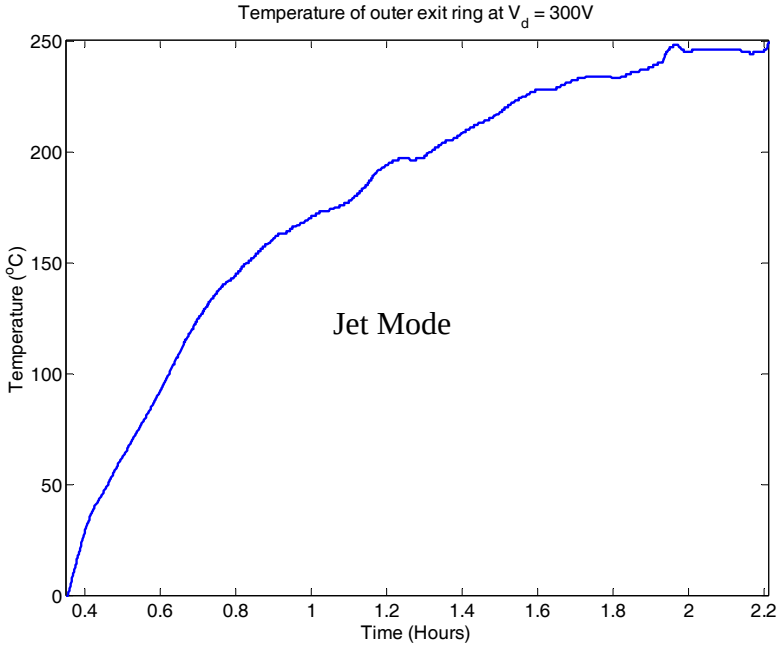

Figure A.19 Outer exit ring temperature of the thruster operating at a discharge voltage of 300V and an anode flow rate of 2.44mg/s. The thruster is run in jet mode.

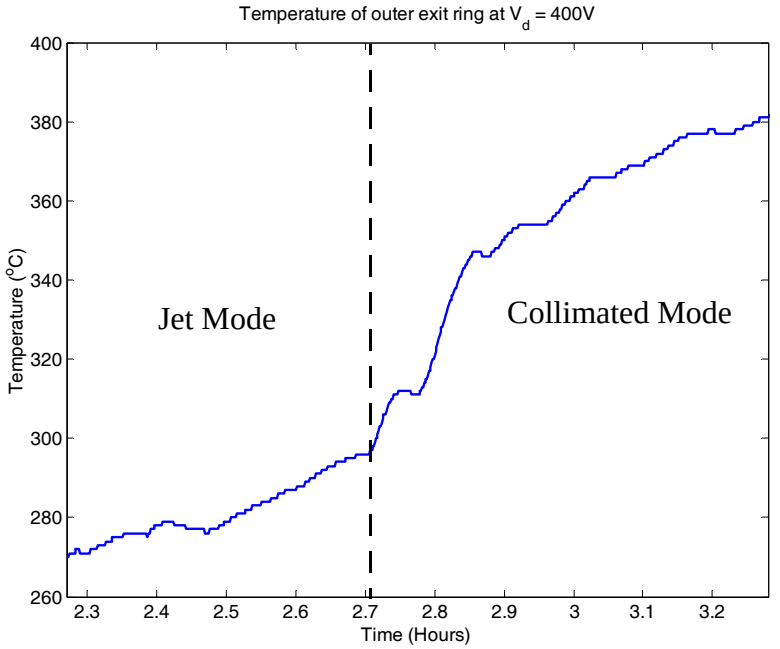

Figure A.20 Outer exit ring temperature of the thruster operating at a discharge voltage of 400V and an anode flow rate of 2.44mg/s. The thruster is run in both jet and collimated modes.

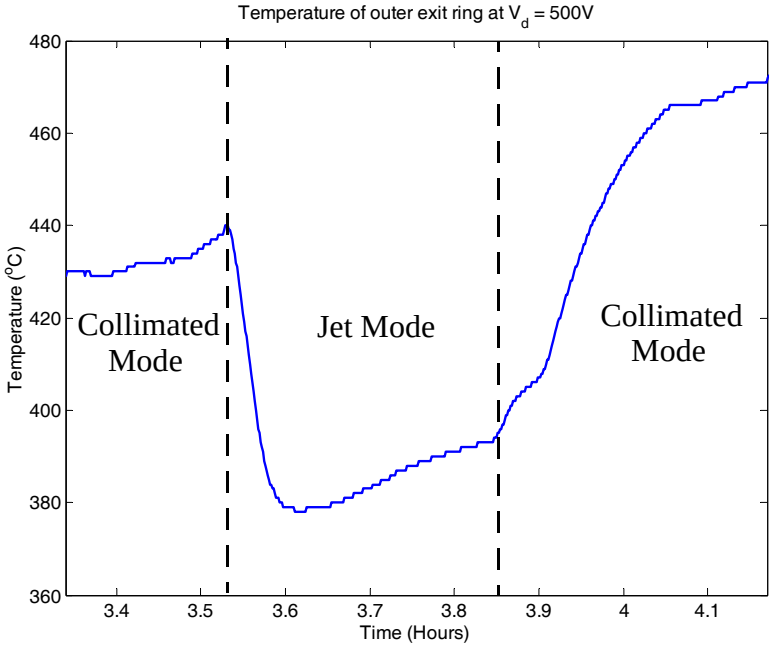

Figure A.21 Outer exit ring temperature of the thruster operating at a discharge voltage of 500V and an anode flow rate of 2.44mg/s. The thruster is run in both jet and collimated modes.

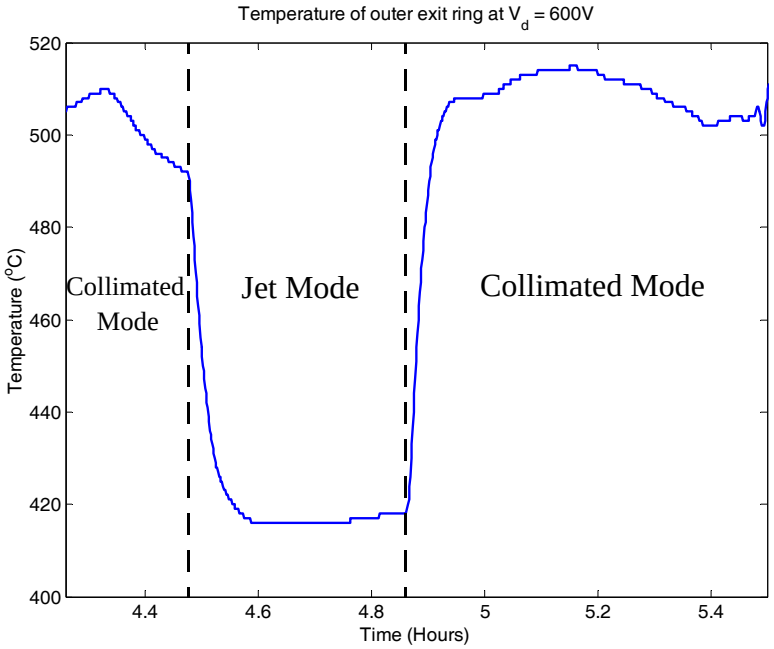

Figure A.22 Outer exit ring temperature of the thruster operating at a discharge voltage of 600V and an anode flow rate of 2.44mg/s. The thruster is run in both jet and collimated modes.

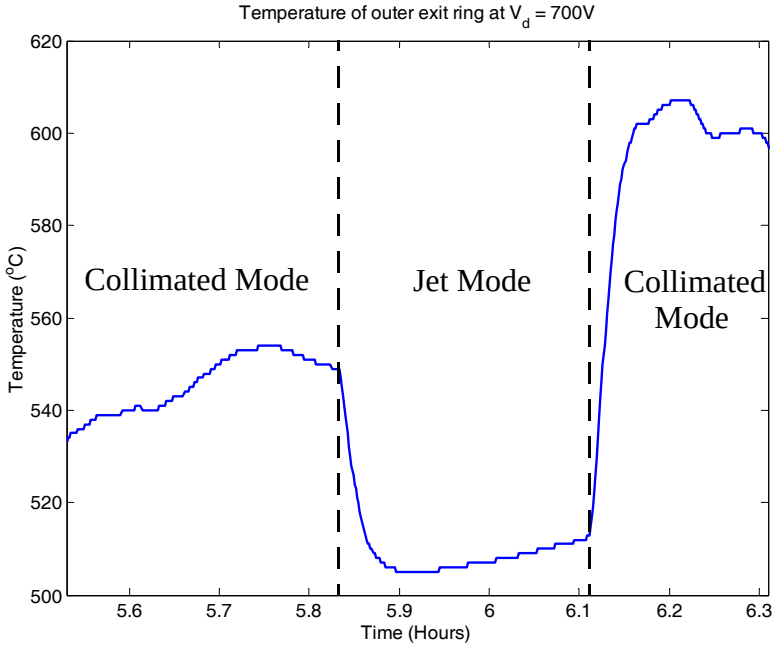

Figure A.23 Outer exit ring temperature of the thruster operating at a discharge voltage of 700V and an anode flow rate of 2.44mg/s. The thruster is run in both jet and collimated modes.

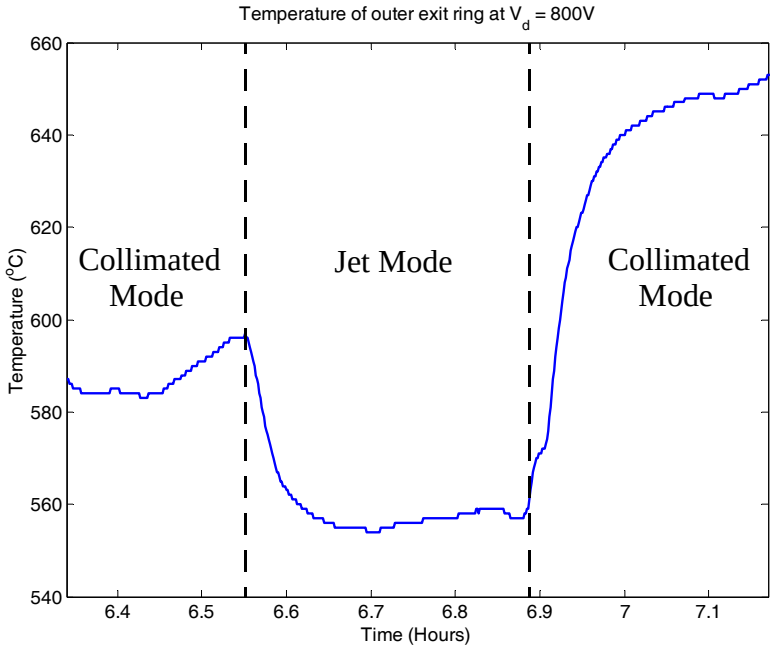

Figure A.24 Outer exit ring temperature of the thruster operating at a discharge voltage of 800V and an anode flow rate of 2.44mg/s. The thruster is run in both jet and collimated modes.

A.4 Summary

In this appendix, it is shown that the thruster can be operated in two modes by adjusting the magnetic field. The first mode is a jet mode, achieved by adjusting the magnetic field to minimize the discharge current. The second mode is a collimated mode, which is obtained by reducing the magnetic field from the jet mode magnetic field setting. The collimated mode is only achieved when the thruster reaches its thermal steady state. The plume measurements show that the two modes have drastically different current density and ion energy distributions. The measurements also show that the beam of the collimated mode is narrower than of the jet mode. The thruster operates in different modes probably due to movement of the ionization region. As the magnetic field is adjusted to run the thruster in one mode, the location of the ionization region is affected. Thermal measurements show that the temperature of the exit rings is higher in the collimated mode than in the jet mode. This indicates that ion loss in the collimated mode is higher, and that the ionization region of the collimated mode is likely closer to the anode.

The benefit of operating the thruster in the collimated mode is the narrower beam. However, it is believed that the plume is narrower because the beam is collimated by the thruster walls, which results in higher erosion and lower thrust. Therefore, the thruster should be operated in jet mode for higher performance and lifetime. The data shown in this appendix serve as a database of measurements from different thruster operating conditions to support ongoing computational models. Numerical modeling of the thruster running in the two modes may help explain the reason the thruster switches from one mode to another. These data also stress the importance of an accurate source model for proper plume modeling. When comparing plume simulation results to experimental data, it is important that the source model includes all the effects of the magnetic field to ensure that the simulation and the experiments are being compared under the same conditions.